Sawtooth Generated Magnetic Islands and the Properties of the Snowflake Divertor

THÈSE N^{O} 6272 (2014)

PRÉSENTÉE LE 15 AOÛT 2014

À LA FACULTÉ DES SCIENCES DE BASE

CRPP - PHYSIQUE DU TOKAMAK TCV

PROGRAMME DOCTORAL EN PHYSIQUE

ÉCOLE POLYTECHNIQUE FÉDÉRALE DE LAUSANNE

POUR L'OBTENTION DU GRADE DE DOCTEUR ÈS SCIENCES

PAR

Gustavo PAGANINI CANAL

acceptée sur proposition du jury:

Prof. V. Savona, président du jury

Dr B. Duval, Dr H. Reimerdes, directeurs de thèse

Dr J. Graves, rapporteur

Dr A. Leonard, rapporteur

Prof. H. Zohm, rapporteur

ÉCOLE POLYTECHNIQUE
FÉDÉRALE DE LAUSANNE

Suisse

2014

Abstract

The potential of nuclear fusion to provide a practically inexhaustible source of energy has motivated scientists to work towards developing nuclear fusion power plants. In this thesis, two outstanding issues encountered on the road to nuclear fusion power plants are addressed: triggering of neoclassical tearing modes (NTMs) by sawteeth (ST) and handling of the exhaust power in the divertor.

The experiments presented in this thesis were performed on the Tokamak à Configuration Variable (TCV), which is a medium sized tokamak that has been operational since 1992 at the CRPP/EPFL in Lausanne, Switzerland. TCV was designed to study the effects of plasma shape on the plasma behavior and, for this reason, features a highly elongated rectangular vacuum vessel and a full set of independently powered shaping coils. Another unique feature of TCV is a high power and current drive capability provided by a flexible electron cyclotron waves system, designed to access a wide range of plasma shapes. Furthermore, with its high degree of operational flexibility, TCV recently became one of the few machines able to test new divertor configurations without hardware modifications, e.g. the snowflake (SF) and the x-divertor.

The first issue addressed in this thesis is the seeding of NTMs by ST crashes. Many tokamaks observed that ST, of sufficient duration, may trigger NTMs that can lead to plasma performance degradation and/or disruptions depending on the plasma conditions. From constraints imposed on the plasma performance, the onset of NTMs poses a threat to the main goal of ITER, which is to demonstrate sustained burning plasma operation with a fusion power gain factor $Q \geq 10$. TCV's ability to accurately control the period of individual ST was exploited to examine the seeding mechanism of NTMs by ST for the purpose of finding routes to safer operation at higher plasma pressures. The electron cyclotron resonance heating and current drive (ECH and ECCD) system of TCV was used to trigger NTMs under controllable conditions and provided an excellent environment for the study of the NTM triggering by ST crashes. Results show evidence for an extremely fast formation of seed islands with poloidal/toroidal mode numbers $m/n = 3/2$ and $2/1$ within a few microseconds after a ST crash. ST with a longer period, were observed to generate larger seed islands but also increase the plasma stability to conventional tearing modes. These effects compete in TCV but the ST generated seed islands were sufficiently large to overcome the increased critical island width leading to an overall more NTM-susceptible plasma to higher period ST crashes. The ST generated seed island width was shown to be reduced and, thereby, the plasma stability improved, by

increasing the value of the edge safety factor (q_{95}). Alternatively, the plasma stability to NTMs can be increased by applying preemptive ECH at the resonant surface of the NTM. Preemptive ECH is found to enlarge the plasma operational domain by improving the conventional tearing stability and by reducing the coupling between the driving ($m/n = 1/1$ or $2/2$) and the driven modes ($m/n = 2/1$ or $3/2$), resulting in smaller ST generated seed islands. This two-fold beneficial effect increases with ECH pulse duration and is more efficient when the pulse is closer to, but before, the ST crash. Since seed islands can be observed in the plasma with finite size within only a few tens of microseconds, strategies for NTM prevention in ITER cannot assume a slow rise of the mode amplitude. The results given in this thesis can be used for the development of new strategies for avoiding ST NTM triggering in ITER.

The second issue addressed in this thesis is the handling of the exhaust power in the divertor. In DEMO and future fusion power plants, the severity of the power handling in the divertor is substantially larger than that foreseen for ITER. Technological constraints on the exhaust properties of a conventional divertor configuration, require research and development of new divertor concepts for a successful fusion power plant based on the tokamak configuration. The SF is one of several magnetic divertor configurations that have emerged to solve this problem. In this work, some of its exhaust properties were investigated experimentally, where the properties of the SF are compared with those of a conventional divertor configuration, and the results interpreted using modeling. An analysis of the geometrical properties of the SF configuration shows that the TCV scrape-off layer (SOL) is not suited to demonstrate the exhaust performance of a reactor. However, it is an excellent device to investigate the underlying physics that determines the exhaust performance of a reactor with a SF divertor. Measurements of the power distribution among the four strike points (SPs) show that the SF- configuration forks one side of the SOL towards two divertor legs with the power largely following the magnetic field lines. Experiments with increased plasma density show that the conventional divertor configuration radiates about 10% more power than the SF, which is consistent with a slightly larger SOL volume of the conventional divertor compared with TCV's SF configuration. A comparison between measurements with simulations of particle, momentum and energy transport in the SOL using the EMC3-Eirene code shows that the observed fraction of the power distributed to secondary SPs in a SF+ configuration cannot be explained by changes in the field line geometry with constant transport coefficients, suggesting an additional cross-field transport channel in the null-point region. Additionally, diffusive cross-field transport is found to be insufficient to explain the observed double-peaked heat flux profiles. An analysis of the discrepancies between measurements and simulations reveals that neglecting $\vec{E} \times \vec{B}$ drift is a possible explanation. The influence of the $\vec{E} \times \vec{B}$ drift on the edge plasma transport in the SF was confirmed in experiments using a reversed toroidal magnetic field.

Keywords: plasma physics, nuclear fusion, tokamak, TCV, NTM, sawteeth, divertor, snowflake, infrared.

Sinossi

Il potenziale della fusione nucleare come sorgente di energia praticamente inesauribile, ha spinto i ricercatori a lavorare verso lo sviluppo di centrali energetiche a fusione nucleare. In questa tesi vengono affrontati due argomenti fondamentali incontrati lungo la strada verso centrali a fusione nucleare : l'innesco (*triggering*) di modi tearing neoclassici (*neoclassical tearing modes* - NTMs) da parte di fenomeni comunemente noti come denti di sega (*sawteeth* - STs) e la gestione della potenza scaricata sul divertore.

Gli esperimenti presentati in questa tesi sono stati effettuati sul Tokamak à Configuration Variable (TCV), una macchina di medie dimensioni operativa dal 1992 presso il laboratorio CRPP/EPFL a Losanna, Svizzera. Il tokamak TCV è stato progettato per studiare gli effetti della forma del plasma (*plasma shaping*) sul comportamento del plasma stesso, ed è quindi caratterizzato da una camera da vuoto rettangolare fortemente elongata ed un insieme di bobine per lo *shaping* alimentate indipendentemente. Un'ulteriore caratteristica unica di TCV è la possibilità di avere un'elevata potenza e *current drive*, fornita da un sistema flessibile di iniezione di onde a frequenza ciclotronica elettronica, progettato per una vasta gamma di forme di plasma. Inoltre, con il suo alto grado di flessibilità operativa, TCV è diventato recentemente una delle poche macchine in grado di testare le nuove configurazioni con divertore, quali il divertore di tipo fiocco di neve (*snowflake* - SF) e il divertore a x, senza dover apportare modifiche strutturali.

La prima tematica affrontata in questa tesi è il *triggering* di NTMs tramite collassi (*crashes*) di STs. Molti tokamak hanno osservato che STs di durata sufficiente possono innescare NTMs, i quali comportato una degradazione delle prestazioni del plasma e/o dirsuzioni, a seconda delle condizioni del plasma. Sulla base di vincoli imposti alle prestazioni del plasma, la comparsa di NTMs costituisce una minaccia al principale obiettivo di ITER, che consiste nel dimostrare la fattibilità di operare con un plasma da fusione autosostenuto ed un fattore di guadagno di potenza di fusione $Q \geq 10$. L'abilità di TCV di controllare accuratamente i periodi dei singoli STs è stata impiegata per esaminare il meccanismo di innesco dei NTMs da parte di ST con l'obiettivo di trovare metodi per operare in modo più sicuro a pressioni di plasma più elevate. In TCV, il sistema per il riscaldamento a risonanza ciclotronica elettronica e per il *current drive* (electron cyclotron resonance heating and current drive - ECH and ECCD) è stato usato per innescare NTMs in condizioni controllate, fornendo le condizioni sperimentali ottimali per lo studio del *triggering* di NTMs risultanti da collassi di STs. I risultati mostrano segni di una formazione estremamente rapida, entro pochi microsecondi dopo il *crash* di

un ST, di isole seme (*seed islands*), caratterizzate da numeri poloidali e toroidali $m/n = 3/2$ e $2/1$. Si è visto che STs con un periodo maggiore generano *seed islands* più grandi ma aumentano anche la stabilità del plasma rispetto a modi *tearing* convenzionali. In TCV questi effetti tendono a competere gli uni con gli altri, ma le isole generate da STs sono sufficientemente grandi da superare la più grande ampiezza critica dell'isola, comportando complessivamente un plasma più suscettibile rispetto ai NTMs da *crash* di STs con un periodo superiore. Si è visto che la larghezza delle *seed islands* generate da STs risulta essere ridotta, e quindi il confinamento del plasma migliorato, per via dell'aumento del valore del fattore di sicurezza la bordo (q_{95}). Alternativamente, la stabilità del plasma rispetto ai NTMs può esser migliorata applicando preventivamente radiazione ECH sulla superficie risonante del NTM. Si è riscontrato che l'applicazione preventiva di ECH aumenta il dominio operazionale del plasma, migliorando la stabilità *tearing* convenzionale e riducendo l'accoppiamento tra i modi eccitanti ($m/n = 1/1$ o $2/2$) e quelli eccitati ($m/n = 2/1$ o $3/2$), che risulta in più piccole *seed islands* generate da STs. Questo aspetto doppiamente benefico aumenta all'aumentare della durata dell'impulso ECH ed è più efficace quando l'impulso è sufficientemente vicino al momento del *crash* del ST, ma prima di esso. Dal momento che nel plasma le *seed islands* di ampiezza finita possono esser osservate solo per poche decine di microsecondi, le strategie per la prevenzione degli NTMs in ITER non possono assumere una lenta crescita dell'ampiezza del modo. I risultati mostrati in questa tesi possono esser usati per lo sviluppo di nuove strategie al fine di evitare il trigger di STs e NTMs in ITER.

Il secondo argomento affrontato in questa tesi è la gestione della potenza scaricata sul divertore. In DEMO, e future centrali a fusione, i vincoli sulla sopportazione della potenza sul divertore sono molto più elevati di quelli previsti per ITER. Limiti tecnologici sulle proprietà di scarico di una configurazione a divertore convenzionale, richiedono la ricerca e lo sviluppo di nuove configurazioni con divertore per garantire il successo di una centrale a fusione basata sul principio del tokamak. Lo SF è una delle numerose configurazioni di divertore che sono state sviluppate al fine di risolvere questo problema, e in questo lavoro alcune delle sue proprietà sullo scarico della potenza sono state investigate sperimentalmente, dove le proprietà dello SF sono confrontate con quelle di un divertore a configurazione convenzionale, e i risultati interpretati con delle modellizzazioni. Un'analisi delle proprietà geometriche della configurazione tipo SF mostra che lo *Scrape-Off Layer* (SOL) di TCV non è adatto a dimostrare prestazioni sullo scarico di potenza migliorate, associate alla configurazione tipo SF, dal momento che gli elementi del divertore sono lontani dall'x-point. Tuttavia, TCV è una macchina eccellente per investigare i principi fisici che determinano le prestazioni dello scarico di potenza di un divertore tipo SF in un reattore. Misure della distribuzione di potenza sui quattro *strike points* (SPs) mostrano che la configurazione tipo SF separa un lato del SOL verso due gambe del divertore con la potenza che segue per lo più le linee di campo magnetico. Esperimenti con densità di plasma più elevata mostrano che la configurazione convenzionale del divertore irradia circa il 10% di potenza in più rispetto a quella di tipo SF, il che è consistente con un volume di SOL in una configurazione con divertore convenzionale leggermente superiore rispetto

alla configurazione SF di TCV. Un confronto tra misure sperimentali e simulazioni del trasporto di particelle, momento e energia nel SOL usando il codice EMC3-Eirene, mostra che la frazione di potenza che si distribuisce sui SPs secondari in una configurazione SF+, osservata sperimentalmente, non puó essere spiegata con cambiamenti nella geometria delle linee di campo con coefficienti di trasporto costanti, suggerendo un ulteriore canale di trasporto trasversale al campo nella regione del null-point. Inoltre, il trasporto trasversale diffusivo si è visto essere insufficiente a spiegare i profili di flusso di calore con due massimi. Un'analisi delle discrepanze tra le misure sperimentali e le simulazioni rivela che una possibile spiegazione potrebbe esser dovuta all'avere trascurato il drift $\vec{E} \times \vec{B}$. L'influenza del drift $\vec{E} \times \vec{B}$ sul trasporto al bordo del plasma nello SF è stato confermato sperimentalmente usando un campo magnetico toroidale invertito.

Parole Chiave: fisica del plasma, tokamak, TCV, NTM, sawteeth, divertore, snowflake, infrarosso.

Contents

List of Figures

List of Tables

1 Introduction

For many decades, scientists have been working on establishing the conditions in which self-sustaining nuclear fusion can become an economically viable energy source. The tokamak concept is, at present, the most promising approach for exploiting thermonuclear fusion and, in this chapter, its main features will be briefly reviewed. This chapter also presents the scientific and technological challenges that will be addressed in this thesis.

1.1 The Growing World Energy Consumption

An energy supply is the most basic of goods needed for producing food, heating and lighting, operating industrial facilities, transport, etc. In general, a substantial energy consumption, at a reasonable price, is required to sustain a high quality of life. Concommittally, the increase of the world average standard of living, together with a strong population increase, has led to an increase in energy consumption. The International Energy Agency predicts that the world energy consumption will increase by approximately 56% between 2010 and 2040 [3, 4]. A large fraction of this increase in global energy demand (over 85%) is expected to be driven by the strong economic growth and expanding populations of developing countries, in particular China and India.

One of the greatest challenges in supplying this increasing demand is finding new energy resources that are safe, sustainable, economic and compatible with the environment. The present energy demand is supplied by a combination of many available energy resources, e.g. fossil fuels, solar, wind, hydropower, nuclear fission, geothermal. As may be expected, each option has both advantages and disadvantages and, therefore, there is not an obvious single solution envisaged for the future.

Most of the industrialized countries in the world mainly rely on burning fossil fuels for their energy supply. Oil and natural gas have been mostly used for heating houses and transportation whereas coal is the main fossil fuel used to generate electricity. One issue related to oil and natural gas is that their reserves are concentrated in only a few regions

of the world. Another issue is that oil reserves are expected to become exhausted in a few decades. In principle, the increased energy consumption could be supplied by increasing the use of coal, of which there remain substantial reserves in many countries, and is capable of supplying the world with electricity at the current usage rate for hundreds of years [5]. However, the CO_2 released by burning fossil fuels is already starting to have an observable negative impact on the environment and the general consensus has concluded that such a solution is strongly pejorative to the earth's future.

The need to reduce the emission of greenhouse gases means that the amount of energy that can be generated from fossil fuels has to be limited. There are, however, few realistic scenarios in which it is completely replaced. Therefore, in the absence of a solution, alternatives must be researched and developed.

1.2 The Thermonuclear Fusion

One potential source of energy that has the potential to become a major part of the agglomerate of energy resources is nuclear fusion. The comparison between nuclear fusion with other existing options shows that it has many advantages in terms of safety, fuel reserves and minimal damage to the environment [6]. However, there are disadvantages, which are related to scientific and technological challenges inherent to the fusion process.

In order to induce a nuclear fusion reaction, the electrostatic repulsion between the two positively charged nuclei, that should fuse, must be overcome requiring high particle kinetic energies. Among the possible exothermic fusion nuclear reactions, the more prominent involve the heavier hydrogen isotopes deuterium (D) and tritium (T), namely

$$ {}_1\mathrm{D}^2 \quad + \quad {}_1\mathrm{T}^3 \quad \longrightarrow \quad {}_2\mathrm{He}^4(3.50\ \mathrm{MeV}) \quad + \quad {}_0\mathrm{n}^1(14.1\ \mathrm{MeV}), \tag{1.1} $$

as it has the highest cross-section at the lowest threshold energy [7, 6]. However, the maximum value of the cross-section of this reaction is much lower than that of a single Coulomb collision. Therefore, nuclei with sufficient energy would have to be confined for a sufficient time before a D-T reaction occurs. The most promising solution is to heat a mixture of deuterium and tritium until the thermal velocity of the particles is sufficiently high for fusion reactions to occur. This process is thus referred to as thermonuclear fusion.

To maintain the high temperatures required for fusion reactions, contact between the particles and surrounding material walls must be minimized. At such temperatures, hydrogenic atoms are fully ionized, i.e. in a plasma state. Since charged particles are influenced by electromagnetic fields, a possible method of confining this plasma is by using magnetic fields.

1.3 The Magnetic Confinement

Several different magnetic configurations for magnetic confinement fusion have been proposed with several geometric configurations of the confining magnetic fields. During the 1960's, a magnetic confinement device called a tokamak was developed to study the conditions for producing power through thermonuclear fusion [8]. The word tokamak is a Russian acronym for "**to**roidalnaja **ka**mera s **ma**gnitnymi **k**atushkami" that can be translated as "toroidal chamber with magnetic coils". The plasma temperatures obtained in the first tokamaks greatly exceeded those in competing devices [9] and, for this reason, tokamak research grew rapidly. Nowadays, tokamaks remain the most developed concept to generate plasmas in conditions necessary for controlled thermonuclear fusion.

Although the tokamak device is the most prominent candidate for controlled thermonuclear fusion, several scientific and technological challenges impose severe constraints on the path towards ignition (a self sustained thermonuclear fusion reaction). Plasma instabilities that develop when the plasma pressure is increased for better performance remain problematic. Another outstanding issue is related to the potential damage to plasma facing components caused by excessive power loads on highly localized areas in the machine. These challenging issues will be further discussed in the motivations for this thesis in section 1.6.

1.4 The Tokamak Concept

In a tokamak, the plasma is confined by a toroidally axisymmetric magnetic field. This magnetic field has a major component in the toroidal direction, B_ϕ, and a smaller component in the poloidal direction, B_θ. The toroidal magnetic field is created by the physical field coils and has a characteristic $1/R$ dependence, where R is the distance from the symmetry axis, and the poloidal magnetic field is created by an electric current flowing in the plasma, figure 1.1.

The introduction of a poloidal magnetic field was a solution proposed to avoid a radially outward displacement of the entire plasma column observed in the first experiments with only a toroidal magnetic field. This displacement generally led to the termination of the discharge and was caused by a combination of two effects. First, the charge dependent particle drifts due to the gradient and curvature of the toroidal magnetic field causes charge separation in the vertical direction and a resulting electric field. With an electric field perpendicular to the magnetic field, a charge-independent $\vec{E} \times \vec{B}$ drift causes an outward displacement of the plasma column. The combination of the poloidal and toroidal magnetic fields gives rise to a helical magnetic field line that averages the time particles spend moving away from a field line with the time particles spend moving towards the field line. This helical magnetic field configuration was found to reduce the charge separation and improve the particle confinement.

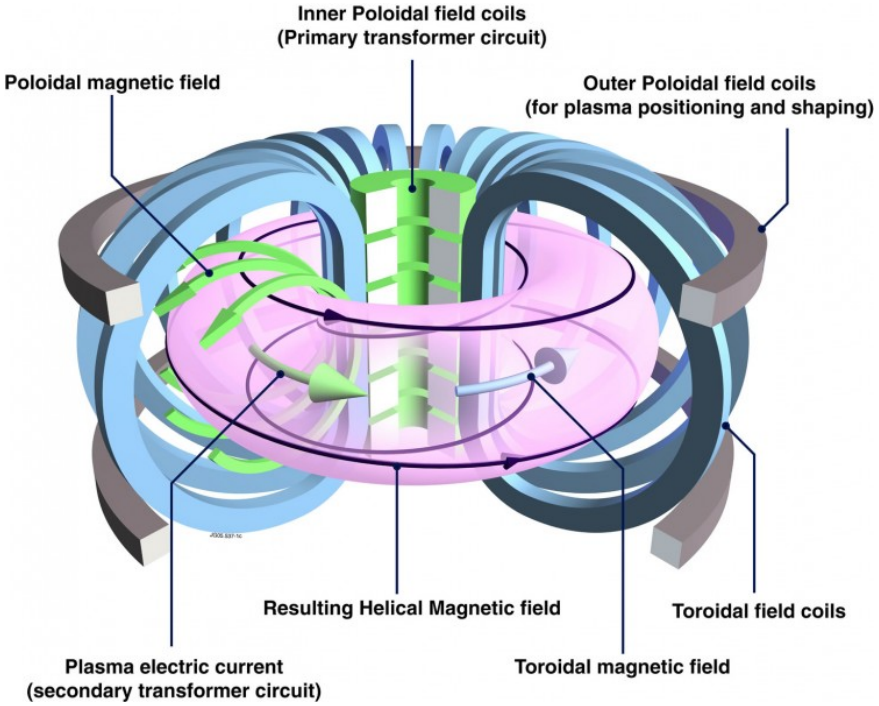

Figure 1.1: Schematic of a tokamak device. *Source: EFDA-JET.*

The plasma current necessary for the plasma confinement in tokamaks was initially driven inductively by transformer action in which a central solenoid acts as the primary coil and the plasma acts as the secondary. Since, with constant electrical resistance, the plasma current is proportional to the ramp rate of the current in the primary coil that cannot be ramped indefinitely, an inductive plasma current I_{P} can be sustained only for a limited time. For a tokamak-based fusion reactor, an alternative solution to drive the plasma current, non-inductively, is desirable. To this end, scenarios where non-inductive currents are generated by a combination of the self-generated bootstrap current [10, 11, 12] and auxiliary current drive [13, 14] are being developed.

Owing to the electrical resistivity of a plasma, a flowing current heats the plasma through the Joule effect. As the plasma resistivity decreases with electron temperature as $T_{\mathrm{e}}^{-3/2}$, less heating is obtained as their temperature increases. To achieve plasma temperatures around 10 keV using only Ohmic heating, a toroidal magnetic field in the plasma center of tens of Tesla would be required [7]. These values are far from those that can be achieved with superconducting coils so auxiliary heating is necessary to achieve thermonuclear fusion conditions.

In tokamaks, the plasma is confined within closed magnetic flux surfaces. The last closed flux surface (LCFS) defines the shape of the plasma cross-section. The plasma can be bounded by (*i*) the intersection of closed magnetic surfaces with a solid surface (limited plasma) or (*ii*) by the magnetic field itself (diverted plasma). The region outside the

LCFS is called the scrape-off layer (SOL) and the magnetic field lines in this region are open and intersect a solid surface (the surrounding machine surfaces) before closing on themselves [15].

Unavoidable radial processes transport heat and particles from the plasma bulk across the LCFS into the SOL. Since charged particles move preferentially along magnetic field lines, the solid surfaces intersected by the open field lines are subjected to direct particle and heat loads. Excessive wall loading leads to erosion producing impurities that can cool the plasma. To separate this source of impurities from the main plasma, a concept called divertor was suggested by Spitzer [16, 17]. In this configuration, the primary plasma-wall interactions occurs in a separate chamber. This configuration has also the advantage of directing particles and heat into a specific region where the wall can be designed to handle the heat loads - the divertor plates. A detailed review of the divertor physics can be found in [15, 18].

In diverted plasmas, the LCFS is determined by additional magnetic coils that shape the magnetic flux surfaces to create a null-point (also called an x-point), i.e. a point in the poloidal plane where the poloidal magnetic field vanishes. The magnetic flux surface passing through the x-point is called the separatrix and the intersection of the "legs" from the separatrix to solid surfaces are called strike points (SPs). The divertor legs are the parts of the separatrix between the x-point and the SPs as shown in figure 1.2, where a region below the x-point can be identified - the so-called private flux region (PFR). In this region, a plasma is only sustained by the transport of particles and heat across the divertor legs.

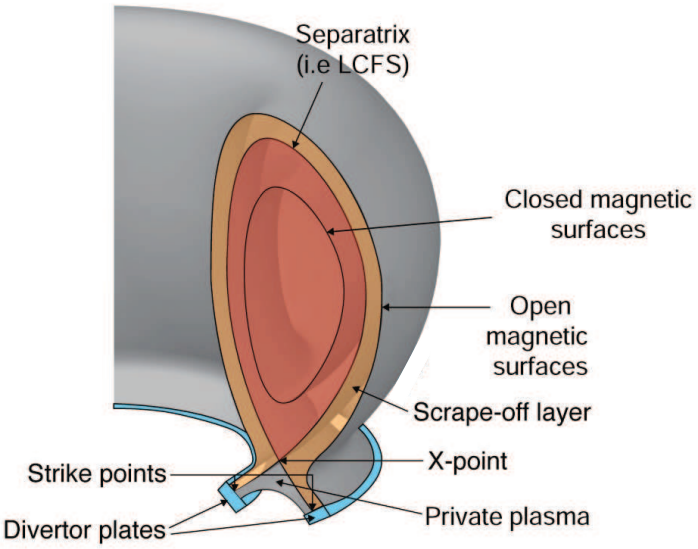

Figure 1.2: Schematic showing the main features of a diverted plasma. *Source: EFDA-JET.*

An important macroscopic plasma quantity, used as a figure of merit for the tokamak performance, is the normalized plasma pressure

$$\beta = \frac{\langle p \rangle}{B_0^2/2\mu_0}, \tag{1.2}$$

where $\langle p \rangle = \frac{1}{V}\int_V p\, dV$ is the volume averaged plasma pressure and B_0 the toroidal magnetic field in the plasma center. Another normalization of the plasma pressure used to express the proximity to plasma stability limits is

$$\beta_{\mathrm{N}} = \frac{\beta\,[\%]\ a\,[\mathrm{m}]\ B_0\,[\mathrm{T}]}{I_{\mathrm{P}}\,[\mathrm{MA}]}, \tag{1.3}$$

where a is the plasma minor radius and I_{P} the total plasma current. A similar parameter is the poloidal β, that can describe the plasma stability and is defined as

$$\beta_{\mathrm{p}} = \frac{\langle p \rangle}{B_\theta^2/2\mu_0}, \tag{1.4}$$

where $B_\theta = \mu_0 I_{\mathrm{P}} / \oint d\ell_\theta$ with the integral taken over the last closed flux surface.

In tokamaks, the twist of the field lines in each flux surface is parameterized by the safety factor :

$$q = \frac{\partial \Phi}{\partial \psi}, \tag{1.5}$$

where ψ is the poloidal magnetic flux and Φ is the toroidal magnetic flux. The value of q on a particular flux surface corresponds to the number of toroidal turns a field line needs to complete one turn in the poloidal direction. When $q = m/n$, where m and n are integer, the magnetic field lines close upon themselves after m toroidal turns and n poloidal turns. The use of the word "safety" when referring to the quantity q is directly related to the magnetohydrodynamic (MHD) stability of the plasma [19].

1.5 The Power Plant Concept

In a future fusion power plant, most of the energy required to maintain the plasma temperature must be supplied by the α-particles released in the D-T fusion reactions. The energy transfer from α-particles to deuterium and tritium particles occurs through Coulomb collisions and it is, therefore, important that the α-particles are sufficiently well confined to transfer a large proportion of their energy of 3.5 MeV to the plasma. The energy must be confined for a sufficiently long time such that the power required to maintain the plasma at the required temperature remains as small as possible. This is expressed by the energy confinement time, τ_{E}, which is defined as the ratio between the total energy of the particles and the power losses. When the energy released by the fusion reactions is sufficient to compensate all the energy losses and maintain the plasma temperature without any auxiliary heating, the plasma is said to ignite. This is the goal condition for a future fusion reactor and can be expressed approximately by the well-known Lawson criterion [20], which may be written as a "triple product",

$$n_0 \, T_0 \, \tau_{\mathrm{E}} \geq 5 \times 10^{21} \, \frac{\mathrm{keV} \cdot \mathrm{s}}{\mathrm{m}^3}. \tag{1.6}$$

Here, n_0 and T_0 are the peak values of assumed parabolic plasma density and temperature profiles. This condition shows the requirements on plasma density and temperature, and energy confinement time to achieve ignition. For example, ignition would be reached in a plasma with $n_0 = 2{\times}10^{20}\,\mathrm{m}^{-3}$, $T_0 = 15\,\mathrm{keV}$ and $\tau_{\mathrm{E}} = 3\,\mathrm{s}$ [7].

Together with achieving the plasma conditions necessary for ignition, there is an issue related to the tritium fuel. Unlike deuterium, tritium is not found in nature as its half life is only 12.3 years so it must be produced artificially. In the blanket, lithium will be used to breed tritium. The natural resources of lithium are estimated to be sufficient to supply the global energy consumption for over 10^6 - 10^7 years. The breeding of tritium from lithium is initially obtained from the neutron induced fission reactions

$$ {}_3\mathrm{Li}^7 + {}_0\mathrm{n}^1 \longrightarrow {}_2\mathrm{He}^4 + {}_1\mathrm{T}^3 + {}_0\mathrm{n}^1 \tag{1.7}$$

$$ {}_3\mathrm{Li}^6 + {}_0\mathrm{n}^1 \longrightarrow {}_2\mathrm{He}^4 + {}_1\mathrm{T}^3. \tag{1.8}$$

The neutrons produced by the D-T reactions do not interact with the plasma and should be absorbed in a blanket surrounding the reactor vessel. In a heat exchanger inside the blanket, the kinetic energy of the absorbed neutrons is carried away by a suitable coolant. A steam generator uses this energy and, finally, a turbine generates electricity as in any conventional thermal power plant. All these different parts of a future fusion power plant

can be seen in figure 1.3.

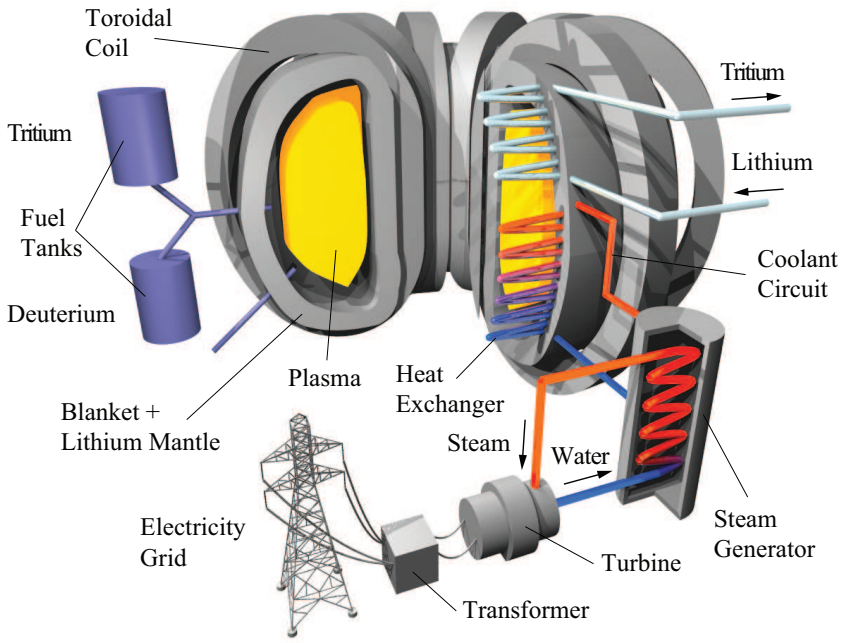

Figure 1.3: Schematic of the main components of a future tokamak-based fusion power plant. *Source: EFDA-JET.*

1.6 Motivation for this Thesis

This thesis seeks to contribute to advancing controlled thermonuclear fusion by challenging two outstanding issues: (*i*) triggering of plasma instabilities that limit plasma performance and (*ii*) handling of the exhaust power in the divertor. Motivations for each of these tasks is given below.

1.6.1 Sawtooth generated magnetic islands

Although many plasma instabilities do not lead to discharge termination in a so-called major disruption [21], they often impose severe constraints on the achievable plasma performance. An example of such instabilities are neoclassical tearing modes (see sections 3.1.3 - 3.1.4). In tokamaks, the maximum achievable plasma pressure is often limited by the onset of these modes [22, 23]. These resistive modes can cause an large confinement degradation and/or lead to full disruptions. They are of major concern in the operation of the next step fusion experiment ITER (international thermonuclear experimental reactor [24]), figure 1.4, since they would cause, possibly catastrophic, thermal and mechanical stresses of the machine components.

The onset of neoclassical tearing modes poses a threat to the main goal of ITER, which

is to demonstrate sustained burning plasma operation (300-500 s) with a fusion power gain factor $Q \geq 10$. With the quadratic dependence of the fusion power on β [25], sustained operation at high plasma pressure is a key ingredient in the development of tokamak-based fusion power plants. Experimental observations from several tokamaks show that neoclassical tearing modes can be triggered at values of normalized β well below to those envisaged for ITER by sawteeth of sufficiently long period [26]. This has serious implications for ITER since the fusion produced α-particles will themselves lead to longer sawteeth periods [27].

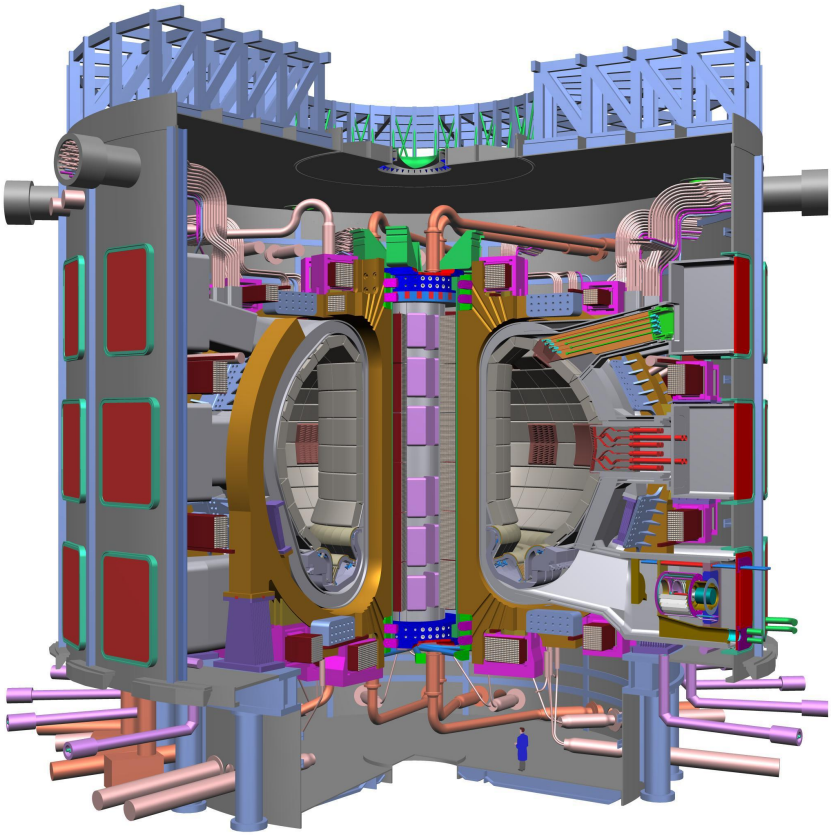

Figure 1.4: Cutout view of ITER. *Source: ITER organization.*

Several methods for preempting neoclassical tearing modes are foreseen for ITER, including electron cyclotron heating and current drive. Studies show that off-axis power deposition decreases the fusion gain factor Q. Another issue is that using such systems adds complexity and decreases reliability. For these reasons, neoclassical tearing modes are thought to be one of the critical limiting plasma instabilities for the ITER $Q = 10$ scenario [28].

This work seeks to improve the understanding of the underlying physics of the triggering of neoclassical tearing mode seeding by sawteeth. This could indicate ways to safer operation at higher plasma pressures in existing tokamaks and, then, ITER. This knowledge would

also help to develop more efficient strategies for avoiding neoclassical tearing mode triggering and for improving the plasma scenarios.

1.6.2 Properties of the snowflake divertor

Even with a core plasma reliably and safely operated at the highest possible performance, there still remain technological challenges. One outstanding issue encountered in controlled nuclear fusion is the handling of the exhaust power in the divertor. In the ITER $Q = 10$ scenario ($P_{\text{fusion}} = 400\,\text{MW}$ and $P_{\text{heat}} = 120\,\text{MW}$), the total power crossing the separatrix and entering the SOL is expected to be around 100 MW. Since the maximum value of the continuous heat flux onto material walls has to be reduced to tolerable values of typically $10\,\text{MW/m}^2$, this power must be distributed on a surface area of at least $10\,\text{m}^2$. This is around three times higher than that predicted in the ITER standard divertor, ($3.5\,\text{m}^2$) including inner and outer targets when assuming that the power is lost through charged particles that follow magnetic field lines. Consequently, about 60-70% of the power flowing in the SOL must be exhausted through radiation from the divertor region in order to spread the power over a larger area on the divertor plates [29].

In the demonstration power plant (DEMO) that is planned to follow ITER, and in future fusion power plants, the fusion power is expected to be about 2500-3600 MW with a corresponding auxiliary heating power of 400-1200 MW [30]. These values are about 4-5 times higher than those of ITER while its linear dimension is expected to be only 50% higher, strongly exacerbating the problem. Assuming that the divertor constraints will be similar to ITER, the allowable power flux across the separatrix will be comparable and hence a larger fraction of the total heating power must be radiated from the plasma core (about 80-90%). It is not clear if these conditions can be sustained or will even be sufficient to maintain operation in the high confinement mode [31]. To mitigate this risk that highly radiating regimes may not be extrapolated towards devices like DEMO, alternatives to the conventional divertor are being researched. The development of a possible new divertor concept would be invaluable on the road to a fusion reactor.

One of several magnetic divertor configurations that have been proposed is the so-called "snowflake" [32]. This thesis seeks to test some of its potential advantages for alleviating the heat loads on the divertor plates using TCV experiments to provide data and modeling to interpret the results. The results from the snowflake discharges are compared with those from a standard divertor in order to evaluate its applicability to a high power device.

1.7 Outline of this Thesis

In this chapter, a brief introduction to nuclear fusion and the tokamak device as a possible concept for exploiting thermonuclear fusion as an energy source was presented. The scientific and technological challenges that are encountered in developing controlled nuclear fusion, that will be addressed in this thesis, were discussed.

- Chapter 2 provides a description of the TCV tokamak in which all the experiments described in this thesis were performed. After a description of the magnetic coil and auxiliary heating systems, which were the main plasma actuators used in this work, the diagnostics used in this thesis will be described. A special attention has been given to the thermocouples and infrared thermography diagnostic systems since their operation and maintenance were part of my responsibilities during the time of this thesis. More details on these diagnostics are also given in appendix A.

- Chapter 3 presents information on the role of the sawteeth (ST) in the triggering of neoclassical tearing modes (NTMs). To better understand this triggering, TCV's electron cyclotron heating system was used to accurately control the ST period. This controlled environment was used in a detailed study of the dynamics of the seeding of NTMs by ST crashes. The study of the modes generated by the ST crash, as a function of ST period, is used to examine the influence of the ST period on the generated seed island widths and measure the stability of seed islands in the post-crash plasma. To examine the dependencies of the coupling between sawteeth and NTMs, the sawtooth triggered NTMs were studied in discharges for a range of plasma parameters. The effects of electron cyclotron heating on the NTM seeding and post-crash stability was also investigated to explore more efficient preemptive actions using pre-knowledge of the ST crash time. This work already features in a journal publication:

  > **G.P. Canal**, *et al.*, "*Fast seeding of NTMs by sawtooth crashes in TCV and their preemption using ECRH*", Nuclear Fusion **53** (2013) 113026
  >
  > F. Felici, **G.P. Canal** *et al.*, "*Integrated real-time control of MHD instabilities using multi-beam ECRH/ECCD systems on TCV*", Nuclear Fusion **52** (2012) 074001

- Chapter 4 provides a detailed analysis of some of the exhaust properties of the snowflake (SF) divertor configurations generated in TCV. The effects of the SF configuration on the main scrape-off layer properties and a geometrical analysis of the magnetic topology of an SF and a standard divertor configuration are presented. The potential advantages of the SF over a standard divertor configuration are examined with the work divided into two parts: experimental and modeling. In the experimental part, the power distribution between the four strike points of several

SF divertor configurations is characterized and for a range of plasma densities and input power. Observations of the activation of the additional strike points is examined. In the modeling part, the EMC3-Eirene code is used to interpret the experimental results and to provide a further insight into the physical processes involved in the plasma transport and power distribution in both the SF and standard divertor configurations. Finally, the experimental observations are compared with the simulations where an analysis of the noted discrepancies suggests the existence of an enhanced cross-field transport in the experiments that cannot be explained with the transport model assumed in EMC3. The work presented in this chapter has substantially contributed to several journal publications:

> **G.P. Canal** *et al.*, "*The influence of the $\vec{E} \times \vec{B}$ drift on the target profiles of the TCV snowflake divertor*", to be submitted to Nuclear Fusion
>
> W.A.J. Vijvers, **G.P. Canal** *et al.*, "*First experimental demonstration of heat load mitigation with an X-divertor in a tokamak*", to be submitted to Nuclear Fusion, 2014
>
> H. Reimerdes, **G.P. Canal** *et al.*, "*Experimental investigation of neon seeding in the snowflake configuration*", submitted to Journal of Nuclear Materials, 2014
>
> W.A.J. Vijvers, **G.P. Canal** *et al.*, "*Power exhaust in the snowflake divertor for L- and H-mode TCV tokamak plasmas*", Nuclear Fusion **54** (2014) 023009
>
> T. Lunt, **G.P. Canal** *et al.*, "*First EMC3-Eirene simulations of the TCV snowflake divertor*", Plasma Physics and Controlled Fusion **56** (2014) 035009
>
> H. Reimerdes, **G.P. Canal** *et al.*, "*Power distribution in the snowflake divertor in TCV*", Plasma Physics and Controlled Fusion **55** (2013) 124027

- Chapter 5 summarizes the main results and conclusions of this work.

2 The Facilities

In this chapter, the experimental facilities used in this thesis will be described. In section 2.1, a brief overview of the main features of the Tokamak à Configuration Variable (TCV) will be presented while, in section 2.2, the main diagnostics used in this work will be described. The TCV tokamak experiment can be seen in figure 2.1.

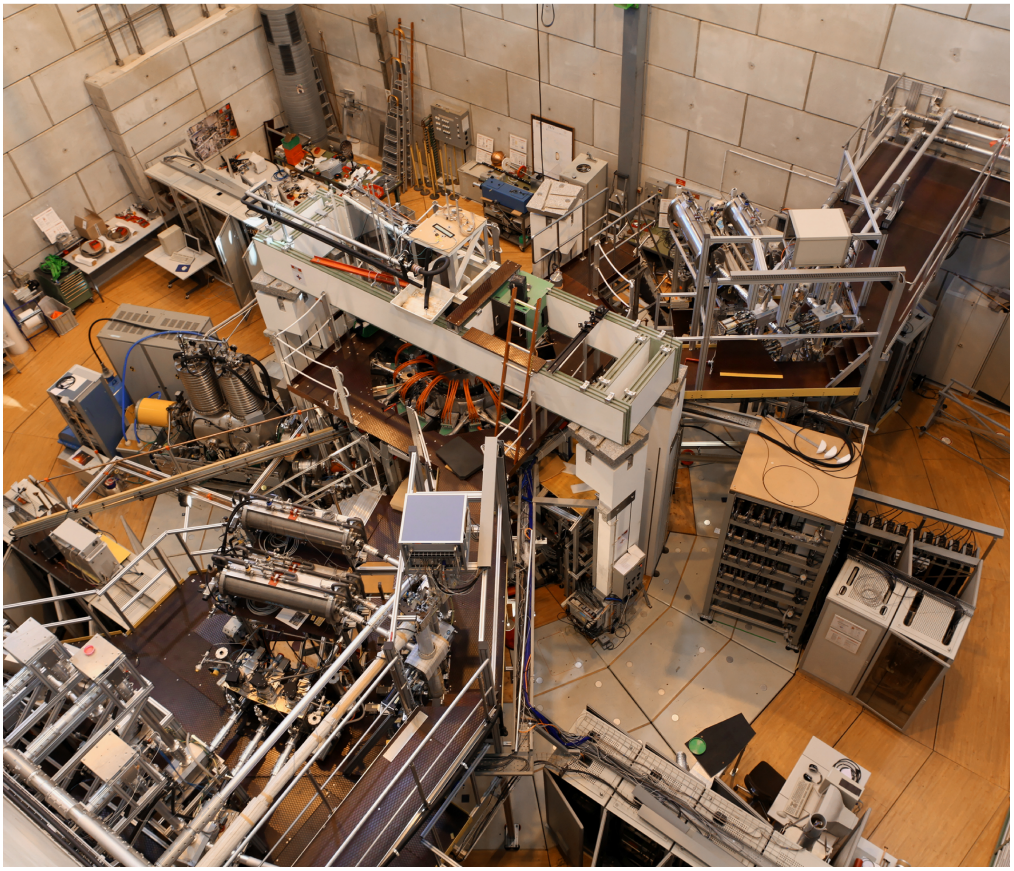

Figure 2.1: The TCV tokamak experiment viewed from the top. *Source: photo by Alain HERZOG, EPFL.*

2.1 The TCV Tokamak

The TCV tokamak is one of the medium sized tokamaks in Europe and it has been operational since 1992 [33] at the CRPP/EPFL in Lausanne, Switzerland. TCV is divided in 16 sectors and was designed for studying the effects of the plasma shape on the plasma behavior, e.g. confinement and stability. For this reason, TCV has a highly elongated rectangular vacuum vessel, as shown in figure 2.2, specifically to accommodate highly elongated plasma configurations. In TCV, the inductive current is driven by an air core transformer that consists of 7 coils specially designed to minimize perturbations of the magnetic field inside the vacuum vessel. The toroidal magnetic field is generated by 16 toroidal field coils connected in series. All these components can also be seen in figure 2.2.

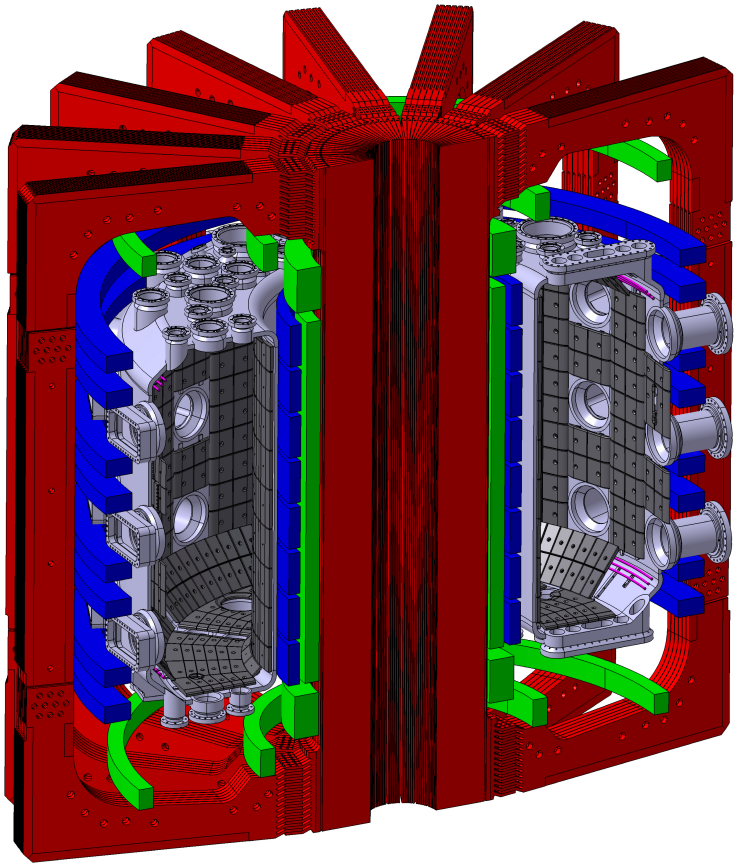

Figure 2.2: Schematic drawing of TCV showing the poloidal (blue) and toroidal (red) field coils, ohmic coils (green), internal coils (magenta), vacuum vessel with acess ports (light gray) and the first wall (dark gray). *Source: TCV 3D views by Matthieu TOUSSAINT.*

In TCV, a typical discharge with duration of about 2 s consumes approximately 100 MJ of energy, where most of it is dissipated in the toroidal field coils. This energy consumption leads to high values of peak power that cannot be directly taken from the electrical grid. For this reason, several hundred kilowatts are drawn from the electrical grid for

approximately 10 minutes and this energy stored in a flywheel connected to a motor-generator. The motor-generator can then supply power to many components of TCV during the plasma discharge. The stored energy is used to supply (*i*) the energy in the toroidal magnetic field, including dissipation in the coils, (*ii*) the energy used for additional plasma heating using electron cyclotron waves, (*iii*) the energy required by the poloidal field coils for plasma shaping and vertical position control, and finally (*iv*) the plasma energy through a plasma current, which is relatively small compared with the other loads.

2.1.1 Plasma shaping capabilities

To access a large variety of plasma shapes, TCV is equipped with a unique magnetic coil system, consisting of 16 independently powered poloidal field (PF) coils. TCV discharges are planned and prepared using the free-boundary equilibrium code FBTE [34] that calculates the necessary PF coil currents for a prescribed magnetic configuration. Figure 2.3 shows a few examples of the more extreme plasma shapes achieved in TCV, and table 2.1 TCV's main parameters.

Parameter	**Symbol**	**Value**
TCV Major radius	R_0	$0.88\,\mathrm{m}$
Plasma minor radius	a	$\leq 0.25\,\mathrm{m}$
Vacuum vessel height	b	$1.45\,\mathrm{m}$
Aspect ratio	$\epsilon = R_0/a$	≈ 3.5
Plasma current	I_P	$\leq 1\,\mathrm{MA}$
Toroidal magnetic field at R_0	B_0	$\leq 1.54\,\mathrm{T}$
Central plasma density	n	$n \leq 20{\times}10^{19}\,\mathrm{m}^{-3}$
Electron temperature	T_e	$\leq 15\,\mathrm{keV}$
Ion temperature	T_i	$\leq 1\,\mathrm{keV}$
Plasma elongation	κ	$0.9 \leq \kappa \leq 2.8$
Plasma triangularity	δ	$-0.8 \leq \delta \leq 1$
Typical/Maximum shot duration		$2\,\mathrm{s}$ / $4\,\mathrm{s}$

Table 2.1: Some parameters encountered in the TCV tokamak.

One of the main goals of TCV has been the creation of plasmas with very high elongation ($\kappa \leq 3$), however, these plasmas are highly unstable with respect to $n = 0$ modes [35]. For this reason, TCV has a toroidally continuous, highly conducting vacuum vessel. Strong eddy currents are thus induced in the vacuum vessel that decrease the vertical instability growth rate to values that can be handled by an active feedback control. In TCV, the feedback stabilization of the vertical plasma position is achieved by using the poloidal field coils located outside of the vacuum vessel in combination with two additional vertical field coils located inside the vacuum vessel. These internal coils can respond within 0.1 ms permitting the stabilization of plasmas with κ as high as 2.8 [36].

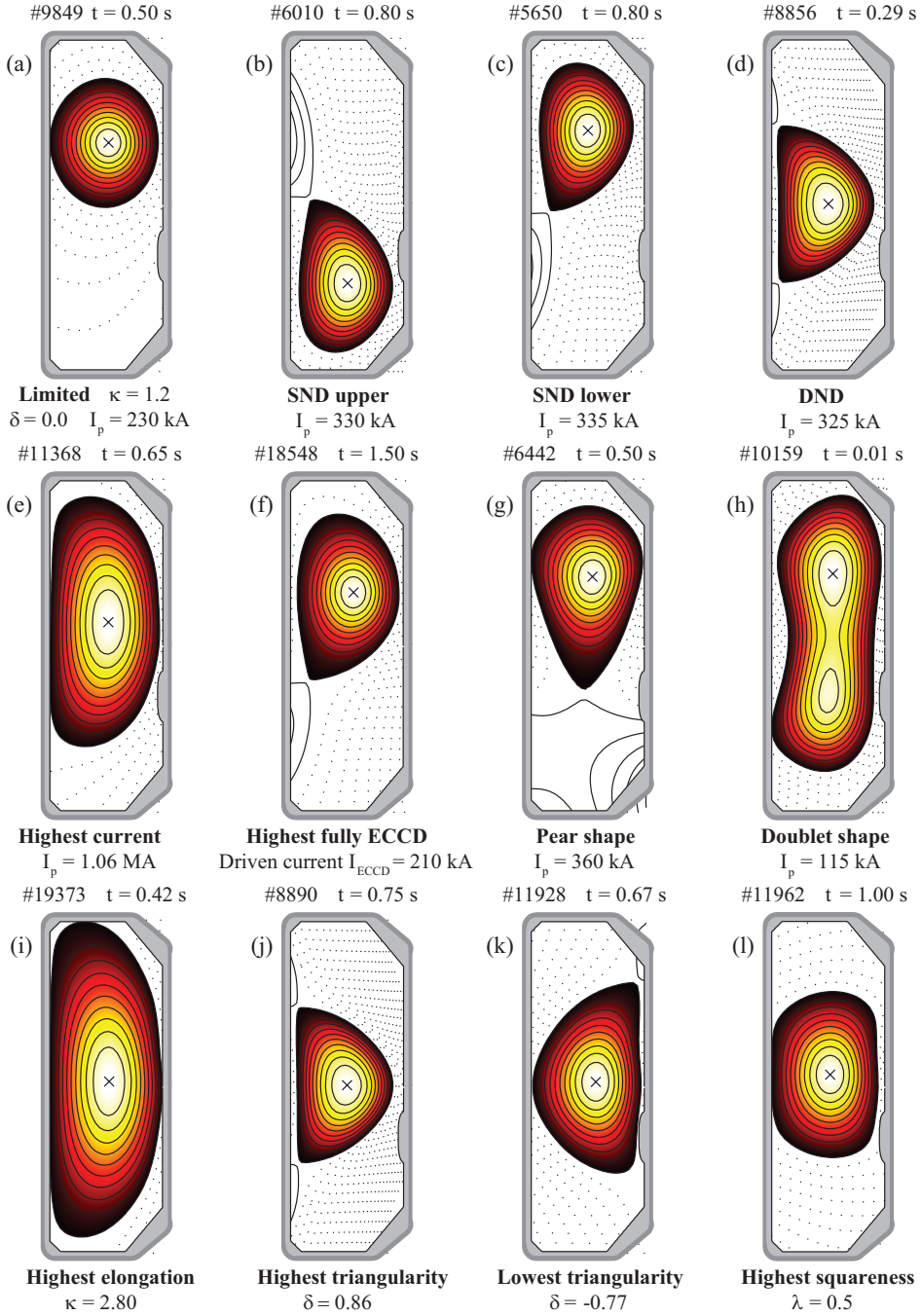

Figure 2.3: Examples of plasma shapes obtained in TCV: The first line shows (a) a standard limited plasma, a diverted plasma with a single null on the (b) upper and (c) lower side of the plasma, and (d) a double null configuration. The middle line shows highest achieved (e) ohmic and (f) non-inductive currents, (g) a near snowflake divertor, and (h) a doublet configuration. The last line shows extremely shaped stable plasmas with the (i) highest achieved elongation, (j) maximum and (k) minimum achieved triangularity and (l) maximum achieved squareness. The colour scale is proportional to the plasma temperature (black: cold; white: hot).

Due to its high degree of shaping and heating flexibility, TCV has becomes one of the few machines capable of creating new divertor configurations without requiring hardware modification, e.g. the snowflake [37] and the x-divertor [38, 39], figure 2.4. The versatility of the magnetic coil system of TCV, in terms of magnetic configuration variability and control, makes it very attractive in the investigation of potential advantages of these new divertor concepts.

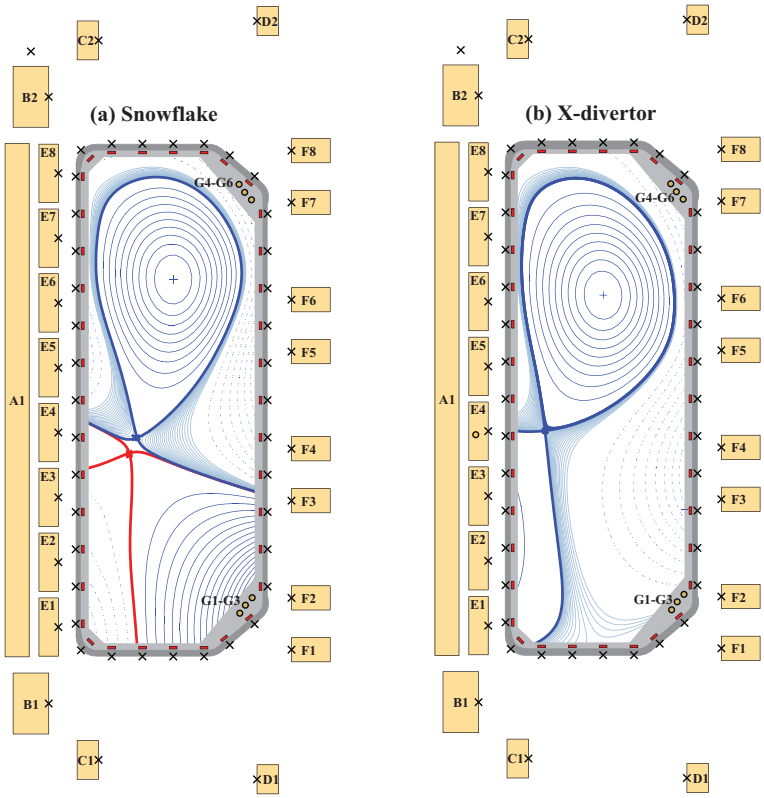

Figure 2.4: Poloidal cross-section of TCV showing the 7 coils forming the Ohmic transformer (A - D), the 16 poloidal field coils (E and F), the internal coils (G), the flux loops (black crosses) and the poloidal magnetic field probes (red rectangles), during (a) a snowflake and (b) a x-divertor discharge.

2.1.2 Electron cyclotron waves system

Another unique feature of TCV is its high power and current drive capabilities provided by a flexible electron cyclotron (EC) wave system that was specially designed to access a wide range of plasma shapes [40, 41]. The TCV EC wave system is composed of nine gyrotrons grouped in three clusters of three gyrotrons. Each cluster is connected to an independent high-voltage power supply. The nominal power delivered by each gyrotron is 0.5 MW with a maximum duration of 2 s. Each gyrotron is coupled to an evacuated transmission line through a matching optics unit used to shape the EC beam to obtain a Gaussian profile, and to set the wave polarization with respect to TCV's magnetic field

direction. The polarizers can be adjusted to produce an ordinary (O) or an extraordinary (X) EC wave (or a combination of both). At the end of the transmission lines, the EC power is delivered to the plasma from up to seven separate antennas (launchers). Six of the gyrotrons (two clusters) operate at the second harmonic of the electron cyclotron frequency ($2\,\omega_{ce} = 82.7\,\text{GHz}$) with the remaining three gyrotrons (one cluster) operated at the third harmonic ($3\,\omega_{ce} = 118\,\text{GHz}$). These values correspond to a nominal toroidal magnetic field $B_0 = 1.45\,\text{T}$. All these elements can be seen in figure 2.5. Power losses in the transmission lines reduce the total power available for heating the plasma and for driving current to approximately 4.2 MW.

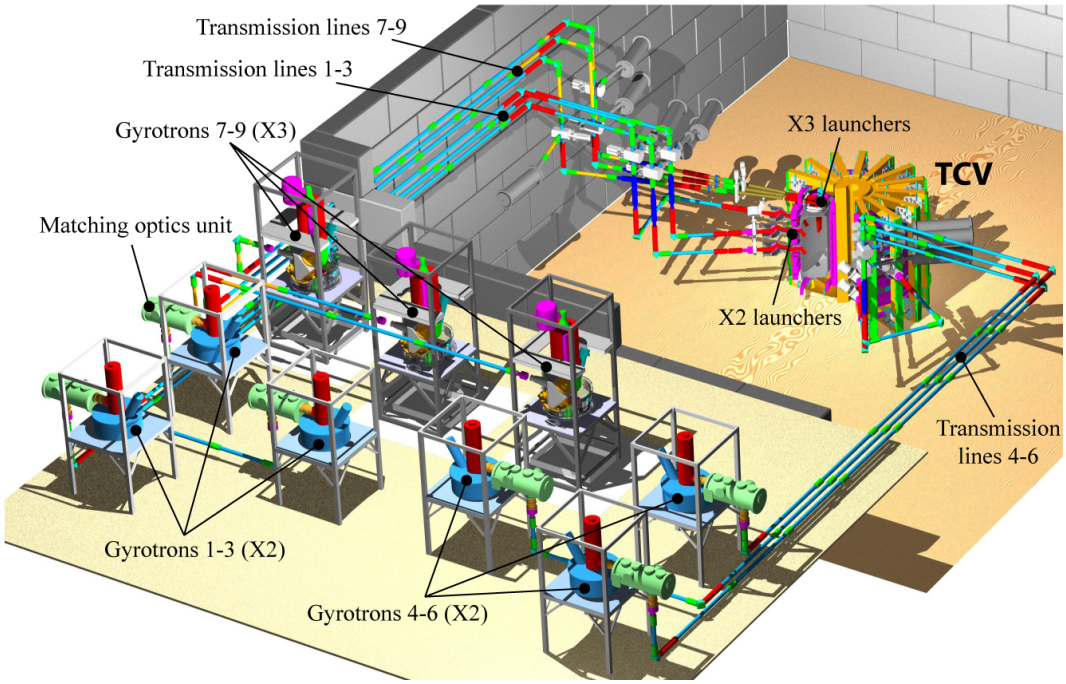

Figure 2.5: Schematic view of the gyrotrons, matching optics unit, transmission lines, and the launchers on TCV.

The X2 system

Each cluster of the second harmonic system is composed by an equatorial launcher ($Z = 0$ - L1 and L4) and two launchers on two upper ports ($Z = 0.46\,\text{m}$ - L2-L3 and L5-L6), figure 2.6. Each launcher is composed of four mirrors, of which the last one can be rapidly moved during a discharge either with a pre-programmed trajectory or under real-time control, e.g. for NTM preemption in real-time [42]. Since the cutoff density for central heating using the X2 system is about $4{\times}10^{19}\,\text{m}^{-3}$, its use is restricted to low density L-mode plasmas or to the edge of H-mode plasmas. The X2 system has also been used for ECH-assisted plasma breakdown studies. Except for plasmas with densities lower than $2{\times}10^{19}\,\text{m}^{-3}$, the power launched by the X2 system, if it reaches the resonance layer, is almost entirely absorbed.

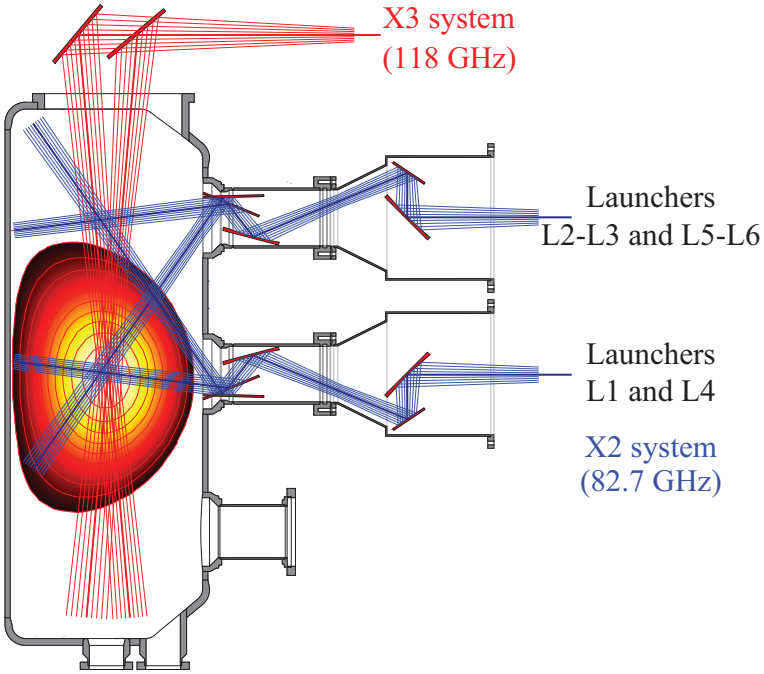

Figure 2.6: Low field side launched X2 and top-launched X3 ECH/ECCD systems. The steering ranges in the poloidal plane are also shown. In addition to the movement in the poloidal plane, the X2 launchers can be rotated toroidally to allow for ECCD.

The X3 system

For heating plasmas with densities higher than $4{\times}10^{19}\,\mathrm{m}^{-3}$ the third harmonic system is used, e.g. in H-mode discharges where the density is typically higher. Due to a lower absorption and a strong dependency on electron temperature, the X3 EC beam is launched from the top of the vessel to pass almost parallel to the resonant layer to increase the single-pass absorption. The EC power from the three gyrotrons of the X3 cluster is delivered to the plasma from a single launcher consisting of a movable mirror, which can be used to inject the EC waves from the LFS or HFS of the resonant layer. The X3 system can be used for heating plasmas with densities up to approximately $11{\times}10^{19}\,\mathrm{m}^{-3}$.

2.1.3 The first wall

In order to avoid excessive radiative losses due to the presence of impurities with high atomic number from the stainless steel vacuum vessel, the inside of the TCV vacuum vessel is almost entirely covered with graphite protection tiles, figure 2.7. For this reason, carbon is the main impurity observed in the TCV plasmas. The details of the design of the TCV's first wall can be found at [43].

Apart from the issue of minimizing the excessive core radiation, the choice of carbon has several other advantages, e.g. easy manufacture and attractive thermal properties.

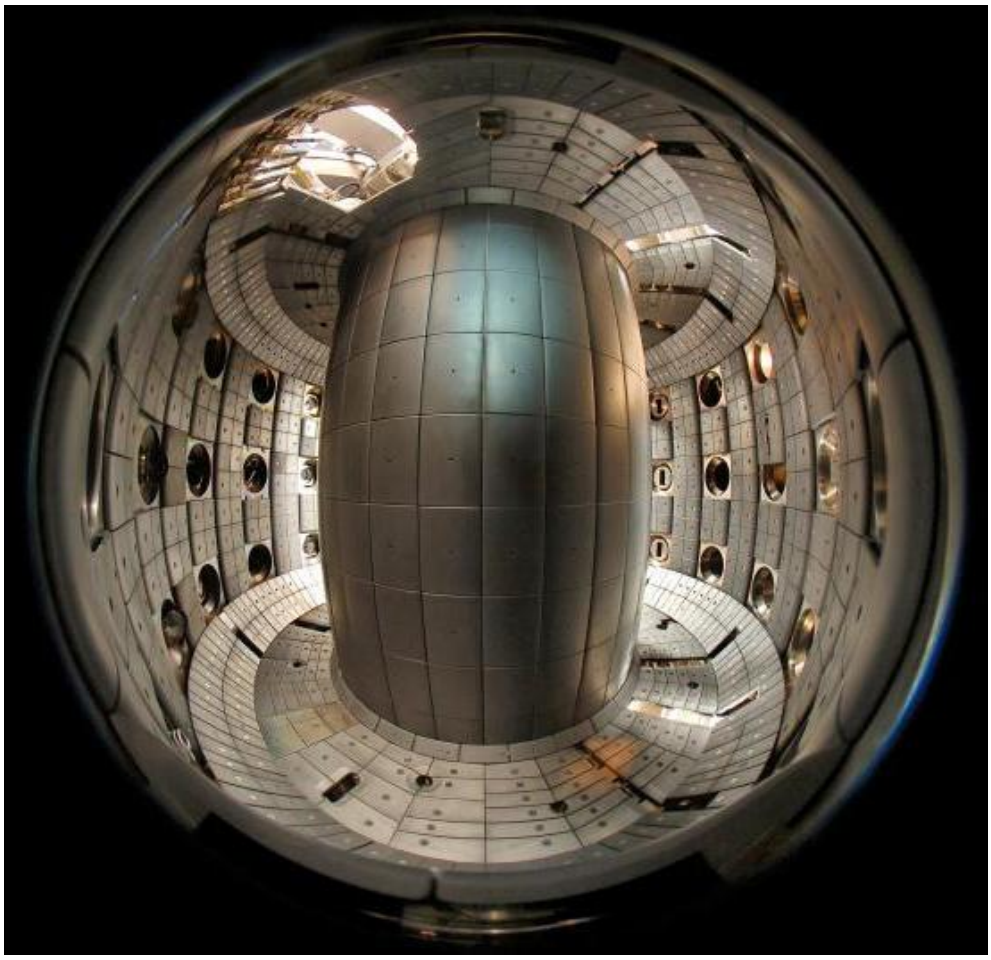

Figure 2.7: Photo of the first wall of TCV, with approximately 23 m^2 of surface area, covered with approximately 1700 graphite tiles.

In particular, carbon sublimes at high temperatures, instead of melting, distinguishing it from other materials. TCV's graphite tiles are made from high purity, fine grained, isotropic polycrystalline graphite and were manufactured by two companies: Schunk and Ringsdorff/SGL. The temperature dependence of some of the thermal properties of the TCV graphite tiles can be seen in figure 2.8.

To further limit plasma contamination, the vessel is regularly baked to temperatures up to 250°C after each exposure to air and then coated with boron through plasma chemical vapor deposition. The boronization is performed through a glow discharge in which a mixture of He (90%) and B_2D_2 (10%) is used to cover the first wall with an approximately 100 nm think layer. To limit the wall gas retention and provide continuous wall conditioning, glow discharges with helium are operated between plasma discharges with a typical duration of 300 s.

Optimal power dispersal on the HFS and LFS walls, whilst accounting for the various plasma configurations achieved in TCV, is achieved by shaping the protection tiles on the central column and outer wall tiles. The roof and bottom of TCV are simply covered with flat surface tiles with a little residual shaping to better resist adjacent tile misalignments.

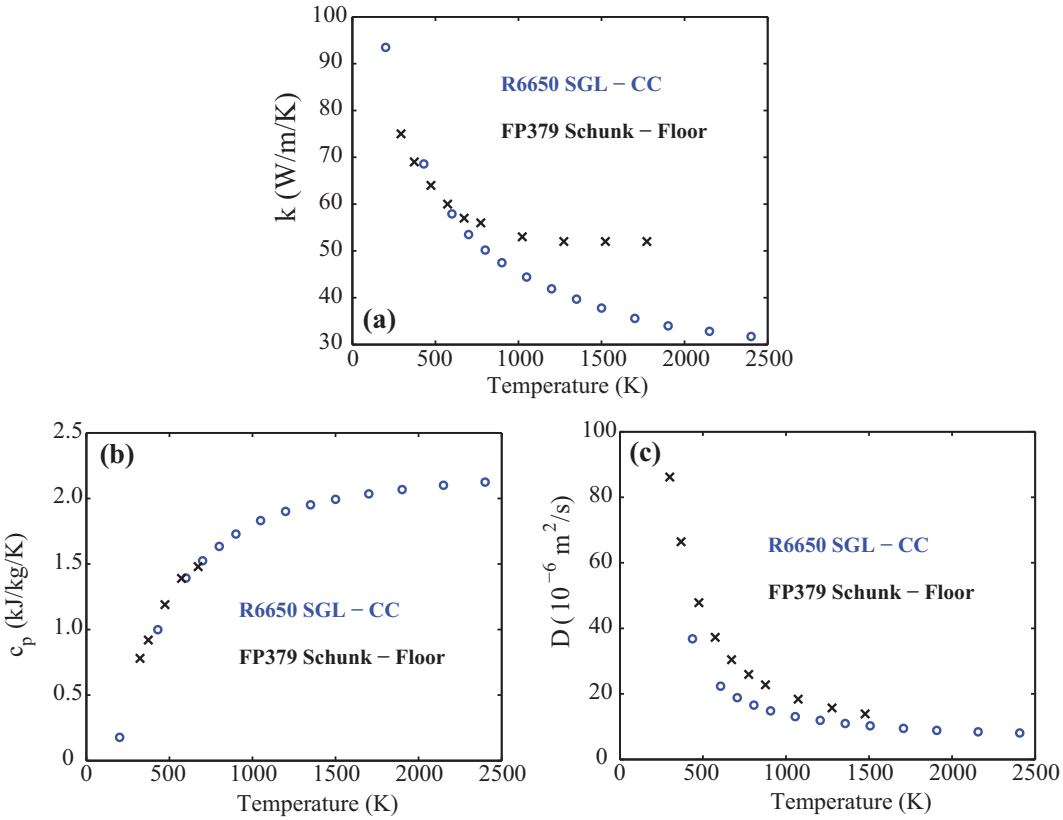

Figure 2.8: The experimental measurements of the dependence on the temperature of (a) the thermal conductivity, (b) the specific heat capacity and (c) the heat diffusivity of the graphite tiles installed on the floor and central column (CC) of TCV.

2.2 Main Diagnostics Used in this Thesis

TCV is equipped with a versatile set of diagnostics with a large spatial coverage of the vessel cross section. Although many of TCV's diagnostics were used during this thesis, only those providing the most important measurements are presented in more details in this section. Since operating and maintaining the IR thermography and thermocouple diagnostics formed a strong part of the diagnostic experimental work in this thesis, a detailed description of their system and data analysis is provided.

2.2.1 Multi-chord far infrared interferometer (FIR)

In TCV, a multi-chord Mach-Zehnder interferometer is used for measuring the line-integrated plasma density, $n_{e,l}$, across the plasma cross section. Interferometry is a family of techniques in which waves are superimposed for extracting information about the waves themselves or the medium in which they propagate. When two wave beams with the same wavelength, λ, combine in an interferometer, the resulting pattern is determined by the phase difference, $\Delta\Phi$, between the two waves traveling the two different paths.

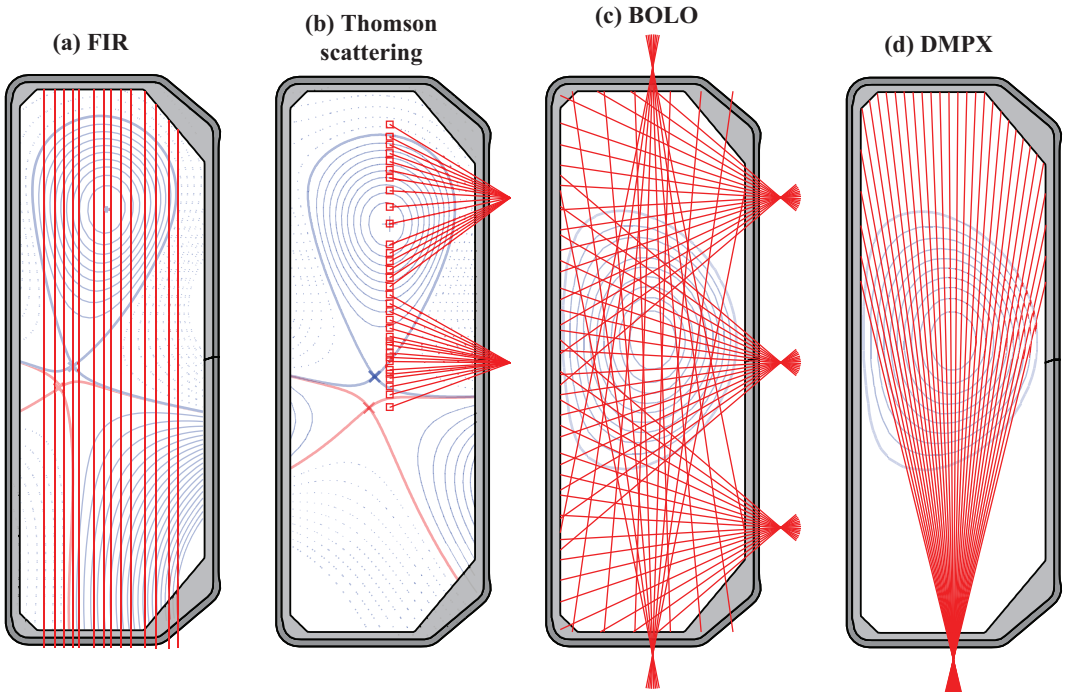

Figure 2.9: Poloidal cross section coverage of the (a) FIR, (b) Thomson scattering, (c) BOLO and (d) DMPX diagnostics. The red squares in (b) represent the scattering volume.

The TCV interferometer uses a far-infrared (FIR) difluormethane (CH_2F_2) laser emitting at a wavelength $\lambda = 214.6\,\mu$m (a few mW) that is optically pumped by a continuous wave CO_2 laser working at a wavelength $\lambda = 9.0\,\mu$m (≈ 40 W). One of the beams, the reference beam, passes outside the plasma while the others pass once through the plasma. The optical length of the beam passing outside is simply the geometrical length while that of the beam passing through the plasma depends on the plasma density. Therefore, the phase difference between the two beams provides a direct measure of the line-integrated density, which is estimated by [44]

$$n_{e,l} = \int n_e(l)\,dl = \frac{4\,\pi\,\epsilon_0\,m_e\,c^2}{\lambda\,e^2}\,\Delta\Phi. \tag{2.1}$$

In the FIR diagnostic, the laser beam is split into 14 beams that traverse the TCV vessel vertically in a single poloidal plane providing 14 radially separated line integrated density measurements, figure 2.9(a). The measurement of the central chord (R = 0.9 m) is used, together with the gas injection valve, to control the plasma density in real time. More details about this diagnostic can be found in [45, 46].

2.2.2 Thomson scattering (TS)

TCV is equipped with a Thomson scattering (TS) system for measuring the local values of electron temperature, T_e, and plasma density, n_e. The measurements are based on the spectral analysis of elastically scattered electromagnetic waves by free charged particles. In the classical electrodynamical description ($\hbar\omega << m_e c^2$), when an electromagnetic wave impinges on a charged particle (incident wave vector $\vec{k}_i$ and frequency ω_i), the electric and magnetic fields of the incident wave cause an acceleration of the particle. The charged particle undergoes acceleration reemits the absorbed electromagnetic wave in all directions at frequencies (scattered wave vector $\vec{k}_s$ and frequency ω_s) due to the Doppler effect, $\omega_s = \omega_i + (\vec{k}_s - \vec{k}_i) \cdot \vec{v}_e$. Note that there is no transfer of energy from the wave to the particle or vice-versa in this process (elastic scattering), implying that $|\vec{k}_i| = |\vec{k}_s| = k$. When the movement of the plasma particles is uncorrelated, the scattered power can be calculated by the sum of the scattered power from individual charged particles. This condition for incoherent scattering may be written $k_i \lambda_D >> 1$, where λ_D is the Debye length (equation 4.15). Assuming a Maxwellian electron distribution, the spectral scattered power in the non-relativistic regime ($T_e \lesssim 1\,\mathrm{keV}$) is given by [44]

$$\frac{d^2 P_s}{d\omega_s\, d\Omega} = \frac{r_e^2\, n_e\, P_i\, L\, \sin^2\theta}{\sqrt{\pi}\, k\, v_{th,e}}\, exp\left[-\left(\frac{\omega_s - \omega_i}{k\, v_{th,e}}\right)^2\right], \tag{2.2}$$

where $r_e = e^2 / (4\pi\epsilon_0 m_e c^2)$ is the classical electron radius, P_i the power in the incident wave, L the length of the scattering volume in the direction of the incident wave, θ the angle between $\vec{k}_s$ and the electric field of the incident wave, and $v_{th,e} = \sqrt{2 k_B T_e / m_e}$ is the electron thermal velocity. Equation 2.2 shows that the width of the measured spectrum provides a measure of the electron temperature while the integral of the power over the spectrum is a measure of the electron density. If the electron thermal velocity exceeds a fraction of a percent of the speed of light ($T_e > 1\,\mathrm{keV}$), relativistic corrections in the scattering spectrum become significant and must be taken into account. However, the same procedures described above are used for determining the local electron temperature and density.

As the TS cross section is extremely small, this measurement requires a powerful radiation source. In TCV, the incident wave is produced by three collinear Q-switched Nd:YAG

lasers (neodymium-doped yttrium aluminium garnet - Nd:$Y_3Al_5O_{12}$) operating at $\lambda = 1.064\,\mu$m, injected vertically at $R = 0.9\,$m with a repetition rate of up to 20 Hz. The lasers can also be sequentially triggered such that the repetition rate is increased to 60 Hz. The present TCV TS system has 35 viewing chords that can be distributed along the laser beam, with each chord viewing a scattering length of $L = 4\,$cm. Figure 2.9(b) shows the TS system in a configuration optimized for a snowflake discharge. For the temperature measurements, the spectral scattered power is measured using filter polychromators equipped with 4 (main plasma) and 3 (plasma edge) spectral channels. For the electron density measurements, regular calibrations are performed using Raman scattering from molecular nitrogen gas filled into the TCV vessel. A comparison of the line integrated density with the results from the FIR diagnostic is performed to derive a correction factor and obtain consistency. More details about this diagnostic can be found at [47, 48].

2.2.3 Metal foil bolometers (BOLO)

In TCV, the BOLO diagnostic provides an estimation of the total radiated power and can be tomographically inverted to provide a 2D spatial profile of the total plasma emissivity. Depending on the plasma conditions, the total radiated power emitted by the plasma can be as high as 80% of the total input power. The measurements of the total radiated power are very important in the study of heat and impurity transport in tokamak plasmas, and in computing the power balance. Bolometers are the most widely used tool for measuring radiation losses. The method is based on the change of the resistance of a metal foil due to a change of the foil temperature caused by the absorption of energy. In tokamaks, this energy deposition on the metal foil can be due to photons originating from the plasma and impinging neutral particles generated by charge exchange processes in the plasma core.

The BOLO diagnostic is composed of 5 pinhole cameras installed at the same toroidal location with a total of 64 line of sights covering the poloidal cross section, figure 2.9(c). The TCV bolometers were designed at the Max Planck Institut für Plasmaphysik at Garching and are identical to the systems installed on the JET and ASDEX-Upgrade tokamaks. Each detector comprises a small metal foil detector consisting of a gold-absorbing layer of $4\,\mu$m thickness deposited on a kapton substrate of $7.5\,\mu$m thickness. The detectors are sensitive to photons with energies from approximately 1 eV up to 10 keV. The BOLO diagnostic allows for tomographic inversion providing a 2D spatial profile of the total plasma emissivity with a spatial resolution of about 4 cm and a temporal resolution of approximately 10 ms. More details about this diagnostic can be found in [49, 50, 51].

2.2.4 Duplex multi-wire proportional X-ray (DMPX)

The soft X-ray emission of the TCV plasmas is measured with a duplex multi-wire proportional X-ray (DMPX) detector. The electromagnetic radiation emitted by the plasma in the range of soft X-ray (120 eV to 120 keV) is produced mostly by three processes, namely (*i*) continuous bremsstrahlung radiation, caused by the charge acceleration during Coulomb collisions, (*ii*) discrete line radiation, due to the transition of a bound electron to a lower energy state, and (*iii*) recombination radiation. Assuming a Maxwellian electron velocity distribution, the spectral power density due to continuous Bremsstrahlung is given by [44]

$$\frac{d^3P}{d\omega\, d\Omega\, dV} = Z_{\mathrm{eff}}\, n_{\mathrm{e}}^2 \left(\frac{e^2}{4\,\pi\,\epsilon_0}\right)^3 \frac{4\,\bar{g}}{3\sqrt{3}\, m_{\mathrm{e}}^2\, c^3} \left(\frac{2\, m_{\mathrm{e}}}{\pi\, k_{\mathrm{B}}\, T_{\mathrm{e}}}\right)^{1/2} exp\left(-\frac{\hbar\,\omega}{k_{\mathrm{B}}\, T_{\mathrm{e}}}\right), \tag{2.3}$$

where $Z_{\mathrm{eff}} = \sum n_{\mathrm{j}}\, Z_{\mathrm{j}}^2 / n_{\mathrm{e}}$ is the effective charge and $\bar{g}$ the so-called Gaunt factor. After integration of this equation over the entire spectrum and solid angle, the total radiated power per unit of plasma volume is given by

$$\frac{dP}{dV} = \int\int \frac{d^3P}{d\omega\, d\Omega\, dV}\, d\omega\, d\Omega = 1.7 \times 10^{-38}\, \bar{g}\, Z_{\mathrm{eff}}\, n_{\mathrm{e}}^2\, \sqrt{T_{\mathrm{e}}}. \tag{2.4}$$

Due to the dependence of the total power density emitted by the plasma on the electron temperature and density (equation 2.4), which are expected to be approximately constant on magnetic flux surfaces, the DMPX diagnostic also provides information on the behavior of MHD instabilities.

The DMPX diagnostic comprises two complete detector chambers designed to provide measurements with high radial and temporal resolutions. The DMPX diagnostic has a spatial resolution of about 8 mm at the equatorial plane, figure 2.9(d), and is acquired at 200 kHz. The two detectors are installed bellow the TCV vessel with one detector placed above the other such that the incoming photons pass through additional filters before reaching the bottom detector, resulting in detection of photons with a different energy range. These detectors are sensitive to photons with energies up to 30 keV. Photons with energies below 1 keV, e.g. due to impurity line radiation, are filtered by a beryllium window located in front of the detectors so that only electrons with energies higher than 400 eV contribute to the signal. Therefore, the DMPX diagnostic is mainly weighted to phenomena occurring in the plasma center. More details can be found at [52, 53].

2.2.5 Magnetic probes (MP)

In TCV, the magnetic measurements are performed using pick-up coils. The measurements are based on the Faraday's law that relates temporal variations of a magnetic field to an induced electric field. Assuming that the spatial variation of the magnetic field within the probe volume is small, the measurement provides information on the temporal variation of the magnetic field along the axis of the probe. Since perturbations of the poloidal magnetic field are typically one order of magnitude higher than those of the toroidal magnetic field, an array of pick-up coils in the poloidal direction is well suited for the analysis of the magnetic perturbations.

Due to the large flexibility in plasma shape and position, TCV requires a high precision magnetic diagnostic system with a large spatial coverage. The TCV magnetic diagnostic system is a fundamental part of the real time control of the plasma position and shape, and it is composed by poloidal field magnetic probes, poloidal flux loops, saddle coils and a diamagnetic loop. The magnetic measurements are used for the magnetic equilibrium reconstruction, which is performed using the LIUQE code [54].

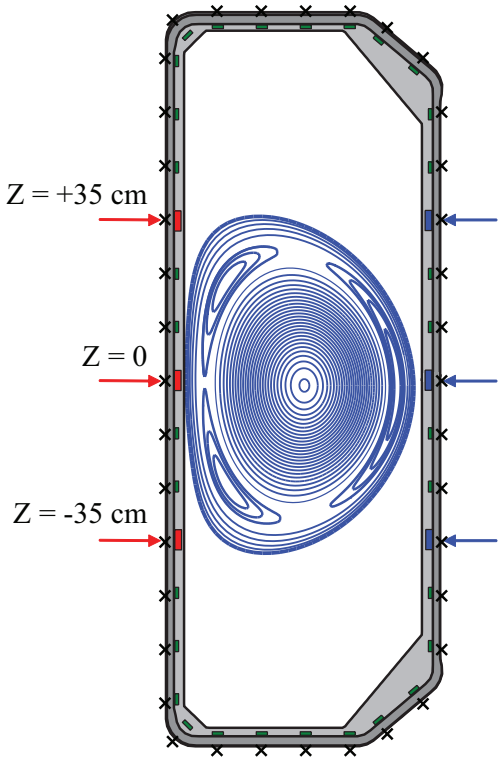

Figure 2.10: (a) Schematic drawing showing the poloidal array of poloidal magnetic field sensors (green, red and blue boxes) composed by 38 probes. The red and blue boxes correspond to probes that are also part of toroidal arrays of poloidal magnetic field probes. The black crosses represent the flux loops.

TCV is equipped with 4 poloidal arrays of magnetic sensors, separated by 90° and consisting of 38 probes each. In addition, toroidal arrays of poloidal field probes are installed on the LFS and HFS, and consist of 16 and 8 equidistant probes, respectively. Three pairs of toroidal arrays are located at three different heights, $Z = 0$, 35 and -35 cm. The up-down symmetric plasmas used in the work described in chapter 3 are at the height of the equatorial LFS and HFS toroidal arrays ($Z = 0$), figure 2.10. Since these probes are located inside the vacuum vessel, measurements are not reduced by the magnetic diffusion time of the TCV conducting vessel, thus providing fast magnetic fluctuation measurements. A total of 61 flux loops are installed around TCV and near each of the magnetic coils, figures 2.4 and 2.10. More details on the magnetic diagnostic systems can be found at [55, 56].

2.2.6 Langmuir probes (LP)

A Langmuir probe is an electrostatic probe and was originally developed by I. Langmuir and H.M. Mott-Smith [57, 58, 59, 60]. A Langmuir probe is a small electrode that is immersed in the plasma and connected to a power supply capable of applying a bias potential, V_b. The dependence of the drained current I_probe on the bias potential yields the Langmuir characteristic curve. Here, the conventional (engineering) direction of the current will be used.

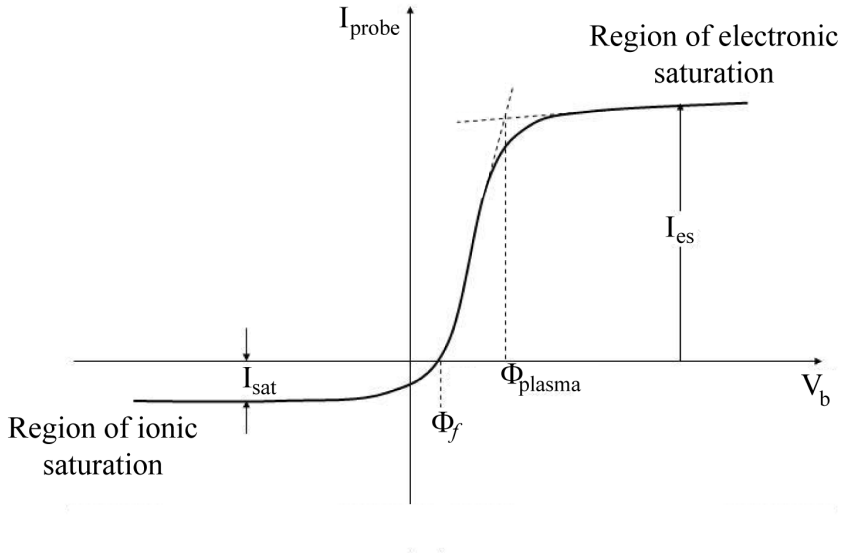

Figure 2.11: Schematic of a characteristic curve obtained from a Langmuir probe.

As an example, figure 2.11 shows an idealized Langmuir characteristic curve characterized by four parameters: plasma potential, floating potential, ion saturation current and sheath expansion coefficient. Here, the plasma potential, Φ_plasma, corresponds to the local value of the electric potential of the plasma at the probe location. For bias potentials $V_\mathrm{b} \geq \Phi_\mathrm{plasma}$,

the ions are strongly repelled and the electrons dominate the electric shielding of the probe. According to classical Langmuir theory [57], the electron saturation current is determined by $I_{es} = n\,e\,A_{probe}\sqrt{k_B\,T_e/(2\,\pi\,m_e)}$. Here, A_{probe} is the surface area of the probe. For bias voltages $V_b \lesssim \Phi_{plasma}$, the drained current from the plasma is composed by electron and ion contributions, with the electrons repelled while the ions are attracted by the probe. For decreasing values of V_b, the drained current from the plasma decreases until the ion and electron currents are equal and the net probe current is zero, $I_{probe} = 0$. This occurs when the bias potential $V_b = \Phi_f$, which is referred to as the floating potential. For very negative bias voltages, $V_b << \Phi_f$, the electrons are strongly repelled while the ions are attracted by the probe. According to the Bohm criterion [61, 62], the ion saturation current can be determined by $I_{sat} = 0.606\,n\,e\,c_s\,A_{probe}$, with $c_s = \sqrt{k_B\,(T_e + T_i)\,/m_i}$ being the isothermal sound velocity.

The presence of a perturbing potential in the plasma caused by a polarized probe leads to the formation of a so-called Debye sheath. Since the thickness of the Debye sheath depends on the probe potential [44], an imperfect saturation of the ion current is observed when the sheath thickness is comparable with the typical probe dimensions. To account for this effect, the experimentally measured Langmuir curves are interpreted using

$$I_{probe}\,(V_b) = I_{sat}\left\{exp\left[\frac{e\,(V_b - \Phi_f)}{k_B T_e}\right] - 1 - \alpha_{sheath}\left[\frac{e\,(V_b - \Phi_f)}{k_B T_e}\right]\right\} \text{ for } V_b \leq \Phi_{plasma}. \tag{2.5}$$

In this equation, the first term on the right hand side corresponds to the electron contribution to the probe current while the other two terms represent the ion contribution. Here, α_{sheath} is the sheath expansion factor that accounts for the increase of the sheath thickness when a negative probe potential increases in magnitude. Imposing $V_b = \Phi_{plasma}$ and $I_{probe} = I_{es}$ in equation 2.5 leads to a relation between the floating and the plasma potential,

$$\Phi_{plasma} = \Phi_f + \Lambda\,T_e \tag{2.6}$$

where $\Lambda = -1/2\ \ln\left[2\,\pi\,m_e\,(1 + T_i/T_e)\,/m_i\right] \approx 3$ for hydrogen or deuterium.

In figure 2.12, a Langmuir curve obtained experimentally during a TCV discharge is shown. The blue curve corresponds to the time averaged probe current measurements while the red one to the fit of the experimental data using equation 2.5. The fitting procedure for the four fit parameters, T_e, Φ_f, α_{sheath} and I_{sat}, uses a minimum temperature approach [63]. Once the electron temperature and ion saturation current are found, the heat flux

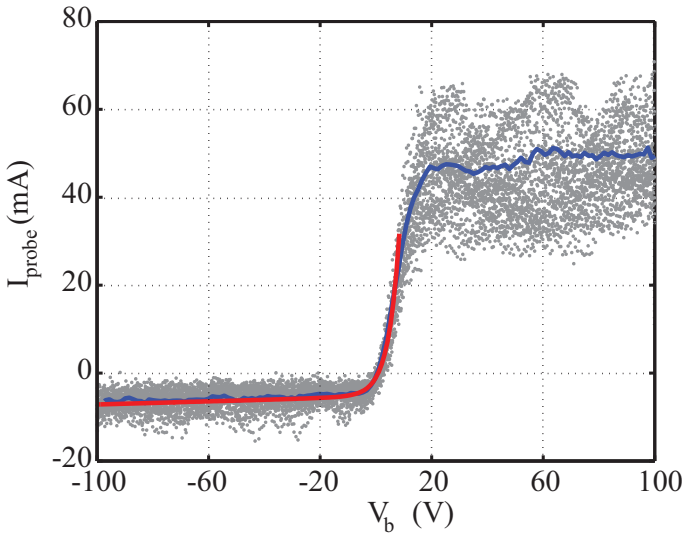

Figure 2.12: Experimentally measured Langmuir characteristic curve (gray dots) obtained from a probe on the TCV floor. The blue and red curves correspond to the time averaged Langmuir curve and the fitting of the experimental data using equation 2.5, respectively. The fitting provides $T_\mathrm{e} = 5.1\,\mathrm{eV}$, $\Phi_\mathrm{f} = -0.82\,\mathrm{V}$, $I_\mathrm{sat} = 5.1\,\mathrm{mA}$ and $\alpha_\mathrm{sheath} = 0.046$.

associated with the plasma interacting with the probe is estimated using,

$$q_\mathrm{t} = \gamma\, T_\mathrm{e}\, J_\mathrm{sat} + \epsilon_\mathrm{pot}\, J_\mathrm{sat}. \tag{2.7}$$

In this equation, $\epsilon_\mathrm{pot} = 15.8\,\mathrm{eV}$ is the potential energy per incident ion that includes its ionization potential of 13.6 eV and half of the molecular binding energy of 2.2 eV, $J_\mathrm{sat} = I_\mathrm{sat}/A_\mathrm{probe}$ is the ion saturation current density perpendicular to the probe surface and

$$\gamma = \frac{5}{2}\frac{T_\mathrm{i}}{T_\mathrm{e}} + \frac{2}{1-\delta_\mathrm{e}} - \frac{1}{2}\ln\left[\left(2\pi\frac{m_\mathrm{e}}{m_\mathrm{i}}\right)\left(1+\frac{T_\mathrm{i}}{T_\mathrm{e}}\right)\frac{1}{(1-\delta_\mathrm{e})^2}\right] \tag{2.8}$$

is the sheath heat transmission coefficient with δ_e being the secondary electron emission coefficient [15]. In this work, $\gamma = 5$, which is the value determined in a previous comparison of Langmuir probe measurements of the heat flux at the LFS strike point in a standard SN configuration with infrared thermography [64]. The uncertainty in γ can introduce systematic errors as its value may depend on many parameters, e.g. the grazing angle of the field lines through δ_e.

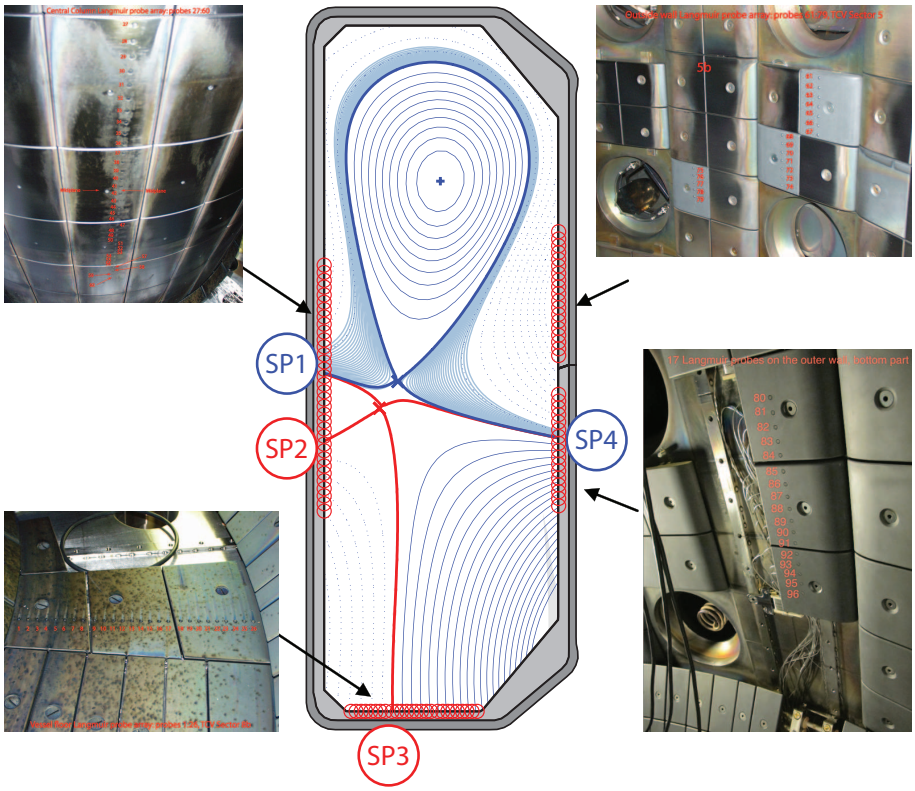

Figure 2.13: Location of the Langmuir probes on the TCV wall and pictures of each of the four arrays.

TCV is equipped with a total of 96 tile embedded Langmuir probes. The probe tips are made of the same material as the tiles, i.e. graphite, and are distributed across the inner contour of the TCV wall as shown in figure 2.13. While the probes on the central column are flush-mounted, the floor and outer wall probes are domed. The spatial resolution of this diagnostic is approximately 1.7, 1.2, 1.6 and 1.6 cm for the central column, floor, and upper and lower arrays on the LFS, respectively. Small sweeps of the plasma vertical position, resulting in sweeps of the strike points on the vertical targets across multiple Langmuir probes, were used to increase the experimental spatial resolution. A similar increase of the spatial resolution for the strike point on the floor is obtained by a small horizontal sweeps of the strike point.

2.2.7 Thermocouples (TC)

Of the many temperature sensors installed on TCV, 29 tile embedded thermocouples are dedicated to monitor the temperature of chosen graphite tiles: 15 distributed in the floor tiles in the field-of-view (FOV) of the vertical infrared camera system and 14 distributed on the central column tiles in the FOV of the horizontal infrared camera system, figure 2.14.

A thermocouple is a temperature-measuring device based on the Seebeck effect. This produces a difference of potential between two different metals put in contact. A thermocouple is composed of two junctions of two different metals: one junction is kept at a constant reference temperature with the other being used to monitor the temperature of the object of interest. In tokamaks, thermocouples are one of the more simple and cheaper solutions for monitoring the temperatures of the plasma facing components.

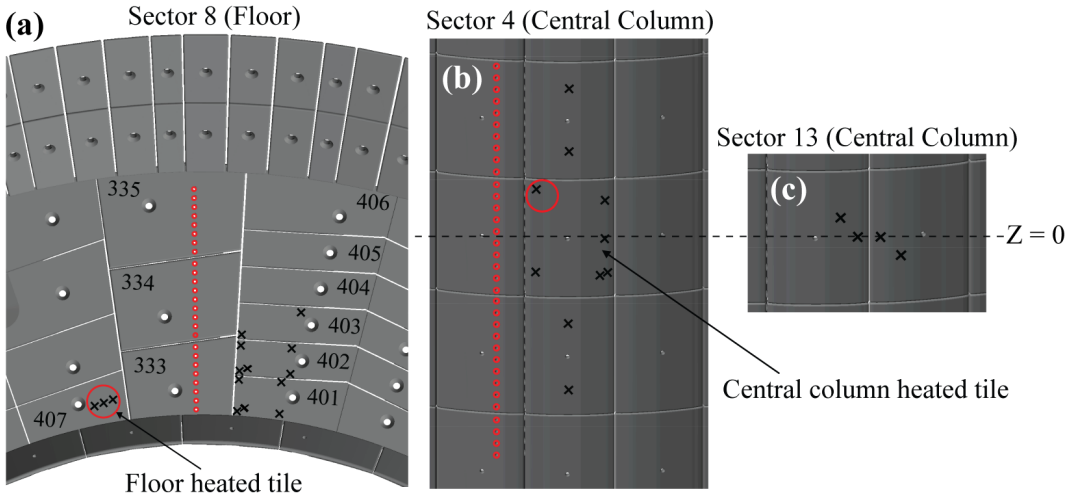

Figure 2.14: Schematic drawing showing the 29 thermocouples (black crosses) monitoring the temperature of some of the carbon tiles on the (a) floor of the sector 8, (b) at the central column in sector 4 and (c) the central column in sector 13. The small red circles in (a) and (b) represent the Langmuir probes and the two large red circles represent a heating system for heating a tile in the FOV of (a) the vertical and (b) horizontal infrared camera system.

One of the main limitations of using thermocouples is a low temporal resolution compared with the typical duration of a TCV discharge (about 2 s). This is imposed by the time the heat deposited on the tile surface takes to propagate into the tile and change the temperature at the thermocouple location. In the TCV graphite tiles, a temperature variation at the thermocouple position is only observed a few seconds after the end of the plasma discharge. This diagnostic only provides the total amount of energy deposited in a tile during a discharge, Q, with no useful temporal resolution.

During a discharge, the thermocouples that are closer to the strike point have a larger temperature rise than those farther away. In addition, thermocouples located closer to the tile surface facing the plasma, e.g. the TCs in the tile 407, usually heat more and faster than the others, e.g. in the tile 401. This can be observed in figure 2.15 that plots typical temperature evolution measured by the TCs in the floor tiles during a diverted discharge in which the strike point is located on the first row of tiles (tiles 407, 333 and 401 in figure 2.14).

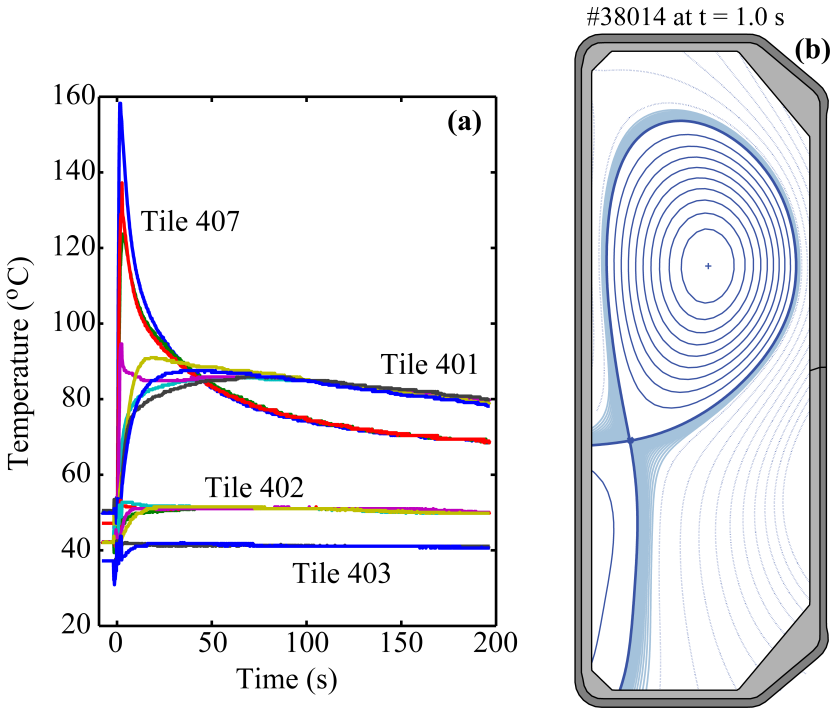

Figure 2.15: (a) Typical temporal evolution of the temperature of the floor tiles 401, 402, 403 and 407 measured using their respective TCs for (b) a diverted plasma with a strike point lying on the first row of tiles. See figure 2.14 for details of the tiles location.

To estimate the total energy stored in the tile during a plasma discharge, the temporal evolution of the tile temperature measured using the TCs is used for a calorimetric analysis. The principle of this method is to use the measurements of the tile temperature before and after the discharge to estimate the energy required to produce such an increase of temperature. This method, however, requires the knowledge of the temperature distribution in the entire volume of the tile.

Some time after the end of the discharge, the temperature distribution inside the tile is approximately constant. For times longer than this equilibration time, t_{equil}, the heat is transported outwards from the tile through the fixation supports in such a way that the whole tile can be characterized by a single temperature value, making the calorimetric analysis possible. Note that small temperature gradients will always persist in the vicinity of the fixation support.

Since the calorimetric analysis has to be performed only at times longer than t_{equil}, the thermocouple data are acquired over a longer period after the discharge (up to 600 s). In TCV, the temperature within the tiles becomes homogeneous approximately 100 s after the end of the discharge. This value has also been confirmed from previous numerical simulations of heat propagation in the TCV tiles using the ANSYS code [64]. The simulations show that the temperature differences inside the tile become smaller than 1°C

approximately 60 s after the end of a discharge. Once the tile has more or less reached an internal thermal equilibrium, the temporal evolution of the tile temperature, T_{tile}, can be modeled by

$$m_{\text{tile}}\, c_{\text{p}}\, \frac{dT_{\text{tile}}}{dt} = -h_{\text{fix}}\, A_{\text{fix}}\, \left(T_{\text{tile}} - T_{\text{env}}\right) - \sigma\, A_{\text{tile}}\, \epsilon\, \left(T_{\text{tile}}^4 - T_{\text{env}}^4\right). \tag{2.9}$$

Here, m_{tile} and c_{p} are the mass and the specific heat capacity of the tile, respectively, T_{env} is the temperature of the surrounding structures, A_{tile} is the surface area of the tile, ϵ is the tile emissivity and h_{fix} is a heat transmission coefficient, which models the transport of heat outwards from the tile through the surface area of the fixation support, A_{fix}. The dependence of c_{p} on the temperature can be seen in figure 2.8(b). In this equation, the first term accounts for the heat transport through the fixation support while the second term accounts for the net-energy leaving the tile through radiation (equation 2.13). Since the tiles are inside the vacuum chamber, convective transport may be neglected. For the range of tile temperatures encountered in this thesis, the second term on the right hand side of equation 2.9 is found to be much smaller than the first, and the inter-shot tile temperature evolution is generally well described by

$$T_{\text{tile}}\,(t) = T_{\text{env}} + \left[T_{\text{tile}}\,(t_{\text{equil}}) - T_{\text{env}}\right] exp\left(-\frac{t - t_{\text{equil}}}{\tau}\right) \quad \text{for} \quad t \geq t_{\text{equil}}. \tag{2.10}$$

Here, $\tau = h_{\text{fix}}\, A_{\text{fix}} \,/\, m_{\text{tile}}\, c_{\text{p}}$. Following the procedure described in [65], this equation is used for fitting the experimentally measured temperature cool-down phase for $t \geq t_{\text{equil}}$. The fit curve is then extrapolated backwards in time until the end of the discharge to estimate an equivalent homogeneous tile temperature at the end of the discharge, $T_{\text{tile,f}}$. Although this procedure reduces the scatter of the measurements in [65], it does not affect substantially the measurements of the total deposited energy, Q, estimated at the equilibration time for the experiments described in this thesis. With the value of $T_{\text{tile,f}}$ and the value of the tile temperature before the discharge, $T_{\text{tile,i}}$, the total amount of heat deposited in a tile during a discharge can be estimated by

$$Q = m_{\text{tile}} \int_{T_{\text{tile,i}}}^{T_{\text{tile,f}}} c_{\text{p}}\,(T)\, dT. \tag{2.11}$$

The typical uncertainty of these measurements is expected to be about 20% [66] and, as discussed in appendix A.11, they are also used to cross-check the infrared measurements.

2.2.8 Infrared thermography (VIR and HIR)

In this section, the infrared thermography systems of TCV will be presented as well as the procedure to estimate the heat flux onto the TCV wall. More details about these diagnostics can be found in appendix A and in [66].

The electromagnetic radiation of a black body

A form of electromagnetic radiation with frequencies below those of red light was discovered by Sir William Herschel. This part of the electromagnetic spectrum was named infrared (IR) and is used for infrared thermal imaging based on radiometric measurements [67]. The basic laws which govern the behavior of the IR radiation (Kirchhoff's law, Stefan-Boltzmann's law, Planck's law and Wien's displacement law) were developed many years after its discovery.

Kirchhoff's law Gustave Kirchhoff, in 1859, found that a material that is a good absorber of radiation is also a good radiator. The ratio of the total radiated power emitted by a body and its absorption coefficient, α_{abs}, is the same for all radiators at that temperature. When a body completely absorbs the impinging radiation on it, it is said to be "black".

The emission of electromagnetic radiation from real objects differs from that of a black body, since physical surface properties affect the angular distribution and the spectral characteristics of the emitted radiation. Furthermore, a real surface does not absorb all incident radiation, but reflects, or transmits, some fraction of it. However, in equilibrium conditions, the absorption coefficient must be equal to the emissivity of the body, ϵ, which is defined as the ratio between its emitted radiation $I(T, \lambda)$ and the emitted radiation of a black body $I_{\text{BB}}(T, \lambda)$ at the same temperature,

$$\epsilon(T, \lambda) = \frac{I(T, \lambda)}{I_{\text{BB}}(T, \lambda)}. \tag{2.12}$$

Stefan-Boltzmann's law In 1884, L. E. Boltzmann derived a theoretical formula describing the radiation emitted by a black body starting from thermodynamic principles. A few years later, in 1879, J. Stefan has stated it empirically by developing the so-called Stefan-Boltzmann's law,

$$P = A\epsilon\sigma\left(T^4 - T_{\text{env}}^4\right), \tag{2.13}$$

where P is the total power radiated by a body at an absolute temperature T, with a surface area A and emissivity ϵ. T_{env} is the temperature of the surrounding environment and σ the Stefan-Boltzmann's constant.

Planck's law of radiation In 1901, the Nobel prize Max Karl Ernst Ludwig Planck developed the so-called Planck's law, which states that the total radiated power emitted by a black body at an absolute temperature T, per unit of surface area dA, solid angle $d\Omega$, and with wavelength λ in the range between λ and $\lambda + d\lambda$, is given by

$$I_{\text{BB}}(T,\lambda) = \frac{d^3P}{dAd\Omega d\lambda} = \frac{2hc^2}{\lambda^5}\frac{1}{exp\left(\frac{hc}{\lambda k_{\text{B}}T}\right)-1}, \tag{2.14}$$

where c is the speed of light, k_{B} is the Boltzmann constant and h the Planck's constant. Equation 2.14 defines a quantity called spectral radiance and figure 2.16 shows its dependence on the wavelength for four different temperature values.

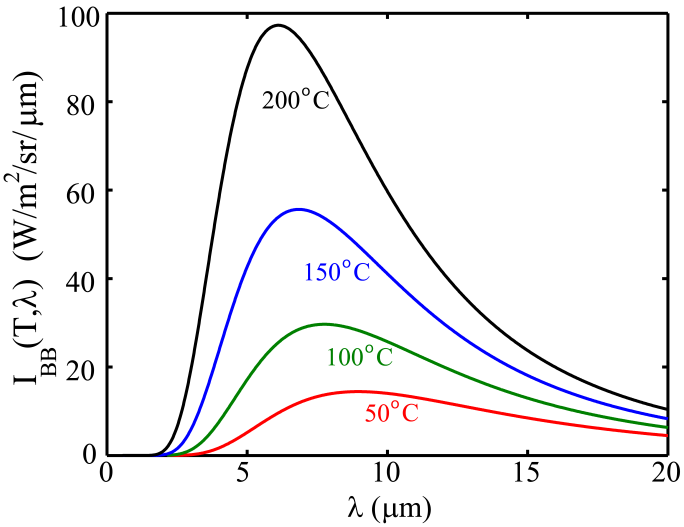

Figure 2.16: Spectral radiance (equation 2.14) of a black body for four different values of temperature.

The radiated power can also be expressed in terms of the spectral photon flux by dividing equation 2.14 by the energy of each emitted photon (hc/λ),

$$\frac{d^3\Phi_{\text{ph}}}{dAd\Omega d\lambda} = \frac{2c}{\lambda^4}\frac{1}{exp\left(\frac{hc}{\lambda k_{\text{B}}T}\right)-1}. \tag{2.15}$$

Wien's displacement law Wilhelm Wien established the Wien's displacement law by differentiating equation 2.14 in order to find the wavelength at which the spectral radiance is maximum for a radiator at a given temperature T,

$$\lambda_{\max} T = 2.8978 \times 10^3 \ \ (\mu m \cdot K). \tag{2.16}$$

This equation shows that the radiance of a body at a higher temperature peaks at a shorter wavelength.

Infrared detectors

Infrared thermal imagers have been used in military and scientific applications for many years. An IR thermal imager is a camera that provides a picture of the electromagnetic energy radiated from an object in the IR spectral band. Whether the formulation in radiated power (2.14) or photon flux (2.15) is appropriate, depends on the kind of IR detector.

A number of detector technologies have been developed for imaging in the IR spectral band. Most modern detectors are based on Focal Plane Arrays (FPA) of photon sensitive detectors. Each individual detector has a different gain and a different offset that may change in time due to detector-to-detector variability in the FPA fabrication process [68], sensor operating temperature, temperature of the observed scene, electronic readout noise, etc. Difference in gain and offset among detectors produces the so-called fixed pattern noise (FPN) in the acquired image.

TCV's infrared camera

TCV is equipped with an IR camera (Thermosensorik CMT 256 M HS) that is based on an FPA composed by 256×256 pixels (detectors) of size 40 μm×40 μm, quantum efficiency $q_{\text{Det}} \approx 0.8$, and with a subframe rate of up to 25 kHz, figure 2.17.

The FPA elements are of Cadmium Mercury Telluride (CdHgTe or CMT), which is is an alloy of CdTe and HgTe. The CdTe is a semiconductor with a band-gap of approximately 1.5 eV at room temperature while HgTe is a semi-metal with a zero band-gap energy. A mixture of these two materials can exhibit any desired band-gap between 0 and 1.5 eV. The proportion of Cd in the alloy is chosen to tune the optical absorption of the material to the desired IR wavelength range. TCV's IR camera is sensitive to wavelengths between 1.5 and 5.1 μm (0.24 to 0.82 eV), i.e. a combination of short- (SWIR) and mid-wave (MWIR) IR, sometimes also referred to as broad-wave infrared (BWIR).

In the CdHgTe, the infrared photons are detected when their energy is sufficient to excite an electron from the valence band to the conduction band. These electrons are collected by an external readout integrated circuit. The resulting signal is subsequently digitized with 14-bit resolution and the detector ensemble acquired by a frame-grabber inside the acquisition system. The main limitation of CdHgTe detectors is a need to cool the detector to low temperatures (about 85 K) in order to sufficiently reduce the background signal due to thermally excited electron-hole pairs. In the Thermosensorik CMT 256 M HS camera, this is performed by a Stirling cooler.

Figure 2.17: Thermosensorik CMT 256 M HS camera.

IR optical systems in TCV

In TCV, two IR optical systems were used to provide measurements of the surface temperature of the wall, figure 2.18(a): a vertical (VIR) and a horizontal (HIR) IR optical system.

The VIR system is located above TCV and used to estimate the surface temperature of the floor tiles. A typical IR image obtained using the VIR system is shown in figure 2.18(b), where the strike point SP3 of a snowflake plus can be seen. This system has a F-number of $\mathrm{F}/\# = 2.3$, a magnification of $|\beta| = 64$, and a spatial resolution of approximately 2.5 mm.

The HIR system is located on the LFS and has been used to estimate the surface temperature of the central column tiles. A typical IR image obtained using the HIR system can be seen in figure 2.18(c), where two strike points of a snowflake plus can be seen (SP1 and SP2). This system has a F-number of $\mathrm{F}/\# = 3.6$, a magnification of $|\beta| = 49$, and a spatial resolution of approximately 2.0 mm.

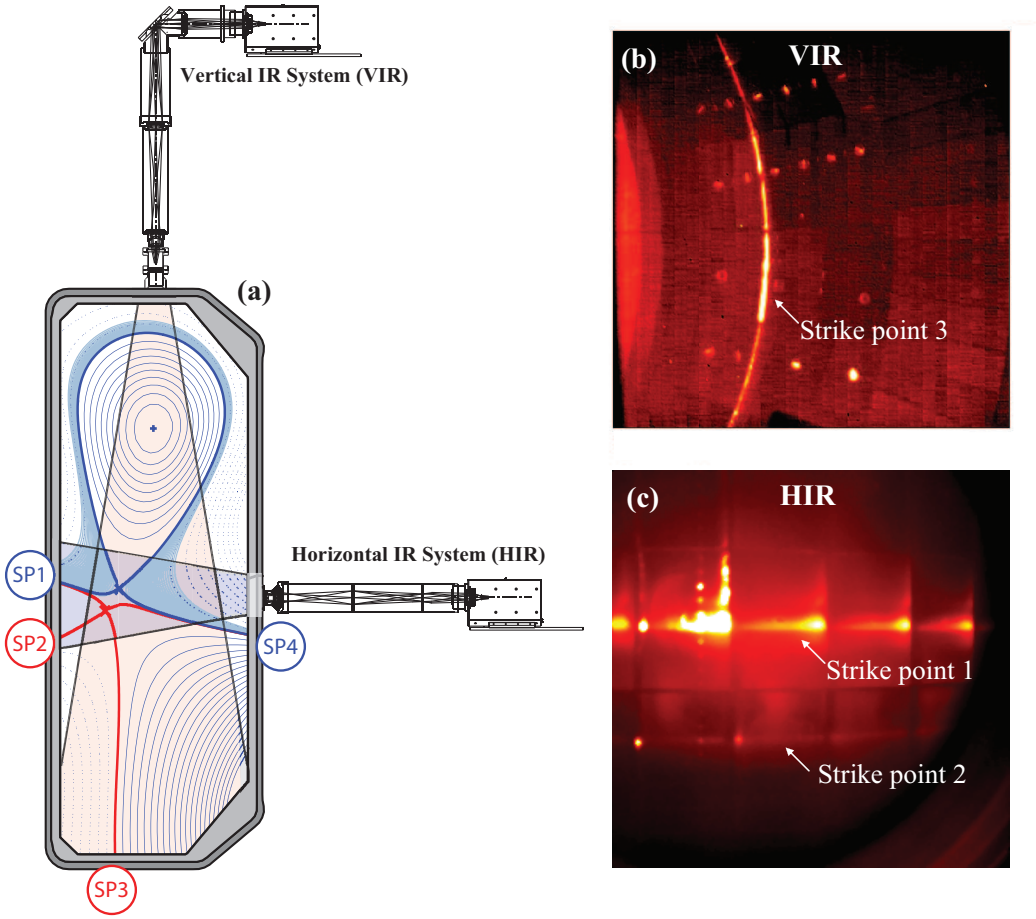

Figure 2.18: (a) Schematic drawing showing the HIR and VIR diagnostic systems. Typical IR images from the (b) VIR and (c) HIR systems from a SF discharge where three of the four strike points can be seen.

Heat flux estimates

Estimates of the target heat flux, q_t, based on IR thermography are obtained through modeling of the evolution of the measured surface temperature of the graphite tiles using the THEODOR code [69]. THEODOR solves the 2D heat diffusion equation relating measured temperatures to heat fluxes numerically, using the measured surface temperature profile as a dynamic boundary condition and accounting for the temperature dependent material properties. Surface modifications of the tile, e.g. due to hydrogen or impurity implantation in erosion dominated regions, result in a decreased heat conductivity in a thin layer at the tile surface and, hence, a lower thermal transport from the tile surface to the bulk of the tile.

In order to include the effect of this thin layer, THEODOR uses the heat transmission boundary condition

$$q_{\mathrm{t}} = \alpha \left(T - T_{\mathrm{bulk}} \right), \tag{2.17}$$

where T is the measured surface temperature, T_{bulk} the temperature in the bulk tile in contact with the thin layer and $\alpha = \kappa_{\mathrm{layer}}/d_{\mathrm{layer}}$ the heat transmission coefficient (see appendix A.9). Here, κ_{layer} is the layer heat conductivity and d_{layer} the layer thickness. As an example, a heat flux profile on the TCV floor obtained from the THEODOR code can be seen in figure 2.19.

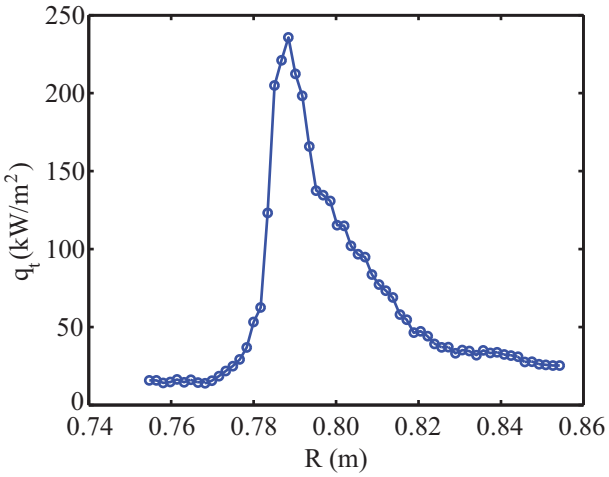

Figure 2.19: Example of a heat flux profile on the TCV floor based on IR thermography and using the THEODOR code.

In figure 2.19, the target heat flux has an offset value of 10-20 kW/m^2. This offset level is thought to be caused by a combination of several effects, mostly due to fast neutral particles originated from charge exchange core neutrals, absorption of the plasma radiated power, reflections of IR light coming from surrounding IR emitters and the emission from optical components with imperfect transmission. Only plasma related power depositions are linked to the magnetic geometry at the target and, therefore, expected to show strong spatial variations while the other processes only vary on longer spatial scales. In order to estimate the power arriving on a strike point target due to the heat transported by the plasma, this offset value of the target heat flux is usually subtracted from the profile. More details about the TCV IR thermography diagnostics can be found in appendix A and in [66].

3 Sawtooth Generated Magnetic Islands

Although sawteeth (ST) and neoclassical tearing modes (NTM) have been intensively investigated, a validated quantitative theory of the triggering of NTMs by ST is still missing. This chapter will present new experimental results on the seeding of NTMs by sawteeth obtained by using the flexible electron cyclotron (EC) waves system of TCV combined with a suited set of diagnostics. During this work, TCV's resources were used to trigger NTMs under controlled conditions, providing an excellent environment for the study of the seeding of NTMs by sawtooth crashes. The work presented in this chapter has already been published [70].

Following a brief review of the present understanding of the sawtooth and NTM physics, the new TCV experiments will be presented. In section 3.3, the experimental setup used for the combined ST period control and NTM "preemption" is described. Section 3.4 presents the dependence of the NTM onset on the value of the ST period in discharges with and without "preemptive" ECH. Section 3.5 presents the evidence of fast seed island formation within a few microseconds following the ST crash. Section 3.6 reports on the influence of the ST period on the NTM stability after the crash and on the generated seed island widths. In section 3.7, the effect of the edge safety factor on the triggering of NTMs is presented. Section 3.8 shows a strategy, based on the pre-knowledge of the triggering time, i.e. the ST crash time, to prevent the NTM seeding. Finally, conclusions are presented in section 3.9.

3.1 The Physics of the Triggering of NTMs by Sawteeth

This section will report on the present understanding of ST and NTM physics. The main features of these two instabilities will be reviewed including recent results related to the physical mechanisms behind the triggering of NTMs by ST.

3.1.1 The sawtooth instability

Sawtooth oscillations are periodic relaxations of the core plasma density and temperature. Their existence was first reported by von Goeler, Stodiek and Sautoff in 1974 on the ST-Tokamak [71]. This instability is the experimental manifestation of an internal $m/n = 1/1$ kink mode, where m and n are the poloidal and toroidal mode numbers, respectively. It is found to occur naturally in tokamaks where the safety factor at the magnetic axis $q_0 < 1$. A typical sawtooth cycle is shown in figure 3.1, in which three phases can be identified: (i) the sawtooth ramp phase, during which the plasma density and temperature increase monotonically with time; (ii) the precursor phase, during which an internal $m/n = 1/1$ kink mode grows until (iii) the fast collapse phase - the ST crash - in which the core density and temperature decrease rapidly. The rapid crash leads to a flattening of the central plasma temperature and density profiles due to the expulsion of particles and energy from the core region and the redistribution of the plasma current inside a so-called "mixing" radius ρ_{mix}. Outside this radius the plasma profiles are not strongly affected whilst inside this radius, two regions may be defined: a region which has radially outward particle and energy transport, and a region that receives the expelled particles and energy. These two regions are delimited by the so-called "inversion radius" ρ_{inv}.

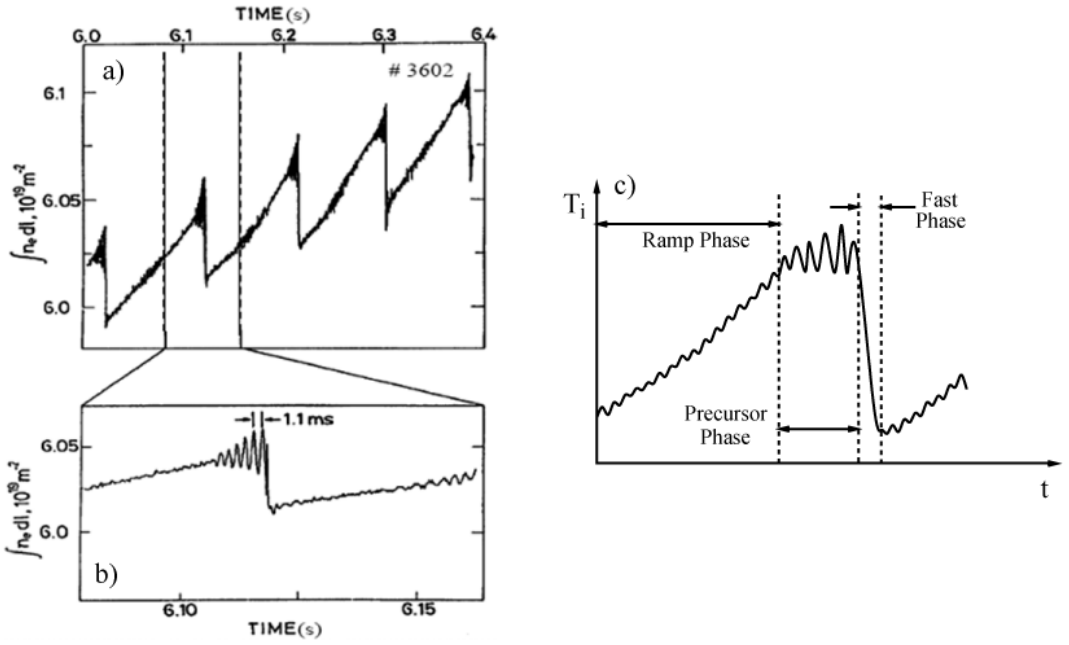

Figure 3.1: The line-integrated electron density of an early JET sawtoothing plasma. The sawtooth oscillation typically consists of a ramp phase, a precursor oscillation followed by the fast collapse phase - the sawtooth crash. Figure reproduced from [1].

Although sawteeth degrade the plasma core confinement by cyclic expulsion of particles and energy, the presence of sawteeth can be beneficial in avoiding accumulation of thermalized α-particles and impurities in the plasma core [21]. However, sawteeth have also the potential to trigger NTMs that further degrade the plasma confinement, and

limits the maximum achievable β. Sawteeth are expected to be the main instability for the generation of seed islands required for the destabilization of NTMs in ITER [72, 28]. For this reason the control of the sawtooth instability is of extreme importance and has been under active research over the last 40 years.

3.1.2 Sawtooth control techniques

This section presents a brief overview of the techniques applied to the control of sawteeth. For a more detailed description see [21, 27, 73, 74].

The trigger criterion of the sawtooth crash

The underlying mechanism responsible for the sawtooth crash comes from the MHD instability of an internal $m/n = 1/1$ kink mode. However, it is clear from experiments that ideal MHD theory alone is not sufficiently accurate to predict the threshold for the onset of the sawtooth crash. Porcelli *et al.* proposed an heuristic model where non-ideal effects, such as kinetic effects associated with energetic particles (including the fusion produced α-particles), finite electrical resistivity, finite ion Larmor radius, among other effects, are combined to provide a set of criteria for the sawtooth crash trigger [75]. In this model, a sawtooth crash occurs as soon as one of the criteria is attained. From [73], the most relevant criterion for determining the onset of the sawtooth crash in plasmas with auxiliary heating is given by :

$$s_1 > s_{\text{crit}} \quad \text{where} \quad s_{\text{crit}} = \max \begin{cases} \frac{4\delta W}{\xi_0^2 \epsilon_1 R B^2 c_\rho \hat{\rho}} \\ \\ s_{\text{crit}}\left(\omega_i^*\right) \end{cases} . \tag{3.1}$$

where, s_1 is the magnetic shear at the $q = 1$ flux surface, $s_{crit}\left(\omega_i^*\right)$ is a critical value of s_1 that depends on the pressure gradient, and δW is the total variation in the potential energy of the internal $m/n = 1/1$ kink mode, which is the sum of several contributions: ideal MHD fluid, δW_{MHD}, collision-less trapped thermal ions, δW_{KO} and a contribution due to fast particles, δW_{fast}.

Control of the sawtooth period

The sawtooth period can be manipulated using actuators that act on different terms of equation 3.1. The fast ion population can be affected by neutral beam injection (NBI) [76] or ion cyclotron heating (ICH) [77, 78, 79], since the δW term in equation 3.1 depends on δW_{fast}. This has been exploited on several tokamaks and may be used to stabilize or

destabilize sawteeth depending on the direction and deposition location of the driven fast ion population. Details of these processes were the subject of a recent review [73].

On TCV, two methods, using locally absorbed EC power, achieved precise and reliable control of the time of the sawtooth crash of individual sawteeth [78, 42]. The control of the ST period was achieved by (*i*) moving the EC power deposition with respect to the $q = 1$ flux surface or (*ii*) by using the possibilities offered by the digital real-time system.

In the first method, the deposition location of the ECCD is changed by simultaneously decreasing the toroidal magnetic field and the plasma current, keeping q_{95} constant. The sawtooth period increases when the deposition location is moved from the plasma center towards the $q = 1$ surface [80]. From the code TORAY-GA [81], ~ 3.8 kA is driven near the $q = 1$ surface and is sufficient to increase the sawtooth period by a factor of 80. This driven current is 3% of the plasma current and it is consistent with effects described in previous work [80].

Varying the location of absorbed ECH or ECCD power is effective because the parameters governing the sawtooth cycle, s_1 and s_{crit} in the Porcelli model [75], react differently to power and/or current deposited in the vicinity of the $q = 1$ surface. The main effect is to slow down or speed up the increase of s_1 during the sawtooth ramp phase, as shown in figure 3.2(a).

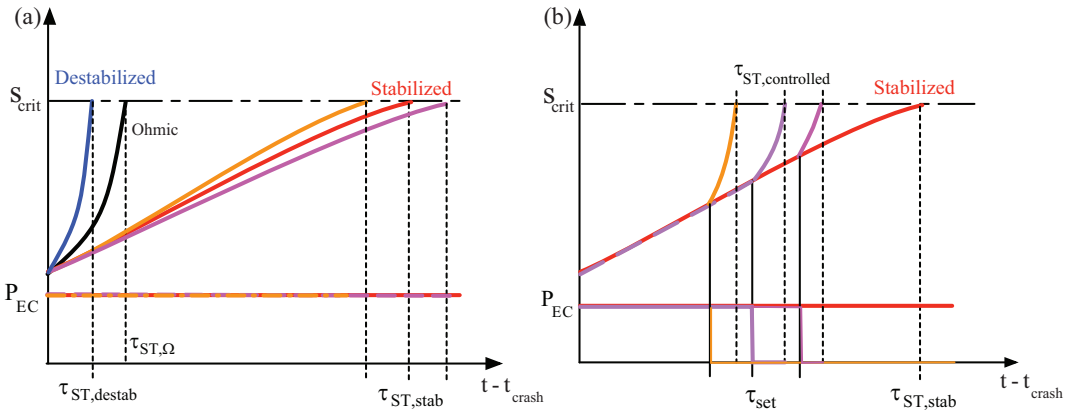

Figure 3.2: Schematic of the control of the sawtooth period by (a) moving the deposition location of the ECH or ECCD with respect to the $q = 1$ surface and by (b) changing the amount of power or current deposited near the $q = 1$ flux surface

In the second method, a real time system controls the on and off times of ECCD power applied at a fixed position in the vicinity of the $q = 1$ surface [82]. ECCD causes the evolution of s_1 to slow. When ECCD is switched off, s_1 evolves naturally towards s_{crit} destabilizing the ST, figure 3.2(b). In TCV, the ST crash typically occurs within a few hundred microseconds following the cessation of ECCD (or τ_{set}), enabling a precise control of τ_{ST} with values ranging from the natural ST period (no ECCD) to the continuous ECCD ST period.

3.1.3 The neoclassical tearing mode instability

Ideal MHD is found to provide the ultimate limits of the maximum achievable β_N in a tokamak, which usually comes in the form of an $n = 1$ kink mode or an $n = \infty$ ballooning mode [83]. However, the maximum achievable values of β_N in high power discharges is limited to values well below the ideal MHD predictions [22, 23], indicating that another instability is responsible for this experimentally observed lower limits.

Typical tokamak plasmas with a monotonic safety factor q profile, $q_{95} \gtrsim 3$, and on axis $q_0 \approx 1$, are expected to be stable with respect to classical tearing modes [84, 72], which are instabilities that break or tear the equilibrium magnetic flux surfaces forming magnetic islands at rational flux surfaces (where the magnetic field lines close upon themselves after a finite number of toroidal and poloidal turns). The deterioration of plasma confinement in high power discharges was experimentally identified as due to resistive tearing modes occurring at low order rational values of the safety factor q, in particular at the $q = 3/2$ and $q = 2/1$ surfaces. To explain these observations, additional physics was added to the classical theory giving rise to a new class of the tearing instability. These are called neoclassical tearing modes and were first identified in the Tokamak Fusion Test Reactor (TFTR) [22].

Since the fusion power scales as β^2 [25], sustained operation at high plasma pressure is required for the tokamak to be a viable candidate for an economically attractive electric power source. NTMs are found to cause a decrease in the plasma confinement [23] and thus in the maximum achievable plasma pressure. This confinement degradation has been observed in many tokamaks [26] and is ascribed to the structure of a magnetic island that arises from the reconnection of adjacent flux surfaces around the mode rational surface, engendering enhanced radial particle and energy flux across the island. An overall confinement degradation of up to 50% has been observed due to the presence of NTMs [85, 86].

Many machines observed that NTM onset is more frequent when β_N is increased [23, 87]. JET and other machines have reported that at intermediate values of β_N ($\approx$ 2-3), 3/2 NTMs are more often observed [88], whilst the onset of 2/1 NTMs are more frequent at higher values of β_N ($\gtrsim 3$) [89]. The onset of 2/1 NTMs are often more catastrophic compared to other NTMs as they can strongly interact with the external conducting structures causing mode rotation to slow down and eventually lock to the static error field [90]. Mode locking often leads to the loss of high confinement operation and disruptions [91, 92], and remains a particular concern for ITER and beyond. NTMs thus impose a severe constraint on the achievable performance of a future power plant using the tokamak concept.

Now follows a brief review of the present understanding of the physics governing the evolution of NTMs. Further information is available in the published literature [84, 88].

The modified Rutherford equation

The modified Rutherford equation (MRE) is a representation of a theoretical model that describes the evolution of NTMs. It has had considerable success in reproducing experimentally observed NTM evolution in tokamak experiments. The MRE describes the nonlinear temporal evolution of the full island width, w, as a function of different stabilizing and destabilizing mechanisms and has the general form

$$\frac{\tau_{\mathrm{R}}}{\rho_{\mathrm{s}}}\frac{dw}{dt} = \sum_i \rho_{\mathrm{s}}\Delta_i'\left(w\right), \tag{3.2}$$

where ρ_{s} is the radial location of the mode rational surface with $\rho = a(\Phi/\Phi_{\mathrm{edge}})^{1/2}$ being the square root of the toroidal magnetic flux Φ, $\tau_{\mathrm{R}} = \mu_0\rho_s^2/(1.22\eta_{\mathrm{neo}})$ is the resistive time, η_{neo} the neoclassical resistivity [23, 93, 94], and the Δ_i's represent the effects of different physical contributions on the evolution of the neoclassical tearing modes that will be discussed below.

The classical tearing mode

In small and medium size tokamaks without auxiliary heating, tearing modes and magnetic islands are mainly driven by the plasma current density gradient [95, 96, 97]. From classical theory, the instability of tearing modes is determined by a parameter usually written in the literature as Δ'. This parameter is related to the modes' linear growth rate, and links the small layer around the mode rational surface, where plasma inertia and resistivity have to be taken into account, and the rest of the plasma, where ideal MHD can be used. This parameter is defined by :

$$\Delta'\left(w\right) = \left[\left.\frac{d\psi_1}{d\rho}\right|_{\rho_s+\frac{w}{2}} - \left.\frac{d\psi_1}{d\rho}\right|_{\rho_s-\frac{w}{2}}\right]/\psi_1\left(\rho_{\mathrm{s}}\right) \tag{3.3}$$

where ψ_1 is the perturbed helical magnetic flux, which can, e.g. be calculated analytically in the cylindrical approximation using ideal MHD in the region external to the resistive layer by solving

$$\frac{1}{\rho}\frac{d}{d\rho}\left(\rho\frac{d\psi_1}{d\rho}\right) - \left[\frac{m^2}{\rho^2} + \frac{\mu_0\frac{dJ_0}{d\rho}}{B_\theta\left(1-\frac{n}{m}q\right)}\right]\psi_1 = 0, \tag{3.4}$$

with B_θ the equilibrium poloidal magnetic field and J_0 the equilibrium plasma current density. Due to a singularity at $q\,(\rho = \rho_s) = m/n$, this equation must be integrated from both sides independently and the value of ψ_1 from both sides must match at $\rho = \rho_s$. Taking into account the modification of the current density profile due to the magnetic island, equation 3.3 can be linearized for small island widths leading to :

$$\Delta'_{classic} = \Delta'_0 - \alpha w, \tag{3.5}$$

where α accounts for the decrease of the instability drive as the island width grows and Δ'_0 (from equations 3.3 and 3.4 with $w \to 0$) determines if the current profile is stable ($\Delta'_0 < 0$) or unstable ($\Delta'_0 > 0$) with respect to tearing modes.

Neoclassical effects

In systems with toroidal symmetry such as tokamaks, the poloidal variation of the toroidal magnetic field can lead to the trapping of particles on the outer (lower field) side of the torus depending on the plasma collisionality regime. When auxiliary heating is applied, the plasma temperature increases and the plasma becomes increasingly collisionless. If the time between collisions of plasma particles becomes larger than the bounce time of the trapped particles, a current proportional to the plasma pressure gradient will arise - the bootstrap current [10, 11, 12]. When a magnetic island exists in the plasma, enhanced transport of particles and energy caused by the magnetic island topological structure leads to a local flattening of the pressure profile inside the island. This flattening causes the loss of the bootstrap current within the island leading to a further increase of the island width whenever the magnetic shear at the resonant surface is positive. This neoclassical contribution to the MRE can be written as :

$$\Delta'_{bs} = a_{bs}\ \beta_{p,s}\ \frac{w}{w^2 + w_d^2}, \tag{3.6}$$

where a_{bs} represents the contribution of the plasma profiles to the bootstrap current [72], $\beta_{p,s}$ is the local poloidal β, and

$$w_d = 5.1\rho_s \left(\frac{1}{\epsilon_s s_s n}\right)^{1/2} \left(\frac{\chi_\perp}{\chi_{||}}\right)^{1/4} \tag{3.7}$$

accounts for small island width effects due to incomplete flattening of the pressure profile inside the island caused by finite $\chi_\perp/\chi_{||}$ [98].

Geometrical effects due to the magnetic field curvature have also been investigated. It was first derived for linear resistive modes by Glasser, Greene and Johnson [99, 100] and has a stabilizing effect as tearing modes bend the magnetic field lines such as to increase the magnetic energy. This term is not found to be significant in conventional aspect ratio tokamaks with $R_0/a \approx 3$ and is usually neglected in the calculations. However, it can become important in tokamaks with low aspect ratio or spherical tori. This term can be written as :

$$\Delta'_{GGJ} = -a_{GGJ}\ \beta\ \frac{1}{\sqrt{w^2 + 0.2w_d^2}}. \tag{3.8}$$

Several authors have also pointed out the effect of a finite polarization current [101, 102] in the NTM behavior caused by perturbations of the electrostatic potential. The propagation of a magnetic island through the plasma rest frame induces a time-varying electric field. The trapped ions experience an average electric field over their orbits while electrons experience a more local effect due to their considerably smaller orbit widths, so that ions and electrons experience different $\vec{E} \times \vec{B}$ drifts. This difference in response leads to a net current if the trapped ion orbit width is comparable to the island size. The polarity of this term is expected to dependent on the difference between the mode and diamagnetic frequencies [103]. According to [94], this term has the following form :

$$\Delta'_{pol} = -a_{pol}\ g\left(\epsilon, \nu_{ii}\right) \frac{w}{w^4 + w_p^4}, \tag{3.9}$$

where a_{pol} accounts for the contribution of the plasma profiles to the polarization current, $g\left(\epsilon, \nu_{ii}\right)$ is a function of order unity and w_p accounts for small island width effects [104].

Effect of localized heating and current drive

Theoretical [105, 106, 84] and experimental [107, 108, 92, 42] works have shown the possibility of stabilizing neoclassical tearing modes by using locally absorbed electron cyclotron waves. The stabilizing effect of these waves in the absence of a magnetic island is usually associated with a modification of the local current density profile due to either localized current drive and/or heating at the position where the NTM is expected. In both cases, stabilization is achieved by generating a current density perturbation, $\delta J_{||}$, parallel to the total equilibrium current density, $J_{||}$, either through non-inductive

current drive and/or a change in the inductive current resulting from a change of the temperature profile [92]. This current density perturbation, $\delta J_{||}$, changes the local $J_{||}$ and thus directly affects the classical tearing mode stability (Δ'). A more negative Δ' can make NTM destabilization more difficult or even impossible. Following the perturbation model described in [109], the change in Δ' due to ECH and/or ECCD in the absence of a magnetic island is given by [84] :

$$\delta\Delta' = -a_{EC}\,\frac{5\pi^{3/2}}{32\rho_s}\,\frac{L_q}{\delta_{EC}}\,\frac{\delta J_{||,peak}}{J_{||}\left(\rho_{dep}\right)}, \tag{3.10}$$

where a_{EC} is a constant that depends on geometrical factors, L_q is the spatial gradient scale length of the q-profile, δ_{EC} is the full width at half-maximum of an assumed Gaussian current density perturbation $\delta J_{||}$, $\delta J_{||,peak}$ is the peak value of $\delta J_{||}$ and ρ_{dep} is the location of the peak of $\delta J_{||}$.

Another effect of ECH and ECCD is to replace the decreased bootstrap current resulting from an island. These effects can be included separately in the MRE by introducing their respective terms Δ'_{CD} and Δ'_{H}. According to [110, 111], this two terms can be written in the same form as given by

$$\Delta'_{H,CD} = -a_{H,CD}\,P_{EC}\,F_{H,CD}\left(w, w_{dep}, \rho_{dep}\right), \tag{3.11}$$

where $a_{H,CD}$ is a constant which depends on the plasma profiles and the efficiency with which the EC power is converted into a perturbative inductive current, P_{EC} is the amount of deposited EC power and $F_{H,CD}\left(w, w_{dep}, \rho_{dep}\right)$ is a function that defines the efficiency of localized heating/current drive depending on the island width w, the EC power deposition width w_{dep} and deposition location ρ_{dep} with respect to the island.

Many other effects may be introduced in equation 3.2, such as the effect of the interaction of an NTMs with a conducting wall, Δ'_{wall} [90], the effect of the coupling between co-existing NTMs leading to a non-resonant energy exchange, $\Delta'_{coupling}$ [72, 112], among others. A more detailed description is beyond the scope of this thesis.

3.1.4 Triggering neoclassical tearing modes

As discussed above, several physical effects, represented by different Δ' terms in equation 3.2, influence the stability and evolution of NTMs that, in turn, depend on the plasma conditions. In low-β plasmas, where the classical drive dominates, a tearing mode can

be linearly destabilized if the current density profile is such that $\Delta'_0 > 0$. The mode will then spontaneously grow and saturate at a finite width equal to $w_{sat} = \Delta'_0/\alpha$. For plasmas with a current density profile stable against tearing modes, ($\Delta'_0 < 0$), and neoclassical effects being important, stabilizing effects at small island width will lead to a critical island width, w_{crit}. Thus, only islands whose size exceeds w_{crit} will experience a dominant neoclassical drive and increase in amplitude [23]. For most of the modestly high β tokamak plasma scenarios, NTMs are found to be metastable (linearly stable but nonlinearly unstable). So, NTMs cannot develop spontaneously in the plasma implying that, to arise, they must be seeded.

Experimental observations from many tokamaks show that several kinds of instabilities, such as sawteeth [113, 114], fishbones [115] and edge localized modes (ELMs) [116], can provide an NTM seed island. Under particular circumstances, such as highly peaked current profiles [117], high values of β [118] or low plasma rotation [119], NTMs can also grow without being seeded by another instability. Here, classical tearing modes are thought to be responsible for the initial island growth.

Several theoretical models have been proposed to explain the triggering of NTMs by ST. In one of the first, an analytic treatment of the coupling between the ST mode and a $m/n = 3/2$ tearing mode was presented [120]. Most models are based on forced reconnection [121], where the seed island source is the magnetic perturbation produced at the driven mode rational surface by another MHD instability, in combination with toroidal geometry that couples the poloidal mode number of the driving mode m to its $m \pm 1$ sidebands [122]. Some models are based on nonlinear three wave coupling that was applied to JET pulses [112], where $m/n = 4/3$ NTMs were observed before and during the ST crash. The difference between the NTM frequency and that of the driving mode, the $m/n = 1/1$ ST mode, provided, in many cases, a close match to the frequency of the $m/n = 3/2$ NTM, indicating a possible nonlinear coupling between these modes. There are also models based on a linear destabilization of tearing modes during the ST crash [123]. Here, a destabilization is induced by the current sheet generated by the $m/n = 1/1$ internal kink reconnection. This model is applicable only when the mixing radius ρ_{mix} approaches the $q = 3/2$ surface, where a current sheet has to be generated to affect the local current density profile leading to positive Δ'_0s large enough to make an island to grow above the critical island width before the induced sheet current decays. Finally in this list, another proposed triggering mechanism is the effect of changes in the plasma rotation profile during the sawtooth crash resulting in the reversal of the polarity of the polarization current term in the modified Rutherford equation [88, 124].

Numerical simulations have been performed to investigate the nonlinear NTM evolution and how the coupling between different modes generated during the sawtooth crash can create a seed island [125, 126]. Simulations using the NFTC code [127] show that as q_0 increases above unity, the $m/n = 1/1$ resistive kink mode and its 2/2 harmonics are effectively suppressed, while their respective $m/n = 3/2$ and 2/1 sidebands remain

constant. Their character simultaneously changes from resistive kink to tearing mode within 100 Alfvén times of the start of the ST crash [125]. These results are similar to subsequent studies performed with the NIMROD code [126, 128], where the $m/n = 1/1$ mode was shown to nonlinearly drive an $n = 2$ mode that has a tearing component at the $q = 3/2$ surface.

NTM seeding becomes increasingly less predictive with so many seed sources, of which ST are identified as of most concern as they are deemed unavoidable in the conventional, mainly inductively driven, high current ITER scenario [129]. Experimental observations from a number of tokamaks show that NTMs are more likely to be triggered at lower values of β_N when the ST period is increased. This may have serious implications for ITER where fusion produced α-particles are predicted to lead to long sawtooth periods [75, 27], reinforcing the need of actuators for sawtooth control capable of reducing the ST period sufficiently to avoid NTM triggering.

It was shown in JET that, using ECH/ECCD, islands with smaller widths may be stabilized more easily [28], implying that the mitigation actions should be initiated as fast as possible once an NTM is detected to maintain the fusion power gain factor Q. However, even though tearing modes typically grow on relatively slow, resistive, time-scales (tens to hundreds of milliseconds in TCV), JET and other machines have observed that relatively large seed islands may form almost immediately following a ST crash [79, 114, 130, 131]. Since NTMs are presently thought to be one of the critical limiting plasma instabilities for the ITER $Q = 10$ scenario [129], an improved understanding of their NTM seeding mechanism is increasingly important.

3.2 Objectives

Understanding the different possible mechanisms behind NTM seeding could lead to the development of a model in which their relative contribution and scalings are known. This model could be used predictively to indicate zones of safer operation at higher plasma pressures in existing tokamaks and in the design of future devices. This thesis seeks to improve the understanding of the underlying physics of the seeding of NTMs by ST using an experimental approach. The specific objectives of this work are :

- to reveal the dynamics involved in the NTM seeding by measuring the magnetic fluctuations from the different modes generated during the ST crash (section 3.5);
- to investigate the effect of the sawtooth period on the generated seed island width and NTM stability in the post-crash plasma profiles (section 3.6);
- to study the dependencies of the coupling of sawteeth and NTMs on several plasma parameters (section 3.7);

- to use the knowledge acquired during this work to develop strategies for avoiding NTMs (section 3.8).

3.3 Experimental Setup and Data Analysis

The experiments described in this chapter were performed using TCV's 82.7GHz gyrotrons for heating and current drive at the second harmonic extraordinary mode (X2)[41]. A typical power orientation for simultaneous control of τ_{ST} and NTM preemption used in this work is shown in figure 3.3. An upper lateral and equatorial launcher apply ECCD close to the $q = 1$ surface for ST control, as described in section 3.1.2. Simultaneously, for a subset of discharges, another equatorial launcher applies ECH at the $q = 3/2$ surface for NTM preemption. In these discharges, "preemptive" ECH power is applied to investigate its effect on the seeding of 3/2 NTMs. The ECH is "preemptive" in the sense that it is applied before a seed island is detected. In TCV, this is possible as the ST crash times are under real-time control (see section 3.1.2). In all this work, the electron cyclotron ray paths and predicted power absorptions are calculated using the ray-tracing code TORAY-GA [81].

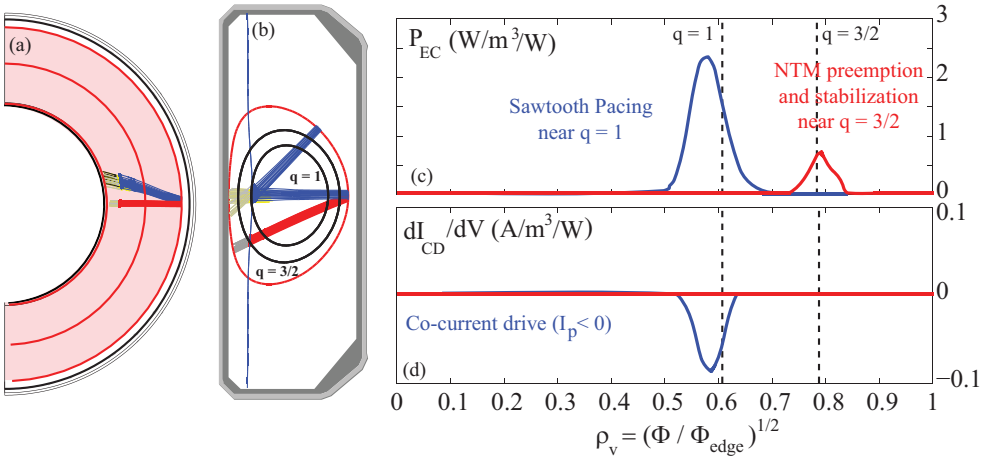

Figure 3.3: (a) Toroidal and (b) poloidal view of plasma and ECH/ECCD system setup for combined τ_{ST} control and NTM preemption. Two launchers (blue rays) apply ECCD in the vicinity of the $q = 1$ surface for ST control and one launcher (red rays) applies ECH in the vicinity of the 3/2 surface for NTM preemption. (c) ECH power density deposition profile per input power. (d) ECCD per volume and per input power. Vertical lines in (c) and (d) indicate the location of low order rational surfaces.

Discharges with a large range of sawtooth periods were programmed on TCV and the MHD activity following each ST crash analyzed and recorded in a database comprising 7767 ST crashes from 75 discharges. The discharges were in L-mode with the same limited configuration and closely matched shape and plasma parameters: elongation $\kappa = 1.53 \pm 0.05$, triangularity $\delta = 0.31 \pm 0.03$, minor radius $a = (0.24 \pm 0.01)$ m, central electron

density $n_{e0} = (1.6 \pm 0.3) \times 10^{19}$ m^{-3} and safety factor $q_{95} = 2.2 \pm 0.1$. By varying the ECCD power from 0.6 to 1.2 MW, its deposition location through changes of the plasma current $I_p = (300 \pm 20)$ kA and toroidal magnetic field $B_0 = (1.20 \pm 0.08)$ T, and the ECCD on/off timing, the values of τ_{ST} were found to range from 1 to 80 ms. The central electron temperature was $T_{e0} = (1.5 \pm 0.4)$ keV. For this work, the experimental magnetic configurations were reconstructed using the LIUQE code [54].

In this thesis, a new approach for the analysis of the fast magnetic fluctuation measurements has been used due to the fast growth of the sawtooth triggered seed islands observed in the experiments. This leads to the need for measurements with high temporal resolution. Furthermore, since this characteristic growth time is comparable with the mode toroidal rotation period (about 50-100 μs), temporal Fourier analysis techniques are not viable to examine the evolution of the mode structure. Instead, instantaneous decomposition into toroidal mode components using the toroidal arrays of poloidal magnetic field probes is used to analyse the magnetic perturbations generated by the ST crash, figure 3.4(a). Another key feature of the analysis is the use of integrated magnetic probe signals for the toroidal mode decomposition, which is necessary when the mode amplitude changes on the same time scale as its phase [132].

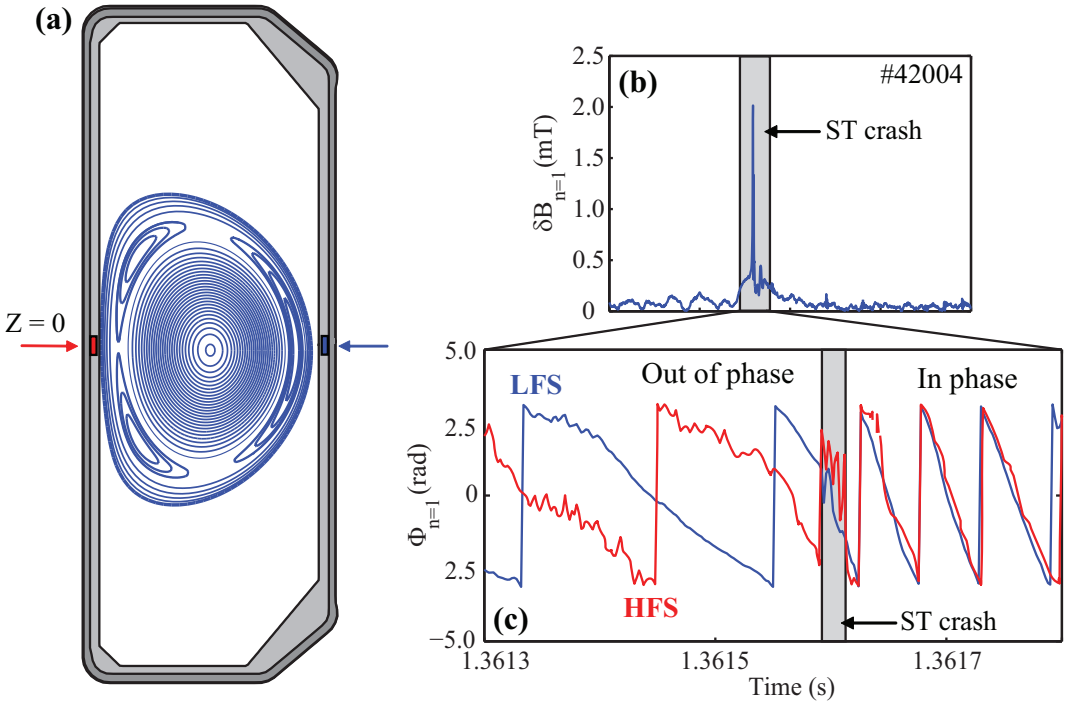

Figure 3.4: (a) Schematic showing a TCV and plasma poloidal cross section and the LFS and HFS toroidal arrays of poloidal magnetic field probes. (b) Amplitude and (c) toroidal phase of modes with toroidal mode number $n = 1$ measured using the LFS and HFS toroidal arrays of MPs.

Comparison of the toroidal phases of a toroidal mode component measured with the LFS and HFS arrays will distinguishes between odd and even dominant poloidal mode numbers. As an example, figure 3.4(b) shows the temporal evolution of the $n = 1$ toroidal component during a sawtooth crash while figure 3.4(c) shows the toroidal phase of the $n = 1$ mode, measured with the LFS and HFS toroidal arrays, for times near the sawtooth crash time. It can be seen that the signals from both arrays is found to be out of phase before the crash, indicating that the dominant mode has an odd poloidal mode number, e.g. the $m/n = 1/1$ sawtooth mode. After the sawtooth crash, the signals become in phase indicating the dominant mode has now an even poloidal mode number, e.g. a $m/n = 2/1$ mode.

3.4 MHD Activity Following the Sawtooth Crashes

In this section, the dependence of the NTM onset on the value of the sawtooth period will be presented phenomenologically.

The TCV data shows that ST of long duration can trigger $m/n = 3/2$ and $m/n = 2/1$ NTMs, leading to confinement degradation and disruptions depending on the value of β_N, figure 3.5. Each point represents a single ST crash as a function of β_N and normalized sawtooth period τ_{ST}/τ_R, where τ_R is the resistive time considering the radial location of the $q = 1$ surface, equation 3.2. In TCV, τ_R ranges typically from 250 to 500 ms.

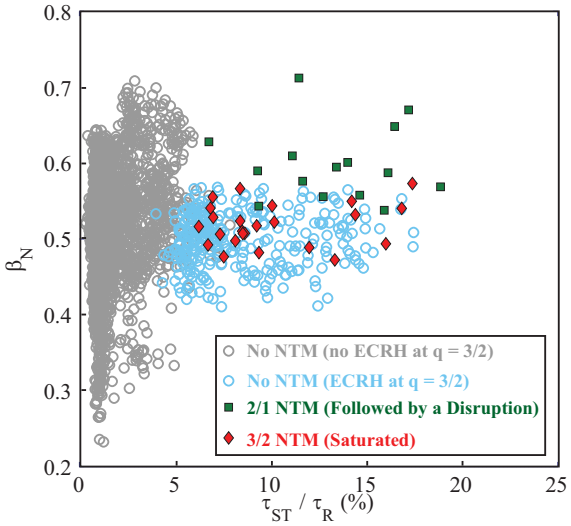

Figure 3.5: Dependence of the MHD activity following ST crashes on β_N and normalised sawtooth period, τ_{ST}/τ_R, for plasmas with $B_0 \approx 1.20$ T, $I_P \approx 300$ kA, $q_{95} \approx 2.2$, $P_{ECH} = 0.6$ - 1.2 MW, $\delta = 0.3$ and $\kappa = 1.5$. Circles (blue/grey refers to cases with/without preemptive ECH at $q = 3/2$) represent ST that did not seed an NTM. The 3/2 NTMs (red diamonds) are modes which persist at least up to the next ST crash while the 2/1 NTMs (green squares) always lock and lead to disruptions.

As shown in figure 3.5, sawteeth may trigger 3/2 and 2/1 NTMs once τ_{ST}/τ_R exceeds ~6% depending on the value of β_N. These observations are consistent with previous results from JET [26], where NTMs are triggered at low β_N when τ_{ST}/τ_R becomes as large as 6-7% [72, 114, 26, 133]. In TCV, sawtooth crashes with $\tau_{ST}/\tau_R \gtrsim 6\%$ occuring at $\beta_N \gtrsim 0.55$ are found to trigger 2/1 NTMs, which then lock to the wall and inevitably lead to plasma current disruptions, whereas sawtooth crashes with $\tau_{ST}/\tau_R \gtrsim 6\%$ occuring at $\beta_N \lesssim 0.55$ are found to trigger 3/2 NTMs. It can also be seen that when preemptive ECH power is applied at the $q = 3/2$ surface, the maximum τ_{ST} that does not trigger a 3/2 NTM increases significantly.

3.5 Fast Seeding of $m/n = 3/2$ and $2/1$ NTMs

In this section, the dynamics of the seeding of NTMs during the ST crash is investigated. The magnetic measurements (see section 2.2.5) show that the amplitude of the $n = 2$ perturbation generated at the ST crash increases with τ_{ST}, figure 3.6. For small values of τ_{ST}, the mode decays within a few milliseconds, whereas for a sufficiently large value of τ_{ST}, the mode grows after a few hundred microseconds, evolving into an NTM. Note that following NTM onset, ST show smaller amplitudes and shorter periods, presumed to result from changes in confinement and profile shapes induced by the presence of the NTM.

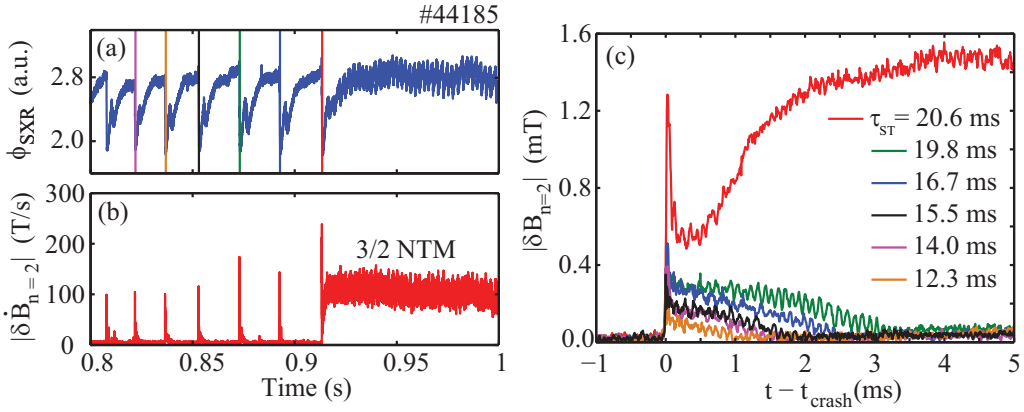

Figure 3.6: (a) Central chord of line integrated soft X-ray emission and (b) amplitude of the $n = 2$ magnetic perturbation. (c) Evolution of the $n = 2$ magnetic perturbation amplitude with respect to the time of the ST crash, t_{crash}, for ST of various duration.

The coupling between modes during the ST crash is expected to play an important role in the mode evolution. For ST of sufficient duration, a peak in the $n = 2$ mode amplitude appears approximately 30 μs after the ST crash time t_{crash}, figure 3.7, which is here defined as the time of the peak in the amplitude of the $n = 1$ magnetic perturbation that coincides with the characteristic drop in the soft X-ray intensity.

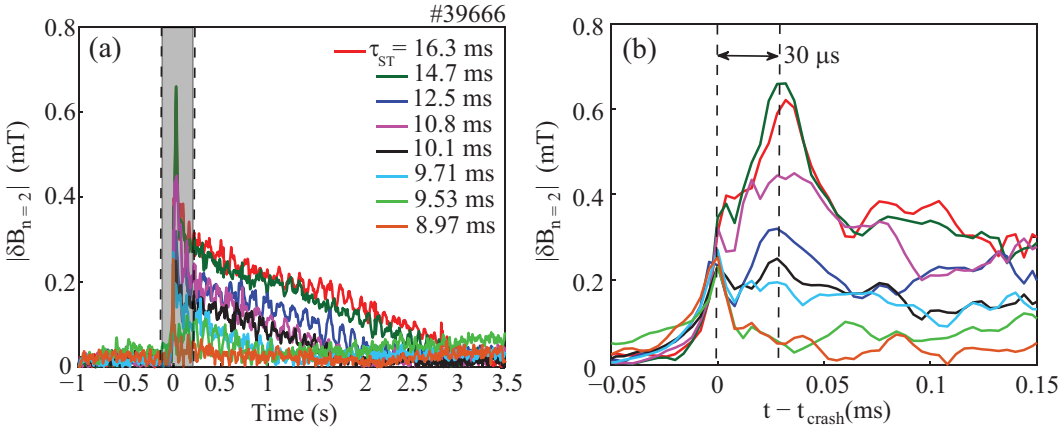

Figure 3.7: (a) $n = 2$ magnetic perturbations for a range of τ_{ST}. (b) Magnified view of the same measurements around t_{crash} showing a peak in the amplitude of the $n = 2$ magnetic component appearing about 30 μs after the ST crash for longer τ_{ST}.

The amplitude of the peak in the $n = 2$ magnetic component increases with τ_{ST}. During the peak in the $n = 1$ mode, the $n = 2$ magnetic components, measured at LFS and HFS, are in phase indicating that the dominant $n = 2$ mode has an even m number, figure 3.8. Immediately after the ST crash, the $n = 2$ components are 180 degrees out of phase between HFS and LFS over a time period corresponding to less than one complete toroidal turn of the mode. This shows that an $n = 2$ mode with an odd m number becomes dominant about 8 μs after t_{crash}, figure 3.8(c). Magnetic measurements strongly suggest that a harmonic $m/n = 2/2$ mode, which grows together with the $m/n = 1/1$ ST mode during the crash, generates a $m/n = 3/2$ mode within tens of microseconds.

In the following, soft X-ray emission will be used to identify this $m/n = 3/2$ mode as a magnetic island. Once the island is sufficiently large, flattening of the emissivity profile across the island leads to a phase reversal of the fluctuating component. Soft X-ray emission is measured along 64 lines of sight (see section 2.2.4) during a discharge in which a ST triggers a 3/2 NTM, figure 3.9(a). The fluctuating component from each chord is extracted using temporal Fourier analysis. The amplitude and phase of the Fourier coefficients at the mode frequency are shown as a function of the tangency radius of each chord in figures 3.9(b,c). The frequency of the 3/2 mode is about 12.5 kHz, whilst the frequency of the 1/1 mode just before the sawtooth crash is about 8.5 kHz.

During the time interval in which the 3/2 mode amplitude saturates at large amplitude, figure 3.9(c), the Fourier coefficients show the characteristics of a magnetic island: the fluctuation amplitude peaks on both, the HFS and LFS of the resonant surface, and the phase changes by 180 degrees at the resonant surface. Using shorter analysis time windows, the phase reversal at the resonant surface characteristic for an island is resolved as early as 800 μs after the ST crash, figure 3.9(b). As incomplete flattening of the plasma profiles across small islands, temporal averaging of the Fourier analysis, finite channel

spacing, and the line integrated nature of the measurements, all limit the detectable island size, this methodology can only overestimate the time of the island creation.

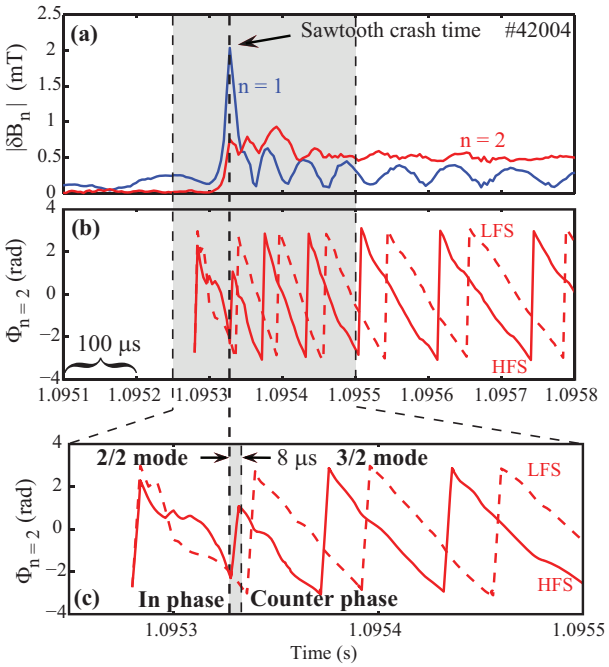

Figure 3.8: (a) $n = 1$ and $n = 2$ magnetic components generated by a ST crash. (b) Toroidal phase of the LFS (dashed) and HFS (solid) magnetic components of the $n = 2$ mode. (c) Magnified view around t_{crash} showing a fast change (about 8 μs) in the mode behaviour at t_{crash}.

Tracking the phase of the magnetic measurements from the LFS and HFS of the 3/2 island backwards in time until a few microseconds after the ST crash shows no change in behavior. This suggests that the 3/2 mode, present a few microseconds after t_{crash}, is already a magnetic island. Its width w can be estimated from the measurements of the $n = 2$ magnetic perturbation. The square root of the magnetic fluctuation amplitude is scaled to match the island width obtained from a reconstruction of the magnetic island assuming a helical current perturbation [134]. The island width evolution following a ST crash is thus estimated even when the seed island size is insufficient to evolve into an NTM. The trajectory of the island growth rate versus its width, shown in figure 3.10 for several ST, reveals several NTM features such as stabilization at small island width, a critical seed island width for NTM onset and a saturated island width. These features suggest that the evolution of the magnetic perturbations can be described by the modified Rutherford equation (equation 3.2). The correspondence between the evolution of the magnetic perturbations in phase-space and the expected behavior of magnetic islands from the modified Rutherford equation further supports the hypothesis that the 3/2 mode generated by the ST crash is already an island in a few microseconds. Note that the small oscillations, seen for the saturated island width, are within the uncertainty of the magnetic perturbation measurements.

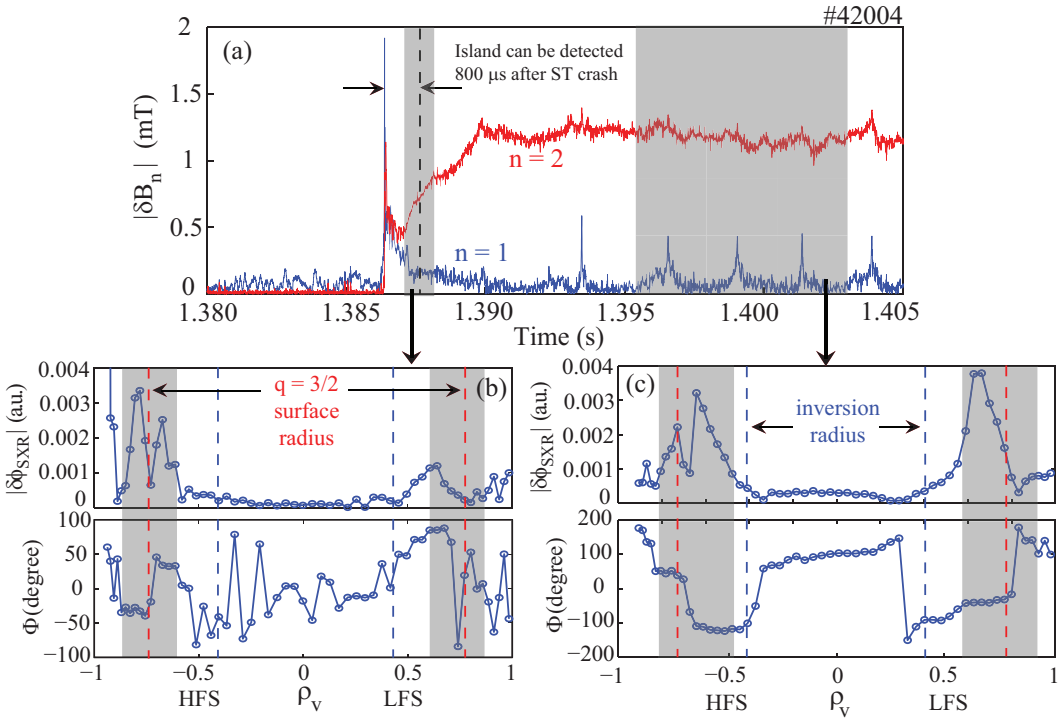

Figure 3.9: (a) Evolution of the $n = 1$ and $n = 2$ magnetic components and (b,c) amplitude and phase of the Fourier coefficients at the $n = 2$ mode frequency of the soft X-ray signals for two time intervals. Vertical bars in (b) and (c) denote the measured ST inversion radius and the $q = 3/2$ surface radius obtained from the LIUQE equilibrium reconstruction code.

In a similar way to the $n = 2$ mode, the phase difference between the $n = 1$ component of the magnetic perturbations at the LFS and HFS suggests also a fast seeding process of 2/1 NTMs. A short time before, and right up to the ST crash, the typical $m/n = 1/1$ mode associated with the ST instability grows. Tens of microseconds after the ST crash, the 2/1 mode becomes the dominant $n = 1$ mode, figure 3.11. The 2/1 NTM occurs at the $q = 2$ surface and induces stronger eddy currents in the vacuum vessel compared to a 3/2 mode of similar size. While the 2/1 mode locks to the conducting wall, its amplitude grows until a major plasma current disruption is triggered, similar to observations from other machines [91]. In all the studied cases where a 2/1 NTM is triggered, a 3/2 mode is also observed. However, in all cases, the 2/1 mode evolution leads to a major current disruption before the 3/2 modes can grow to large amplitude precluding the study of the 3/2 modes in these discharges.

Observations of the fast seeding of $m/n = 3/2$ and 2/1 NTMs in TCV have been compared with numerical studies performed to investigate nonlinear NTM evolution and the temporal evolution of coupling of different modes generated during the ST crash [125, 106, 126]. As mentioned in section 3.1.4, these simulations show that a seed island

can be present within 100 Alfvén times, τ_A, of the ST crash. The rapid formation of the $m/n = 2/1$ and $3/2$ modes in TCV (few microseconds) is consistent with the time scale found in the simulations ($100\,\tau_A$ = 3-5 μs in TCV).

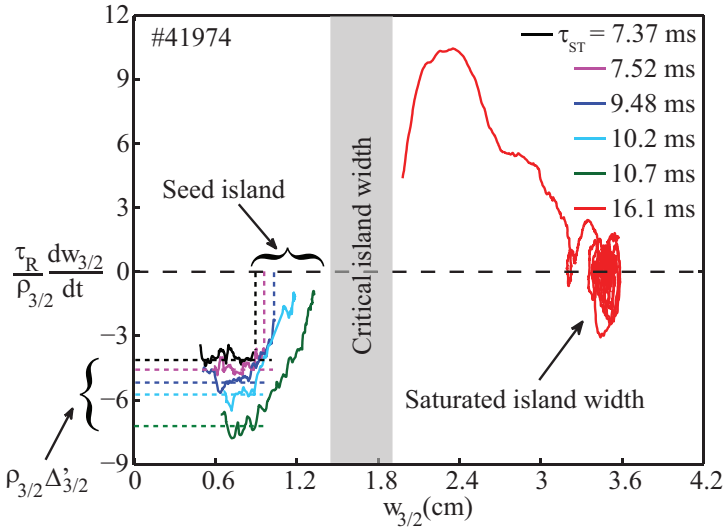

Figure 3.10: Evolution of the width of the supposed 3/2 magnetic island $w_{3/2}$ in phase-space showing some features which are in agreement with a magnetic island evolving according to the modified Rutherford equation, equation 3.2.

3.6 Effect of the Sawtooth Period on the Onset of NTMs

The onset of NTMs is expected to depend on many plasma parameters [26]. Depending on the conditions encountered, a ST triggered seed island may decay, grow and saturate, or grow and lead to a disruption, as already discussed in 3.5. This section discusses two questions on the effect ST crashes on NTM seeding: (i) how the ST period influences the formation of the seed island width w_{seed} and (ii) how the post-crash plasma profiles affect the NTM stability (or the classical tearing stability index Δ'_0).

In discharge #41974, the value of τ_{ST} was scanned and ST of longer duration were seen to generate larger seed islands, figure 3.10. This observation, within a single discharge, agrees with the ST database that shows a positive correlation between ST generated m/n = 3/2 seed island width and ST period, figure 3.12.

Variations in the conventional tearing stability Δ'_0, due to changes in the plasma profiles caused by the ST crash, can be estimated from measured $\frac{\tau_R}{\rho_s}\frac{dw}{dt}$ for $w_{3/2} \approx 0$, which is interpreted as an effective classical tearing index Δ'_{eff}. This parameter is defined here as the sum of the classical tearing index Δ'_0 and the stabilizing curvature term Δ'_{GGJ} at

zero island width

$$\Delta'_{\text{eff }(m/n)} = \Delta'_{0\,(m/n)} + \underbrace{\frac{2.23\,a_{\text{GGJ}}}{w_{\text{d}}}}_{\Delta'_{GGJ}(w_{3/2}=0)} \quad . \tag{3.12}$$

The curvature term is usually small compared with the others in the modified Rutherford equation. To simplify the text, $\Delta'_{\text{eff}\,(3/2)}$ will be denoted by $\Delta'_{3/2}$ from here on.

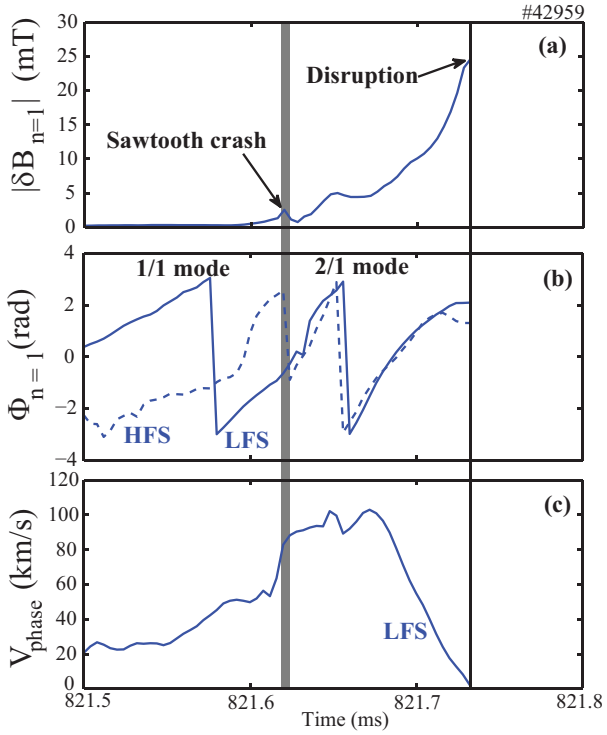

Figure 3.11: Evolution of the $n = 1$ magnetic perturbation (a) amplitude and (b) phase from LFS and HFS measured during a ST crash that triggers a 2/1 NTM, showing the transition from an odd to an even m number. (c) The LFS $n = 1$ phase velocity showing the eventual locking of the mode to the wall.

Interestingly, the measurements in discharge #41974, figure 3.10, indicate that ST of longer duration lead to more negative values of $\Delta'_{3/2}$, i.e. an increased plasma stability with respect to classical tearing modes, after the ST crash. More negative values of $\Delta'_{3/2}$ are thought to increase the critical island width w_{crit}. In the measurements, w_{crit} can be ascribed to the island width, during the time interval, in which the amplitude of the $n = 2$ magnetic component remains approximately constant ($\text{d}w/\text{dt} \approx 0$). This usually occurs from 100 - 400 μs after t_{crash}. After this time, the neoclassical drive starts to dominate causing further growth of the island width, as seen for example in figure 3.6(c).

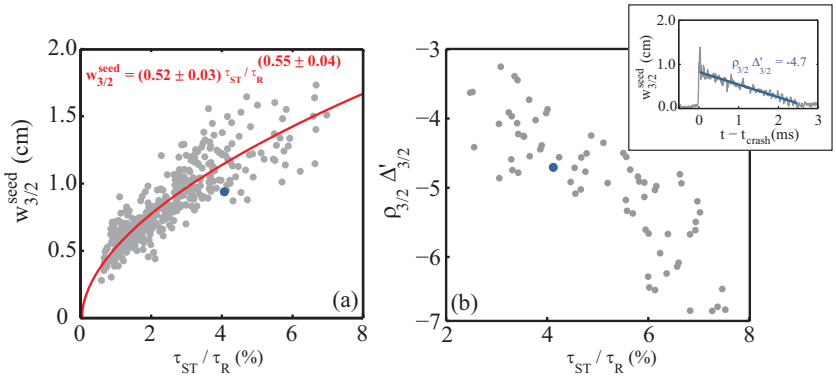

Figure 3.12: Effect of the normalized ST period τ_{ST}/τ_R on (a) the $m/n = 3/2$ seed island width, $w^{seed}_{3/2}$, and (b) the tearing mode index, $\rho_{3/2}\Delta'_{3/2}$, obtained from a linear fit of the mode amplitude decay after the ST crash in plasmas with $q_{95} = 2.2 \pm 0.05$. The insert shows, as an example, the fitting of the $m/n = 3/2$ mode amplitude generated by a ST crash that corresponds to the larger solid blue circles in (a) and (b). The red curve in (a) corresponds to a fitting of the experimental data.

Similarly to the 3/2 NTMs, ST of longer duration also generate larger 2/1 seed island widths that, if sufficiently large, can lead to the onset of the 2/1 NTMs, red diamond in figure 3.13(a). Sawteeth of longer duration also leave the plasma more stable with respect to 2/1 tearing modes after the crash, which can be seen by an increase in the decay rate of the $m/n = 2/1$ mode, $\gamma_{2/1}$, figure 3.13(b).

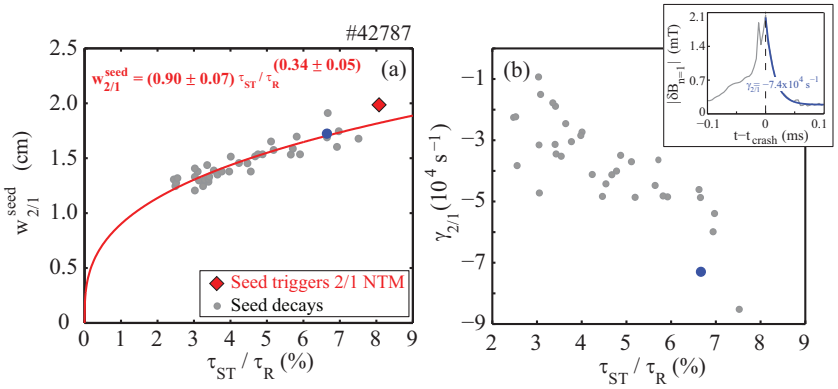

Figure 3.13: Effect of the normalized ST period τ_{ST}/τ_R on (a) the 2/1 seed island width $w^{seed}_{2/1}$ and (b) the growth rate of the $m/n = 2/1$ mode $\gamma_{2/1}$, obtained from an exponential fit, both measured at 10 μs after the ST crash. The insert shows, as an example, the fitting of the $m/n = 2/1$ mode amplitude generated by the ST crash that corresponds to the larger solid blue circles in (a) and (b). The red curve in (a) corresponds to a fitting of the experimental data.

The analysis of the magnetic measurements show that sawteeth of longer duration lead to larger widths for both the $m/n = 3/2$ and 2/1 seed islands, whilst leaving the plasma more stable with respect to conventional tearing modes. Since this improved plasma stability translates into a larger critical island width for NTMs, these effects compete.

However, for the TCV experiments, any increase in the critical island width was not sufficient to overcome the larger ST generated seed islands. The plasma is thus more prone to the destabilization of NTMs with increasing ST period. While this observation may scale differently in a reactor, in present tokamaks, ranging from TCV ($R_0 = 0.88$ m) up to JET ($R_0 = 2.96$ m), crashes of longer sawtooth periods can trigger NTMs at lower values of β_N [26].

3.7 Effect of the Edge Safety Factor on the NTM Seeding

The coupling of the sawtooth mode, resonant at the $q = 1$ surface, to a seed island on another surface is expected to depend strongly on geometrical factors such as the $q = 1$ radius and its proximity to the rational surfaces of the driven modes, toroidicity, and plasma shape [122]. In this section, parts of these parametric dependencies will be presented. In order to address them, a shot-to-shot q_{95} scan was performed. In each discharge the value of τ_{ST} was increased by moving the ECCD deposition location across the $q = 1$ radius (see section 3.1.2).

The longest ST period that did not trigger an NTM increases with q_{95}, figure 3.14(a). The 3/2 NTMs were only triggered for $q_{95} \lesssim 2.4$ whilst 2/1 NTMs were observed over the entire range of q_{95} values and, in all cases, lead to mode locking and disruptions. 3/2 seed islands are also observed after sawtooth crashes that trigger 2/1 modes. However, in these cases, the 2/1 mode dominates, locks and leads to a disruption within one toroidal mode revolution (about 100 μs) precluding the study of the 3/2 mode evolution, as discussed in section 3.5.

The $n = 1$ component of the magnetic perturbation $|\delta B_{n=1}|$ is the main driver for the seed island and thus directly related to the triggering of NTMs by ST. Its amplitude is estimated using the LFS toroidal array of magnetic probes (see section 2.2.5). The amplitude of the $n = 1$ magnetic perturbation $|\delta B_{n=1}|$ is found to increase with τ_{ST} at a constant q_{95}, and to decrease with increasing q_{95} at constant τ_{ST}, figure 3.14(b). The decrease of $|\delta B_{n=1}|$ at higher values of q_{95} can be explained by the observed smaller $q = 1$ surface radius. This also leads to a weaker NTM drive. In figure 3.14(b) and (c), two quantities should be distinguished: the amplitude of the driver mode, which is intimately related to the formation of the 2/1 seed island, and its critical amplitude, i.e. the amplitude necessary to destabilize the NTM. The critical amplitude for 2/1 NTMs is found to decrease with increasing values of q_{95}, figure 3.14(c), even though neither the magnetic shear nor the distance between rational surfaces were found to change significantly over this range of q_{95}.

In view of the wide range of physical processes that could contribute to seed island generation, some of the more plausible explanations are now considered. The decrease of the critical $|\delta B_{n=1}|$ needed to trigger an NTM could be an effect related to the increase

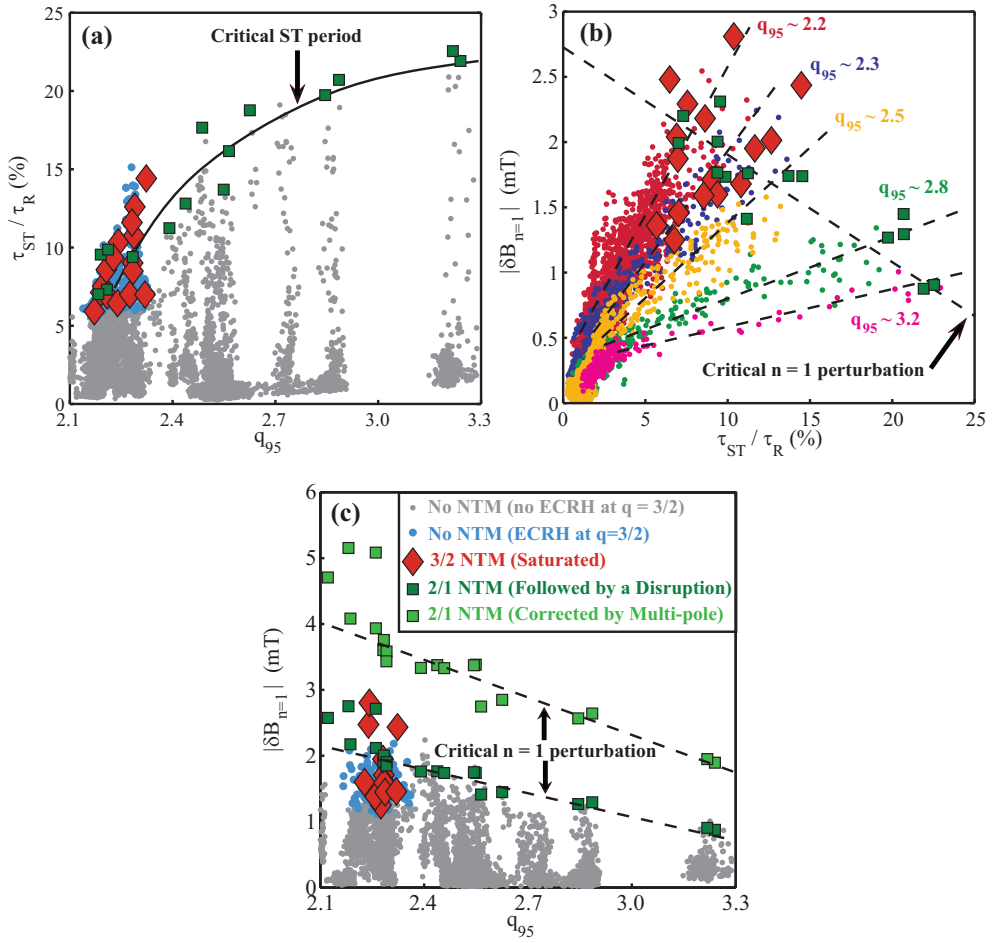

Figure 3.14: (a) Dependence of the MHD activity following ST crashes on the normalised sawtooth period $\tau_{\mathrm{ST}}/\tau_{\mathrm{R}}$ and on q_{95}. (b) Dependence of the measured $n = 1$ magnetic perturbation amplitude at the ST crash time $|\delta B_{n=1}|$ on $\tau_{\mathrm{ST}}/\tau_{\mathrm{R}}$ for various values of q_{95}. (c) Dependence of $|\delta B_{n=1}|$ on q_{95}. The legend in (c) also applies to (a) and (b).

of the distance between the $q = 1$ surface and the magnetic probes with increasing q_{95}. To account for this diagnostic geometrical effect, the measured critical values of $|\delta B_{n=1}|$ were corrected for the rapid radial multipole decay [132]. The local magnetic perturbation amplitude at the $q = 1$ surface $|\delta B_{n=1}|_{q=1}$, in cylindrical approximation but with no plasma effects taken into account, is estimated by

$$|\delta B_{n=1}|_{q=1} = \frac{1}{2}\left[\left(\frac{\rho_{\mathrm{wall}}}{\rho_1}\right)^{m+1} - \left(\frac{\rho_1}{\rho_{\mathrm{wall}}}\right)^{m-1}\right]|\delta B_{n=1}|\,, \tag{3.13}$$

where ρ_{wall} is the radial position of a perfectly conducting wall and m is the poloidal mode number of the driver mode ($m/n = 1/1$). As shown in figure 3.14(c), this correction

to the measured critical $|\delta B_{n=1}|$ leads to higher values for $|\delta B_{n=1}|_{q=1}$, but retains the decreasing trend with increasing q_{95}. Therefore, the decrease of the measured critical $|\delta B_{n=1}|$ needed to trigger an NTM at larger q_{95} values cannot solely be explained by geometrical effects.

Another possibility is a variation of w_{crit} resulting from changes in β_{p}, that increases by 70% when q_{95} is increased from 2.1 to 3.3. Imposing $\mathrm{d}w/\mathrm{d}t = 0$ in equation 3.2, using the definition of a_{bs} given in [84] and neglecting other contributions to equation 3.2, yields an approximation for the dependence of the critical seed island width with respect to β_{p},

$$w_{\mathrm{crit}} = \frac{1}{2}\epsilon^{1/2}\frac{L_q}{L_p}\frac{\beta_{\mathrm{p}}}{(-\Delta_0')}\left[1 - \sqrt{1 - \frac{4w_{\mathrm{d}}^2 L_p^2 \Delta_0'^2}{\epsilon L_q^2 \beta_{\mathrm{p}}^2}}\right]. \tag{3.14}$$

Substituting into equation 3.14, the critical island width is found to decrease by a factor 1.5 for the larger q_{95} value, showing good agreement with the experimental data in figure 3.14(c). Smaller amplitudes of the driver $|\delta B_{n=1}|$ are now sufficient to generate a seed island width larger than the threshold island size for larger q_{95}.

Although smaller seed islands are required for destabilizing 2/1 NTMs at larger values of q_{95}, the $q = 1$ surface radius and the inversion radius ρ_{inv} are observed to decrease ($\rho_{\mathrm{inv}} \propto 1/q_{95}$). This results in lower amplitude perturbations generated during the crash leading to smaller seed islands. The overall result of these two competing effects leads to more stable plasma against NTM triggering. Higher values of q_{95} are thus found to be particularly efficient for avoiding ST triggered NTMs. This is not altogether surprising as the faster decay of stable 2/1 seed islands at higher values of q_{95} already indicated q-profiles that are more stable with respect to NTMs.

The dependence of $|\delta B_{n=2}|$ on q_{95} and $\tau_{\mathrm{ST}}/\tau_{\mathrm{R}}$ is similar to that of $|\delta B_{n=1}|$ shown in figure 3.14 with components only differing in their amplitudes.

3.8 Effect of Preemptive ECH on the Triggering of NTMs

Applying ECH/ECCD at the rational surface where the NTM is expected to appear can prevent their excitation [135, 136, 42, 28]. In this section, two experiments were performed to examine this experimentally observed stabilization mechanisms. In the first, NTM excitation is studied with respect to the time delay between preemptive ECH pulses and the following ST crash. In the second, NTM stability is studied with respect to the mean preemptive ECH power deposited over the ST cycle. In these TCV discharges, q_{95} was set to 2.2 and the ST period was set to $\tau_{\mathrm{ST}} = (21 \pm 0.5)$ ms using the real-time system to control the timing of the ECCD deposition near the $q = 1$ surface (see section

3.1.2). Note that since the ST period is constant, the inversion radius is also constant i.e. unaffected by the power deposited near the $q = 3/2$.

In this section, the parameters used to quantify any improvement on the plasma stability due to the presence of the preemptive ECH power are the ST generated seed island width $w_{3/2}^{\text{seed}}$ and the classical tearing index, $\Delta'_{3/2}$.

In the first experiment, the effect of the time delay between the off time of preemptive ECH pulses $t_{\text{ECH off}}$ and the following ST crash t_{crash} (here defined as ΔT_{crash}) was studied in a shot-to-shot scan, where ΔT_{crash} was varied from 1 to 10 ms. The typical EC power time traces are illustrated in figure 3.15. The preemptive pulse duration ΔT_{ECH} was set to 7 ms in order to maintain a constant mean ECH power deposited over the ST cycle.

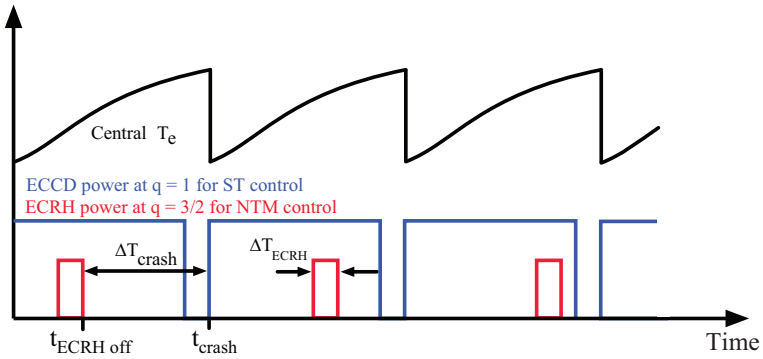

Figure 3.15: Schematic of the time traces of the ECH/ECCD system setup used for combined τ_{ST} control (blue) and NTM preemption (red) varying the time interval between the off time of the preemptive pulse and the next ST crash.

The results from this experiments are summarized in figures 3.16. $w_{3/2}^{\text{seed}}$ and $\rho_{3/2}\Delta'_{3/2}$, for the case with $\Delta T_{\text{crash}} = 8.1$ ms and preemptive ECH power $P_{\text{ECH}} = 0.5$ MW, are shown in the panels (a) and (b). When the preemptive ECH pulse approaches the following ST crash, i.e. ΔT_{crash} decreases, smaller seed islands are generated, figure 3.16(c), indicating a reduction in the coupling between driving ($m/n = 1/1$ and its harmonic $m/n = 2/2$) and driven ($m/n = 2/1$ and $m/n = 3/2$) modes. In addition, as shown in figure 3.16(d), the ST crashes leave the plasma more stable with respect to tearing modes (more negative $\rho_{3/2}\Delta'_{3/2}$), indicating a larger critical island width $w_{3/2}^{\text{crit}}$ (see equation 3.14). These two effects make the plasma more resilient against NTM triggering when the preemptive ECH pulse is applied closer to the time of the ST crash. In these experiments, the preemptive ECH pulses were always turned off before the ST crash and, hence, did not coincide with the seed island. ECH does, therefore, not directly affect the seed island formation and the observed evolution can be attributed to more favorable profiles (more negative $\rho_{3/2}\Delta'_{3/2}$). Although no ECCD is applied, ECH modifies the plasma density and temperature profiles affecting the total current density through modifications of the bootstrap current and neoclassical conductivity.

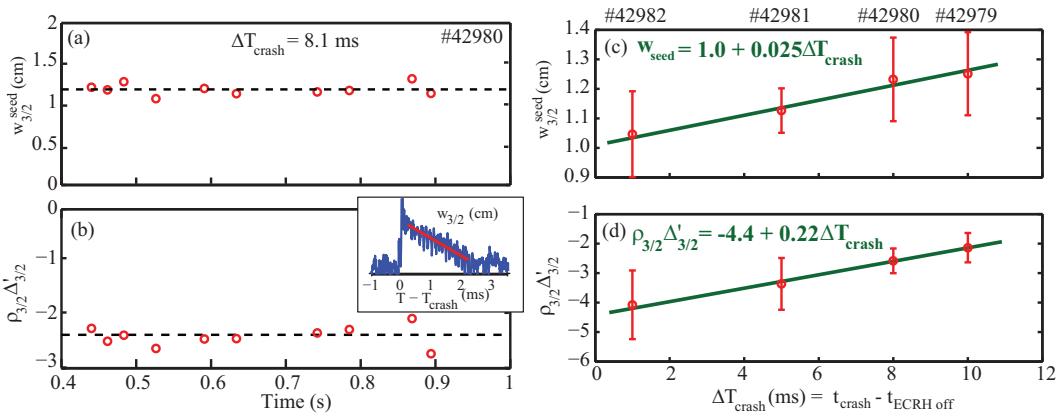

Figure 3.16: (a) Seed island width, $w_{3/2}^{\text{seed}}$ and (b) conventional tearing index, $\rho_{3/2}\Delta'_{3/2}$, generated by 21 ms ST crashes for a constant time delay ($\Delta T_{\text{crash}} = 8.1$ ms), ECH power ($P_{\text{ECH}} = 0.5$ MW) and ECH pulse duration ($\Delta T_{\text{ECH}} = 7$ ms). Dependence of (c) $w_{3/2}^{\text{seed}}$ and (d) $\rho_{3/2}\Delta'_{3/2}$ on ΔT_{crash}. Error bars represent the standard deviation of the measurements and the green lines are linear regressions.

In the second experiment, the effect of the mean preemptive ECH power deposited during the ST cycle on the seeding of the 3/2 NTM was investigated by varying the duration of the ECH pulse, ΔT_{ECH}.

In discharge 42964, the preemptive ECH at the $q = 3/2$ surface was programmed to turn on when the ECCD power at the $q = 1$ surface for ST control is turned off. The duration of the preemptive ECH pulse was scanned from $\Delta T_{\text{ECH}} = 0$ ms (no preemptive ECH power) to $\Delta T_{\text{ECH}} = 7$ ms, which can be seen in figure 3.17(a) and (b). Part of the preemptive ECH pulse occurs before the ST crash (a few hundred microseconds) and the ECH is present during the seed island formation. In addition to affecting the seed island formation through a change of the background profiles at the crash time, the preemptive ECH now also directly affects the seed island evolution. However, as the timing between the turn on of the preemptive ECH and the formation of the seed island is unchanged, any change in the seed formation and evolution is attributable to the fraction of the ECH pulse that is applied since the preceding ST crash, i.e. the ECH pulse duration ΔT_{ECH}.

Longer preemptive pulses, in which larger mean power is deposited at the $q = 3/2$ surface over the ST cycle, lead to smaller seed islands and more negative values of $\rho_{3/2}\Delta'_{3/2}$, figure 3.17(c) and (d), respectively. For the ST crashes without preemptive ECH ($\Delta T_{\text{ECH}} = 0$ ms), a less negative $\rho_{3/2}\Delta'_{3/2}$ is found and a ST and a period of 21 ms is sufficient to trigger a 3/2 NTM. Again, smaller seed islands and a more negative $\rho_{3/2}\Delta'_{3/2}$, both contribute to a greater resilience against NTM triggering.

Preemptive ECH has been shown to lead to local variations of the current profile that are sufficient to change the conventional tearing stability and decrease the coupling between ST and seed islands. The beneficial effect of preemptive ECH on the NTM stability is

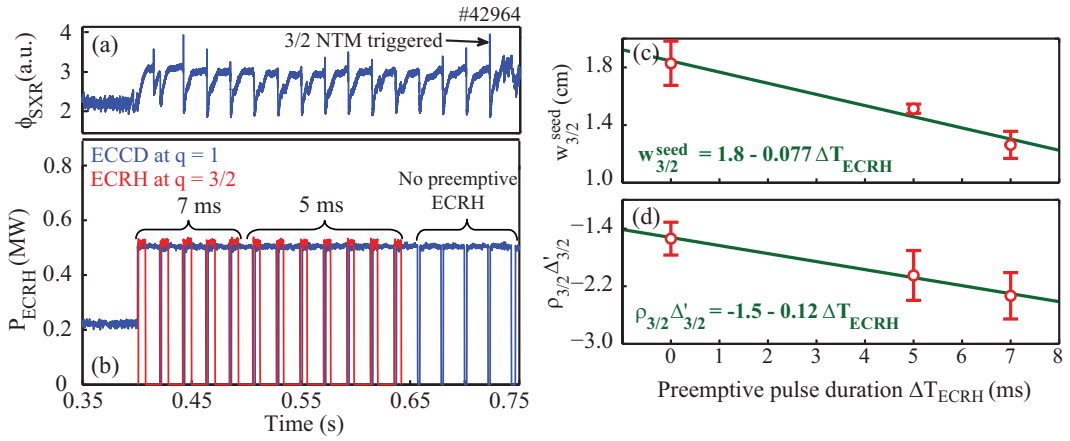

Figure 3.17: (a) Soft X-ray signal viewing the plasma centre. (b) Time evolution of the ECCD power applied at $q = 1$ used to keep a constant τ_{ST} (blue) and of the preemptive ECH at $q = 3/2$ (red). Dependence of (c) ST generated seed island width $w_{3/2}^{seed}$ and (d) $\rho_{3/2}\Delta'_{3/2}$ on the duration of the preemptive ECH pulse ΔT_{ECH}. Error bars represent the standard deviation of the measurements and the green lines are linear regressions.

therefore two-fold with the improved conventional tearing stability further implying a larger critical island width.

A model based on a local characteristic time for current redistribution τ_{local}, during the preemptive ECH pulse is proposed to describe the beneficial effect on the current density profile. The model provides an estimation of the tearing stability index $\rho_{3/2}\Delta'_{3/2}$ at the time of the ST crash,

$$\rho_{3/2}\Delta'_{3/2} = \rho_{3/2}\Delta'_0 - \delta A\, P_{ECH} \left(1 - e^{-\frac{\Delta T_{ECH}}{\tau_{local}}}\right) e^{-\frac{\Delta T_{crash}}{\tau_{local}}}, \tag{3.15}$$

where δA is a scalar and Δ'_0 is the tearing mode index without preemptive ECH. The resulting time evolution of Δ' for a typical ECH power time trace is sketched in figure 3.18. Assuming that the local characteristic time τ_{local} is much larger than ΔT_{ECH} and ΔT_{crash}, after linearization the model reduces to :

$$\rho_{3/2}\Delta'_{3/2} \approx \rho_{3/2}\Delta'_0 - \delta A\, \frac{P_{ECH}\, \Delta T_{ECH}}{\tau_{local}} \left(1 - \frac{\Delta T_{crash}}{\tau_{local}}\right). \tag{3.16}$$

Linear regression of the experimental measurements in figures 3.16(d) and 3.17(d), and equation 3.16, yields an estimate of the local current redistribution time τ_{local}, and the scalar δA: $\tau_{local} \approx 13$ ms ($\approx \tau_R/30$) and $\delta A \approx 11$ MW^{-1}. The agreement between this

simple model and the experiment supports the hypothesis that preemptive ECH mainly affects the equilibrium current profile thereby increasing the classical tearing stability that inhibits seed island formation, since w_{seed} is observed to decrease with preemptive ECH, figure 3.16(c) and 3.17(c). This provides an explanation for the longer τ_{ST} tolerated by the plasma when preemptive ECH is applied, compared with no preemptive ECH, figure 3.5. Using equation 3.15, this results from the finite value of both $\delta A\, P_{\text{ECH}}$, which is related to the capability of changing $\Delta'_{3/2}$, and $\Delta T_{\text{ECH}}/\tau_{\text{local}}$ that is, in turn, related with the time taken to change the local current density profile. Although efficient in these experiments, it may not be the case for larger tokamaks, where higher temperatures result in increased τ_{local}. Preemptive stabilization may, however, remain efficient through direct stabilization using ECH deposition inside the seed island. This is represented by the terms Δ'_{ECCD} and Δ'_{ECH} in the MRE and have a specific dependence on the island width (see section 3.1.3). All these effects are proportional to the ECH power and may be written in the following way,

$$\rho_{3/2}\Delta'_{3/2} = \rho_{3/2}\Delta'_0 - \left[\delta A \left(1 - e^{-\frac{\Delta T_{\text{ECH}}}{\tau_{\text{local}}}}\right) e^{-\frac{\Delta T_{\text{crash}}}{\tau_{\text{local}}}} + \delta B\left(w_{3/2}\right)\right] P_{\text{ECH}}, \qquad (3.17)$$

where the δA represents the effect of ECH on the tearing stability in the absence of an island, i.e. on $\Delta'_{3/2}$, and $\delta B(w_{3/2})$ the direct effect of ECH deposited within an existing island. Experiments focusing on the effect of direct stabilization by acting on the δB term have already been performed and the results can be found in [42].

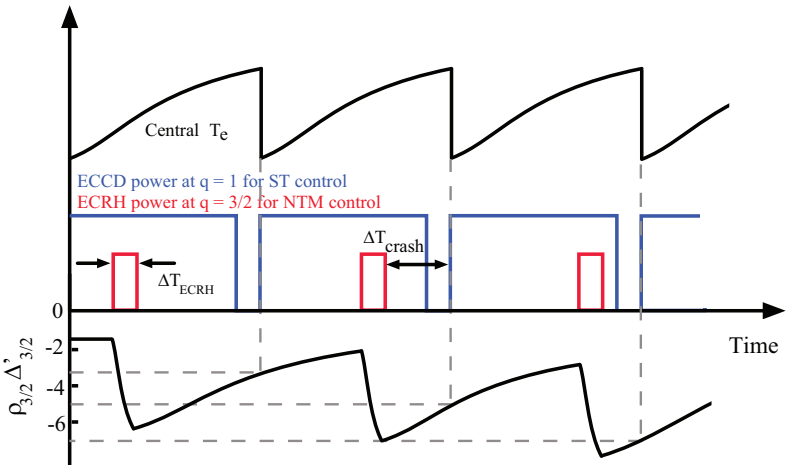

Figure 3.18: Schematic drawing to show dependence of $\rho_{3/2}\Delta'_{3/2}$ with preemptive ECH power according to the proposed model.

3.9 Conclusions

This work provides new insight into the role of the sawteeth (ST) in the triggering of neoclassical tearing modes (NTMs). In order to study the MHD activity at times close to the ST crash in detail, a new analysis based on the full toroidal array of magnetic probes of TCV was developed (section 3.3). In this work, the electron cyclotron heating and current drive (ECH and ECCD) system of TCV was used to control the period of individual ST using slow I_P and B_0 ramps, and the real-time control of the ECCD power at the $q = 1$ surface (section 3.1.2). This was employed to trigger NTMs under controlled conditions providing an excellent environment for studying ST triggered NTMs.

A strong result is that seed islands for both, 3/2 and 2/1 NTMs, are already present in the plasma within a few microseconds after the ST crash time (see section 3.5). This time scale for fast seeding is consistent with the time scale of about 100 Alfvén times obtained from numerical simulations of the seed island formation during ST crashes using nonlinear three-dimensional resistive magnetohydrodynamic codes [125, 126]. After the crash, the generated seed island can be stable or unstable depending on the plasma parameters where it decays or grows to large width, respectively. It therefore becomes important to distinguish between the effect of the ST crash on the seed island generation from the effect on the NTM stability once the seed island is present.

An increase of the ST period results in an increase of the ST generated seed island widths (see section 3.6). However, an increase of the ST period also has a stabilizing effect on NTMs, by leaving the plasma with a more negative Δ'_0 and with a faster seed island decay. This change in Δ'_0 implies in a global change of the current density profile towards more stable profiles at the $q = 3/2$ and 2/1 flux surfaces. Although, these two effects compete in TCV, the larger seed island generation prevails leading to an overall more NTM-susceptible plasma for larger values of τ_{ST}. This is also observed on other machines and, particularly, on larger machines. This would imply that the destabilizing effect will prevail when scaling towards larger devices such as ITER.

Modifying the plasma current and increasing q_{95} from low ($q_{95} \approx 2.1$) to higher values ($q_{95} \approx 3.3$) results in generally more NTM-stable plasmas (see section 3.7). This is demonstrated by the longer τ_{ST} required to trigger 2/1 NTMs at larger values of q_{95}. The size of the seed island decreases with increasing q_{95}, confirming a weaker coupling. Additionally, 3/2 NTMs were only observed for low values of q_{95}, whereas 2/1 modes were found to be triggered across the entire range of investigated q_{95} values. The critical island width necessary to trigger an NTM was seen to decrease with increasing q_{95}. This is consistent with the increasing β_p found experimentally. The smaller ST generated seed islands are, however, not sufficient to overcome the lower critical island width and higher q_{95} values are found to be very efficient in avoiding ST triggered NTMs. It has also been found that the global q-profile is also more NTM-stable at higher q_{95} due to a faster decay of 2/1 seed islands.

It was shown that ST of longer duration are required to destabilize an NTM when preemptive ECH is applied (see section 3.8). This beneficial effect increases by increasing the duration of the pre-ST ECH pulse and is more efficient when the pulse is closer to, and before, the ST crash. This was examined with a simple model related to the modification of Δ' due to ECH power with the local resistive time taken from the local current density profile evolution time. The beneficial effect of preemptive ECH on TCV is thought to result from a more negative Δ'. The more NTM-stable profiles lead to smaller seed islands, but also imply a critical island width increase. The effect of localized ECH/ECCD inside the island, if present, can also also play a role and a model is proposed that allows both effects to be studied.

Since seed islands can be triggered, at a finite size, directly at the ST crash time, strategies for NTM prevention cannot assume a slow rise of the mode amplitude, particularly in ITER (as discussed in [28]). Therefore, accurate knowledge of the time of the upcoming ST crash time is important for efficient ECH usage: immediately prior to the expected ST crash [82, 137]. This work shows that preemptive ECH is found to lead to a more NTM-stable plasma and to reduce the seed island triggered at the ST crash. In addition, it can help suppressing a finite sized island in its early phase, which is also beneficial since non-continuous ECH power increases the overall efficiency of a future fusion power plant.

4 Properties of the Snowflake Divertor

In this chapter, some potential advantages of the snowflake (SF) divertor are investigated experimentally and through numerical modeling. After a brief review of the scrape-off layer and divertor physics in section 4.1, the exhaust properties of the SF configuration will be presented and compared with those of a standard divertor configuration. Section 4.2 lists the specific objectives of the studies presented in this chapter. In section 4.3, the geometrical features of the SF divertor realized in TCV are described in detail. Section 4.4 presents the machine configuration of the experimental part this work. Section 4.5 shows the effects of the SF configuration on the power distribution among strike points. Sections 4.6 and 4.7, present the effect of the input heating power and plasma density on the power distribution among the strike points and on the radiated fraction, respectively. In section 4.8, numerical simulations of the TCV SF divertor using the EMC3-Eirene code are presented. In section 4.9, the influence of particle drifts on the shape of target profiles are investigated. Some conclusions are presented in section 4.10. The results presented in this chapter have provided strong contributions to several recent journal publications [138, 2, 139, 39, 140, 141].

4.1 The SOL and Divertor Physics

Before discussing the main effects that dominate the plasma behavior in the SOL and in the divertor, it is appropriate to briefly review the main quantities used in characterizing the SOL.

4.1.1 The geometrical features of the SOL and divertor

The flux expansion, wetted area and the connection length, i.e. the most relevant geometrical quantities related to the SOL and divertor, are now introduced.

The flux expansion

The flux expansion, f_{exp}, is related to the distance between two flux surfaces in the SOL. Figure 4.1 shows how the distance $d\rho$ between a flux surface and the separatrix varies along the SOL. The distance $d\rho$ at three different locations are shown: $d\rho_{\mathrm{u}}$, at the outboard midplane (upstream), $d\rho_{\mathrm{npt}}$, in the null-point region and $d\rho_{\mathrm{t}}$, at the target.

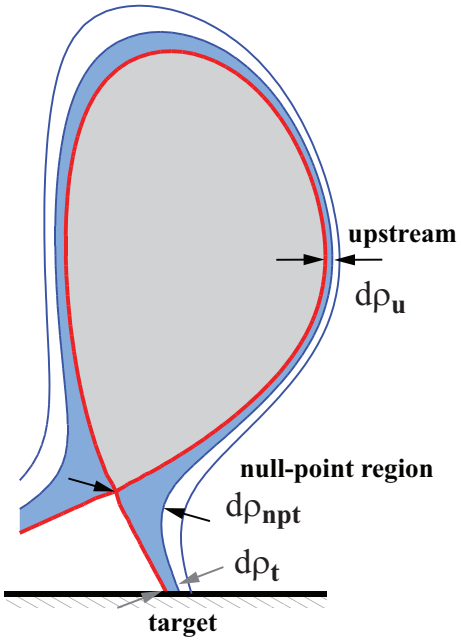

Figure 4.1: Schematic showing the distance $d\rho$ between two flux surfaces along the SOL.

The difference in poloidal magnetic flux between adjacent flux surfaces, $d\psi$, can be expressed as $d\psi = |\vec{\nabla}\psi|\, d\rho$. Using $|\vec{\nabla}\psi| = R\, B_\theta$, where B_θ is the poloidal magnetic field, yields $d\psi = R\, B_\theta\, d\rho$. The flux expansion is defined as the change in the distance $d\rho$ between two flux surfaces relative to that at a reference location in the SOL. By convention, the distance $d\rho$ at the upstream location is often used as the reference since radial fall-off lengths at the upstream location are largely determined by the core plasma parameters. For example, the target flux expansion is given by :

$$f_{\mathrm{exp,t}} \equiv \frac{d\rho_{\mathrm{t}}}{d\rho_{\mathrm{u}}} = \frac{R_{\mathrm{u}}\, B_{\theta,\mathrm{u}}}{R_{\mathrm{t}}\, B_{\theta,\mathrm{t}}}, \tag{4.1}$$

where $B_{\theta,\mathrm{u}}$ and $B_{\theta,\mathrm{t}}$ are the magnitudes of the poloidal magnetic field at the upstream (R_{u}, Z_{u}) and target (R_{t}, Z_{t}) locations, respectively.

Mapping of divertor parameters to the upstream location

In order to compare SOL parameters in different magnetic divertor configurations, profiles measured at any location are mapped to the upstream location. This mapping assumes that the heating power enters the SOL upstream and follows the magnetic field lines to the target without diffusing across them. Heat sources and sinks along the SOL are also neglected. Under these conditions, the power flowing in a flux tube, δP_{SOL}, is conserved along the SOL. Therefore, δP_{SOL} can be calculated by

$$\delta P_{\mathrm{SOL}} = \int_{R_{\mathrm{sep}}}^{R_{\mathrm{u}}} 2\pi R \, q_{\mathrm{u}}\left(R\right) dR \, . \tag{4.2}$$

Differentiating this equation with respect to the upstream coordinate R_{u} using the Leibniz integral rule, one finds

$$\frac{d}{dR_{\mathrm{u}}}\delta P_{\mathrm{SOL}} = \frac{d}{dR_{\mathrm{u}}} \int_{R_{\mathrm{sep}}}^{R_{\mathrm{u}}} 2\pi R \, q_{\mathrm{u}}\left(R\right) dR = 2\pi R_{\mathrm{u}} \, q_{\mathrm{u}}\left(R_{\mathrm{u}}\right) . \tag{4.3}$$

Using the distance of the flux surfaces from the separatrix, ρ_{u}, as an independent coordinate at the upstream, with $R_{\mathrm{u}} = R_{\mathrm{sep}} + \rho_{\mathrm{u}}$, yields

$$\delta P_{\mathrm{SOL}} = 2\pi R_{\mathrm{u}}\left(\rho_{\mathrm{u}}\right) \; q_{\mathrm{u}}\left(\rho_{\mathrm{u}}\right) d\rho_{\mathrm{u}}. \tag{4.4}$$

Applying the same calculation at the target, where s_{t} is a coordinate along the target surface, one finds

$$\delta P_{\mathrm{SOL}} = 2\pi R_{\mathrm{t}}\left(s_{\mathrm{t}}\right) \; q_{\mathrm{t}}\left(s_{\mathrm{t}}\right) \; \sin\left[\beta\left(s_{\mathrm{t}}\right)\right] ds_{\mathrm{t}}, \tag{4.5}$$

where $R_{\mathrm{t}} = R_{\mathrm{SP}} + s_{\mathrm{t}} \cos\beta_{\mathrm{target}}$, with R_{SP} the radial location of the strike point, β the poloidal angle between the field lines and the target surface, and β_{target} the angle between the target surface and the radial direction, figure 4.2. In TCV, $\cos\beta_{\mathrm{target}} = 0$ at the HFS and LFS walls while $\cos\beta_{\mathrm{target}} = 1$ at the floor.

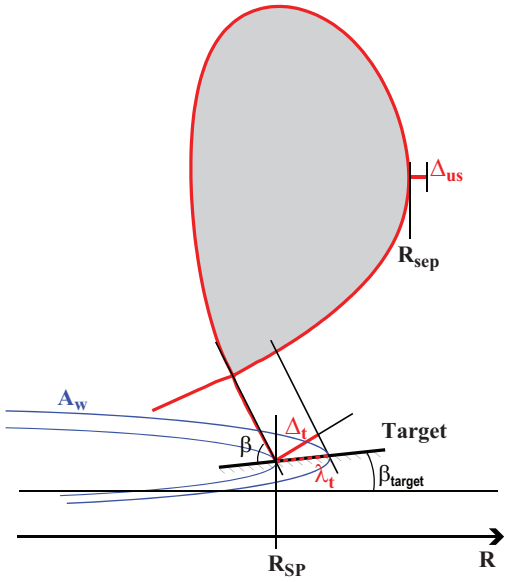

Figure 4.2: Schematic showing the main variables involved in the mapping of a target profile to the upstream. The blue curves determine the typical size of the wetted area on the divertor target.

Equating the last two expressions, yields an equation that maps the target heat flux profile to upstream,

$$q_{\mathrm{u}} = \frac{R_{\mathrm{t}}}{R_{\mathrm{u}}} \frac{\sin\beta}{f_{\mathrm{exp,t}}} q_{\mathrm{t}}. \tag{4.6}$$

The mapping of a distance λ_{t} on the target surface from the SP to upstream follows from integrating equation 4.1 combined with the relation $d\rho_{\mathrm{t}} = ds_{\mathrm{t}} \sin\beta$,

$$\int_0^{\Delta_{\mathrm{u}}} R_{\mathrm{u}}\left(\rho_{\mathrm{u}}\right) B_{\theta,\mathrm{u}}\left(\rho_{\mathrm{u}}\right) d\rho_{\mathrm{u}} = \int_0^{\lambda_{\mathrm{t}}} R_{\mathrm{t}}\left(s_{\mathrm{t}}\right) B_{\theta,\mathrm{t}}\left(s_{\mathrm{t}}\right) \sin\left[\beta\left(s_{\mathrm{t}}\right)\right] ds_{\mathrm{t}}. \tag{4.7}$$

Assuming that the upstream quantities do not vary significantly within the interval Δ_{u}, such that $R_{\mathrm{u}}\left(\rho_{\mathrm{u}}\right) \approx R_{\mathrm{sep}}$ and $B_{\theta,\mathrm{u}}\left(\rho_{\mathrm{u}}\right) \approx B_{\theta,\mathrm{sep}}$, this equation becomes

$$\Delta_{\mathrm{u}} \approx \frac{\int_0^{\lambda_{\mathrm{t}}} R_{\mathrm{t}}\left(s_{\mathrm{t}}\right) B_{\theta,\mathrm{t}}\left(s_{\mathrm{t}}\right) \sin\left[\beta\left(s_{\mathrm{t}}\right)\right] ds_{\mathrm{t}}}{R_{\mathrm{sep}} B_{\theta,\mathrm{sep}}}. \tag{4.8}$$

In addition, if the target quantities do not vary substantially within the distance λ_t across the target surface, such that $R_t(\rho_t) \approx R_{SP}$ and $B_{\theta,t}(\rho_t) \approx B_{\theta,SP}$, an approximate equation for mapping λ_t to the upstream is found,

$$\Delta_u \approx \frac{\sin\beta_{SP}}{f_{exp,SP}} \int_0^{\lambda_t} \frac{R_t(s_t)\, q_t(s_t)}{R_{SP}\, q_{SP}} ds_t = \frac{\sin\beta_{SP}}{f_{exp,SP}}\, \lambda_t = \frac{\Delta_t}{f_{exp,SP}}. \tag{4.9}$$

This equation can also be obtained by integrating equation 4.6, assuming an exponential heat flux profile of width λ_t on the target surface.

The wetted area

The wetted area, A_w, is crucial in determining the exhaust performance of a tokamak device. It is the surface area of the divertor plate that is in contact with the plasma and is usually defined as an effective area such that $P_{SOL} = q_{t,peak}\, A_w$. Here, P_{SOL} is the power entering the SOL that arrives at the divertor target and $q_{t,peak}$ is the peak value of the heat flux perpendicular to the target surface. Neglecting toroidal asymmetries, such as gaps between divertor tiles, and assuming an exponential heat flux profile of width $\lambda_t = \Delta_t / \sin\beta_{SP}$ (see figure 4.2) in the SOL at the target, yields (per target)

$$A_w = 2\pi R_{SP}\, \lambda_t = \frac{2\pi R_{SP}\, \Delta_t}{\sin\beta_{SP}}. \tag{4.10}$$

Assuming that a SOL width Δ_u exists upstream, and that parallel transport dominates, the SOL width at the target and upstream can be approximated by $\Delta_t \approx f_{exp,SP}\, \Delta_u$ (equation 4.9) yielding

$$A_w = \frac{2\pi R_{SP}\, \Delta_u}{\sin\beta_{SP}} f_{exp,SP}. \tag{4.11}$$

This equation shows that the wetted area increases linearly with the flux expansion. However, an increased flux expansion reduces the angle between the magnetic field lines and the target plate, α, which cannot be arbitrarily small [142, 143]. Due to mechanical alignment tolerances of the divertor target plates, α is limited to values above approximately 1^o.

Using equation 4.1 in combination with the relation between the poloidal tilt angle of the target, β and the grazing angle of the field lines are given by

$$\tan\alpha = \frac{B_{\theta,\mathrm{t}}}{B_{\phi,\mathrm{t}}} \frac{\sin\beta}{\sqrt{1+\left(\frac{B_{\theta,\mathrm{t}}}{B_{\phi,\mathrm{t}}}\cos\beta\right)^2}} \approx \frac{B_{\theta,\mathrm{t}}}{B_{\phi,\mathrm{t}}}\sin\beta, \tag{4.12}$$

equation 4.11 can be rewritten as

$$A_{\mathrm{w}} = \frac{2\pi R_{\mathrm{SP}}}{\tan\alpha_{\mathrm{SP}}} \frac{B_{\theta,\mathrm{sep}}}{B_{\phi,\mathrm{sep}}} \Delta_{\mathrm{u}}\ , \tag{4.13}$$

where $B_{\phi,\mathrm{t}}$ and $B_{\phi,\mathrm{sep}}$ are the magnitude of the toroidal field at the target and upstream on the separatrix.

The magnitudes of $B_{\theta,\mathrm{sep}}$ and $B_{\phi,\mathrm{sep}}$ are determined by the core plasma configuration. Therefore, assuming a minimum value of α_{SP} [142, 143], equation 4.13 shows that A_{w} may only be increased by increasing the major radius of the divertor target, R_{SP}, or by increasing the upstream SOL width Δ_{u}.

The connection length

The connection length, $L_{||}$, is also important in determining the exhaust capabilities of a divertor. Different definitions of $L_{||}$ appear in the literature. In this work, the connection length is defined as the distance, along the magnetic field lines, between a target and the corresponding upstream location,

$$L_{||}\left(\rho_{\mathrm{u}}\right) \equiv \int_{\mathrm{target}}^{\mathrm{upstream}} ds_{||} = \int_{\mathrm{target}}^{\mathrm{upstream}} \frac{B\left(\rho_{\mathrm{u}}, s_\theta\right)}{B_\theta\left(\rho_{\mathrm{u}}, s_\theta\right)}\, ds_\theta. \tag{4.14}$$

Here, $ds_{||}$ is an infinitesimal displacement along a magnetic field line and ds_θ its projection into the poloidal plane. Figure 4.3, shows a schematic typical trajectories of $ds_{||}$ and ds_θ.

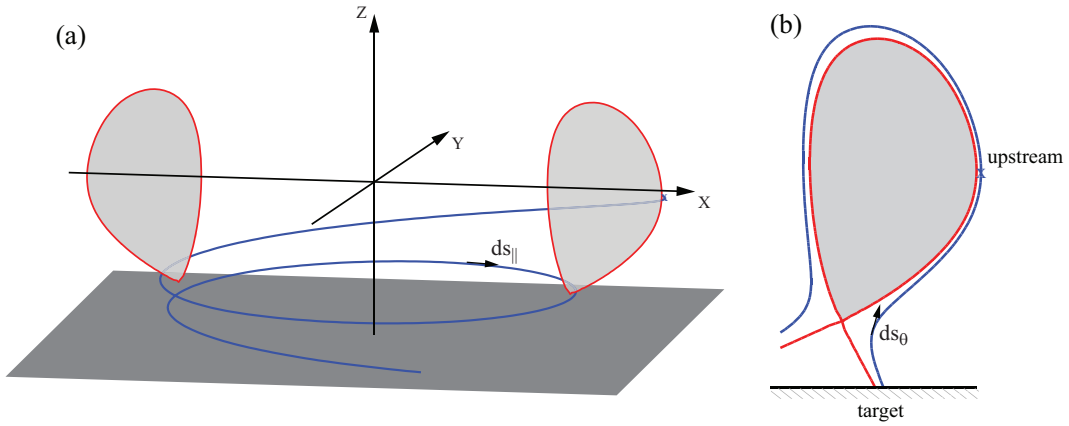

Figure 4.3: Schematic showing (a) the distance along the magnetic field lines and (b) its projection into the poloidal plane.

4.1.2 The plasma transport in the scrape-off layer

Plasma transport in the SOL is a complex, not completely understood, but crucial phenomena that determines the exhaust performance of tokamaks. It is thought to be responsible in determining the main plasma parameters, and heat and particle fluxes at the target. Above all, understanding, control and predictions of the behavior of the plasma in the SOL are of extreme importance in the development of economically viable electric power sources using tokamaks. For these reasons, transport of the plasma in the SOL has been under intense theoretical and experimental investigation. In this section, a brief review of the present understanding of the underlying physics of the plasma transport in the SOL is presented.

Parallel transport

In the SOL of Ohmicaly heated plasmas with moderate plasma density, the total plasma pressure along the open magnetic field lines, p_{total}, is usually thought to be constant and composed by the sum of the thermal and kinetic pressures. For a plasma composed only of electrons and one ion species, the thermal pressure is $p_{\text{thermal}} = nk_{\text{B}}(T_{\text{e}} + T_{\text{i}})$ and the kinetic pressure is $p_{\text{kin}} = p_{\text{thermal}}M^2$, where n is the plasma density, T_{e} and T_{i} are the electron and ion temperatures, respectively, and $M = u_{||}/c_{\text{s}}$ is the Mach number, with $u_{||}$ being the local parallel plasma flow velocity, $c_{\text{s}} = \sqrt{k_{\text{B}}(T_{\text{e}} + T_{\text{i}})/m_{\text{i}}}$ the Bohm velocity and m_{i} the ion mass.

Particle sinks at the end of the open magnetic field lines (the limiter in the case of a limited plasma or the target plates in the case of a diverted plasma), result in a thermal plasma pressure drop. This provides a force that generates a plasma flow along the SOL directed towards the solid surfaces. Since the electrons move faster than the ions due to their smaller mass and higher mobility, they arrive first at the solid surfaces (within a few

microseconds after plasma is initiated). These electrons charge the solid surface negatively and leave an excess of positive charge behind them, giving rise to an electric field in the same direction of the plasma flow. This electric field accelerates the ions increasing the ion loss rate and slows down the electrons decreasing the electron loss rate. The electric potential of the solid surface adjusts with respect to the main plasma potential until the loss rates of the two charge species become equal. This combined transport, in which the loss rates of ions and electrons become equal due to the spontaneously generated electric field, is known as ambipolar plasma transport [15]. These electrostatic potentials on the surfaces in contact with the plasma are almost entirely shielded within a short distance called the Debye sheath. Debye shielding occurs over distances of the order of tens of the so-called Debye length, given by

$$\lambda_{\mathrm{Debye}} = \sqrt{\frac{\epsilon_0 \, k_{\mathrm{B}} \, T_{\mathrm{e}}}{n \, e^2}}. \tag{4.15}$$

The ambipolar electric field cannot be completely shielded and a remaining electric field always penetrates the SOL towards upstream. This field is called pre-sheath electric field and it accelerates the ions in the SOL towards the target to velocities of the order of c_{s}. Once the electrons and ions reach the target surfaces, opposite charges are sourced leading to the plasma neutralization. The resulting neutral atoms are then thermally re-emitted into the plasma, where they can be re-ionized, a process called recycling. At low enough values of plasma density and recycling flux, the mean free path for neutral ionization may be as large as the size of the system, implying almost uniform ionization across the SOL. In this case, the SOL is said to be in the so-called sheath limited regime, in which the plasma particles move at velocities of the order of c_{s} through almost the entire SOL leading to a typical characteristic SOL dwell time of the order of $\tau_{\mathrm{SOL}} \approx L_{||}/c_{\mathrm{s}}$. This characteristic SOL dwell time is of the order of 0.1 ms in TCV and about 1 ms in larger machines like JET. At higher plasma density, the divertor becomes opaque. Here, the SOL is said to be in the so-called conduction limited regime, in which the region where the plasma particles are accelerated is now restricted to a small region in front of the target.

Perpendicular (cross-field) transport

Plasma transport across the magnetic field has been precisely formulated theoretically in the case where Coulomb collisions are the only cause of the cross-field transport [144, 145]. This model is referred to as classical transport theory and provides the classical transport coefficients. Later on, this model was modified to account for the effect of the particle orbits in an axisymmetric inhomogeneous toroidal magnetic field [146]. This improved model is referred to as neoclassical transport theory and it sets the lowest level of plasma

transport that can be achieved in a tokamak. While the neoclassical transport exceeds classical transport, it is still too low to explain the perpendicular transport levels observed experimentally. For the low confinement regime (L-mode), neoclassical transport theory predicts particle confinement times that are two orders of magnitudes greater than measured. Many studies suggest that plasma turbulence is the dominant cause of the plasma cross-field transport [147]. In some, so called, "improved" confinement regimes and in localized regions of the plasma, transport can sometimes be reduced to the neoclassical level [148, 149, 150]. An extensive review of the several possible known explanations for this experimental large cross-field transport can be found in [146, 147, 151].

Since the mechanisms responsible for the cross-field transport are not well understood, cross-field transport coefficients are often considered anomalous and their values estimated experimentally. In some cases, experimental measurements can be used to determine the relative importance of convective and diffusive transport. If the cross-field transport can be described by a diffusive process, with a cross-field diffusivity $D_\perp$, the SOL radial width at the target, Δ_t, can be estimated from the characteristic diffusion length. This leads to a typical SOL width of the order of $\Delta_t \approx (D_\perp \, \tau_{SOL})^{1/2}$. Using the previous approximation of $\tau_{SOL} \approx L_{||}/c_s$ yields $\Delta_t \approx \left(D_\perp \, L_{||}/c_s\right)^{1/2}$. However, if the cross-field transport is better described by convective transport, with a cross-field velocity $v_\perp$, then the typical radial width of the SOL at the target is approximately given by $\Delta_t \approx L_{||} \, v_\perp/c_s$. In both cases, the SOL width increases with connection length.

4.1.3 Particle drifts in the scrape-off layer

In addition to classical transport described above, several other mechanisms can strongly influence the plasma transport in both parallel and perpendicular directions in the SOL. In this section, a brief review of the main features related to the presence of particle drifts on the plasma transport in the SOL is presented. More detailed reviews of the experimental manifestation of particle drifts in tokamaks can be found in [152, 153, 154, 155, 156, 157, 158].

Particle drifts depend on the direction of the toroidal magnetic field but not on the direction of the plasma current [15]. They are thought to be the cause of the power imbalances between inner and outer divertor targets observed in many tokamaks [159, 152, 153, 18]. This identification results from the observed change of the power imbalance, although not necessarily completely reversing, when the direction of the toroidal magnetic field is reversed and from the invariance of the power imbalance with the direction of the plasma current.

To minimize the power load on the plasma facing components (PFC), the exhaust power and particles must be distributed, as evenly as possible, over the wetted area. Since the inner divertor target is located at a smaller major radius than the outer target, higher heat

fluxes are expected owing to its smaller wetted area (equation 4.13). A beneficial effect of the power imbalance between the inner and outer divertor targets is the possibility of distributing the exhaust power more evenly over the wetted area. Improved understanding of the effects of particle drifts on the plasma transport in the SOL can be important for an efficient power distribution in the divertor.

Two alternative approaches to describing the particle drifts can be used: (*i*) the fluid or (*ii*) the average guiding centre approach. Using the fluid approach, the single-fluid momentum conservation equation can be used to calculate the total particle flux in stationary conditions [152],

$$\vec{\Gamma} = \underbrace{n\,\vec{u}_{||}}_{\substack{\text{Parallel}\\ \text{plasma}\\ \text{flux}}} + \overbrace{\underbrace{n\frac{\vec{E}\times\vec{B}}{B^2}}_{\substack{\vec{E}\times\vec{B}\\ \text{drift}}} + \underbrace{\frac{\vec{R}\times\vec{B}}{e\,B^2}}_{\substack{\text{Drift due to}\\ \text{the friction}\\ \text{between}\\ \text{ions and}\\ \text{neutrals}}} + \underbrace{\frac{\vec{B}\times\vec{\nabla}p_{\perp}}{e\,B^2}}_{\substack{\text{Diamagnetic}\\ \text{drift}}} + \underbrace{\frac{\left(p_{||}-p_{\perp}+n\,m\,u_{||}\right)}{e\,B^3}\,\vec{B}\times\left[\left(\vec{B}\cdot\vec{\nabla}\right)\frac{\vec{B}}{B}\right]}_{\substack{\text{Combined curvature-}\\ \text{and gradient-B drift}}}}^{\text{Drift terms}}. \tag{4.16}$$

In this equation, $\vec{R}$ is the friction force between the ion and neutral fluids, $p_{||}$ is the parallel plasma pressure and $p_{\perp}$ the perpendicular plasma pressure.

In equation 4.16, the first term represents the usual parallel particle flux and the other terms the effects of different particle drifts. The second term corresponds to the $\vec{E}\times\vec{B}$ drift, the third term accounts for the cross-field transport due to the collision between the ion and neutral fluids, the fourth term represents the diamagnetic drift and the fifth accounts for the contribution from both the curvature and gradient of the magnetic field. Apart from the parallel plasma flow term in equation 4.16, the $\vec{E}\times\vec{B}$ drift is typically the dominant term. For this reason, its effect on the SOL plasma transport will be discussed in more detail.

Using a coordinate system (ρ, θ, ϕ) with the steady state (time averaged) electric field being $\vec{E} = E_{\rho}\hat{e}_{\rho} + E_{\theta}\hat{e}_{\theta} + E_{\phi}\hat{e}_{\phi}$ and the magnetic field $\vec{B} = B_{\theta}\hat{e}_{\theta} + B_{\phi}\hat{e}_{\phi}$, figure 4.4, the $\vec{E}\times\vec{B}$ drift velocity can be written as

$$\vec{u}_{\mathrm{D}} = \frac{(E_{\theta}B_{\phi} - E_{\phi}B_{\theta})}{B^2}\hat{e}_{\rho} - \frac{E_{\rho}B_{\phi}}{B^2}\hat{e}_{\theta} + \frac{E_{\rho}B_{\theta}}{B^2}\hat{e}_{\phi}. \tag{4.17}$$

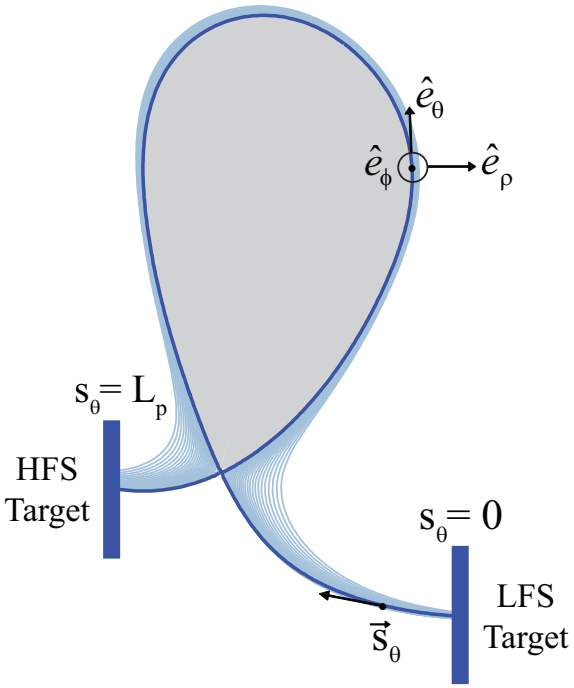

Figure 4.4: (ρ, θ, ϕ) coordinate system used for decomposing the $\vec{E} \times \vec{B}$ particle drift velocity $\vec{u}_\mathrm{D}$.

Here, E_ρ is the "radial" electric field, $E_\phi = V_\mathrm{loop}/(2\pi R)$ is the inductive toroidal electric field with V_loop being the loop voltage, and $E_\theta = B\,E_{||}/B_\theta$ is the poloidal electric field, which can be calculated by using the parallel electron momentum balance equation,

$$E_{||} = \frac{J_{||}}{\sigma_{||}} - 1.71\,\frac{\partial}{\partial s_{||}}\left[\frac{k_\mathrm{B}\,T_\mathrm{e}}{e}\right] - \frac{k_\mathrm{B}\,T_\mathrm{e}}{e\,n}\,\frac{\partial n}{\partial s_{||}}. \tag{4.18}$$

Note that here, and in section 4.9, the "radial" direction $\hat{e}_\rho$ corresponds to a direction perpendicular to the magnetic flux surfaces rather than the direction of the major radius, while the poloidal direction $\hat{e}_\theta$ is parallel to the flux surface in the poloidal plane.

The poloidal component of the $\vec{E} \times \vec{B}$ drift velocity is caused by a radial electric field while its radial component is caused mainly by a poloidal electric field, equation 4.17. Figure 4.5 shows the poloidal projection of the usual, no-drift, parallel plasma flow to the target, i.e. the plasma flow resulting from ionization, and the expected direction of the poloidal and radial components of the $\vec{E} \times \vec{B}$ flow in forward and reversed toroidal magnetic field. The forward direction is here defined such that the direction of the ion gradient-B drift points downwards, i.e. towards the x-point. This figure shows that, depending on the direction of the toroidal magnetic field, the poloidal $\vec{E} \times \vec{B}$ flow competes with the plasma flow on one side of the SOL and enforces the plasma flow on the other side. It also shows

that the radial $\vec{E} \times \vec{B}$ flow in forward B_ϕ direction tends to displace particles from the LFS side of the SOL into the main plasma and PFR, and also from these two regions to the HFS side of the SOL, figure 4.5(b). This behavior reverses with reversed B_ϕ direction, figure 4.5(c).

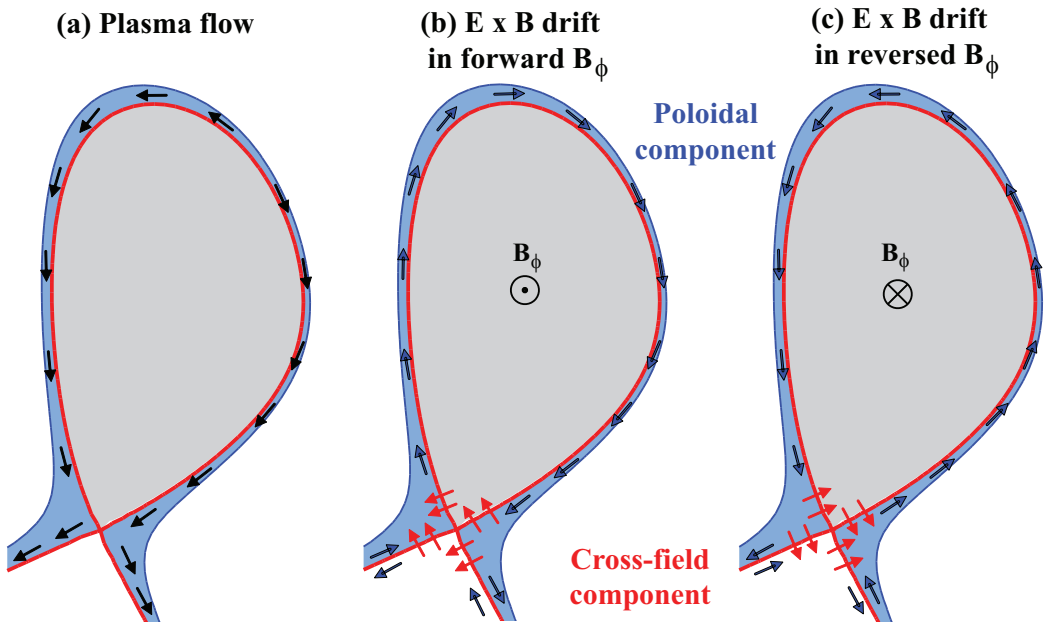

Figure 4.5: Schematic showing the direction of (a) the poloidal projection of the parallel plasma flow resulting from ionization and the $\vec{E} \times \vec{B}$ flow in the SOL of a plasma with (b) forward and (c) reversed toroidal magnetic field.

Associated with the non-divergence-free $\vec{E} \times \vec{B}$ particle flux, exists a heat flux that can influence the deposition of the exhaust power onto the solid surfaces. This convective $\vec{E} \times \vec{B}$ heat flux is believed to explain part of the observed asymmetries between the power detected at the inner and outer divertor targets [18, 160], and is given by

$$\vec{q}^{\,\mathrm{E\times B}} = \frac{5}{2}\, p\, \vec{u}_\mathrm{D} = \frac{5}{2}\, \frac{p}{B^2}\, \vec{E} \times \vec{B}. \tag{4.19}$$

The $\vec{E} \times \vec{B}$ drift can strongly influence the plasma transport in both parallel and perpendicular directions in the SOL. In section 4.9, experiments carried out to demonstrate the effect of the $\vec{E} \times \vec{B}$ drift on the target profiles of SF and standard single-null configurations are presented.

4.1.4 The snowflake divertor

In the ITER $Q = 10$ scenario, the steady-state power that crosses the separatrix and enters into the SOL is expected to be about 100 MW. At the divertor plates, this power has to be distributed such that the peak heat fluxes at the plasma facing components are below typical tolerable values of $10\,\mathrm{MW/m^2}$. For power handling to be possible in ITER, about 60-70% of the power entering the SOL must be exhausted through radiation in order to spread enough power over a larger area [29].

Steady-state power handling in future fusion reactors will only be possible with plasmas operated with an extremely high radiation fraction [30, 31]. However, it is not clear if these conditions can be sustained or if this will be compatible with maintaining operation in the high confinement mode. Alternative divertor concepts are being considered to control the heat loads on the divertor targets and are currently under intense investigation. In some of these, the main goal is to maximize the wetted area, which can be achieved by acting on different parameters of equation 4.13, e.g. by

1. decreasing the grazing angle α of the magnetic field lines at the target surface. This can be obtained by either tilting the target plates poloidally or by increasing the target flux expansion, which requires a modification of the magnetic divertor configuration;
2. increasing the major radius of the divertor target, R_t;
3. increasing the upstream SOL width, Δ_u.

One of the proposed alternatives is the x-divertor [161, 30, 39], which creates additional x-points in the vicinity of the SPs to increase $f_\mathrm{exp,t}$. The x-divertor also increases the connection length and decreases the grazing angle of the field lines at the target. The small grazing angle would not be a problem for the toroidal homogeneity of the power distribution if stable operations in a fully detached regime would be achieved, as is qualitatively argued in [162, 163]. Another divertor concept, the super-x divertor, has been proposed and studied in MAST [164, 165]. This configuration can be viewed as a variation of the x-divertor where, in addition to the increased $f_\mathrm{exp,t}$, a toroidal expansion (increased divertor target radius R_t) is used, in combination with a strongly modified divertor chamber, to further increase of the wetted area.

The snowflake configuration [32] is another new divertor concept that has emerged as an alternative solution for reducing the heat loads to the divertor plates. A conventional single-null (SN) divertor configuration requires at least one divertor coil to cancel the poloidal magnetic field, $\vec{B}_\theta$, at a single-null point, figure 4.6(a). In the SF configuration, additional divertor coils are used to cancel also the gradient of the poloidal field at the null-point ($\vec{\nabla} B_\theta = 0$), figure 4.6(b), thereby creating a second order null-point.

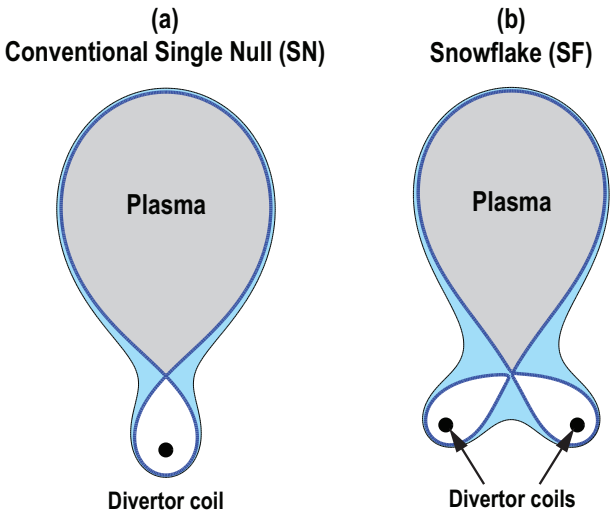

Figure 4.6: Schematic of (a) a conventional single-null and (b) a snowflake divertor. The black circles represent divertor coils.

In practice, the currents in the poloidal field coils always differ slightly from those required for an exact SF resulting in two nearby first order null-points. An exact SF configuration, figure 4.7(a), is a single point in an operational domain and, in practice, a SF always features two separate x-points rather than a single second order null-point. In such a quasi-SF configuration, the primary x-point determines the LCFS with the other located either (*i*) in the PFR of the primary separatrix, usually referred to as snowflake plus (SF+), figure 4.7(b), or (*ii*) in its common flux region, usually referred to as snowflake minus (SF-), figure 4.7(c). The proximity of any quasi-SF configuration to an exact SF can be characterized by a parameter σ, defined as the distance between the x-points, d_{xpt}, normalized with the plasma minor radius, a.

The SF divertor configuration was first demonstrated experimentally in the TCV tokamak [37, 166] and has since also being demonstrated in the NSTX spherical torus [167, 168, 169] and in the DIII-D tokamak [170]. Experiments performed in these devices have shown that a substantial decrease of the peak heat flux on the divertor plates can be achieved. The configuration provides an easier access to detachment whilst keeping the energy confinement, L-H threshold and H-mode pedestal height, similar to those obtained from similarly shaped SN plasmas [166, 167, 168, 170, 169, 138, 2].

Many geometrical properties of the SF divertor, associated with the smaller magnitude of the magnetic poloidal field in the null-point region, are expected to lead to a reduction of the peak and total heat flux onto the divertor plates. These geometrical properties will be further discussed in section 4.3. The SF configuration is also expected to stabilize MHD modes due to the increased magnetic shear in the pedestal region [171]. An enhanced stability of ideal MHD modes is consistent with experimentally observed different ELM behavior between SN and SF plasmas [166].

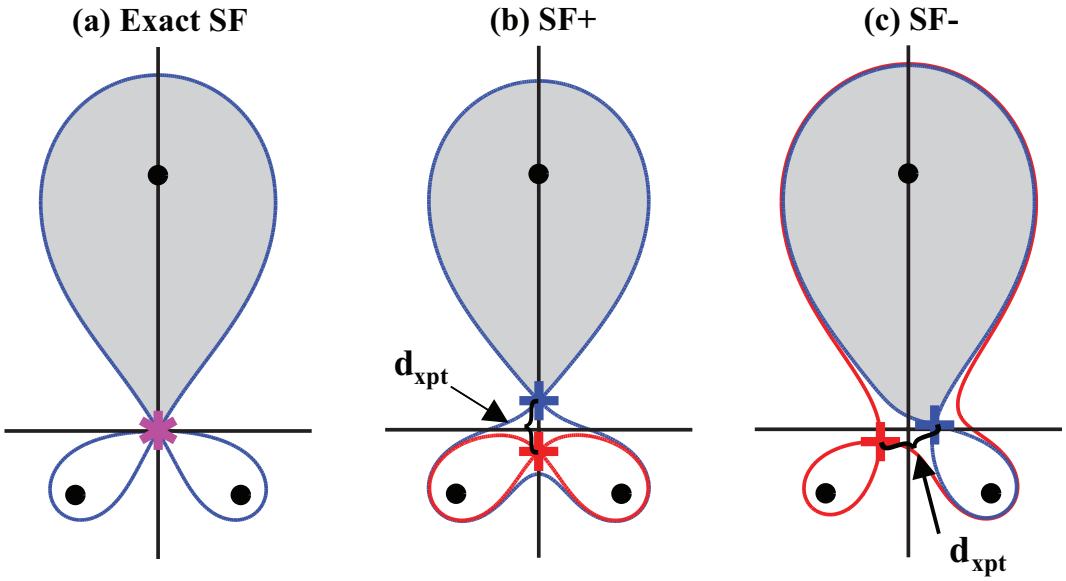

Figure 4.7: Schematic of different SF configurations: (a) An exact SF, (b) a snowflake plus and (c) a snowflake minus configuration. The blue and red crosses represent the primary and secondary x-points, respectively, and the black circles represent the plasma and the divertor coils.

The local properties of the SF configuration

A quasi SF configuration can be characterized by two parameters that express the location of the secondary x-point relative to the primary x-point: the σ parameter and the angle θ, defined as the angle between a line connecting the two x-points and a line perpendicular to a line connecting the primary x-point and the magnetic axis [32, 172]. While σ defines the proximity to an exact SF, θ parameterizes the transition between the SF+ and SF-. When $60^o \lesssim \theta \lesssim 120^o$, the configuration is a SF+, with the secondary x-point located in the PFR of the primary x-point. When $\theta \gtrsim 120^o$ or $\theta \lesssim 60^o$, the configuration is said to be SF-, with the secondary x-point located in the common flux region of the primary one. Due to the location of the secondary x-point with respect to the primary one, a SF- with $\theta \gtrsim 120^o$ is also referred to HFS SF- whereas a SF- with $\theta \lesssim 60^o$, is also referred to LFS SF-. Since these definitions are based on the expansion of the poloidal flux function near the primary x-point [32, 172], the transition between SF+ and SF- in practice is not exactly at 60^o and 120^o.

The proximity criteria

The proximity of a quasi-SF configuration to an exact SF can be parametrized by $\sigma = d_{\mathrm{xpt}}/a$. This implies there exists a continuous trajectory between a SN and an exact SF configuration. Here, some of the criteria that estimate the values of σ at which some SF features are expected to appear will be reviewed. Several proximity conditions have

been proposed depending on the specific property to be considered, e.g. the larger flux expansion, connection length, divertor volume and magnetic shear in the pedestal region [173]. Here, the proximity criteria corresponding to each of these will be described.

If the distance between the x-points is small enough compared with the plasma minor radius, the magnitude of B_θ at a distance ρ_{npt} from the primary null-point becomes indistinguishable from that of an exact SF [174]. Under this assumption, the magnitude of the poloidal field in the null-point region of a quasi-SF configuration can be approximated by

$$B^{\mathrm{SF}}_{\theta,\mathrm{npt}} \approx C_{\mathrm{SF}}\, B_{\theta,\mathrm{u}} \left(\frac{\rho_{\mathrm{npt}}}{a}\right)^2 , \tag{4.20}$$

while in the null-point region of a SN configuration, the magnitude of the poloidal field is approximately given by

$$B^{\mathrm{SN}}_{\theta,\mathrm{npt}} \approx C_{\mathrm{SN}}\, B_{\theta,\mathrm{u}} \frac{\rho_{\mathrm{npt}}}{a} , \tag{4.21}$$

with C_{SN} and C_{SF} constant factors. Using the definition of the flux expansion in section 4.1.1 and equation 4.20, an estimation of the upstream SOL width, mapped into the null-point region of a SF configuration, is given by

$$\Delta_{\mathrm{npt}} \approx a \left(\frac{3}{C_{\mathrm{SF}}}\, \frac{R_{\mathrm{u}}}{R_{\mathrm{npt}}}\right)^{1/3} \left(\frac{\Delta_{\mathrm{u}}}{a}\right)^{1/3} . \tag{4.22}$$

According to [173], in order to see an increased flux expansion, connection length, divertor volume and magnetic shear in the pedestal region, the distance between the x-points, d_{xpt}, should be smaller than Δ_{npt},

$$\frac{d_{\mathrm{xpt}}}{a} \equiv \sigma < \sigma_{\mathrm{crit}} \equiv \frac{\Delta_{\mathrm{npt}}}{a} \approx \left(\frac{3}{C_{\mathrm{SF}}}\, \frac{R_{\mathrm{u}}}{R_{\mathrm{npt}}}\right)^{1/3} \left(\frac{\Delta_{\mathrm{u}}}{a}\right)^{1/3} . \tag{4.23}$$

Another enhancement expected with a SF configuration comes from its effect upon a hypothesized plasma convective cell in the null-point region caused by pressure-driven instabilities [175]. It is argued that, due to the enlarged region of low B_θ in the null-point region, the plasma pressure can overcome the available magnetic pressure in the regions

where $\beta_{\mathrm{p}} >> 1$. This leads to the loss of the plasma equilibrium and the formation of the convective cell. Therefore, inside a certain radius around the primary null-point, the plasma is expected to experience an intense convective transport spreading heat and particles over the region of weak B_θ. This mechanism would provide a way of activating the two additional plasma legs of a SF+ that are not directly connected to the upstream plasma, leading to a more even power distribution between the SPs. This mechanism would also be present in a SN configuration but in a smaller region near the null-point. Using equation 4.20, the local value of β_p in the null-point region is

$$\beta_{\mathrm{p,npt}} \approx \frac{\beta_{\mathrm{p,u}}}{C_{\mathrm{SF}}^2} \left(\frac{a}{\rho_{\mathrm{npt}}}\right)^4 . \tag{4.24}$$

Following [173], the typical size of the convective zone corresponds to the region where the plasma pressure is much larger than the poloidal magnetic field pressure. This will be defined as the region where $\beta_{\mathrm{p,npt}} \geq 10$. The criteria for having an enhanced power distribution among the SPs due to the existence of a plasma convective cell becomes

$$\frac{d_{\mathrm{xpt}}}{a} \equiv \sigma < \sigma_{\mathrm{crit}} = \frac{\rho_{\mathrm{conv}}^{\mathrm{SF}}}{a} \approx \left(\frac{\beta_{\mathrm{p,u}}}{10\, C_{\mathrm{SF}}^2}\right)^{1/4} . \tag{4.25}$$

In a SN configuration, the plasma convective cell is expected to occur in a region whose the typical radius can be estimated by

$$\rho_{\mathrm{conv}}^{\mathrm{SN}} \approx \frac{a}{C_{\mathrm{SN}}} \left(\frac{\beta_{\mathrm{p,u}}}{10}\right)^{1/2} . \tag{4.26}$$

4.2 Objectives

The robust SF configurations available on TCV makes it one of the few machines in which the details of the plasma transport in the complex topologies of the SF+ and SF- divertor can be studied. This work seeks to compare some of the the exhaust properties of the SF divertor with those of a standard single-null divertor. The specific objectives of this work are:

- to provide a detailed analysis of the geometrical properties of the SF divertor (section 4.3);

- to characterize the power distribution among the four SPs and the radiated fraction of SF configurations (section 4.5), input power (section 4.6) and plasma density (section 4.7);
- to interpret the experimental results using modeling of the plasma transport in the SOL (section 4.8);
- to investigate the influence of particle drifts on the target profiles (section 4.9).

4.3 The Geometrical Properties of the Snowflake Divertor in TCV

In many studies it was argued that the SF configuration may alleviate the wall heat loads due to its geometrical properties in the vicinity of the null-point [32, 172, 174]. In this section, the most relevant SOL geometrical properties will be calculated for SF+ configurations with a range of separations between x-points and also compared with those of a similar single-null configuration. The main geometrical properties are (*i*) the target flux expansion, $f_{\mathrm{exp,t}}$, (*ii*) the minimum distance of a flux surface to the primary x-point, ρ_{npt}, which is closely related to the divertor volume, (*iii*) the smallest magnitude of the poloidal field on a flux surface in the vicinity of the primary x-point, $B_{\theta,\mathrm{npt}}$, and (*iv*) the connection length, $L_{||}$, here defined as the length of field lines between the upstream location and the LFS divertor target. In this thesis, the strike points in the SF configuration are labelled in a counter clock-wise direction from one to four (SP1 to SP4) starting at the highest strike point on the HFS.

4.3.1 Snowflake equilibria created using the SPIDER code

The main feature of an exact SF configuration is that the magnitude and gradient of the poloidal magnetic field at the primary x-point $|\vec{\nabla}B_\theta|_{\mathrm{xpt}}$ vanish. The value of $|\vec{\nabla}B_\theta|_{\mathrm{xpt}}$ is, thus, another parameter that indicates the proximity of a configurations to an exact SF. To investigate the effects of σ and thus $|\vec{\nabla}B_\theta|_{\mathrm{xpt}}$ on the geometrical properties described above, a set of equilibria with different values of σ was generated using the free boundary equilibrium code SPIDER [176, 177]. The set of equilibria was created with the same plasma profiles and similar plasma boundaries, obtained from a TCV SF discharge. The plasma minor radius of these configurations is $a = 0.22\,\mathrm{m}$ and the poloidal field at the upstream position, $R_{\mathrm{u}} = 1.097\,\mathrm{m}$, is equal to $B_{\theta,\mathrm{u}} = 0.215\,\mathrm{T}$.

For small values of σ, the values of $|\vec{\nabla}B_\theta|_{\mathrm{xpt}}$ varies approximately linearly with σ, figure 4.8. However, the values of $|\vec{\nabla}B_\theta|_{\mathrm{xpt}}$ remain approximately the same for $\sigma \gtrsim 1.00$ and any SF configuration with $\sigma \gtrsim 1.00$ is expected to behave like a SN divertor. Therefore, a SF configuration with $\sigma = 1.00$ will be used as a reference for evaluating the changes of the SOL properties caused by changing σ.

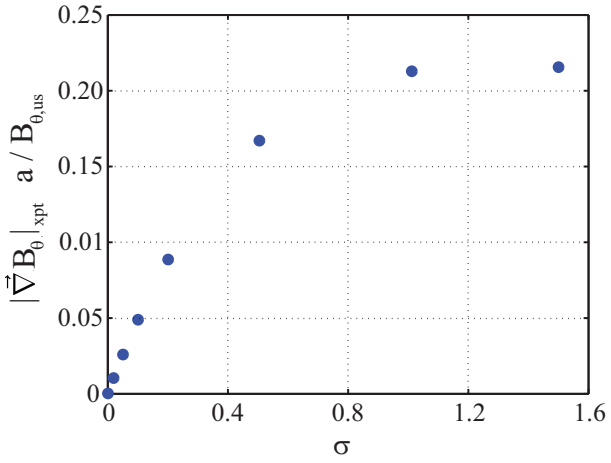

Figure 4.8: Gradient of the magnitude of the poloidal magnetic field at the primary x-point, normalized with $B_{\theta,\mathrm{u}}/a$, as as function of σ.

4.3.2 The effect of σ on the divertor and SOL properties

Surprisingly, the first result from the analysis of the equilibria with a range of σ, figure 4.9(a), appears to contradict the promise of a SF divertor. The target flux expansion, $f_{\mathrm{exp,t}}$, decreases when the divertor configuration approaches an exact snowflake ($\sigma \to 0$), figure 4.9(b) (Only SP4 results are shown). This dependence occurs because the divertor targets for these SF configurations are not optimized to take advantage of the increased flux expansion that mostly occurs close to the null-point. In TCV, the divertor targets are situated far from the null-point, where the flux surfaces are recompressed. To take advantage of the enhanced flux expansion, the targets would have to be placed closer to the null-point, as on the NSTX [167, 168] and DIII-D [170] SF experiments.

The region of the SOL where $L_{||}$ is longer and the amplitude of $B_{\theta,\mathrm{npt}}$ is lower is limited to a small region in the immediate vicinity of the separatrix, compared with a SN configuration ($\sigma = 1.00$), figures 4.9(c) and (d) respectively. Outside this region, $L_{||}$ is significantly shorter for configurations closer to the exact SF. This region is significantly smaller than the typically observed SOL width in TCV, $\Delta_{\mathrm{u}} = 8\,\mathrm{mm}$, defined by the measured power fall-off length at the upstream position. TCV is thus not expected to gain any advantage from an increased $L_{||}$ in the SF configuration.

The main feature that is expected in the TCV SF configurations is an increased ρ_{npt}, which is closely related to the divertor volume. As shown in figure 4.9(e), the value of ρ_{npt} exceeds its value in a SN configuration across almost the entire SOL width. However, in the SF configuration, the decrease of the angle between the primary divertor legs and the separatrix enclosing the plasma, in addition to the recompression of the field lines close to the targets, overcomes the increase of ρ_{npt} in the null-point region so that the total SOL volume of the TCV SF configuration is slightly smaller compared with a SN.

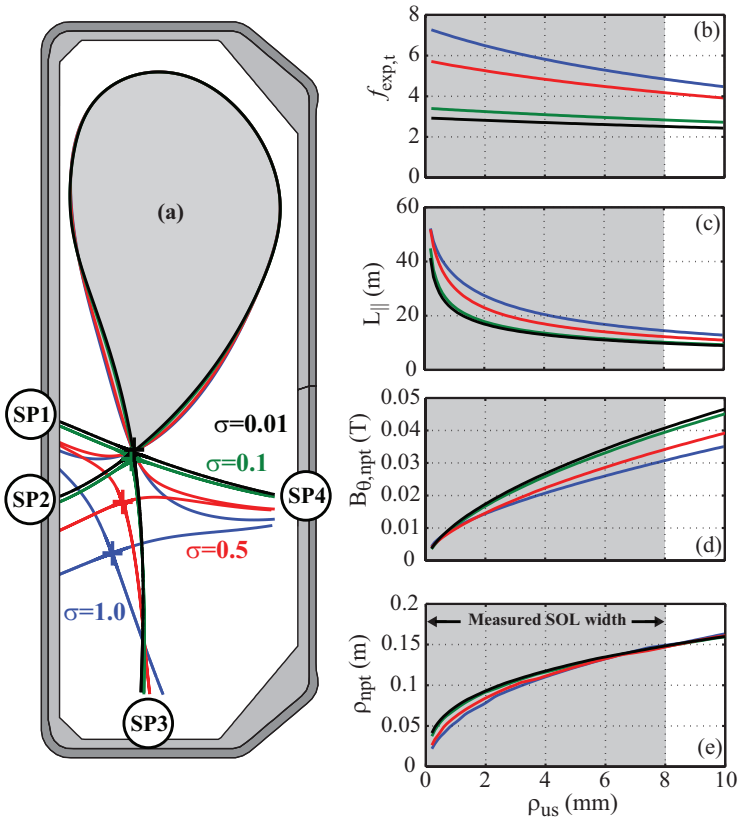

Figure 4.9: (a) Set of equilibria created using the SPIDER equilibrium solver. Main geometrical properties of a set of SF magnetic equilibria with various values of σ as a function of the upstream coordinate ρ_u. (b) Target flux expansion $f_{exp,t}$ at SP4. (c) Connection length $L_{||}$ between upstream position and SP4. (d) Smallest magnitude of the poloidal field in the vicinity of the primary x-point $B_{\theta,npt}$. (e) Minimum distance of the flux surface specified to the primary x-point ρ_{npt}.

4.4 Experimental Setup

In the experiments described in this chapter, the primary x-point was placed near the center of the TCV vessel to separate the null-point region from each of the four strike points. Typical plasma parameters used during the experimental part of the SF studies are: elongation $\kappa = 1.6 \pm 0.1$, triangularity $\delta = 0.16 \pm 0.04$, minor radius $a = (0.20 \pm 0.02)$ m, edge safety factor $q_{95} = 3 \pm 0.5$, plasma current $I_p = (280 \pm 50)$ kA, toroidal magnetic field $B_0 = (1.46 \pm 0.02)$ T and central electron temperature $T_{e0} = (1.2 \pm 0.3)$ keV. The experiments are performed at sufficiently low densities to keep the divertor legs in the attached regime, so that most of the power entering the SOL is exhausted in the vicinity of the strike points. The reference line averaged density is set to $n_{e,l} = (2.5 \pm 0.5) \times 10^{19}$ m^{-3}, i.e. well below $n_{e,l} \approx 6.0 \times 10^{19}$ m^{-3} where the recycling current measured at the HFS primary SP is largest, figure 4.10, that could be interpreted as a sign of partial divertor detachment [178].

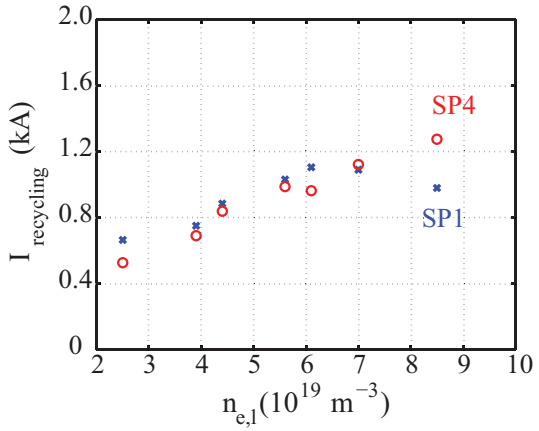

Figure 4.10: Lagmuir probe measurements of the recycling current at the SP1 and SP4 targets as a function of the line integrated plasma density.

The discharges were prepared using the free-boundary equilibrium code FBTE [34] that calculates the required currents in the PF coils for creating a prescribed magnetic configuration. During the experiments it was observed that, for a given set of divertor coil currents, the divertor configuration in the vicinity of an exact SF configuration is very sensitive to the vertical position of the plasma. Small vertical plasma displacements can therefore affect the divertor topology, if σ is sufficiently small. Unintended transitions between SF+ and SF- configurations caused by vertical oscillations in the control loop have been observed when $\sigma \lesssim 0.2$. Furthermore, a systematic error in the reconstructed vertical position of the plasma would lead to a systematic error in the derived divertor topology.

4.5 The Power Exhaust in the TCV SF Divertor

One potential advantage of the SF divertor is its four divertor legs that could all distribute the exhausted power from the confined plasma. An equal distribution between the divertor legs would reduce the power at each strike point by a factor 2. This section will focus on determining in which conditions the two additional plasma legs are "active" and whether an even power distribution can be obtained. In this context, a plasma leg is said to be active when part of the exhausted power can be detected at its SP.

To understand how the magnetic geometry affects the power distribution amongst the SPs, discharges with a range of σ and θ were performed. To identify any improvement on the divertor performance associated with a SF geometry, the measurements were compared with those of a standard SN divertor. As mentioned in section 4.3.2, configurations with values of $\sigma \gtrsim 1.00$ do not have values of $\vec{\nabla} B_\theta$ at the primary x-point significantly different from those observed in SN configurations. For this reason, a SF+ with $\sigma = 1.5$ was used as a reference configuration for the comparison. This reference configuration is referred

to as a SF-like SN. In the following, measurements of the power distribution among the four SPs of the SF+ (section 4.5.2) and SF- (section 4.5.3) will be compared with those obtained in the reference SF-like SN (section 4.5.1).

4.5.1 The SF-like SN configuration

The SF-like SN configuration has been defined as the reference configuration for any future comparison and, from here, it will be referred to as SN for simplicity. In such a reference discharge, the values of $\sigma = 1.5$ and $\theta = 90^{o}$ are kept constant while small sweeps of the plasma vertical position, resulting in sweeps of the SP across the divertor targets, are used to increase the measurements' spatial resolution. The Ohmic heating power was $P_{\mathrm{Ohm}} \approx 280\,\mathrm{kW}$ with about 30% being radiated ($P_{\mathrm{rad}} \approx 80\,\mathrm{kW}$). Figure 4.11(a) shows that most of the radiation originates from the region in front of the HFS target. The radiation density was normalized with its peak value to provide a spatial profile that can be directly compared with those obtained in the SF configurations.

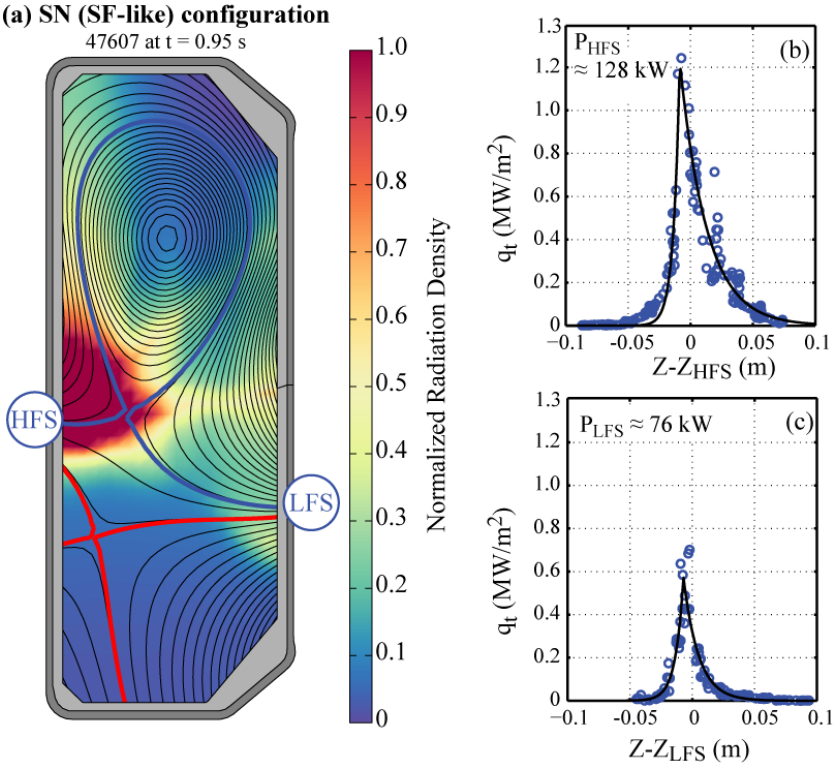

Figure 4.11: (a) Normalized radiation density and target heat flux profiles at the (b) HFS and (c) LFS strike points in a SN configuration. The radiated power and deposited power on the targets are estimated from the BOLO and LP diagnostics, respectively.

The total power deposited near the SP on the HFS wall, measured by an array of Langmuir probes, was $P_{\mathrm{HFS}} \approx 128\,\mathrm{kW}$, figure 4.11(b), while the total deposited power on the LFS SP was $P_{\mathrm{LFS}} \approx 76\,\mathrm{kW}$, figure 4.11(c). The sum of the power arriving in the vicinity

of the SPs, $P_{SOL} = P_{HFS} + P_{LFS} \approx 204\,kW$, is in agreement with the value expected from the power balance, $P_{SOL} = P_{Ohm}$ - $P_{rad} \approx 200\,kW$. In both HFS and LFS divertor targets, the position of the peak heat flux is a few millimeters below the reconstructed SP position, which is within the estimated uncertainty in the equilibrium reconstruction.

4.5.2 The SF+ configuration

In the SF+ configuration, SP1 and SP4 are the primary SPs and are directly connected to the upstream location by continuous magnetic field lines, while SP2 and SP3 are in the PFR. The main objective of the experiments in the SF+ configuration is to determine the values of σ at which the SPs in the PFR are activated, and the fraction of the input power that can be exhausted through them. To study the power distribution among the SPs in this configuration, a SF+ with $\sigma \approx 0.3$ was created with all the other plasma parameters approximately the same as the reference SN case, section 4.5.1.

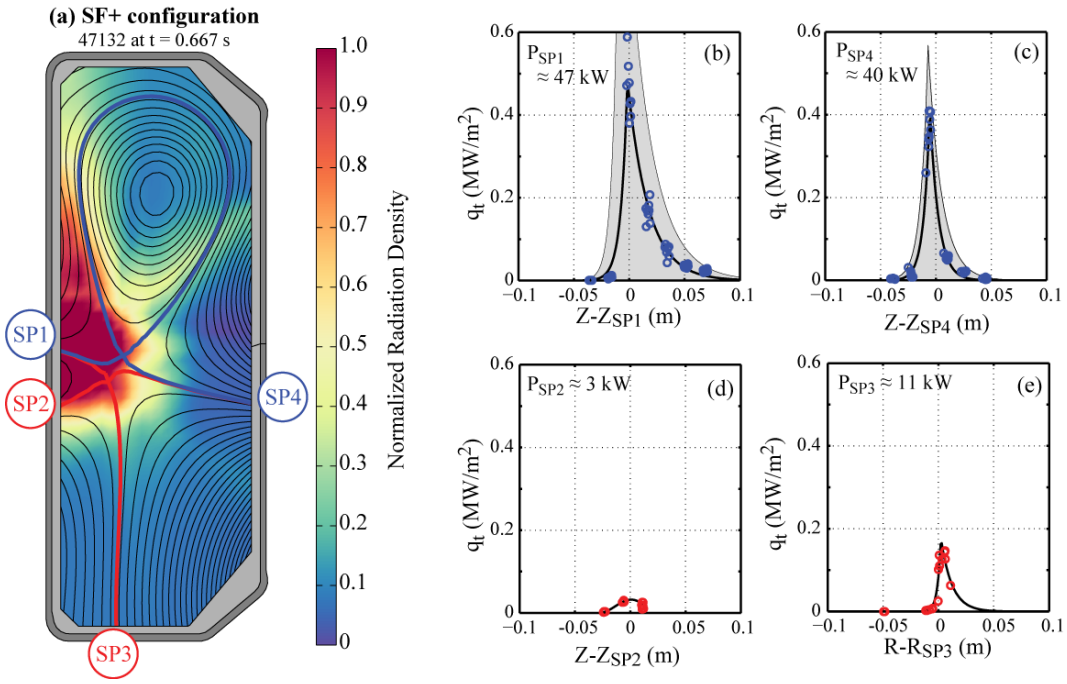

Figure 4.12: (a) Normalized radiation density and measured heat flux perpendicular to the TCV wall at the four SPs (b-e) in a SF+ configuration. The shadow in (b) and (c) correspond to the measured profiles at the HFS and LFS SPs in the SN reference, figures 4.11(b) and (c). The radiated power and deposited power on the targets are estimated from the BOLO and LP diagnostics, respectively.

In this discharge, P_{Ohm} and P_{rad} are approximately the same as in the SN discharge ($P_{Ohm} \approx 280\,kW$ and $P_{rad} \approx 80\,kW$). Figure 4.12(a) shows that, although the total power being radiated is the same as in the SN, the peak radiation emissivity decreases leading to a larger radiating zone in front of the HFS wall of the SF+ configuration.

The heat flux profiles measured at SP1 and SP4 can be directly compared with those obtained in the SN. Figures 4.12(b) and (c) show that both the peak heat fluxes in the SF+ configuration ($q_{\mathrm{SP1,peak}} \approx 0.5\,\mathrm{MW/m^2}$ and $q_{\mathrm{SP4,peak}} \approx 0.4\,\mathrm{MW/m^2}$) are significantly smaller than those obtained in the SN ($q_{\mathrm{HFS,peak}} \approx 1.2\,\mathrm{MW/m^2}$ and $q_{\mathrm{LFS,peak}} \approx 0.6\,\mathrm{MW/m^2}$). The widths of the heat flux profiles at the SP1 and SP4 targets in the SF+ configuration are found to be similar to that of the HFS and LFS targets in the SN.

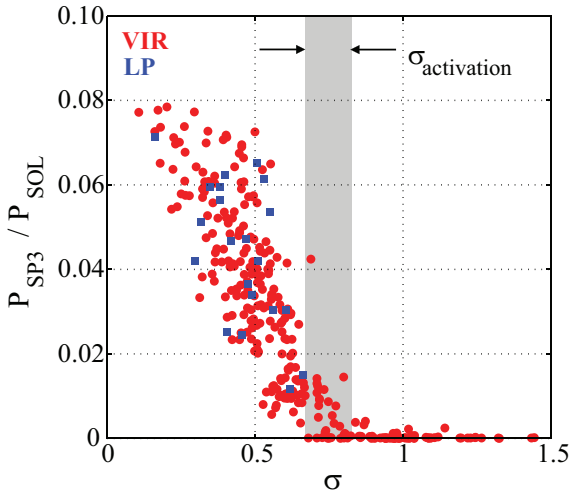

Figure 4.13: Dependence of the power deposited at SP3, normalized with P_{SOL}, in a SF+ configuration. The power is estimated from LP measurements (blue squares) and IR thermography (red circles).

In these SF+ experiments, a small fraction of the exhaust power was detected at the secondary SPs, figures 4.12(d) and (e). Since SP2 and SP3 are located in the PFR of the primary separatrix, the measured power must have transited across the primary separatrix into the PFR. The SP3 activate when $\sigma \lesssim 0.7$ and the deposited power increases when the exact SF is approached ($\sigma \to 0$), figure 4.13. However, extrapolating this curve towards $\sigma = 0$ indicates that, even for an exact SF, only about 10% of $P_{\mathrm{SOL}} = P_{\mathrm{Ohm}}$ - P_{rad} can be deposited on SP3. In section 4.5.6, this SP3 activation will be compared with the proximity conditions proposed in [175]. The power arriving on the SP2 target is usually found to be even smaller (about 1-2% of the total input power). In this discharge, the total power detected at the SPs is significantly smaller than that observed in the SN configuration leading to a deficit of power in the power balance. As it will be shown in section 4.7, this power deficit decreases with increasing plasma density.

4.5.3 The SF- configuration

The magnetic topology of the SF- configuration forks one side of the SOL onto two SPs. To study the power distribution in these configurations, a SF- discharge with the secondary x-point located in the HFS was created. In the HFS SF- configuration, SP3

and SP4 are primary strike points while SP1 and SP2 are secondary. The LFS side of the SOL arrives at SP4 while the HFS side forks onto SP1 and SP3. The fraction of the SOL that is forked towards SP1 depends on σ, which in this particular discharge is 0.4.

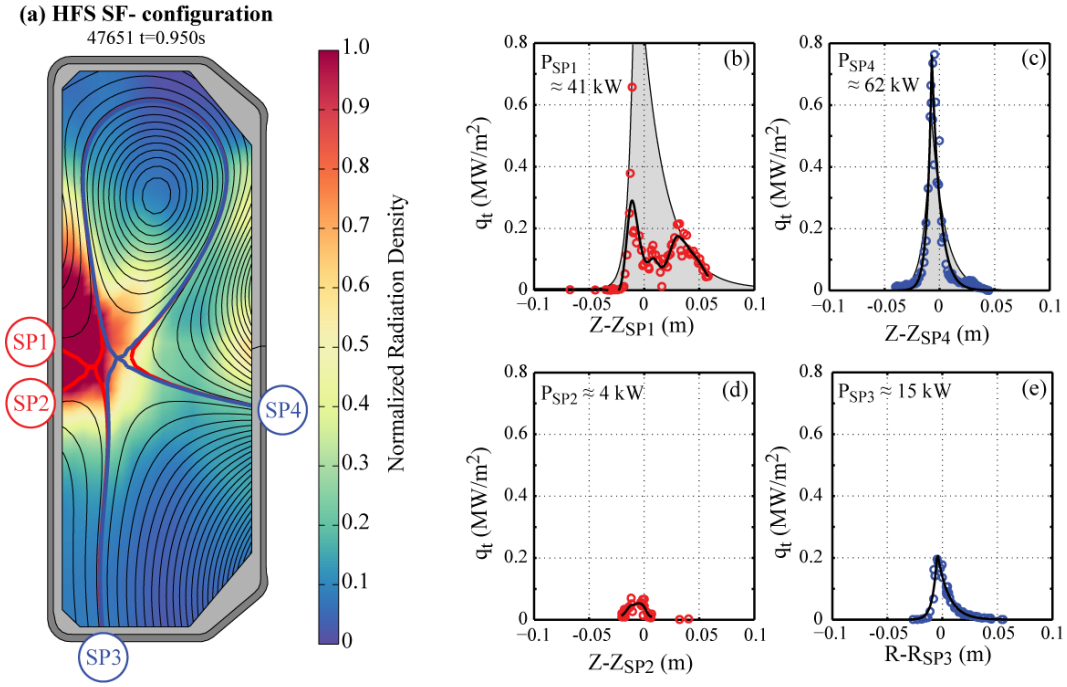

Figure 4.14: (a) Normalized radiation density and measured heat flux perpendicular to the TCV wall at its four SPs (b-e) in a HFS SF- configuration. The shadow in (b) and (c) correspond to the measured profiles at the HFS and LFS SPs in the SN reference, figures 4.11(b) and (c). The radiated power and deposited power on the targets are estimated from the BOLO and LP diagnostic, respectively.

As in the SF+ discharge, the values of P_{Ohm} and P_{rad} are approximately equal as in the SN and, similarly to the SF+ configuration, a larger radiating zone in front of the HFS wall is found, figures 4.14(a). The measurements of the heat flux at the primary SP4 shows a profile with a peak value ($q_{\mathrm{SP4,peak}} \approx 0.7\,\mathrm{MW/m^2}$) similar to that measured at the LFS SP of the SN ($q_{\mathrm{LFS,peak}} \approx 0.6\,\mathrm{MW/m^2}$), figure 4.14(c). However, the profile width decreases by approximately 20%, leading to a decrease of the total power arriving on SP4. This is consistent with the results presented in section 4.3.2, showing a target flux expansion in the TCV SF configuration that is smaller than that for a SN. In the particular case of figure 4.14, $f_{\mathrm{exp,SP4}}$ varies from 1.35 (SN) to 0.92 (SF+).

The total power at the primary SP3 target is found to be much lower than the power at the HFS target of the reference SN. For $\sigma = 0.4$, most of the HFS SOL power arrives at the secondary SP1. Measurements of the heat flux at the secondary SP1 target show a significant reduction in peak value across the whole profile with the profile width remaining comparable with the HFS profile of the SN, figure 4.14(b). The total power detected at the SP1 and SP3 together is similar to the power at SP1, but still smaller

than the power at the HFS SP of the SN. As in the SF+ configuration, the heat exhaust at SP2 is found to be negligible in the power balance, figure 4.14(d). In conclusion, for the SF- configuration, the SOL power on the HFS SOL is divided by the secondary x-point onto SP1 and SP3. This result is qualitatively consistent with a dominant transport along the field lines.

4.5.4 The effect of σ and θ on the power distribution

The power at each SP strongly depends on the geometrical configuration of the SF divertor. In a SF+ configuration, the power at SP3 increases with decreasing values of σ while in the SF- configuration, the value of σ determines the fraction of the exhaust power in one side of the SOL that is forked between two divertor legs.

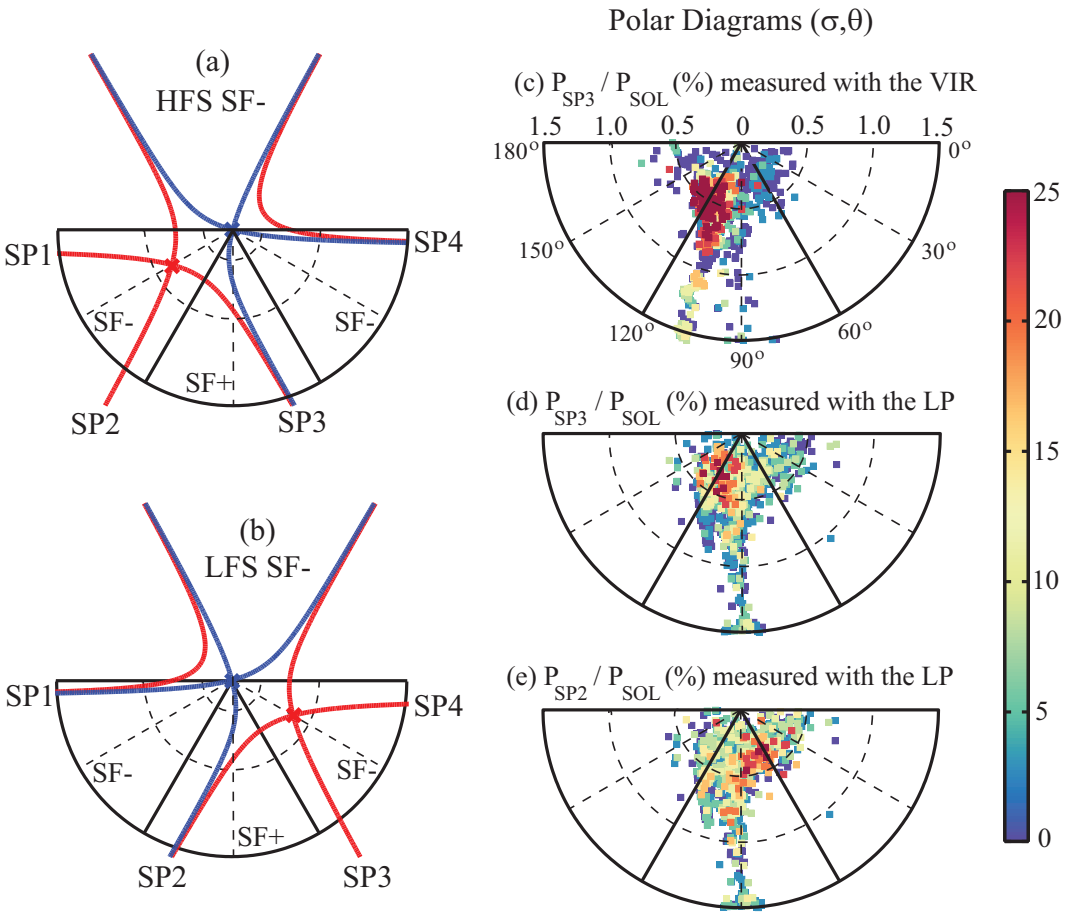

Figure 4.15: (a) HFS and (b) LFS SF- configurations with a polar diagram centred at the primary SP. (c-e) Dependence of the power deposited at the SP3 target, normalized with P_{SOL}, for SF configurations with different values of σ and θ. The power is estimated from Langmuir probe measurements VIR thermography.

To visualize the effects of σ and θ on the power distribution between SPs, the fraction of the exhausted power measured at SP2 and SP3 is plotted in a polar color-coded diagram, figure 4.15. In this diagram, σ and θ describe the relative position of the secondary x-point with respect to the primary x-point and the color scale corresponds to the fraction of the exhausted power measured at the SP with the VIR or LP diagnostics.

In a HFS SF-, figure 4.15(a), the measurements show that the values of the power at SP3, normalized with $P_{\mathrm{SOL}} = P_{\mathrm{Ohm}}$ - P_{rad}, indicate that a significant fraction of the exhaust power is distributed to SP3 when $\theta \gtrsim 110^{\mathrm{o}}$ and $\sigma \gtrsim 0.3$, figures 4.15(b) and (c). This is consistent with the observations presented in section 4.5.3. The results also show that in this configuration, less power is detected at SP3 for $\sigma \lesssim 0.3$. This is explained by the divertor magnetic geometry that distributes most of the power to SP1 for smaller values of σ rather than SP3. In a LFS SF- configuration, figure 4.15(b), LP measurements indicate that a significant fraction of P_{SOL} is detected at SP2 when $\theta \lesssim 70^{\mathrm{o}}$, figure 4.15(e). This observation is qualitatively consistent with the divertor magnetic geometry, that is expected to distribute more power to SP4 than SP2 for smaller values of σ.

The ratio $P_{\mathrm{SP3}}/P_{\mathrm{SOL}}$ increases for values of θ larger than 110^{o} and smaller than 70^{o}, instead of $\approx 120^{\mathrm{o}}$ and $\approx 60^{\mathrm{o}}$, respectively, which are approximately the expected values of θ for the transition from a SF+ to a SF-. This could indicate a systematic error in the reconstructed equilibrium of the null-point region due to an uncertainty of the plasma vertical position, but could also be attributed to the fact that $\theta = 60^{\mathrm{o}}$ and $\theta = 120^{\mathrm{o}}$ are not the exact values for the transitions between SF+ and SF-.

In conclusion, the measurements show that for the SF- configuration, power to one side of the SOL can be evenly distributed between two SPs depending on the values of σ and θ. Therefore, in configurations and scenarios with a significant asymmetry between the power distribution to the primary SPs on the LFS and HFS, the SF- permits a more even distribution of the exhaust power amongst three of the four SPs. Thereby, compared with the SF+ configuration, the SF- is better able to reduce the peak heat loads on the divertor targets.

4.5.5 The SOL width in the TCV SF

The SOL width is a parameter that affects the wetted area (equation 4.13) and therefore the peak heat loads on the divertor targets. To study the effects of the SF geometry on the SOL width, the target heat flux profile at the SP located on the LFS wall is mapped to the upstream using equation 4.6. This approach is chosen in order to remove the influence of local flux expansion and field line grazing angle at the target surface. To determine the upstream SOL width, $\Delta_{\mathrm{u}}^{\mathrm{LFS}}$, the heat flux profiles were fitted using an exponentially decaying functional form.

The upstream heat flux profiles of a SN ($\sigma = 1.5$) are similar to those of a SF ($\sigma = 0.15$), figure 4.16(a). Additionally, the values of Δ_u^{LFS} obtained from SF configurations with a range of σ remain approximately the same when σ is reduced, figure 4.16(b). The observed invariance of the SOL width is consistent with configuration changes being restricted to a small region in the immediate vicinity of the separatrix, section 4.3.2.

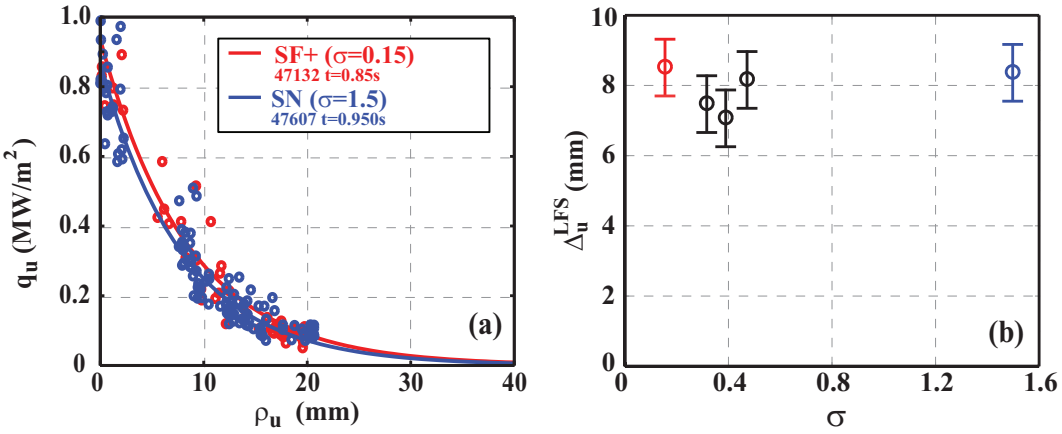

Figure 4.16: (a) Upstream heat flux profiles for $\sigma = 0.15$ and 1.5. (b) Dependence of the upstream SOL width on σ.

4.5.6 Evaluation of the proximity criteria

In section 4.1.4, the proximity criteria proposed in [175] were reviewed. These criteria express (*i*) the conditions for which a divertor may start to exhibit some SF-like features (equation 4.23), and (*ii*) when a SF may benefit from the onset of an enhanced convective cross-field transport in the null-point region (equation 4.25). In this section, these criteria will be calculated and compared with experimental observations.

To evaluate the proximity conditions specified by equations 4.23 and 4.25, σ_{crit} was evaluated by estimating the SOL width in the null-point region, Δ_{npt}. This was obtained by calculating the minimum distance of a field line labelled by ρ_u to the primary x-point and comparing it with the distance between the x-points d_{xpt}. In figure 4.17, the value of Δ_{npt}/a is plotted as a function of σ for two different values of the upstream SOL width, $\rho_u = \Delta_u = 4$ and 8 mm, where the latter correspond to the experimentally measured value of Δ_u^{LFS}. In the range of $\sigma \approx 0.7$, the distance between the x-points becomes comparable with the local SOL width for $\Delta_u = 8$ mm. This estimate of σ_{crit} agrees with the observed values of σ in which the secondary SP3 is active, figure 4.13.

Although the criterion $d_{xpt} < \Delta_{npt}$, equation 4.23, is related to the appearance of some SF geometrical features[175], namely larger flux expansion, connection length, divertor volume and magnetic shear in the pedestal region, it can also be interpreted as a condition for activating the secondary SPs in a SF+. When the exact SF is approached ($\sigma \to 0$),

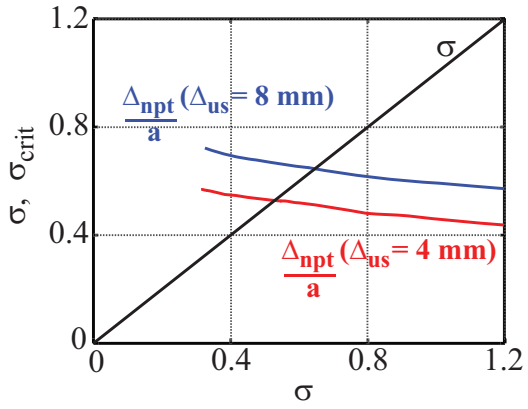

Figure 4.17: Evaluation of the condition $\sigma < \sigma_{\mathrm{crit}}\,(\Delta_{\mathrm{u}})$ for $\Delta_{\mathrm{u}} = 4$ and 8 mm.

the distance between the primary and secondary separatrices decreases in physical and in flux space. Consequently, a larger fraction of the exhausted power, transported across the primary separatrix due to conventional cross-field transport, should also cross the secondary separatrix and arrive at the secondary SPs.

One consequence of the proximity criterion given by equation 4.23 is that a smaller value of Δ_{u} decreases σ_{crit}, figure 4.17, implying that a smaller value of σ is required to activate SP3. To verify this prediction, the σ-scan shown in figure 4.13 was performed with 20% higher plasma current. According to [179], Δ_{u} in Ohmic L-mode plasmas is found to scale approximately as $I_{\mathrm{P}}^{-0.59}$. Therefore, Δ_{u} is expected to decrease with increasing plasma current leading to a decrease of σ_{crit}. This consequence of the criterion given by equation 4.23 is in agreement with the observed activation of SP3 at smaller values of σ_{crit} in plasmas with higher plasma current.

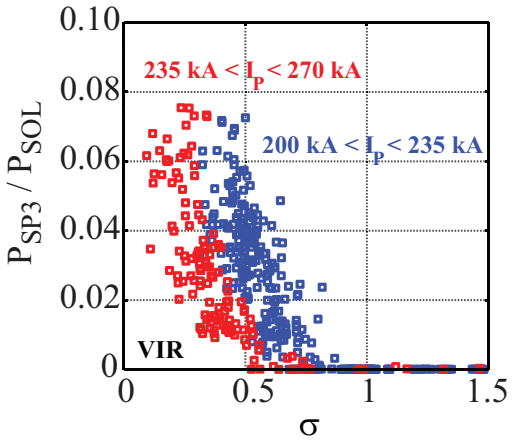

Figure 4.18: Dependence of the power deposited at SP3, normalized with P_{SOL}, in a SF+ configuration for two different intervals of plasma current. The power is estimated using IR thermography.

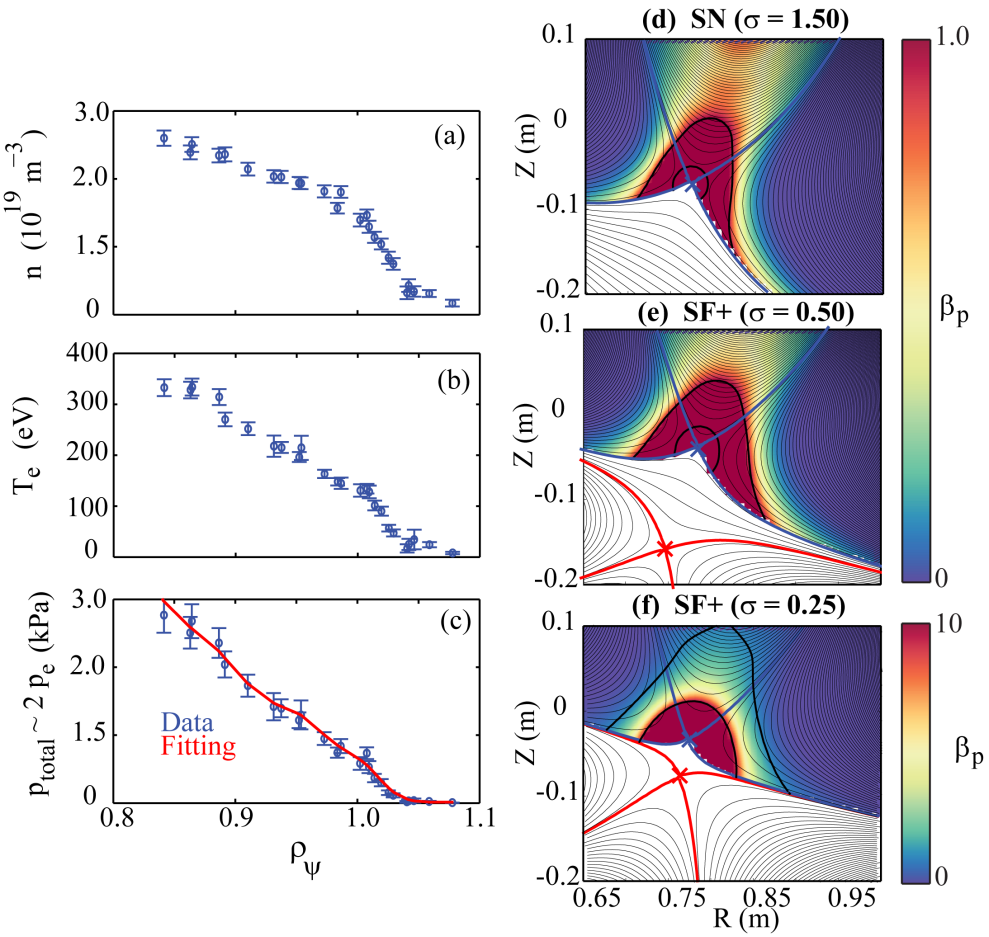

Figure 4.19: (a) Plasma density and (b) electron temperature used to calculate the (c) total plasma pressure $p_{\text{total}} = p_{\text{e}} + p_{\text{i}} \approx 2\,p_{\text{e}}$. Evaluation of β_{p} for configurations with (d) $\sigma = 1.5$, (e) $\sigma = 0.5$ and (f) $\sigma = 0.25$, using the spline fitting of the total plasma pressure profile (red line in (c)). The thin black lines in (d-f) are the contours of $\beta_{\text{p}} = 1$ and $\beta_{\text{p}} = 10$. Note that the color scale in (f) was changed for a better visualization.

The second criterion, related to the onset of a convective cross-field transport in the null-point region, will now be investigated. To estimate the size of the plasma convective cell, Thomson scattering data were used to estimate the total plasma pressure profile in the confined region and SOL, figure 4.19(a-c). The pressure measurements were mapped to the normalized flux coordinate $\rho_\psi \equiv \sqrt{\psi_{\text{N}}} = \sqrt{(\psi - \psi_0)\,/\,(\psi_{\text{b}} - \psi_0)}$, where ψ is the poloidal flux function, ψ_0 is the value of ψ at the magnetic axis and ψ_{b} the value at the plasma boundary. The pressure profile is then fitted from the plasma core up to the far SOL, figure 4.19(c). Using a 2D map of B_θ and assuming plasma pressure is constant along the flux tubes independently of the value of σ, the 2D map of β_{p} is estimated, figure 4.19(d-e). Although this procedure can only be expected to provide a rough estimate of the region where $\beta_{\text{p}} \gtrsim 10$, it shows that the size of the convective zone, here defined as the contour of $\beta_{\text{p}} = 10$, increases when the exact SF is approached ($\sigma \to 0$).

For the case $\sigma = 1.5$, the radius of the convective zone is approximately 2.5 cm. For the case $\sigma = 0.5$, the radius of the convective zone (approximately 3 cm) is still significantly smaller than the distance between the null-points ($d_{\mathrm{xpt}} \approx 10$ cm). As σ is further reduced to 0.25, the radius of the convective zone becomes approximately 6 cm. In this configuration, the radius of the convective zone is approximately 20% larger than the distance between the x-points ($d_{\mathrm{xpt}} \approx 5$ cm), fulfilling the criterion for the onset of an enhanced convective transport in the null-point region. The existence of such a convective zone would imply an increased power distribution to SP2 and SP3 for valued of $\sigma \lesssim 0.3$. However, the dependence of the ratio $P_{\mathrm{SP3}}/P_{\mathrm{SOL}}$ on the values of σ, figure 4.13, does not show a change in slope is this range. Another observation suggesting that this mechanism is not relevant for these plasma conditions is that the power arriving on the SP2 target remains negligible for all investigated values of σ. In conclusion, observations suggest that the cross-field transport mechanism proposed in [175] does not appear to be relevant in the investigated plasma conditions.

4.6 Effect of the Input Power on the Power Distribution

The mechanism hypothesized in [175] responsible for the onset of a convective cell in the null-point region of a SF does not seem to affect the power distribution to SP2 and SP3. Since the region of enhanced cross-field convection is expected to increase with $\beta_{\mathrm{p,u}}$, equation 4.25, the activation of SP2 and SP3 in discharges with higher $\beta_{\mathrm{p,u}}$ is expected to occur at larger values of σ compared with the low input power experiments. To further question the existence of this convective cell, a series of experiments with increased input power, P_{in}, were performed, increasing β_{p} at the upstream location.

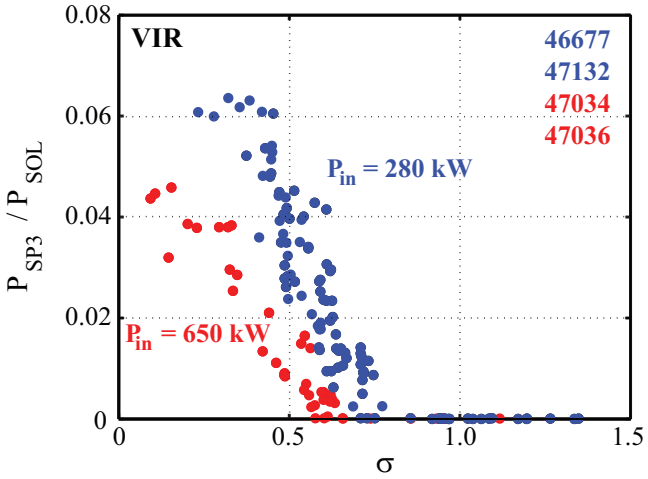

Figure 4.20: Dependence of the power deposited at SP3, normalized with P_{SOL}, on the total input power in a SF+ configuration. The power is estimated from IR thermography.

The input power was increased by a factor approximately 2, from $P_{\mathrm{Ohm}} \approx 280\,\mathrm{kW}$ to $P_{\mathrm{in}} = P_{\mathrm{Ohm}} + P_{\mathrm{EC}} \approx 650\,\mathrm{kW}$, leading to a plasma pressure and β_{p} increase at the upstream of about 50%. A somewhat larger σ_{crit} would be expected in these experiments. However, the total power arriving at SP3 for a certain value of σ is found to decrease, with respect to the low input power discharges, figure 4.20. This further supports the conclusion that the hypothesized convective cell in the null-region of a SF is not relevant in these plasma conditions.

The observed decrease of σ_{crit} can be explained by expecting Δ_{u} to decrease for larger values of P_{in} [179], since the temperature and the parallel heat conductivity in the near-SOL region increase. Using the first criterion ($d_{\mathrm{xpt}} < \Delta_{\mathrm{npt}}$), a decrease of Δ_{u} leads to a decrease of σ_{crit}, which explains the smaller value of σ_{crit} observed in the experiments with higher input power. In addition to a decrease of σ_{crit}, figure 4.20 also exhibits a decrease of the slope of the curve corresponding to the high input power case.

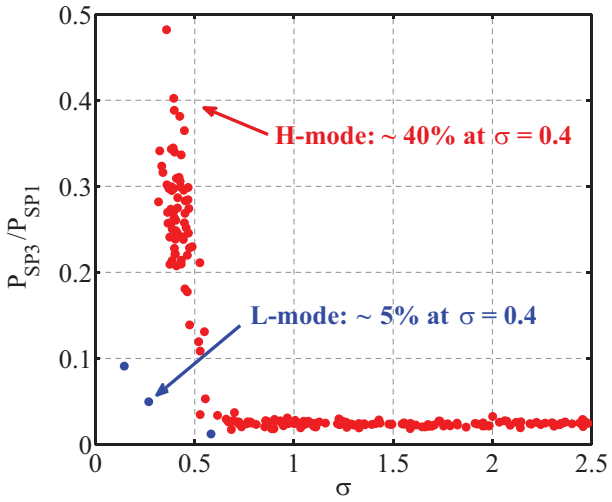

Figure 4.21: Dependence of the total power arriving at SP3, normalized with P_{SP1}, on σ during L-mode and H-mode discharges. The data corresponding to the H-mode discharge is taken at the ELM peak. Figure reproduced from [2].

Although a convective cell does not appear to be pertinent in these L-mode experiments, it could still explain the observed increased power distribution to SP3 during ELMs in H-mode discharges in TCV [2]. The measurements in SF+ configurations show an increased proportion of power to SP3 with decreasing σ, figure 4.21. For a given value of σ, the distribution to SP3 is significantly larger than in Ohmically heated L-mode discharges. However, this increased power distribution to SP3 during ELMs could equally well be explained by a transient change in the equilibrium during the ELM leading a HFS SF- configuration that directly connects SP3 to the SOL [2].

4.7 Effect of the Plasma Density on the Power Exhaust

For steady-state power handling to be possible in future fusion reactors, plasmas will have to operate in regimes with high radiation fractions [30, 31]. One of the potential advantages of the snowflake configuration is that its alleged increased divertor volume may help to achieve such a high fraction of radiation in the divertor. To investigate this, the effect of the plasma density on the target profiles, radiation fraction and power distribution amongst SPs was investigated and will be discussed in this section.

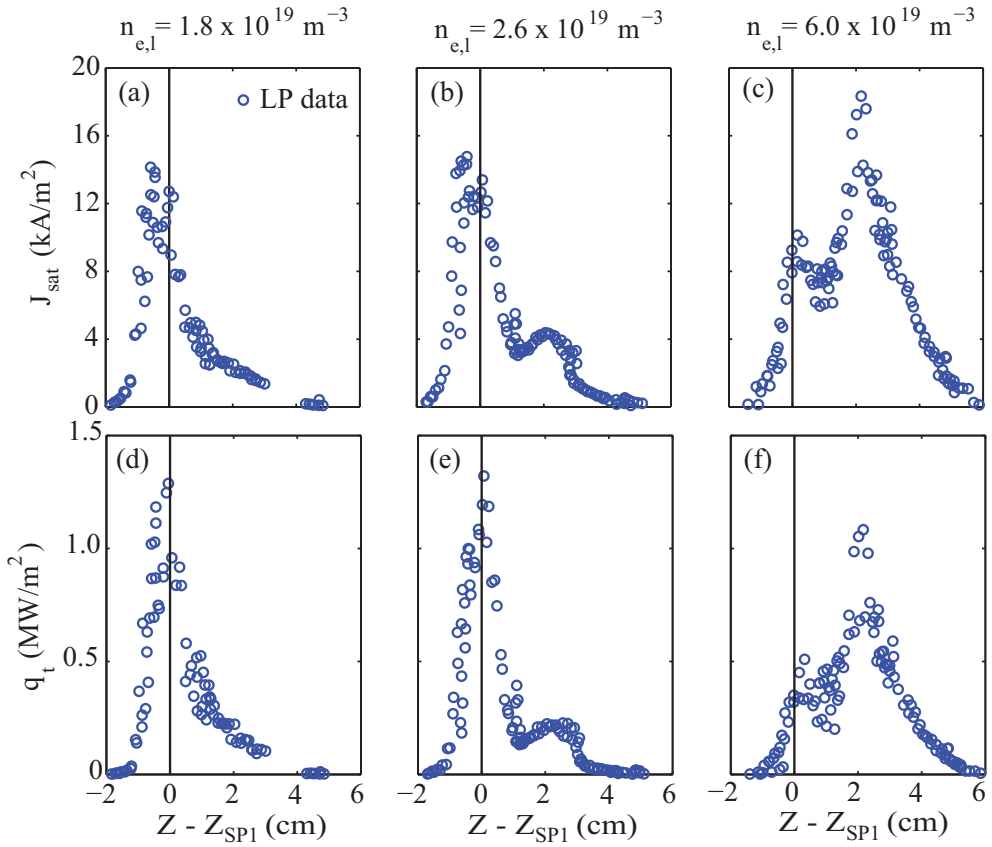

Figure 4.22: Ion saturation current J_{sat} measurements across the SP1 target from a discharge with $\sigma = 0.4$ and line averaged plasma density equal to (a) $n_{\mathrm{e,l}} \approx 1.8{\times}10^{19}$ m^{-3}, (b) $n_{\mathrm{e,l}} \approx 2.6{\times}10^{19}$ m^{-3} and (c) $n_{\mathrm{e,l}} \approx 6.0{\times}10^{19}$ m^{-3}. (d-f) are the heat flux profiles corresponding to the J_{sat} profiles shown in (a-c), respectively.

Discharges were performed where the plasma density was increased in steps of 250-300 ms duration. The values of the line averaged density investigated ranged from $n_{\mathrm{e,l}} \approx 2{\times}10^{19}$ m^{-3} to $10{\times}10^{19}$ m^{-3}. The experiments were carried out in Ohmicaly heated L-mode discharges in a SF+ configuration with $\sigma = 0.4$ and the measurements have been compared with those from a SN configuration. Langmuir probe measurements indicate that both primary strike points remain attached for the entire range of plasma densities.

While the target profiles at SP4 were not affected by increasing the plasma density, the measured target profiles at SP1 show a distinct plasma density dependence. The ion saturation current and the heat flux profiles at lower values of plasma density have a single-peak, figures 4.22(a) and (d), whereas for larger values, a second peak on the SOL side of SP1 appears. The amplitude of the second-peak increases with the plasma density, figures 4.22(b-c) and (e-f), and for plasma densities larger than $6{\times}10^{19}\,\mathrm{m}^{-3}$ the second exceeds the first peak. The amplitude of the second peak at SP1 also increases when σ decreases. As shown in figures 4.23(a) and (c), a single-peaked SP1 density profile in the SN configuration becomes double-peaked when σ decreases. Increasing the plasma density also influences electron temperature profile at SP1, becoming more peaked near the separatrix with lower temperature values in the far SOL compared with a SN configuration, figures 4.23(b) and (d). One possible candidate to explain these variations in the target profile shapes is the effect of the $\vec{E} \times \vec{B}$ particle drifts [158] that will be further discussed in section 4.9.

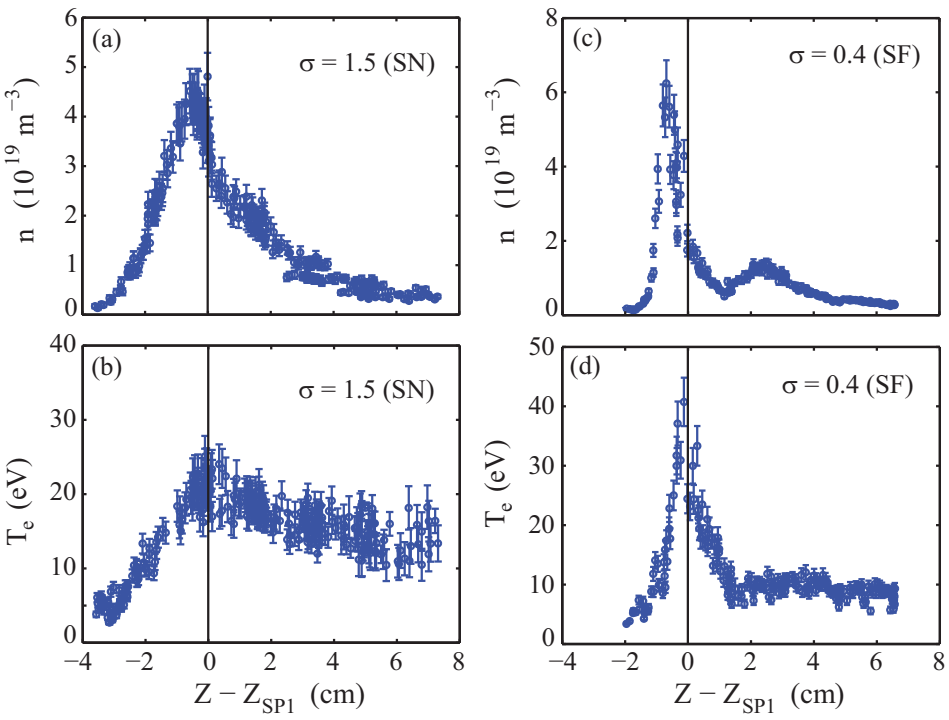

Figure 4.23: Electron density and temperature target profiles for (a,b) a SN and (c,d) a SF+ configuration both with $n_{\mathrm{e,l}} \approx 3{\times}10^{19}\ \mathrm{m}^{-3}$.

Concerning the effects of the plasma density on the fraction of the radiated power, the experiments show that increasing the plasma density from $n_{\mathrm{e,l}} \approx 2{\times}10^{19}\,\mathrm{m}^{-3}$ to $10{\times}10^{19}\,\mathrm{m}^{-3}$ leads to an increase in the radiated power, P_{rad}, from approximately 35% to 60% of the Ohmic power, P_{Ohm}, figure 4.24(a). In both SN and SF configurations, the dependencies of $P_{\mathrm{rad}}/P_{\mathrm{Ohm}}$ on the plasma density are similar. However, the measurements suggest that at higher plasma densities the SN configuration radiates about 10% more

power than the SF. Although this observation is opposite to the expected behaviour of a SF divertor, it is consistent with the fact that in TCV the SOL volume in a SN is slightly larger than that in a SF configuration.

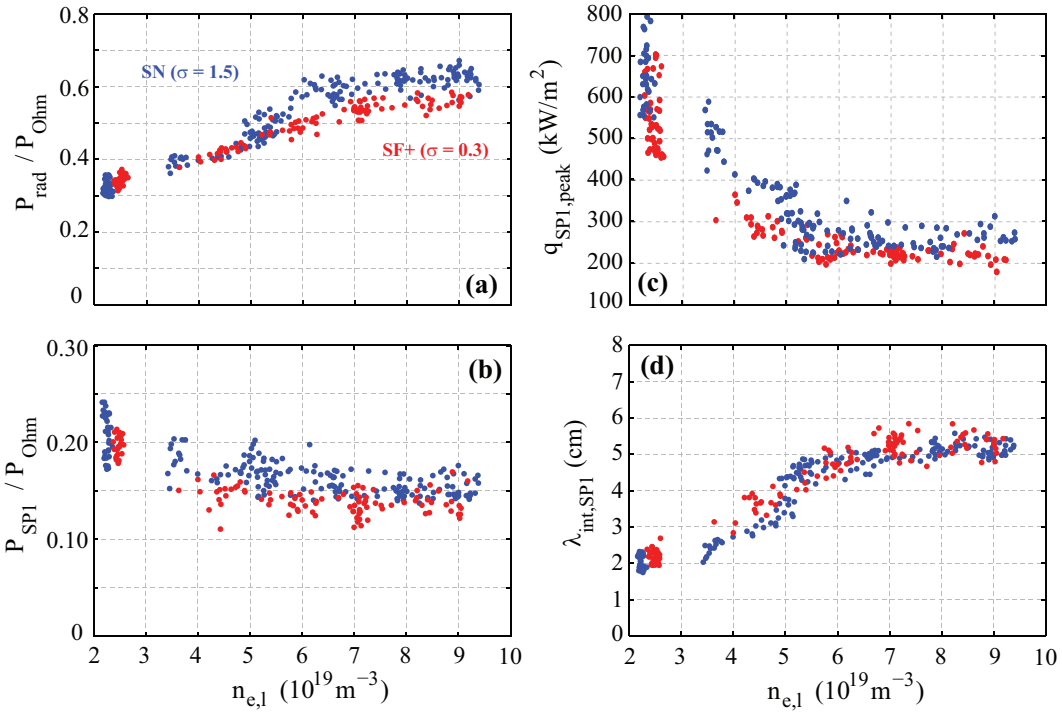

Figure 4.24: Dependence of (a) the power load fraction at the primary HFS strike point $P_{\mathrm{SP1}}/P_{\mathrm{Ohm}}$, (b) the maximum heat flux at that strike point $q_{\mathrm{SP1,peak}}$, and (c) the corresponding target heat flux scale length $\lambda_{\mathrm{int,SP1}}$ in SF and SN configurations on the line averaged density $n_{\mathrm{e,l}}$.

Since the value of $P_{\mathrm{rad}}/P_{\mathrm{Ohm}}$ increases with $n_{\mathrm{e,l}}$, the fraction of the Ohmic power expected to be exhausted on the SPs has to decrease. The IR measurements of the heat flux at SP1 indicate only a weak decrease of $P_{\mathrm{SP1}}/P_{\mathrm{Ohm}}$ with increasing $n_{\mathrm{e,l}}$ in both SN and SF configurations, figure 4.24(b). The power at SP1 is generally somewhat lower in the SF than in the SN configuration. The same behaviour is also seen in the Langmuir probe measurements, figure 4.25. This figure also shows that the power distribution to SP2 and SP3 decreases with increasing plasma density. This observation will be further discussed in section 4.9. Note that for $n_{\mathrm{e,l}} \lesssim 6{\times}10^{19}\,\mathrm{m}^{-3}$, a deficit of power is observed while for $n_{\mathrm{e,l}} \gtrsim 6{\times}10^{19}\,\mathrm{m}^{-3}$, an excess of power is measured. This issue of the power balance was not solved within the time of this thesis and it clearly merits further investigation since it is required to test the effectiveness of new divertor configurations.

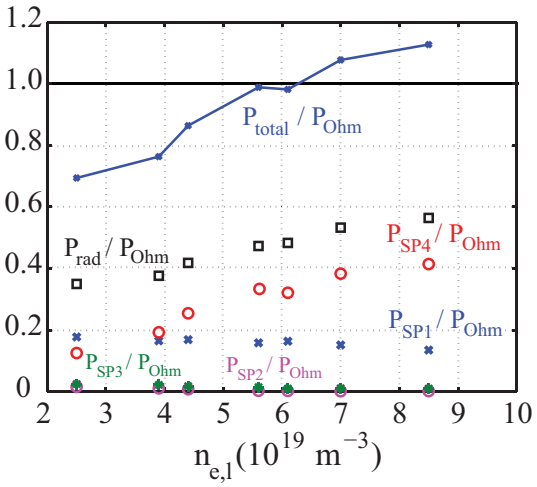

Figure 4.25: Dependence of the fraction of the input power distributed among the SPs from 1 up to 4, and radiated in a SF+ configuration with $\sigma = 0.35$ and forward B_ϕ. The blue line corresponds to the total measured power with respect to the total input power.

To characterize the dependence of the double-peaked heat flux profiles on plasma density, they were parametrized by two quantities: their peak value, q_{peak}, and an effective fall-off length, λ_{int}, defined as

$$\lambda_{\mathrm{int}} = \frac{\int (q_{\mathrm{peak}} - q_{\mathrm{BG}})\, ds_{\mathrm{t}}}{q_{\mathrm{peak}} - q_{\mathrm{BG}}}. \tag{4.27}$$

In this equation, s_{t} is a coordinate along the divertor target surface and q_{BG} a background heat flux caused by absorption of the radiated power, neutral particle flux and reflections within the optical system as well as on the tile surface.

As shown in figure 4.24(c), the peak heat flux on the SP1 target, $q_{\mathrm{SP1,peak}}$, in both the SN and SF configurations decreases with $n_{\mathrm{e,l}}$. Since the fraction of power at SP1 has only a weak dependence on $n_{\mathrm{e,l}}$, $\lambda_{\mathrm{int,SP1}}$ increases with $n_{\mathrm{e,l}}$, figure 4.24(d). For $n_{\mathrm{e,l}} \gtrsim 6{\times}10^{19}\,\mathrm{m}^{-3}$, the profiles cease to change with the plasma density. As will be further discussed in section 4.8.4, these features can be partially reproduced in simulations of the TCV SF divertor.

At low plasma densities ($n_{\mathrm{e,l}} \approx 2.4{\times}10^{19}\,\mathrm{m}^{-3}$), the spatial distribution of the radiated power in the SF differs from the distribution in the SN configuration, figure 4.26(a-b). The radiating zone in the SN configuration is more localized in front of the SP1 target than in the SF configuration. At higher plasma densities ($n_{\mathrm{e,l}} \approx 9.5{\times}10^{19}\,\mathrm{m}^{-3}$), the radiating zone in the SN configuration is slightly reduced compared with the low density case, figure 4.26(c). However, a strong reduction of the radiating zone is observed in the

SF, figure 4.26(d), with most of the power being radiated in the null-point region and in the vicinity of the SP1 plasma leg, figure 4.26(d). The peak of the radiation density at higher values of plasma density is found to be above the primary x-point, i.e. in the confined region.

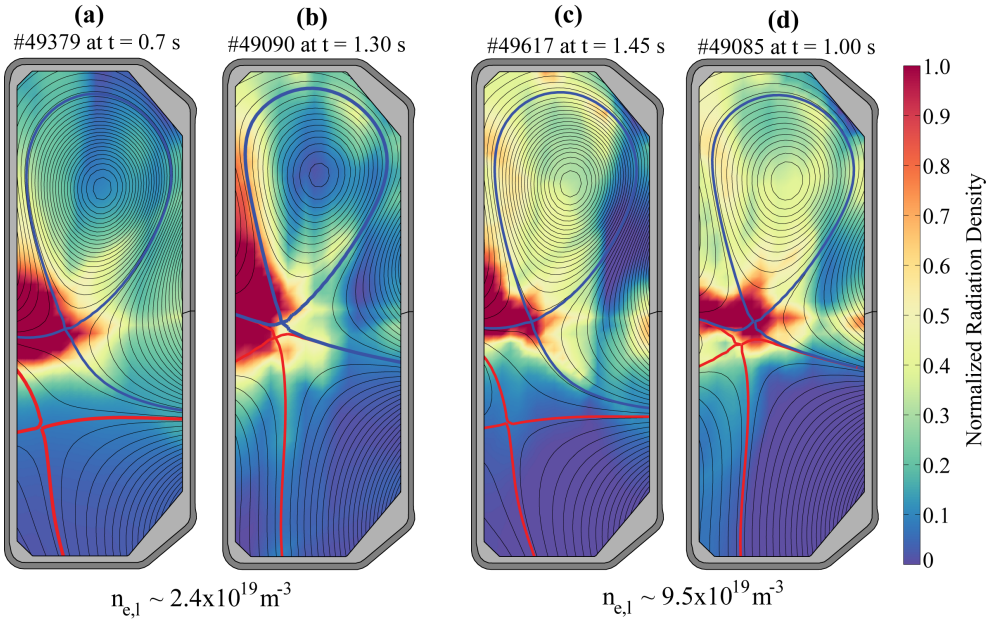

Figure 4.26: Dependence of the normalized radiation density at (a,b) low density and (c,d) high plasma density in the SN and SF configurations. The radiated power is estimated using the BOLO diagnostic.

4.8 The Simulations of the TCV Snowflake Divertor

To provide some insight into the underlying physics of the plasma transport in the SOL of a SF divertor, the experimental measurements were interpreted using modeling. This section will present numerical simulations of the plasma and neutral particles transport in the SOL of a series of TCV snowflake equilibria with a range of separations between the primary and the secondary x-points for a range of input powers and plasma densities.

After a brief description of the EMC3-Eirene model in section 4.8.1, the data will be presented as follows: in section 4.8.2, the results from the σ-scan simulations with spatially constant and varying cross-field diffusion coefficients are discussed. Section 4.8.3 presents the results from the simulations using different values of the input power and in section 4.8.4 simulations with different plasma densities are discussed.

4.8.1 The EMC3-Eirene code

The edge Monte Carlo 3D (EMC3) code [180, 181, 182, 183] is a steady state model for the edge plasma transport based on a fluid approach. In the EMC3 code, the fluid (Braginskii's [184]) equations are solved by a Monte Carlo technique in real space using a field-aligned local orthogonal vector basis [181, 180], which reduces the diffusion tensor into a diagonal form [182]. Although a Monte Carlo principle is applied to solve the equations numerically, EMC3 describes the plasma edge using a fluid approach. The dynamics of the neutral particle production and transport are modeled using the Eirene code [185, 186] and are treated with a kinetic approach, where the Fokker-Planck equation [145] is solved and coupled self-consistently with the EMC3 plasma simulations.

The motivation for using a 3D code to model a toroidally symmetric configuration, such as the SF divertor, is purely technical, namely a considerably simpler computational grid construction. Many 2D codes require a computational grid aligned with the magnetic flux surfaces in the poloidal plane. This requirement significantly increases the complexity for the SF configuration because of the increased number of zones, figure 4.27. The advantage of a 3D code, like EMC3, is that it only requires alignment of the computational grid with the magnetic field, considerably decreasing the complexity in building such a grid.

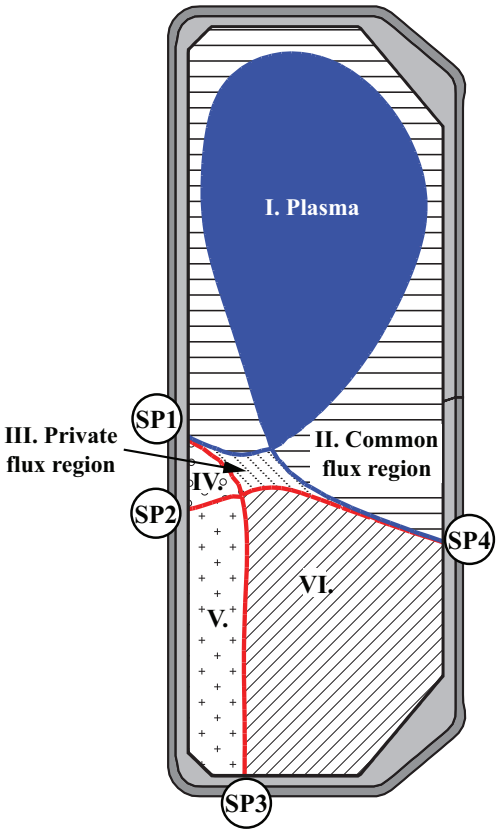

Figure 4.27: Schematic drawing showing six different zones of a snowflake configuration.

The validity of the fluid approach

Two approaches are widely used for modeling the plasma transport in the SOL: the kinetic and the fluid approach. In the kinetic approach, the velocity distribution function $f_\alpha(\vec{r}, \vec{v}, t)$ is calculated for each particle species α, for each time and at every point in real and velocity space, using the Fokker-Planck equation [145],

$$\frac{\partial f_\alpha}{\partial t} + \vec{v} \cdot \vec{\nabla} f_\alpha + \vec{a} \cdot \vec{\nabla}_\mathrm{v} f_\alpha = \sum_\beta C_{\alpha\beta}(f_\alpha, f_\beta). \tag{4.28}$$

Here, $\vec{a}$ is the acceleration of the charged particles due to the presence of electromagnetic fields and $C_{\alpha\beta}(f_\alpha, f_\beta)$ describes the change of the velocity distribution function for particles of species α due to collisions with particles of species β. In the fluid approach, only the moments of the distribution function $f_\alpha(\vec{r}, \vec{v}, t)$ are calculated, thus providing some macroscopic quantities that characterize the fluid at each point in space and time, e.g. the average fluid velocity

$$\vec{u}_\alpha(\vec{r}, t) \equiv \frac{1}{n} \int \vec{v}\, f_\alpha(\vec{r}, \vec{v}, t)\, d^3v\,. \tag{4.29}$$

The moments of equation 4.28 then provide the fluid transport equations that governs the evolution of macroscopic fluid quantities. Taking the moments of equation 4.28 leads to the well known closure problem: the time evolution of each fluid quantity depends on the next higher order fluid quantity, leading to an infinite hierarchy of moments for equation 4.28. To achieve the closure, a postulate must be made for the higher order term in the highest order fluid equation. This usually becomes an assumption on the heat flux $\vec{q}$. The derivation of the fluid equations is beyond the scope of this thesis and a review of such a derivation can be found in [145, 15]. Obviously, the kinetic approach is more complex than the fluid approach since equation 4.28 is solved self-consistently for all particle species, leading to a set of coupled non-linear integral-differential equations in seven dimensions $(x, y, z, v_\mathrm{x}, v_\mathrm{y}, v_\mathrm{z}, t)$. For this reason, the fluid approach is the more widely used.

One also needs to determine under which conditions the SOL plasma can be modeled with a fluid approach. The fluid approximation is found likely to be appropriate when the SOL collisionality $\nu^*_\mathrm{SOL} \equiv L/\lambda$ is sufficiently large, typically $\nu^*_\mathrm{SOL} \gtrsim 10$ [15]. Here, L can be either the connection length $L_{||}$ or the typical scale length of the parallel gradients of the plasma density or temperature, while λ can be either the self-collisionality length (mean free path) for electrons λ_ee or ions λ_ii. This condition for the validity of a fluid

approach states that the electron and ion mean free paths, given by

$$\lambda_{\mathrm{ee}}[\mathrm{m}] \approx 10^{16}\,\frac{T_{\mathrm{e,u}}[\mathrm{eV}]^2}{n_{\mathrm{u}}[\mathrm{m}^{-3}]} \qquad \text{and} \qquad \lambda_{\mathrm{ii}}[\mathrm{m}] \approx 10^{16}\,\frac{T_{\mathrm{i,u}}[\mathrm{eV}]^2}{n_{\mathrm{u}}[\mathrm{m}^{-3}]} \tag{4.30}$$

must be small compared to other characteristic lengths in the SOL. Typical average values of the plasma parameters from the experiments carried out during this thesis are shown in table 4.1. One can see that a fluid approach is expected to provide a reasonable approximation of the SOL plasma transport in the conditions encountered during this work though the validity of the fluid approach becomes marginal for the low density case.

Parameter	Low Density	High Density
$T_{\mathrm{e,u}}$ (eV)	80	40
n_{u} (m^{-3})	2.5×10^{19}	1.0×10^{20}
λ_{ee} (m)	0.6	0.04
$L_{\|\|}$ (m)	25	25
ν^*_{SOL}	10	156

Table 4.1: Typical average values of the physical parameters for the SOL plasma conditions encountered in this thesis.

The EMC3-Eirene model

In the EMC3 model, the particle conservation equations of the plasma fluid are obtained by summing the particle conservation equations of each plasma species. The model is based on the assumptions of quasi-neutrality ($\sum q_{\mathrm{j}}\, n_{\mathrm{j}} = -q_{\mathrm{e}}\, n_{\mathrm{e}} = e\, n$) and ambipolar plasma flow ($u_{\mathrm{e},||} = u_{\mathrm{i},||} = u_{||}$). Introducing the anomalous cross-field particle transport coefficient, $D_\perp$, the plasma particle conservation equation becomes

$$\vec{\nabla} \cdot \left[n\, \vec{u}_{||} - D_\perp\, \vec{\nabla}_\perp n \right] = S_{\mathrm{p}}\,, \tag{4.31}$$

where S_{p} is the plasma particle source/sink due to the ionization of neutrals and charge exchange. The subindexes $||$ and $\perp$ refer to the parallel and perpendicular directions with respect to the magnetic field.

The EMC3 equation of the plasma parallel momentum is obtained by summing the momentum equations of each plasma species. The assumption of ambipolar flow implies that all the terms multiplied by m_{e} may be neglected, since it reflects the fact the $m_{\mathrm{e}} << m_{\mathrm{i}}$. In addition, the contribution of the electric field in the ion and electron

momentum equations cancel since quasi-neutrality holds. Introducing the anomalous cross-field parallel momentum transport coefficient (viscosity) for the ions, $\eta_{\mathrm{i},\perp} = m_{\mathrm{i}} n D_\perp$, the EMC3 parallel momentum equation of the plasma becomes

$$\vec{\nabla} \cdot \left[n\, m_{\mathrm{i}}\, u_{||}\, \vec{u}_{||} - \eta_{\mathrm{i},||}\, \vec{\nabla}_{||} u_{||} - D_\perp \vec{\nabla}_\perp \left(n\, m_{\mathrm{i}}\, u_{||} \right) \right] = -\nabla_{||} p + S_{\mathrm{m}}. \tag{4.32}$$

In this equation, $\eta_{\mathrm{i},||}$ is the classical ion parallel fluid viscosity, $p = n k_{\mathrm{B}} (T_{\mathrm{e}} + T_{\mathrm{i}})$ the total fluid thermal pressure and S_{m} represents a source/sink of parallel momentum due to ion-neutral friction, ionization and charge exchange.

To calculate the electron and ion temperature profiles, EMC3 uses their respective energy conservation equations. Closure of the fluid equations is achieved by assuming that the heat flux of each plasma particle species, $\vec{q}_\alpha$, can be modeled by a conductive process as

$$\vec{q}_\alpha = -\kappa_{\alpha,||}\, \vec{\nabla}_{||} T_\alpha - n\, \chi_{\alpha,\perp}\, k_{\mathrm{B}}\, \vec{\nabla}_\perp T_\alpha. \tag{4.33}$$

Here, $\kappa_{\alpha,||}$ and $\chi_{\alpha,\perp}$ are the classical parallel heat conductivity and the anomalous cross-field heat diffusivity of the species α, respectively. The latter has the same units as the particle transport coefficient D and the same order of magnitude as $D_\perp$. Using this closure in the electron and ion energy conservation equations, the EMC3 equations for calculating the electron and ion temperature profiles are

$$\vec{\nabla} \cdot \left[\frac{5}{2} p_{\mathrm{e}} \vec{u}_{||} - \kappa_{\mathrm{e},||} \vec{\nabla}_{||} T_{\mathrm{e}} - \frac{5}{2} k_{\mathrm{B}}\, T_{\mathrm{e}}\, D_\perp \vec{\nabla}_\perp n - n\, k_{\mathrm{B}}\, \chi_{\mathrm{e},\perp} \vec{\nabla}_\perp T_{\mathrm{e}} \right] = -Q_{\mathrm{eq}} + S_{\mathrm{ee}} \tag{4.34}$$

and

$$\vec{\nabla} \cdot \left[\frac{5}{2} p_{\mathrm{i}} \vec{u}_{||} - \kappa_{\mathrm{i},||} \vec{\nabla}_{||} T_{\mathrm{i}} - \frac{5}{2} k_{\mathrm{B}}\, T_{\mathrm{i}}\, D_\perp \vec{\nabla}_\perp n - n\, k_{\mathrm{B}}\, \chi_{\mathrm{i},\perp} \vec{\nabla}_\perp T_{\mathrm{i}} \right] = Q_{\mathrm{eq}} + S_{\mathrm{ei}}\,. \tag{4.35}$$

In these equations, S_{ee} and S_{ei} are the source/sink of energy for electrons and ions, respectively, due to the ionization of neutrals and charge exchange, while $Q_{\mathrm{eq}} = \frac{3 m_{\mathrm{e}}}{m_{\mathrm{i}}} (p_{\mathrm{e}} - p_{\mathrm{i}})\, \nu_{\mathrm{ei}}$ represent the thermal equipartition between the electron and ion fluid.

The EMC3 code also allows for the presence of impurities in the plasma. Since impurities and the main plasma ions have similar masses (contrasted with m_e), the EMC3 model of the transport of impurities assumes a local temperature of the impurities at each ionization stage, z, equal to the local ion temperature ($T_\mathrm{z} = T_\mathrm{i}$). For this reason, only the particle and parallel momentum conservation equations need to be solved for the impurities. The particle conservation equation for the impurities in the ionization stage z is given by

$$\vec{\nabla} \cdot \left[n_\mathrm{z} \, \vec{u}_{||,\mathrm{z}} - D_{\perp,\mathrm{z}} \, \vec{\nabla}_\perp n_\mathrm{z} \right] = S_{\mathrm{z}-1\to\mathrm{z}} + R_{\mathrm{z}+1\to\mathrm{z}} - S_{\mathrm{z}\to\mathrm{z}+1} - R_{\mathrm{z}\to\mathrm{z}-1} \,, \tag{4.36}$$

where $S_{\mathrm{z}-1\to\mathrm{z}}$, $S_{\mathrm{z}\to\mathrm{z}+1}$, $R_{\mathrm{z}+1\to\mathrm{z}}$ and $R_{\mathrm{z}\to\mathrm{z}-1}$ are source/sink terms representing ionization (S) and recombination (R) processes, respectively. The parallel momentum conservation equation of the impurity particles in the ionization stage z is given by

$$-\nabla_{||} p_\mathrm{z} + \mu_{\mathrm{z,i}} \, n_\mathrm{z} \left(u_{||} - u_{||,\mathrm{z}} \right) \nu_{\mathrm{z,i}} + Z \, n_\mathrm{z} \, e \, E_{||} + \alpha_{\mathrm{z,e}} \, n_\mathrm{z} \, k_\mathrm{B} \, \nabla_{||} T_\mathrm{e} + \alpha_{\mathrm{z,i}} \, n_\mathrm{z} \, k_\mathrm{B} \, \nabla_{||} T_\mathrm{i} = 0 \,, \tag{4.37}$$

where $\mu_{\mathrm{z,i}}$ is the reduced mass between the impurity and the main plasma ions, $\alpha_{\mathrm{z,e}}$ and $\alpha_{\mathrm{z,i}}$ are constant factors that represent the effect of thermal forces on the impurities from interactions with the electron and ion fluids, respectively, $\nu_{\mathrm{z,i}}$ is the collision frequency between the impurity and the main plasma ion species, and the parallel electric field $E_{||}$ is obtained from the electron parallel momentum balance, where terms containing the electron mass have been neglected,

$$e E_{||} = -\frac{1}{n} \nabla_{||} p_\mathrm{e} - \alpha_{\mathrm{i,e}} \, k_\mathrm{B} \, \nabla_{||} T_\mathrm{e} \,. \tag{4.38}$$

To calculate the source/sink terms S_p, S_m, S_ee, S_ei, $S_{\mathrm{z}-1\to\mathrm{z}}$, $S_{\mathrm{z}\to\mathrm{z}+1}$, $R_{\mathrm{z}+1\to\mathrm{z}}$ and $R_{\mathrm{z}\to\mathrm{z}-1}$, the EMC3 code is coupled with the Eirene code. The codes are coupled iteratively to generate a self-consistent solution of the interaction between the plasma and the neutral particles. In a very general way, the coupling between the codes works as follows: (*i*) EMC3 first calculates the plasma density, n, and parallel fluid velocity, $u_{||}$, profiles. Since the source terms are not yet calculated, one initially assumes that the plasma is isothermal ($T_\mathrm{e} = T_\mathrm{i} = T$ everywhere) and without interaction with neutrals, implying that all the source terms are equal to zero; (*ii*) the resulting n, $u_{||}$, T_e and T_i profiles are then passed to the Eirene code that calculates a first estimation of the source terms; (*iii*) the initial assumptions are then removed and these source terms are sent back to the EMC3 code to calculate updated plasma kinetic profiles; (*iv*) this procedure is repeated

until a reasonable convergence of the profiles is achieved. Convergence is evaluated by comparing plasma and neutrals parameters between iterations. Iteration changes are usually required to be smaller than a few percent, typical of the noise associated with the Monte Carlo technique. Note that the EMC3-Eirene code neither takes into account volumetric recombination nor particle drifts. The validity of these assumptions will be further discussed later in this section and in section 4.9, respectively.

The computational grid

The advantage of using a field aligned computational grid comes from the numerical technique used to separate parallel and perpendicular transport, which minimizes the numerically induced cross-field diffusion due to cumulative errors in the magnetic field line tracing. The induced error may be estimated by the ratio between the "radial extent" of a magnetic flux surface after following a field line for a certain number of toroidal turns, $\Delta\rho$, and the corresponding length followed in the parallel direction, $\delta L_{||}$, which must be much larger than the typical values of connection length. Using the 4^{th} order Runge-Kutta method for tracing a magnetic field line, this ratio can be reduced to approximately $\Delta\rho/\delta L_{||} \approx 1 \times 10^{-10}$, while acceptable values were found empirically to be about $\Delta\rho/\delta L_{||} \approx 1 \times 10^{-6}$. These numbers much smaller than unity mean that the Monte Carlo particles will have enough time to diffuse across the magnetic field in the physical sense before experiencing a numerically induced cross-field diffusion. The generation of such a 3D grid, may be described in some basic steps:

1. the toroidal range of the simulation domain, $\Delta\phi_{\text{sim}}$, has to be defined. In this work, it is chosen to be $\Delta\phi_{\text{sim}} = 20^{\text{o}}$, i.e. 1/18 of the full torus circumference. This value was chosen in order to obtain a faster convergence of the results;
2. the simulation domain has to be divided into N_{z}+1 toroidal locations separated by $\Delta\phi = \Delta\phi_{\text{sim}}/N_{\text{z}}$ degrees;
3. a 2D "base grid" in the poloidal plane of a specified toroidal location is first prepared. In the base grid, the inner and outer simulation boundaries, the divertor target surfaces and the "radial" and "poloidal" grid points for each individual zone are defined. The base grid has, for each zone, a "radial" resolution defined by the number of "radial surfaces", N_{r}, and a "poloidal" resolution defined by the number of points in the "poloidal" direction, N_{p};
4. finally, the 3D grid is created by tracing the magnetic field lines from each grid point in the base grid to the last toroidal location with grid points being the intersection points of the field lines with the poloidal planes at each toroidal location.

As an example, a base grid for a SF+ configuration with $\sigma = 0.5$ is shown in figure 4.28, where the confinement and SOL regions, both, are aligned with the magnetic flux surfaces,

while the private flux region, including the complicated structures around the secondary x-point and the secondary separatrix, are covered by a single regular grid.

To verify that the grid resolution is sufficient, a simulation with $N_r = 40$ "radial surfaces" was compared with a simulation where the radial resolution was doubled. The particle and heat fluxes at the targets agreed to within a few percents, which is a typical Monte Carlo noise between iterations. Furthermore, the divertor target plates (inner wall of TCV) were moved a few centimeters inward for technical reasons, in particular on the LFS and on the floor, as indicated in figure 4.28. Extending the computational domain of the equilibrium would solve this issue but as the shift is of the order of only 10% of the divertor leg length, the simulated geometry is considered sufficiently close to the actual geometry.

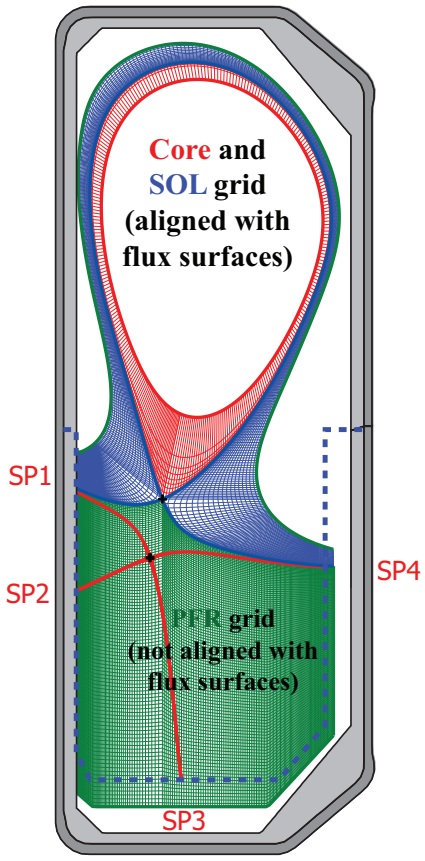

Figure 4.28: Base grid created for the EMC3-Eirene simulations. The red and green thick lines correspond to the inner and outer simulation boundaries. The blue thick line corresponds to the separatrix and the dashed blue thick line corresponds to the prescribed divertor target surface.

Effect of volume recombination

The present version of the EMC3 code does not account for volumetric recombination. To examine the validity of this assumption, the total number of recombination processes is calculated and compared with the total recycling flow. According to [187], the recombination process

$$e \; + \; H^{+} \; \longrightarrow \; H\,(k) \; + \; h\nu \tag{4.39}$$

has a rate coefficient $\langle \sigma_{\rm rec}\, v \rangle$ that is given by

$$\langle \sigma_{\rm rec}\, v \rangle\,(k, \ell, T_{\rm e}) = 1 \times 10^{-20}\, A_{{\rm k},\ell} \left(\frac{I_{\rm k}}{R_{\rm y}} \right)^{1/2} \frac{\beta_{\rm k}^{3/2}}{\beta_{\rm k} + \chi_{{\rm k},\ell}}, \tag{4.40}$$

where k is the principal quantum number of the final state of the captured electron, $I_{\rm k} = 13.6/k^2$ eV is the ionization potential of the electron in the state defined by k, $R_{\rm y} = 13.6$ eV is the Rydberg constant, $\beta_{\rm k} \equiv I_{\rm k}\,/\,T_{\rm e}$, with $T_{\rm e}$ being the electron plasma temperature (expressed in eV), and the values of the constants $A_{{\rm k},\ell}$ and $\chi_{{\rm k},\ell}$ are given in table 4.2.

$A_{1,{\rm s}} = 3.92$	$A_{2,{\rm s}} = 2.47$	$A_{2,{\rm p}} = 6.22$
$\chi_{1,{\rm s}} = 0.35$	$\chi_{2,{\rm s}} = 0.12$	$\chi_{2,{\rm p}} = 0.61$

Table 4.2: Typical values of the physical parameters $A_{{\rm k},\ell}$ and $\chi_{{\rm k},\ell}$ for k and $\ell = 1$ and 2.

Using the recombination rate from 4.40 and the plasma density and electron temperature profiles calculated by EMC3-Eirene, the total number of recombination processes, for a particular simulation, is estimated to be

$$\left. \frac{dN}{dt} \right|_{\rm rec} = \int \; n^2 \; \langle \sigma_{\rm rec}\, v \rangle\,(k, \ell, T_{\rm e}) \; dV \approx 9.8 \times 10^{18} \;\; {\rm s}^{-1}. \tag{4.41}$$

This is about three orders of magnitude lower than the total recycling flow $\Gamma_{\rm recycling} \approx 8.6 \times 10^{21}$ s^{-1}. Therefore, unless other effects contribute to the increase of the number of recombination process dramatically, e.g. molecule assisted recombination, dielectronic recombination or divertor cooling due to impurity radiation, it is well justified to neglect volume recombination as a plasma sink.

4.8.2 Effect of σ on the power distribution

To understand the physical mechanism behind the activation of SP3 when σ decreases, a series of SF equilibria with a range of σ were used to model the plasma transport in the SOL using the EMC3-Eirene code. After constructing a computational grid based on the equilibrium plasma profiles of the TCV discharge #43418, the input parameters of the code had to be defined. In these simulations, the boundary conditions on the energy conservation equations were imposed by setting the input power that crosses the inner simulation boundary to be the same as in the experiment, $P_{\text{in}} = 238\,\text{kW}$, assuming an equal distribution between the electrons and ions. The boundary condition on the particle conservation equation is imposed by fixing the plasma density at the most inner simulation boundary to be constant. This value is then changed until the plasma density at a point in the separatrix, farthest away from the primary x-point, reaches $n = 2.5 \times 10^{19}$ m^{-3}, corresponding to the value measured by the Thomson scattering diagnostic for discharge #43418. This procedure was chosen because the plasma density is not constant on the flux surfaces in the vicinity of the separatrix as it will be discussed later in this section.

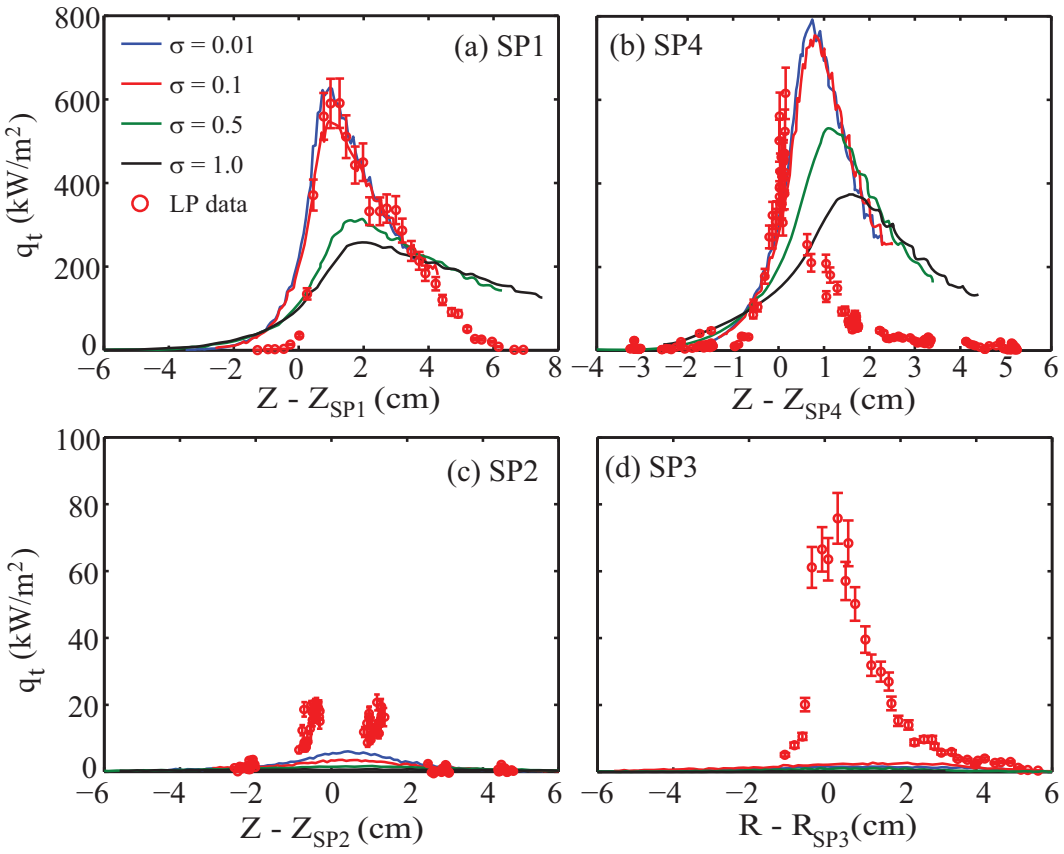

Figure 4.29: Target heat flux profiles from the simulations with $\sigma = 0.01$, 0.10, 0.50 and 1.00. The lines correspond to the simulations while the data points represent Langmuir probes measurements for the $\sigma = 0.1$ SF configuration.

The transport coefficients were adjusted to $D_\perp = \chi_{e,\perp} = \chi_{i,\perp} = 0.6\ \mathrm{m}^2/\mathrm{s}$ in order to match the heat flux profile at SP1 measured with the LPs. The simulations were performed for the SF+ configurations with $\sigma = 0.01$, 0.10, 0.50 and 1.00 presented in section 4.3. In figure 4.29, the experimental and simulated target heat flux profiles, q_t, at the four SPs are shown. The experimental data points should be compared with the simulation of the SF configuration with $\sigma = 0.1$.

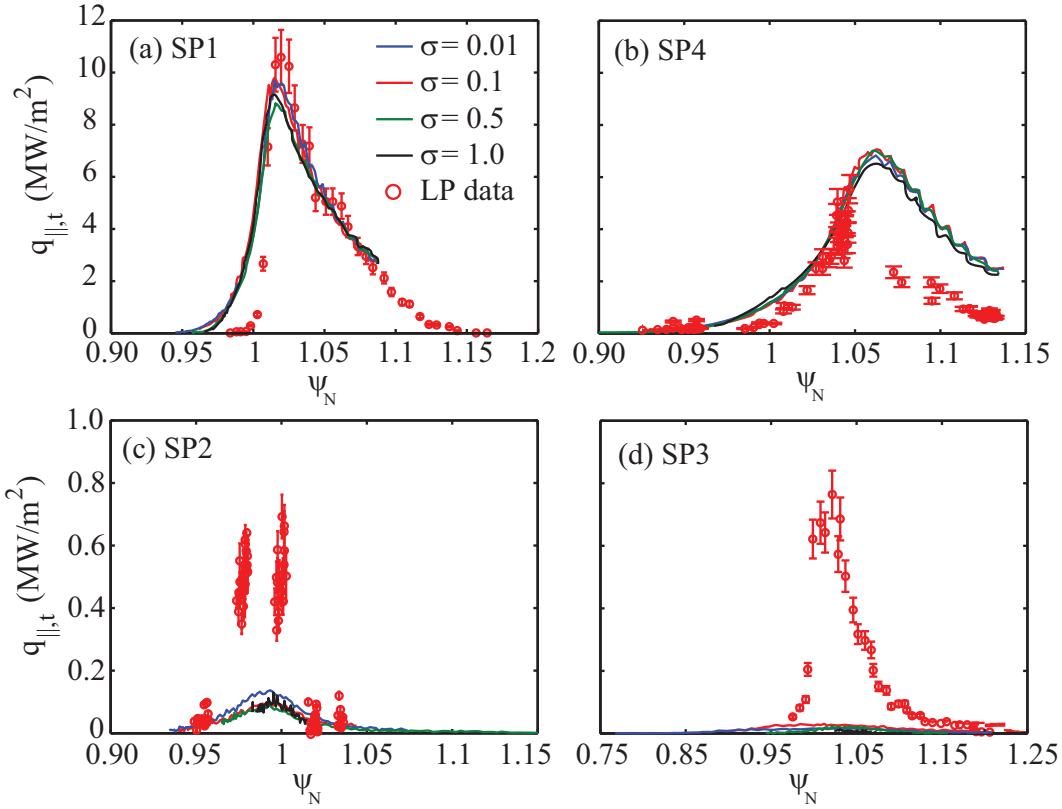

Figure 4.30: Parallel heat flux profiles in magnetic coordinates at the target from the simulations with $\sigma = 0.01$, 0.10, 0.50 and 1.00. The lines correspond to the simulations while the data points represent Langmuir probes measurements for the $\sigma = 0.1$ SF configuration.

The simulated profile at SP1 is well matched to the measurement, figure 4.29(a). However, the measured heat flux profile at SP4 is narrower than that simulated. Since spatially constant transport coefficients were used, they could not be adjusted to match the measured and simulated profiles at both primary SPs. In addition, the simulations show that the peak value of the heat flux on the primary SPs increases while its width narrows when σ is reduced, figures 4.29(a) and (b). This is obviously in contradiction with the expected behavior of a SF divertor in which the values of the peak heat fluxes are expected to decrease. This can be explained by the decrease of the flux expansion at the targets with decreasing σ. This idea is confirmed when the parallel heat flux at the target $q_{||,t} = q_t/\sin\gamma$ is plotted as a function of the magnetic coordinate $\psi_N = (\psi - \psi_{axis})/(\psi_{separatrix} - \psi_{axis})$,

which is directly related with the upstream coordinate ρ_u, figure 4.30. Assuming spatially constant transport coefficients, the parallel heat flux profiles at the target from simulations with different values of σ are extremely similar.

A comparison between the measured heat flux at SP3 and the simulations show that the measurements are an order of magnitude larger than those simulated, figures 4.29(d) and 4.30(d). This strongly suggests the existence of an additional cross-field transport channel, other than diffusion with spatially constant coefficients. Additionally, the experimental power detected at SP3 is always larger than that reaching SP2 while the simulations show an opposite behavior. The measured heat flux profile at SP3 is found to be asymmetric with respect to its maximum value while the simulations show a rather symmetric profile.

Some possible explanations have emerged to explain the observed enhanced transport across the separatrix into the PFR and the discrepancies between the simulated and measured profiles on the secondary SPs. One possibility is the mechanism described in [175, 173] in which a plasma convective cell acts in the null-point region. This does not, however, seem to be justified for the plasma conditions encountered in this thesis, section 4.5.6. Another possibility is the effect of particle drifts that can significantly affect the plasma transport near the null-point depending on the plasma conditions [188, 189, 157, 190]. The particle drifts are not included in the EMC3 model and their effects on the target profiles will be discussed in section 4.9.

The formation of a density blob

In the simulations of the SF equilibria with different values of σ, the plasma density peak originally located in front of the SP1 target (the ionization front) is found to move towards the null point when σ is reduced. This leads to the formation of a region of high plasma density in the null-point region, figure 4.31. In this thesis, this density peaking will be referred to as density blob.

The most relevant physical quantities related to the formation of this density blob are shown in figures 4.32 and 4.33. Associated with its formation, the electron temperature in the null-point region is found to decrease when σ is reduced, figures 4.32(a) and 4.33(a). A similar behavior is found for the ion temperature (not shown). However, the total plasma pressure along the flux tubes, $p_{\text{total}} = nk_B(T_e + T_i)(1 + M^2)$, is approximately constant between the upstream and the null-point region, figures 4.32(b) and 4.33(b). This local reduction of T_e and T_i in the null-point region is caused by (*i*) a local energy loss associated with the ionization of the neutrals near the null-point and along the primary plasma legs, figures 4.32(c) and 4.33(c), and (*ii*) by energy transported from the null-point region towards the targets by the convective flow of the ionized particles, figures 4.32(d) and 4.33(d). Since the plasma flux is stronger along the primary divertor legs, most of the loss of the plasma parallel momentum to the neutrals, and thus plasma pressure,

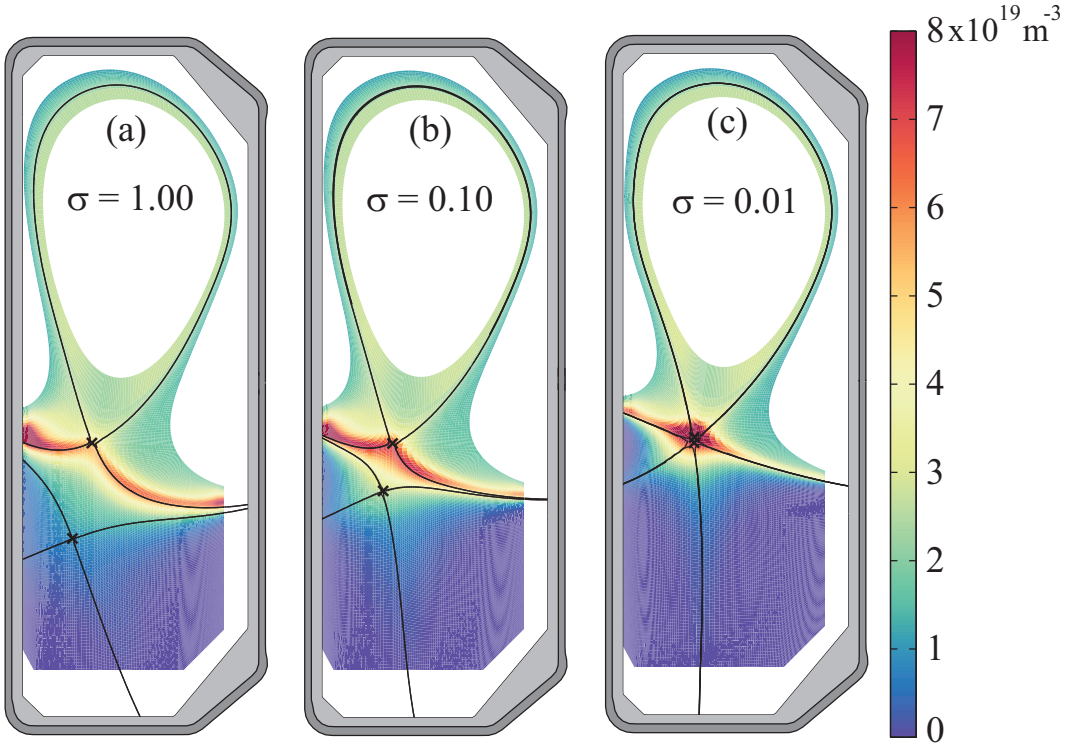

Figure 4.31: Plasma density poloidal distributions for (a) $\sigma = 1.00$, (b) $\sigma = 0.10$ and (c) $\sigma = 0.01$ showing the formation of a density blob in the null-point region when σ decreases.

occurs in that region, figures 4.32(e) and 4.33(e). For the $\sigma = 1.00$ case, the parallel heat transport into the null-point region is sufficient to suppress even small temperature gradients. However, at low values of σ the parallel length corresponding to a certain poloidal interval in the null-point region is significantly enhanced allowing poloidal n, T_e and T_i gradients to develop in that region. As the cross section for neutral ionization by electronic impact, σ_ioniz, has only a weak dependence on T_e for temperatures above 20 eV [187], the neutral ionization rate $R_\mathrm{ioniz} = n\, n_\mathrm{D}\, \langle \sigma_\mathrm{ioniz}\, v \rangle$ depends mostly on the plasma and neutral particle densities. An increase of the plasma density in the null-point region, therefore, causes a larger ionization rate increasing the plasma density even further. This increase is expected to stop when $T_\mathrm{e} \lesssim 10$ eV, since a further drop of T_e results in a significant reduction of R_ioniz.

Simulations with enhanced transport coefficients in the null-point region

To attempt to mimic an additional cross-field transport channel in the null-point region, a local increase of the transport coefficients, with a gaussian profile centered at the primary x-point, was assumed. Far from the null-point region, the transport coefficients remained as before ($D_\perp = \chi_{\mathrm{e},\perp} = \chi_{\mathrm{i},\perp} = 0.6$ m^2/s).

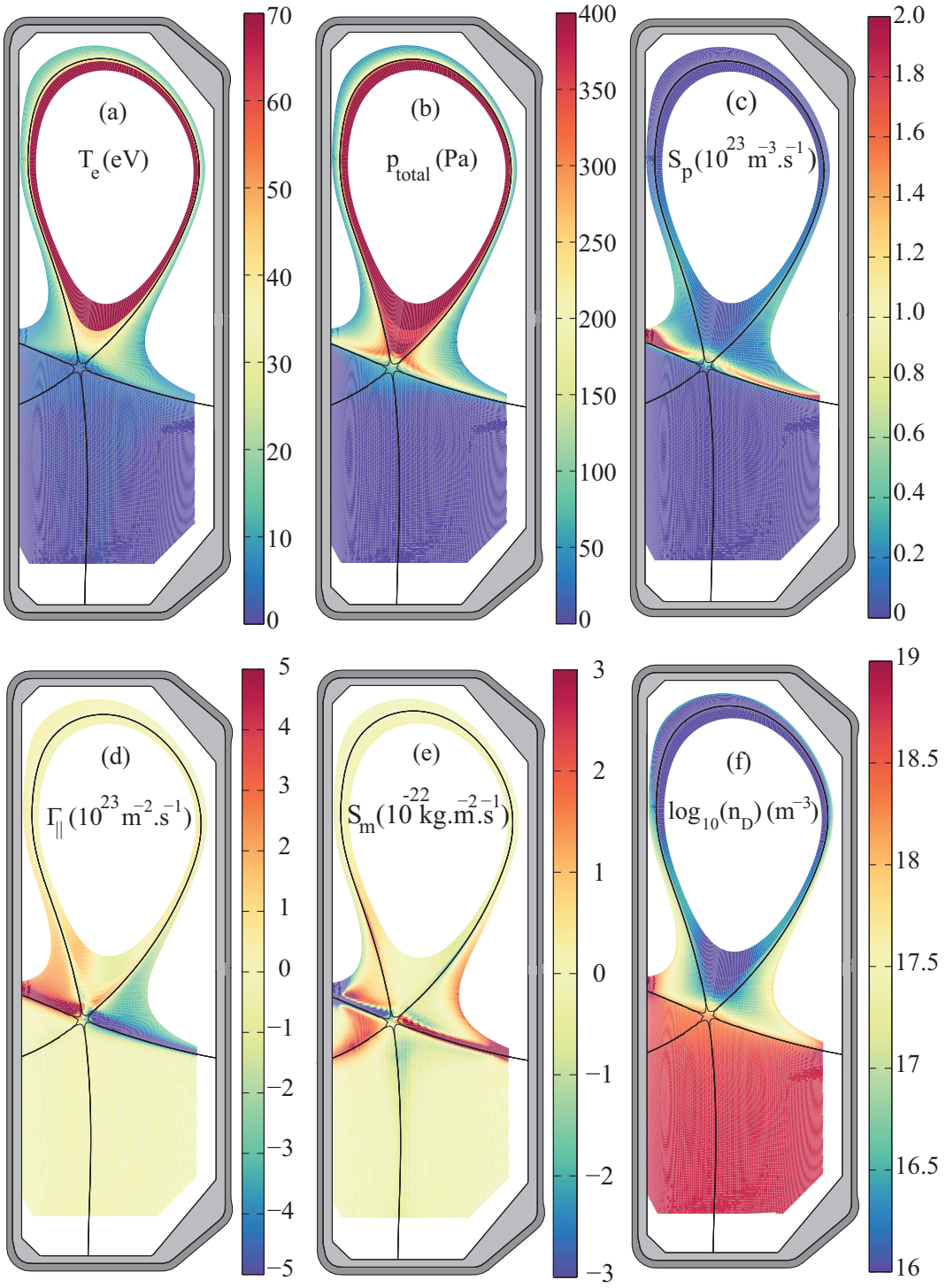

Figure 4.32: Poloidal distributions of the (a) electron temperature T_e (which is similar to T_i), (b) total plasma pressure p_{total}, (c) particle source/sink S_p, (d) parallel plasma flux $\Gamma_{||} = nu_{||}$, (e) parallel plasma momentum source/sink S_m and (f) neutral deuterium density n_D in a logarithmic scale for the case $\sigma = 0.01$.

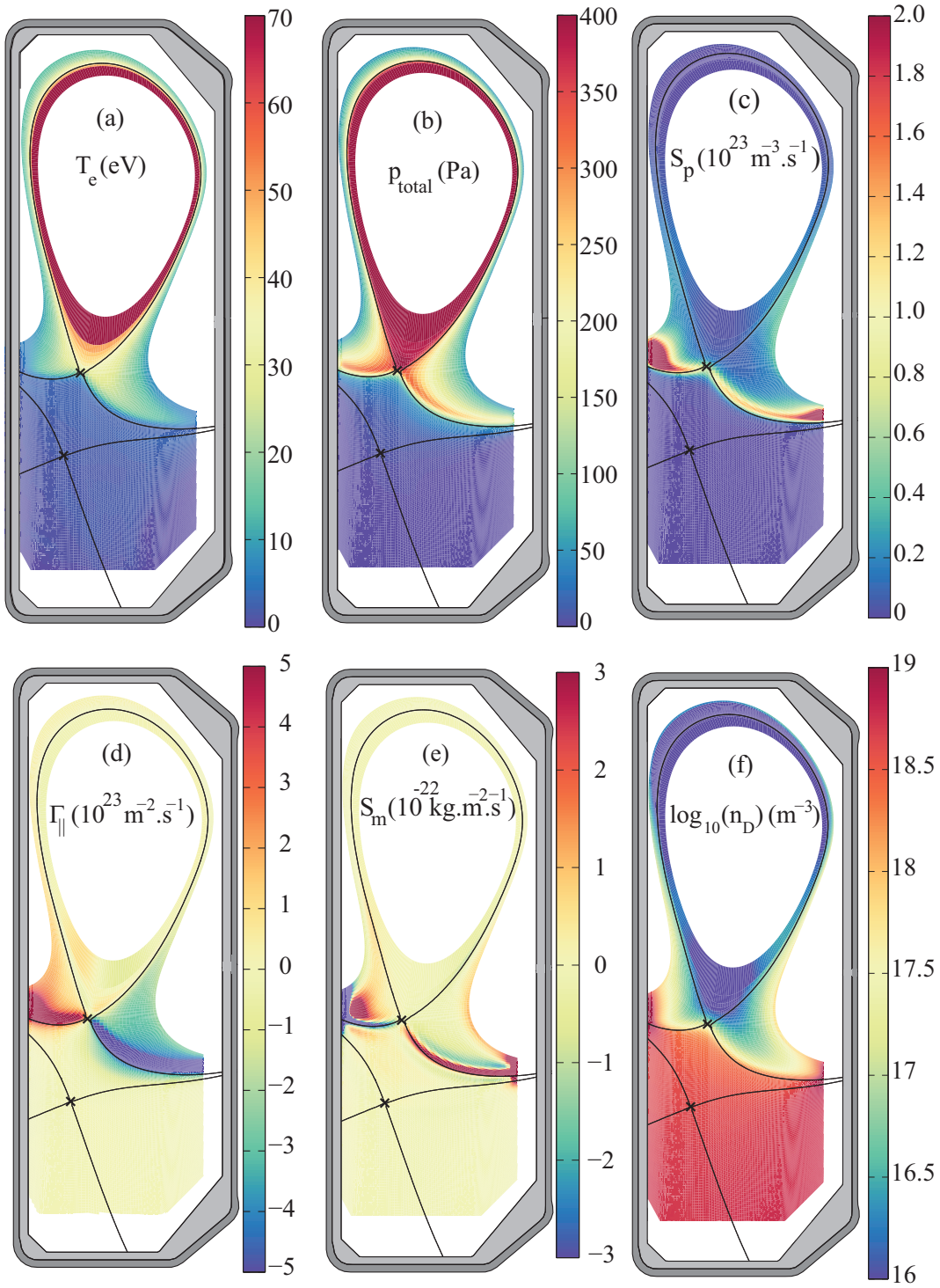

Figure 4.33: Poloidal distributions of the (a) electron temperature T_e (which is similar to T_i), (b) total plasma pressure p_{total}, (c) particle source/sink S_p, (d) parallel plasma flux $\Gamma_{||} = nu_{||}$, (e) parallel plasma momentum source/sink S_m and (f) neutral deuterium density n_D in a logarithmic scale for the case $\sigma = 1.00$.

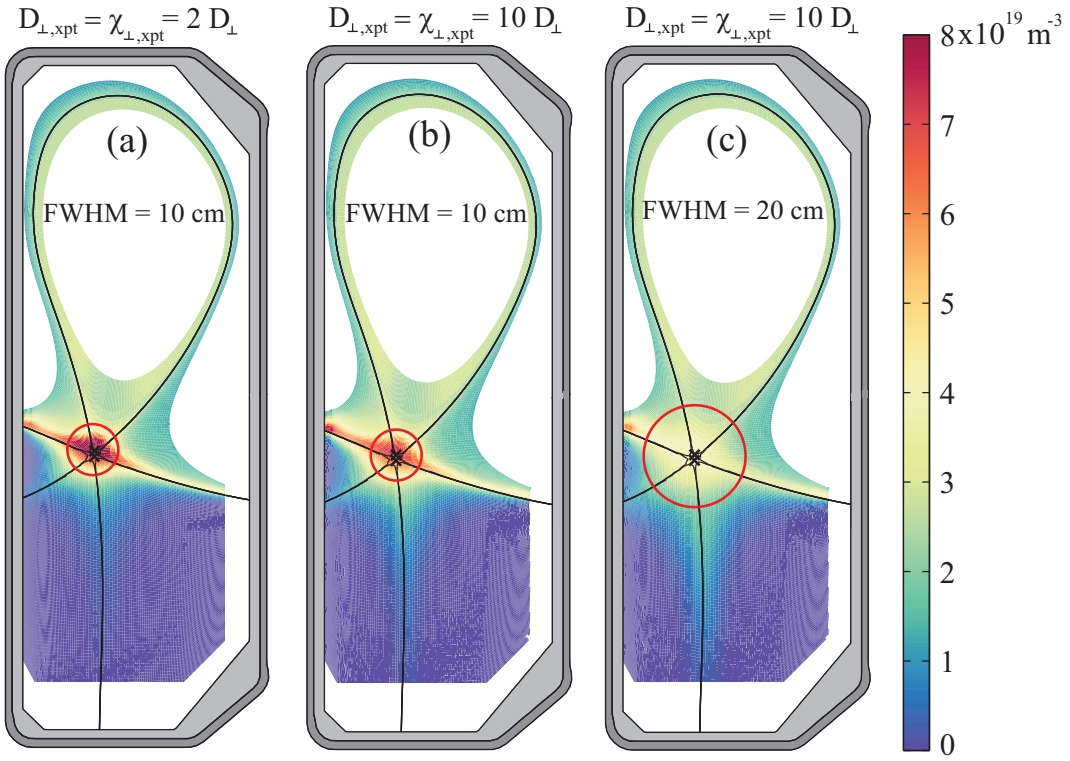

Figure 4.34: Plasma density poloidal distributions from the simulation with spatially varying transport coefficients (a) two times larger than the original values and FWHM = 10 cm, (b) ten times larger than the original values and FWHM = 10 cm, and (c) ten times larger than the original values and FWHM = 20 cm.

Three simulations with spatially varying transport coefficients were performed :

1. the transport coefficients at the peak of the gaussian are a factor 2 higher than the original value ($D_{\perp,\mathrm{xpt}} = \chi_{\perp,\mathrm{xpt}} = 2\,D_{\perp}$) and the full width at half maximum is set to FWHM = 10 cm, which is the typical size of the region in which $\beta_{\mathrm{p}} \approx 10$, figure 4.34(a);

2. the transport coefficients at the peak of the gaussian are a factor 10 higher than the original value ($D_{\perp,\mathrm{xpt}} = \chi_{\perp,\mathrm{xpt}} = 10\,D_{\perp}$) and FWHM = 10 cm, figure 4.34(b);

3. the transport coefficients at the peak of the gaussian are 10 times larger than the original value ($D_{\perp,\mathrm{xpt}} = \chi_{\perp,\mathrm{xpt}} = 10\,D_{\perp}$) and FWHM = 20 cm, which is the typical size of the region in which $\beta_{\mathrm{p}} \approx 1$, figure 4.34(c).

Enhancing the transport coefficients in the null-point region can indeed strongly reduce the density blob, figure 4.34, suggesting that enhanced cross-field transport in the null-point region could be responsible for the absence of the density blob in experiments. However,

although the total power at SP3 ($P_{SP3}/P_{SP1} = 5.3\%$) approaches the experimental value ($P_{SP3}/P_{SP1} = 8.3\%$), a large discrepancy between the measured and simulated SP3 heat flux profiles is still observed, figure 4.35. In conclusion, diffusive cross-field transport alone is not sufficient to explain the shape of the measured target profile and observed power distribution to secondary SPs in the SF+ configuration.

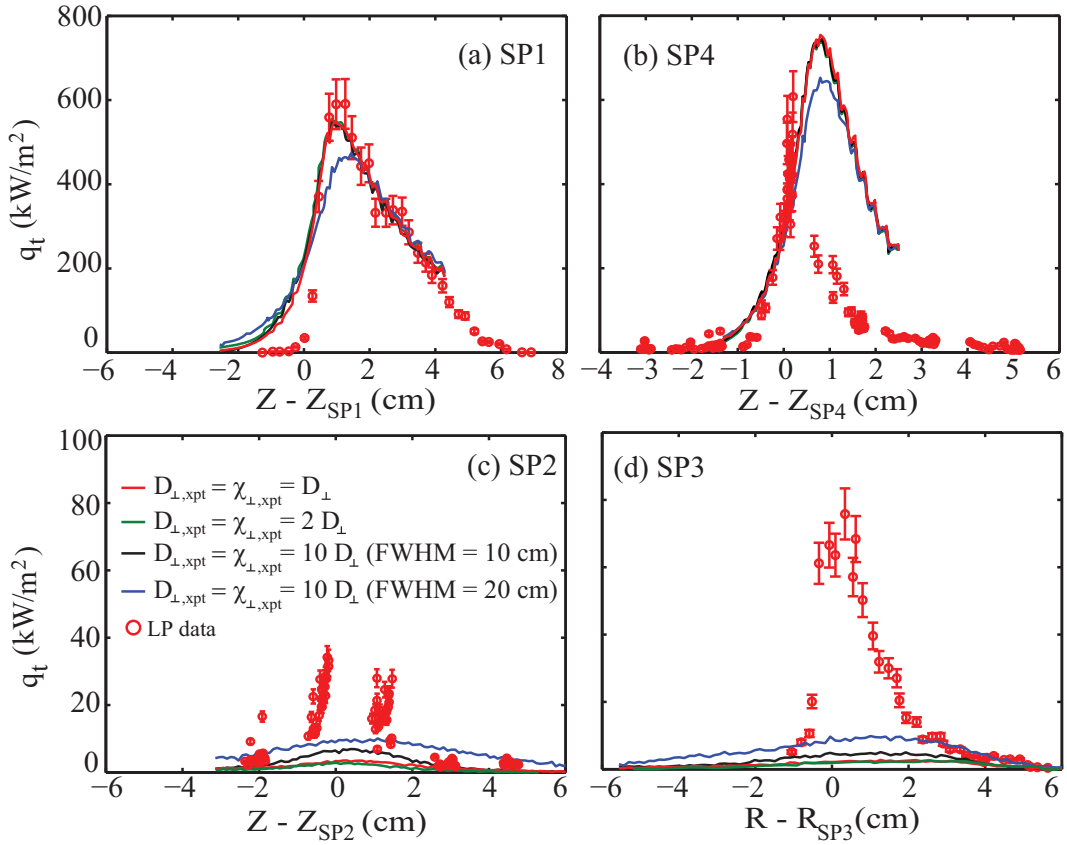

Figure 4.35: Target heat flux profiles from the simulations with spatially varying transport coefficients. The lines correspond to the simulations while the data points represent Langmuir probes measurements.

4.8.3 Effect of the input power on the power distribution

The observed decrease of the power distribution to SP3 with increasing input power, P_{in}, presented in section 4.6, was examined using simulations with different values of input power using a SF+ configuration with $\sigma = 0.1$. The input power in these simulations was chosen to be multiples of the reference input power, namely (*i*) 119 kW, (*ii*) 238 kW (the reference value), (*iii*) 476 kW and (*iv*) 714 kW. The plasma density was the same as for the reference simulation ($n = 2.5{\times}10^{19}\,\mathrm{m}^{-3}$).

The target heat flux profiles from these simulations are shown in figure 4.36 after scaling them by a factor P_{ref}/P_{in}, with $P_{ref} = 238$ kW, to make the profiles directly comparable.

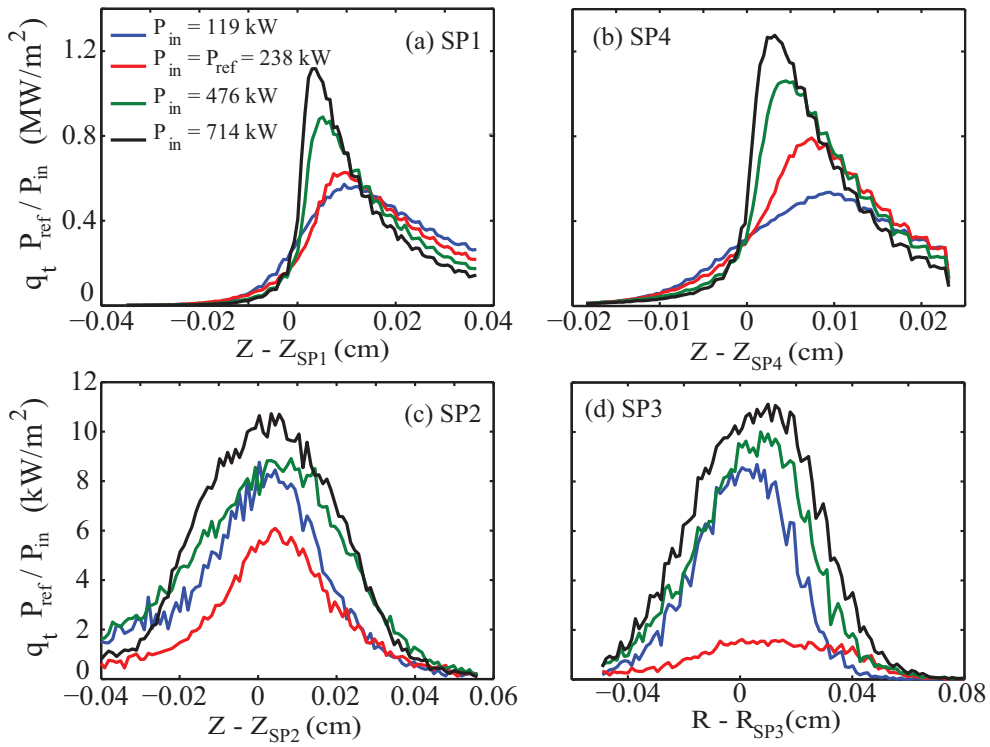

Figure 4.36: Target heat flux profiles for four different values of input power P_{in} of a SF configuration with $\sigma = 0.1$. For the sake of comparability the profiles are scaled with the factor $P_{\text{ref}}/P_{\text{in}}$.

The profiles are found to peak near the separatrix for larger values of the input power leading to a decrease of the power fall-off length at the target, λ_t. This is due to the strong temperature dependence of the classical parallel heat conductivity used in equation 4.33, $\vec{q}_{||,\alpha} = -\kappa_{0,\alpha} T_\alpha^{5/2} \vec{\nabla}_{||} T_\alpha$, implying that more power can be transported in the near-SOL, where the temperature is higher. In these simulations, the power distribution to the secondary SPs (SP2 and SP3) increases with the input power. However, the experimental measurements presented in section 4.6 show a decrease of the power distribution to SP3 with higher input power. A comparison between the measurements and simulations suggests that the cross-field transport responsible for the activations of SP3 weakens at larger values of input power.

4.8.4 Effect of the plasma density on the power distribution

In section 4.7 an increase in the plasma density lead to a smaller power distribution to SP3, and broader heat flux profiles at primary SPs with reduced peak values. The measurements showed a second peak appearing in the SOL side of the SP for higher values of plasma density with its amplitude increasing with plasma density and decreasing with σ. Simulations over a range of plasma densities were performed in a SF+ with $\sigma =$

0.01 and a SN ($\sigma = 1.00$) configuration. Only the main ion species was used (deuterium) with the plasma density at the most inner simulation boundary varied from 0.5 up to $10\times10^{19}\,\mathrm{m}^{-3}$. The input power is kept as in the reference simulation ($P_{\mathrm{in}} = 238\,\mathrm{kW}$).

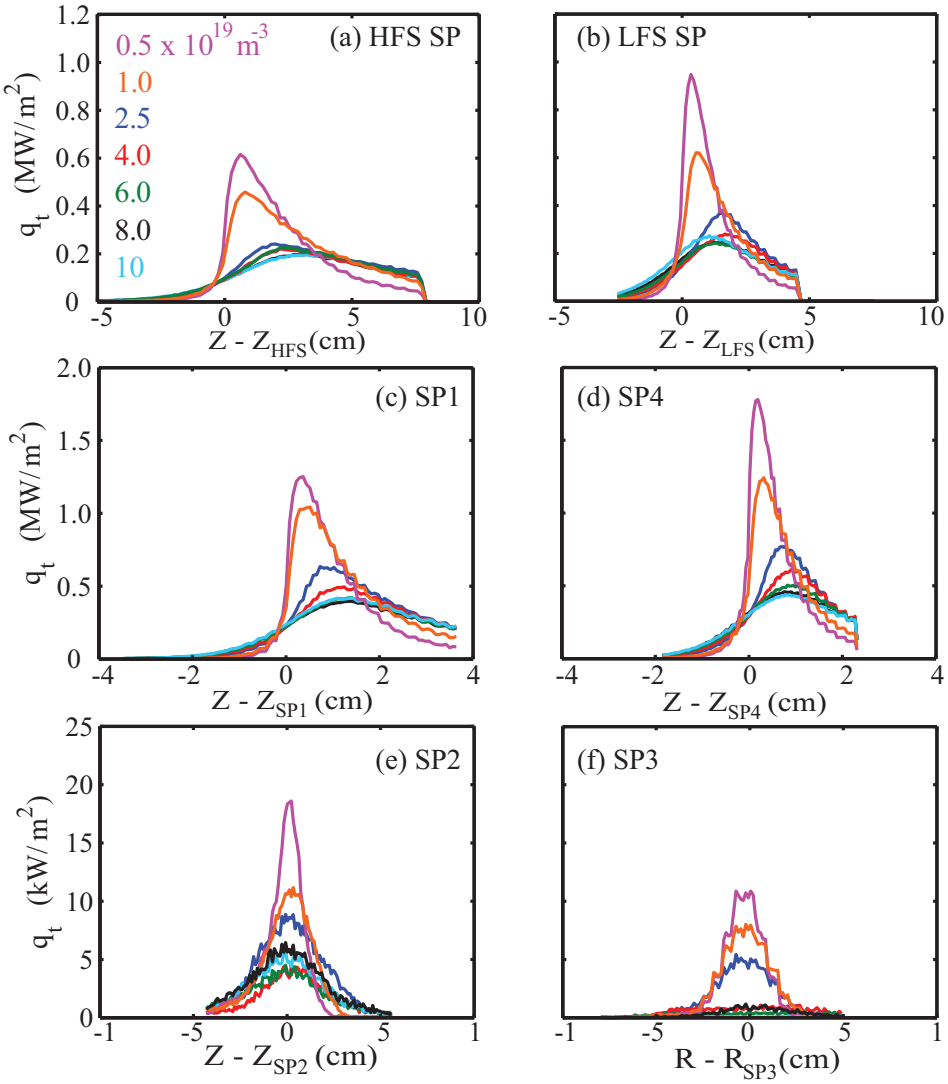

Figure 4.37: Target heat flux profiles from the simulations of a (a-b) SN and (c-f) a SF+ configuration ($\sigma = 0.01$) for various values of the plasma density.

An increase of the plasma density leads to a similar broadening of the target heat flux profiles at the primary SPs of the SF+ and SN configurations and a decrease of their peak values, figures 4.37(a-d). The profile variations are a result of the closure of the fluid equations used in the EMC3 model in which the cross-field heat transport, $\vec{q}_{\alpha,\perp} = -n\,\chi_{\alpha,\perp}\,k_{\mathrm{B}}\,\vec{\nabla}_{\perp}T_{\alpha}$, depends linearly on the plasma density. For plasma densities lower than $6\times10^{19}\,\mathrm{m}^{-3}$, an increase of n causes an increase of the cross-field heat transport leading to the broadening of the radial temperature profiles. As a consequence, the flattening of the radial temperature profiles cause a decrease of the cross-field heat

transport and, for $n \gtrsim 6{\times}10^{19}\,\mathrm{m}^{-3}$, the variations of $\vec{q}_{\perp}$ become negligible compared with $\vec{q}_{||}$. As in the experiments, the simulations show that the target density profiles in both the SN and SF configurations were not affected by an increase of the plasma density beyond $n \approx 6{\times}10^{19}\,\mathrm{m}^{-3}$. The dependence of q_{peak} and λ_{t} on the plasma density is found to be in qualitative agreement with the experimental measurements presented in section 4.7.

The power distribution to the secondary SPs, figures 4.37(e-f), show that a larger fraction of the exhaust power is detected at SP3 for lower values of plasma density. This is in qualitative agreement with the experimental results presented in section 4.7. However, the simulations underestimate the power distributed to SP2 and SP3.

Despite this qualitative agreement in q_{peak} and λ_{t} on the plasma density, a strong discrepancy in the shape of the profiles is seen, in particular at SP1 and SP3. The simulated heat flux profiles at SP1 with higher values of plasma density remain single-peaked while the measured profiles are double-peaked, figure 4.22 and 4.37(c-d). This further supports the argument presented in section 4.8.2 that an important transport mechanism is missing in the simulations. Since diffusive cross-field transport tends to decrease the radial gradients of the plasma kinetic profiles, the transport mechanism missing in the EMC3 model is expected to be of convective nature. The importance of particle drifts on the transport simulations of the TCV SF plasmas will be discussed in the next section.

4.9 Particle Drifts in the Snowflake Divertor

Diffusive cross-field transport is found to be insufficient to explain the experimentally observed power distribution to the secondary SP targets, section 4.8.2. Additionally, a strong mechanism responsible for the shape of the target profiles is missing in the EMC3 model, section 4.8.4. Since the EMC3 code does not take into account the effects of particle drifts such a mechanism merits investigation. In this section, the importance of particle drifts on the EMC3-Eirene simulations is investigated.

4.9.1 Importance of drifts in the EMC3-Eirene simulations

The effect of particle drifts in the null-point region, in particular the $\vec{E} \times \vec{B}$ drift across the private region, was investigated theoretically [188, 189] and experimentally [157, 190]. In this work, only a dominant drift effect will be addressed. Amongst the non-divergence-free drift terms in equation 4.16, the $\vec{E} \times \vec{B}$ term is expected dominate since it scales as the inverse of the local scale length of the kinetic plasma profiles while the combined curvature- and gradient-B drift scales inversely with the major radius. The diamagnetic drift was neglected as it is divergence-free and, therefore, does not contribute to the

plasma transport. The drift term due to friction between ions and neutrals is much smaller than the others due to the range of SOL temperatures found in the simulations and has, therefore, also been neglected.

To estimate the importance of the $\vec{E}\times\vec{B}$ particle drift on the plasma transport, the particle flux calculated by EMC3-Eirene is compared with the $\vec{E}\times\vec{B}$ particle flux estimated using the kinetic profiles calculated by EMC3-Eirene. According to equation 4.17, the radial component of the $\vec{E}\times\vec{B}$ drift velocity depends on the poloidal electric field, equation 4.18, which, by neglecting the parallel current and using the relation $\frac{\partial}{\partial s_{||}} = \frac{B_\theta}{B}\frac{\partial}{\partial s_\theta}$, can be rewritten as :

$$E_\theta\left(\rho, s_\theta\right) = -1.71\,\frac{\partial}{\partial s_\theta}\left[\frac{k_\mathrm{B}\,T_\mathrm{e}\left(\rho, s_\theta\right)}{e}\right] - \frac{k_\mathrm{B}\,T_\mathrm{e}\left(\rho, s_\theta\right)}{e\,n\left(\rho, s_\theta\right)}\,\frac{\partial n\left(\rho, s_\theta\right)}{\partial s_\theta}\,. \tag{4.42}$$

Since $J_{||}$ is not the dominant term in equation 4.18, its neglect is not expected to change the results substantially. After calculating E_θ, the plasma potential Φ can be calculated by :

$$\Phi\left(\rho, s_\theta\right) = \frac{k_\mathrm{B}\,T_\mathrm{e}\left(\rho, 0\right)}{2\,e}\,\ln\left\{\frac{m_\mathrm{i}}{2\pi\,m_\mathrm{e}}\left[1+\frac{T_\mathrm{i}\left(\rho,0\right)}{T_\mathrm{e}\left(\rho,0\right)}\right]^{-1}\right\} - \underset{\substack{s_\theta\,=\,0\\ \text{(LFS target)}}}{\int^{s_\theta}} E_\theta\left(\rho, s'_\theta\right)\,ds'_\theta\,. \tag{4.43}$$

The first term on the right hand side of equation 4.43 is the floating potential resulting from the assumption $J_{||} = 0$ and calculated at the LFS target for each flux tube. With $\Phi\left(\rho, s_\theta\right)$, the radial electric field can be calculated, $E_\rho\left(\rho, s_\theta\right) = -\vec{\nabla}\Phi\cdot\hat{e}_\rho$. Note that the radial electric field is dominated by the radial variation of the plasma sheath boundary condition at the target, given by the first term on the right hand side of equation 4.43. As an example, the electric potential, and the poloidal and radial electric fields in the common flux region of a SF+ configuration with $\sigma = 0.1$ can be seen in figure 4.38(a-c).

Using equation 4.17, the particle flux due to the $\vec{E}\times\vec{B}$ drift, $\vec{\Gamma}^{E\times B} = n\vec{u}_\mathrm{D}$, can be calculated and compared with the poloidal projection of the parallel particle flux calculated by EMC3-Eirene, $\Gamma_\theta = \Gamma_{||}\,B_\theta/B$. The particle fluxes Γ_θ and $\vec{\Gamma}^{E\times B}$ are found to be of the same order of magnitude in some regions of the SOL, figures 4.38(d) and (e). The radial component of $\vec{\Gamma}^{E\times B}$, is larger than Γ_θ in the null-point region, while its poloidal component is larger than Γ_θ in almost the entire SOL. This again implies that a significant convective transport, in both parallel and cross-field directions, is missing in the simulations presented in this chapter [191]. This could explain the observed discrepancies between the measured and simulated target profiles.

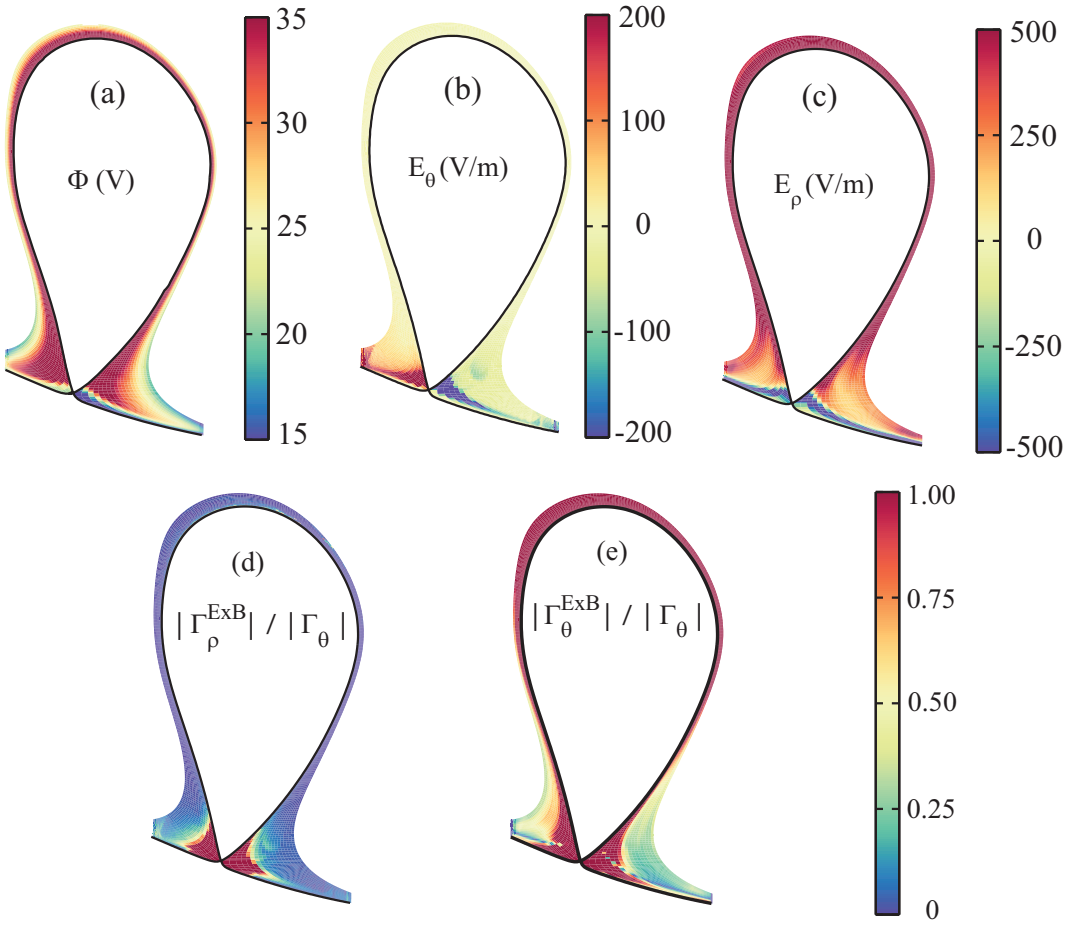

Figure 4.38: (a) Electric potential, (b) poloidal and (c) radial electric fields for a SF configuration with $\sigma = 0.1$. Ratio between (d) the radial and (e) the poloidal component of the particle flux due to drifts with the poloidal projection of the parallel plasma flux for a SF configuration with $\sigma = 0.1$.

To investigate the effects of the $\vec{E} \times \vec{B}$ drift on the plasma transport in the SF divertor, the EMC3 equations and boundary conditions would have to include drift terms. Unfortunately, a self-consistent treatment of the $\vec{E} \times \vec{B}$ drift using the EMC3 code was not available during this thesis. However, the EMC3-Eirene results can still be used to evaluate whether the discrepancies between the simulated and measured target profiles can be qualitatively explained by the presence of $\vec{E} \times \vec{B}$ drift.

4.9.2 Activation of secondary strike points

According to equation 4.42, the radial component of the $\vec{E} \times \vec{B}$ drift depends on the poloidal gradients of n and T_e, as well as on the value of T_e. The poloidal gradients of the simulated plasma kinetic profiles (n, T_e and T_i) are larger in the null-point region of the SF configuration, figures 4.39(a-c). The longer parallel length, corresponding to a certain

poloidal interval in the null-point region of a SF, allow for larger poloidal gradients of the plasma kinetic profiles to develop, leading to a higher poloidal electric field, figure 4.39(d).

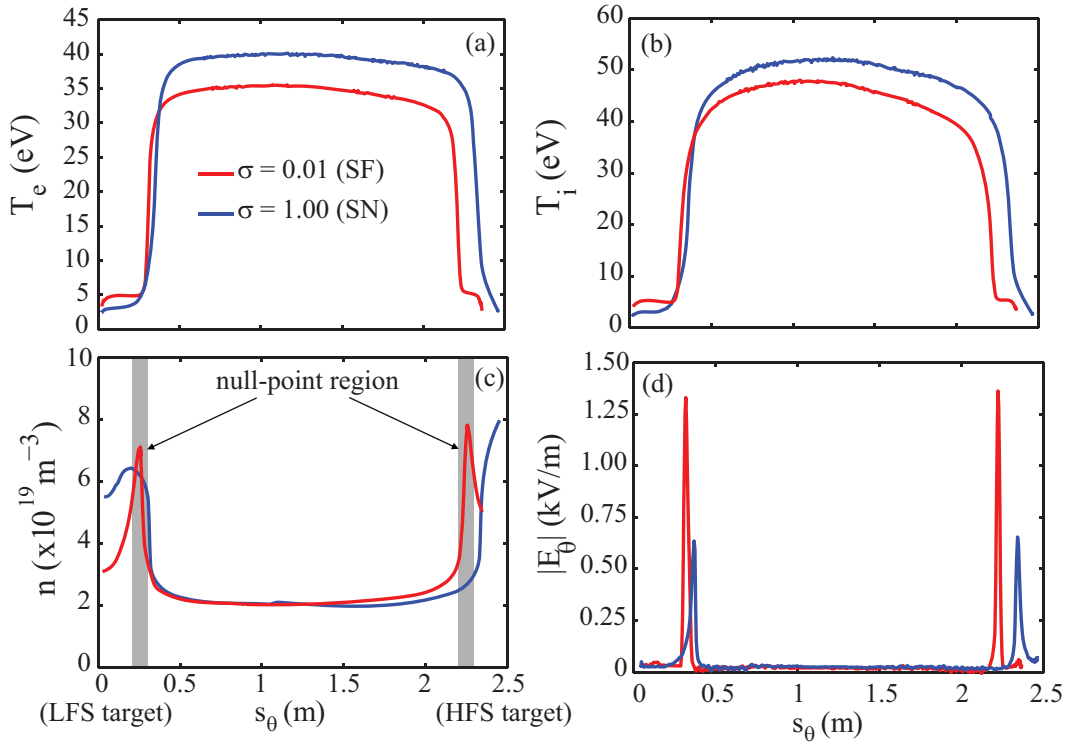

Figure 4.39: Poloidal profiles of the EMC3-Eirene simulated (a) electron and (b) ion temperatures, (c) plasma density and (d) poloidal electric field for a SN ($\sigma = 1.00$) and a SF+ configuration ($\sigma = 0.1$). The origin $s_\theta = 0$ corresponds to the LFS target (SP4) while the position $s_\theta = L_\mathrm{p} \approx 2.5\,\mathrm{m}$ corresponds to the HFS target (SP1) (see figure 4.4).

Since the radial component of the $\vec{E} \times \vec{B}$ drift depends on E_θ, an enhanced transport from the LFS side of the SOL into the PFR between the primary and secondary separatrices is expected when σ is reduced. In addition, at smaller values of σ, the distance between the primary and secondary separatrices decreases in physical and in flux space, and a larger fraction of heat and particles transported across the primary separatrix is able to cross the secondary separatrix, figure 4.40(a). The poloidal component of the $\vec{E} \times \vec{B}$ drift, allows these particles to be convected towards SP3. This predicted effect of the $\vec{E} \times \vec{B}$ drift is in qualitative agreement with the enhanced power distribution to SP3 observed in the experiments and underestimated in the EMC3-Eirene simulations. The $\vec{E} \times \vec{B}$ drift also provides an explanation for the observed asymmetry of the heat flux profile at SP3. The $\vec{E} \times \vec{B}$ flow along the SP3 divertor leg is expected to enforce the plasma flow in the LFS side of SP3 while in the HFS side it is against the flow, figure 4.40(b). The poloidal $\vec{E} \times \vec{B}$ drift is expected to convect heat and particles from the HFS side of SP3 to the bottom side of SP2, while on the upper side of SP2 the poloidal $\vec{E} \times \vec{B}$ drift transports heat and particles towards SP1, figure 4.40(a). This effect is also in qualitative agreement

with the observed lower values of power detected at SP2 compared with that detected at SP3.

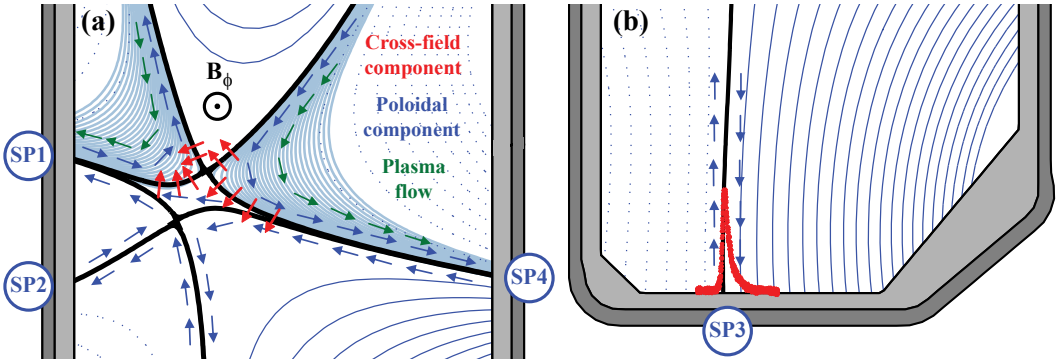

Figure 4.40: Schematic showing the expected $\vec{E} \times \vec{B}$ drifts (a) in the null-point region and (b) along the SP3 plasma leg of a SF+ configuration with forward toroidal magnetic field.

A comparison between the measurements (section 4.6) and simulations (section 4.8.3) suggests that the cross-field transport responsible for the activations of SP3 weakens at larger values of input power. This observation is consistent with the fact that at larger values of input power, smaller parallel temperature gradients are expected in the SOL due to the dependence of the classical parallel heat conductivity $\kappa_\alpha = \kappa_{0,\alpha} T_\alpha^{5/2}$, thus reducing the radial $\vec{E} \times \vec{B}$ particle flux.

From section 4.7, the power distribution to SP2 and SP3 decreases when the plasma density increases, figures 4.25 and 4.41(a). To evaluate the effect of the $\vec{E} \times \vec{B}$ drift on the activation of SP2 and SP3, the $\vec{E} \times \vec{B}$ particle flux in the common flux region was estimated for two values of plasma density. At low plasma density, the radial component of the $\vec{E} \times \vec{B}$ drift extends up to the separatrix whereas at higher values of plasma density, the region with enhanced cross-field transport moves upstream. Therefore, the enhanced transport across the separatrix into the PFR due to the $\vec{E} \times \vec{B}$ drift is expected to decrease at higher plasma densities, as observed in the experiments. For $n_{e,l} \gtrsim 6 \times 10^{19}$ m^{-3}, the power distribution to SP2 and SP3 remains approximately the same. This observation suggests that the radial $\vec{E} \times \vec{B}$ drift does not contribute to the plasma transport across the primary separatrix and that the remaining power distribution is provided by, e.g. diffusive transport into the PFR. The values of power detected at the SP2 and SP3 for higher values of plasma density are of the same order of magnitude to those obtained in the simulations presented in section 4.8.4.

4.9.3 The double-peaked target profiles

Since the radial $\vec{E} \times \vec{B}$ drift depends on the poloidal gradients of the plasma kinetic profiles, its effects are expected to be more pronounced in the conduction-limited regime

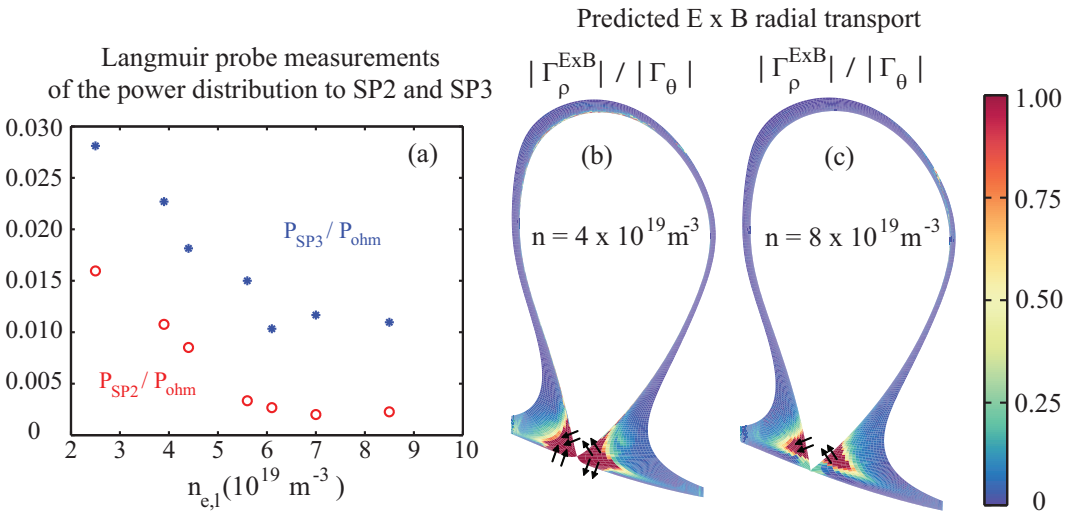

Figure 4.41: (a) Dependence of the power distribution to SP2 and SP3 in a SF+ configuration with $\sigma = 0.35$ and forward B_ϕ. Ratio between the calculated radial component of the particle flux due to the $\vec{E} \times \vec{B}$ drift and the poloidal projection of the EMC3-Eirene parallel plasma flux for (b) $n_{\mathrm{e,l}} = 4 \times 10^{19}$ m^{-3} and (c) $n_{\mathrm{e,l}} = 8 \times 10^{19}$ m^{-3}.

than in the sheath-limited regime [192, 193]. The effects of the $\vec{E} \times \vec{B}$ drift should therefore become stronger at larger values of the plasma density. In order to estimate the effects caused by the $\vec{E} \times \vec{B}$ drift on the target profiles, the continuity equation 4.31 was modified to include the effects of the $\vec{E} \times \vec{B}$ drift, which becomes

$$\vec{\nabla} \cdot \left[n \, \vec{u}_{||} - D_\perp \, \vec{\nabla}_\perp n \right] = S_\mathrm{p} + S_\mathrm{p}^{\mathrm{E\times B}} . \tag{4.44}$$

In this equation, $S_\mathrm{p}^{\mathrm{E\times B}} = -\vec{\nabla} \cdot \left(\vec{\Gamma}^{\mathrm{E\times B}} \right)$ is a particle source term that accounts for the non-divergence-free part of the $\vec{E} \times \vec{B}$ particle flux. The same can be performed with the electron and ion energy conservation equations 4.34 and 4.35 by adding an energy source term $S_{e\alpha}^{\mathrm{E\times B}} = -\vec{\nabla} \cdot \left(\frac{5}{2} \, k_\mathrm{B} \, T_\alpha \, \vec{\Gamma}^{\mathrm{E\times B}} \right)$ corresponding to the energy transported by the non-divergence-free part of the electron ($\alpha = e$) and ion ($\alpha = i$) $\vec{E} \times \vec{B}$ particle flux. These source terms were calculated for a SF+ configuration with $\sigma = 0.1$ and forward B_ϕ, figures 4.42(a) and (b).

The calculations show that the $\vec{E} \times \vec{B}$ drift is predicted to have a stronger effect on the SP1 target profiles compared with SP4. The $\vec{E} \times \vec{B}$ drift is expected to cause a small reduction on the total particle source, $S_{\mathrm{p,total}} = S_\mathrm{p} + S_\mathrm{p}^{\mathrm{E\times B}}$, in the far-SOL of SP4 thus leading to a slightly narrower profile in the vicinity of the separatrix. This effect is in qualitative agreement with the experimental observations of a more peaked heat flux profile at SP4, compared with that simulated, figure 4.29(b). The $\vec{E} \times \vec{B}$ drift is also

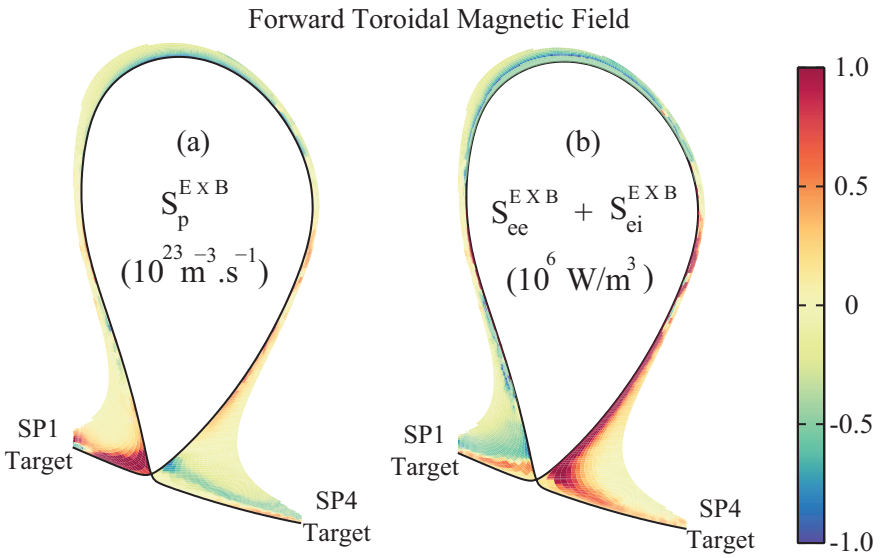

Figure 4.42: (a) Particle source, $S_{\mathrm{p}}^{\mathrm{E\times B}}$, and (b) energy source, $S_{e}^{\mathrm{E\times B}}$, due to the $\vec{E}\times\vec{B}$ drift calculated using the EMC3-Eirene plasma density and temperature profiles for a SF+ configuration with $\sigma = 0.1$ and forward B_ϕ.

expected to reduce $S_{\mathrm{p,total}}$ in the near-SOL of SP1 and to increase it in the far-SOL, figure 4.42(a). This is seen experimentally appearing as a double-peaked density profile, figure 4.23(c). Double-peaked target profiles have already been reported in previous works [155, 156] and were thought to be caused by the $\vec{E}\times\vec{B}$ drift [158].

Concerning the total energy source, $S_{\mathrm{e,total}} = S_{\mathrm{ee}} + S_{\mathrm{ei}} + (S_{\mathrm{ee}}^{\mathrm{E\times B}} + S_{\mathrm{ei}}^{\mathrm{E\times B}})$, the $\vec{E}\times\vec{B}$ drift is expected to reduce $S_{\mathrm{e,total}}$ in the far-SOL of SP1 and increase it near the separatrix, figure 4.42(b). This would lead to a more peaked temperature profile near the separatrix compared with a SN configuration. It is also observed experimentally as presented in section 4.7.

4.9.4 Experiments with reversed B_ϕ

The $\vec{E}\times\vec{B}$ drift provides, at least qualitatively, explanations for some of the discrepancies between the measured and the simulated target profiles as well as the activation of the secondary SPs of a SF+ configuration. As the direction of the $\vec{E}\times\vec{B}$ drift depends on the direction of the toroidal magnetic field, B_ϕ, dedicated experiments in reversed B_ϕ were performed in order to examine the influence of the $\vec{E}\times\vec{B}$ drift on the plasma transport in the SF configuration. In these experiments, the plasma density was increased, as described in section 4.7. The recycling current measured at the HFS primary SP shows a maximum value at $n_{\mathrm{e,l}} \approx 7.0\times10^{19}\ \mathrm{m}^{-3}$, figure 4.43, which may be taken as an initial sign of partial divertor detachment and is slightly higher than that for forward B_ϕ, figure 4.10.

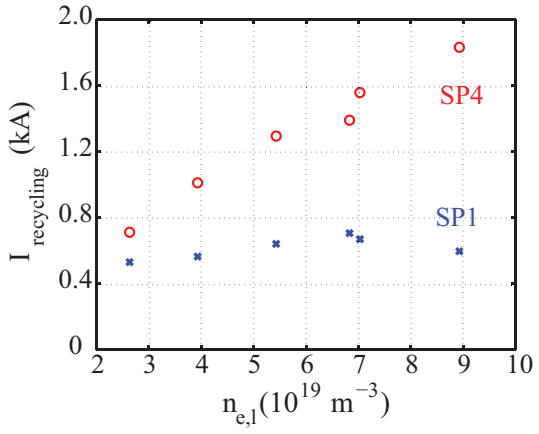

Figure 4.43: Langmuir probe measurements of the recycling current measured at the SP1 and SP4 targets as a function of the line integrated plasma density in reversed B_ϕ.

To anticipate the effects caused by the $\vec{E} \times \vec{B}$ drift on the target profiles, the particle and energy sources $S_p^{E\times B}$ and $S_e^{E\times B}$ were calculated assuming a reversed B_ϕ, figure 4.44. The $\vec{E} \times \vec{B}$ drift is expected to increase the total particle source $S_{p,total}$ in the LFS side of the SOL and decrease it in the HFS side of the SOL. This result is consistent with the observed higher $I_{recycling}$ at the SP4 and lower $I_{recycling}$ at the SP1 for reversed B_ϕ, figure 4.43, compared with the forward B_ϕ configuration, figure 4.10.

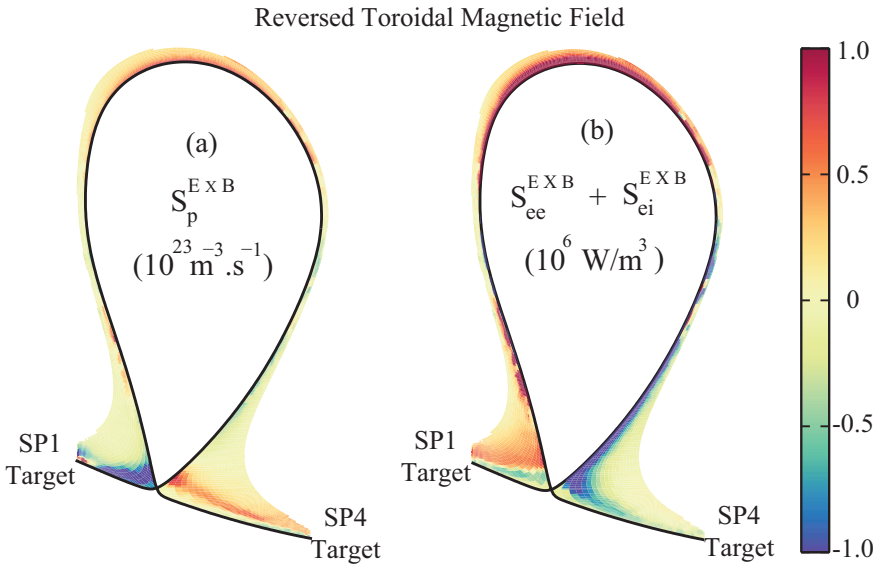

Figure 4.44: (a) Particle source, $S_p^{E\times B}$, and (b) energy source, $S_e^{E\times B}$, due to the $\vec{E} \times \vec{B}$ drift calculated using the EMC3-Eirene plasma density and temperature profiles for a SF+ configuration with $\sigma = 0.1$ and reversed B_ϕ.

The $\vec{E} \times \vec{B}$ drift in reversed B_ϕ is expected to reduce $S_{p,total}$ in the far-SOL of SP1 and to increase it near the separatrix, figure 4.44(a). Therefore, the SP1 target profile in reversed

B_ϕ should have a conventional single-peaked density profile instead of the observed double-peaked profile in forward B_ϕ. This was seen in the reversed B_ϕ experiments, figure 4.45(c), where a single-peaked density profile at SP1 is observed. No significant change of the measured SP4 target profile was observed.

The $\vec{E} \times \vec{B}$ drift in reversed B_ϕ is also expected to reduce the total energy source $S_{\mathrm{e,total}}$ in the near-SOL of SP1 and increase it in the far-SOL, figure 4.44(b), leading to a flatter temperature profile in the SOL side of SP1 instead of the peaked temperature profile observed in forward B_ϕ. This was also observed in the experiments, as shown in figure 4.45(d). The peak value of the density profile in forward B_ϕ occurs in the PFR side of SP1 whereas, in the reversed B_ϕ, it occurs in the SOL side, figures 4.45(a) and (c). This is in qualitative agreement with the expected $\vec{E} \times \vec{B}$ particle flux shown in figure 4.40.

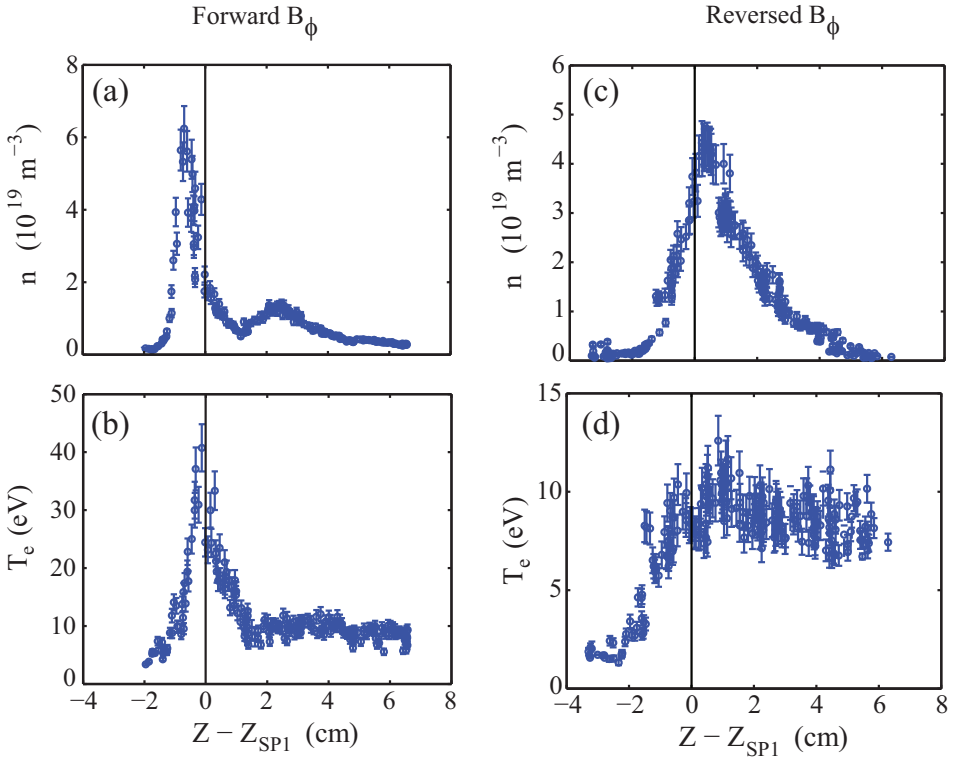

Figure 4.45: Plasma density and electron temperature measured at the SP1 target in (a-b) forward and (c-d) reversed B_ϕ. The measurements in the panels (a,b) are the same of the figure 4.23(c,d).

In figure 4.46, the fraction of the input power detected at each SP and the radiated power fraction are shown for different values of plasma density. While the power distribution to the main SPs and being radiated is not strongly affected by reversing B_ϕ, the power distribution to both secondary SPs is significantly lower than in forward B_ϕ. This observation is consistent with the expected direction of the poloidal component of the $\vec{E} \times \vec{B}$ particle flux that removes particles from SP2 and distribute to SP3. Note that,

as observed in the discharges with forward B_ϕ, figure 4.25, there is also an issue on the power balance that requires further investigation.

The qualitative agreement between the experiments and the expected effects of the $\vec{E} \times \vec{B}$ drift on the simulated profiles strongly suggests that $\vec{E} \times \vec{B}$ drift is responsible for a significant fraction of the observed cross-field transport in the null-point region. Therefore, its effects has to be accounted in numerical modeling in order to obtain more realistic results. In particular, the simulations of the plasma transport in the SOL of the snowflake divertor, which is found to enhance the effect of the $\vec{E} \times \vec{B}$ drift.

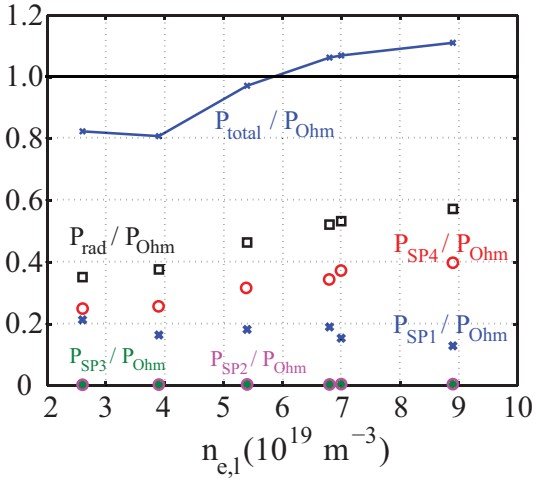

Figure 4.46: Dependence of the fraction of the input power distributed among the SPs from 1 up to 4, and radiated in a SF+ configuration with $\sigma = 0.35$ and reversed B_ϕ. The blue line corresponds to the total measured power with respect to the total input power.

4.10 Conclusions

In this work, a detailed analysis of some of the exhaust properties of the SF divertor configurations generated in TCV is provided. An analysis of the geometrical properties of the SOL in snowflake (SF) configurations with different distances between primary and secondary x-points reveals that only the inner part of the TCV SOL in the vicinity of the separatrix has the properties typically associated with the SF whereas the outer part exhibits characteristics of a conventional single-null (SN) configuration. Therefore, the TCV SF configurations are not suited to demonstrate the exhaust performance of a reactor with a SF divertor but can only be used to investigate SF features in the vicinity of the separatrix.

To increase the insight into the physical processes involved in the SOL plasma transport of the SF divertor, the experimental characterization of some of its exhaust properties was followed by a modeling of the particle, momentum and energy transport. In the experimental part, a wide range of SF configurations were generated in TCV using

the unique capabilities of its shaping coil system. The experiments were performed at sufficiently low densities as to keep the divertor legs in the attached regime, so that most of the power that enters the SOL is exhausted in the vicinity of the strike points allowing for a study of the transport in the null-point region through measurements at the targets. Target heat fluxes are measured at each of the four SPs in both the SF+ and SF- configurations. These experiments demonstrated some basic properties of the SF+ and SF- configurations. The SF- configuration forks one side of the SOL towards two divertor legs with the power largely following the magnetic field lines. The power on one side of the SOL can therefore be shared between two SPs. However, the power on the other side of the SOL remains unaffected. In configurations and scenarios with a significant asymmetry between the power distribution to the primary SPs on the low- and high-field side, the SF- allows for a better distribution of the exhaust power among three of the four SPs. In the SF+, the secondary SPs are located in the private flux region (PFR) of the primary separatrix. Therefore, the heat fluxes detected at the secondary SPs are caused by transport across the primary separatrix. As expected, the fraction of the power detected at the secondary SPs increases with decreasing distance between primary and secondary separatrices, i.e. decreasing σ. The SOL width was not affected by the decrease of σ. This invariance is consistent with changes of the connection length and SOL volume being limited to a small fraction of the TCV SOL in the immediate vicinity of the separatrix. In both SF+ and SF- configurations, a significant reduction of the peak heat fluxes on the targets is observed with respect to the reference SN configuration. Since the input power and the radiated power fraction remain about the same, the power balance features a, so far unexplained, power deficit, which raises a concern about the accuracy of the heat flux measurements.

Activation of the additional strike points of a SF+ configuration was examined where the exact SF is approached with two proximity criteria evaluated. The first links the appearance of some SF features with the distance between the two x-points becoming smaller than the SOL width in the vicinity of the null points, so that conventional cross-field transport should lead to heat fluxes across the region between primary and secondary separatrices towards secondary SPs. The second criterion is based on the hypothesis that a convective plasma cell in the null-point region of any diverted configuration enhances the transport into the PFR [175]. The observed activation of the secondary SPs is found to be consistent with the first criterion, but not the second. Experiments with increased heating power have further demonstrated that convective cells did not contribute to the observed power distribution to SP3. Although the convective cell appears to be unimportant in the L-mode experiments presented in this thesis, it may still explain the observed increased power distribution to SP3 during ELMs in H-mode discharges in TCV [2].

Experiments with high values of plasma density were carried out in order to study the effect of the SF configuration on the radiated power fraction. Contrary to the initial expectations, the measurements show that at higher plasma densities the SN configuration

radiates about 10% more power than the SF. Although this observation is opposite to the expected behaviour of a SF divertor, it is consistent with the fact that in TCV the SOL volume in a SN is slightly larger than that in a SF configuration. Concerning the target heat flux profiles, the measurements show a double-peaked heat flux profile at SP1 in the SF configuration while a conventional single-peaked profile is observed in the SN configuration. This second peak appears in the SOL side of the profiles and its amplitude increases with the plasma density. In order to interpret these experimental observations, full particle, momentum and energy transport simulations were performed using the EMC3 code, which models the steady state edge plasma transport based on the fluid approach, coupled to the Eirene code, which models the dynamics of the production and transport of neutral particles using a kinetic approach. The motivation for the use of a 3D code to model a toroidally symmetric configuration such as the SF divertor is purely technical, namely to use the 3D feature of the code to treat the complex magnetic geometry of the SF divertor. These were the first simulations of a SF divertor including both the primary and secondary x-points [139].

A comparison between the EMC3-Eirene simulations of the SF+ and the measurements of the power distribution to the secondary SPs shows that the transport cannot be described by the change in the field line geometry while keeping transport coefficients constant, suggesting the existence of an additional transport channel in the null-point region. Furthermore, the simulations predict that when σ is reduced, the density peak originally located in front of the target moves upstream leading to the formation of a density blob at the null-point. Experiments to verify the existence of this predicted density blob remain to be carried out.

Diffusive cross-field transport was insufficient to explain the observed enhanced power distribution to the secondary SPs and the double-peaked heat flux profiles at SP1. Two assumptions present in the EMC3 model were examined to explain the discrepancies between measurements and simulations: the absence of volume recombination and particle drifts. Whilst neglecting volumetric recombination is well justified, the $\vec{E} \times \vec{B}$ drift is expected to significantly affect the plasma transport in the entire SOL. Qualitative extrapolations of the expected effects of the $\vec{E} \times \vec{B}$ drift on the target particle and heat flux profiles show that the $\vec{E} \times \vec{B}$ drift can explain some discrepancies between measurements and simulations. As the $\vec{E} \times \vec{B}$ drift direction depends on the toroidal magnetic field direction, experiments with reversed toroidal magnetic field were performed to ascertain the influence of this term. The qualitative agreement between the experiments and the expected effects of the $\vec{E} \times \vec{B}$ drift on the simulated target profiles strongly suggests that the $\vec{E} \times \vec{B}$ drift is responsible for a significant fraction of the transport in the SOL of a SF configuration. Therefore, its effects have to be accounted in numerical modeling to obtain more meaningful results.

5 Conclusions

In this thesis, two outstanding issues encountered in nuclear fusion were addressed: the triggering of neoclassical tearing modes by sawteeth and the handling of the exhaust power in the divertor. In this final chapter, the main achievements of this thesis will be summarized and are provided separately for each subject. It should be noted that a more detailed discussion of the results is provided in sections 3.9 and 4.10.

5.1 Sawtooth Generated Magnetic Islands

In the ITER $Q = 10$ scenario, the presence of fusion produced α-particles is expected to engender sawtooth periods sufficiently long to destabilize NTMs. As NTMs can impose severe constraints on the plasma performance possibly leading to disruptions, NTMs pose a threat to the main goal of ITER, which is to demonstrate a sustained burning plasma operation with a fusion power gain factor $Q \gtrsim 10$.

Different methods for NTM prevention are foreseen for ITER, e.g. electron cyclotron heating and current drive. However, studies have shown that off-axis power deposition decreases the fusion gain factor Q [28]. In addition, the use of such methods adds complexity and affects reliability. NTMs are, therefore, thought to be one of the critical limiting plasma instabilities for the ITER $Q = 10$ scenario.

This work provides a new insight into the role of ST on NTM triggering that can be used for the development of more efficient strategies in their avoidance to improve the plasma scenarios available in future devices like ITER. This study was made possible using TCV's ability to accurately control the period of individual ST using localized ECH and ECCD. TCV's high power and flexible EC heating system was used to trigger NTMs under controlled conditions providing an excellent, and somewhat unique, environment for the study of the triggering of NTMs by ST crashes. The study of the MHD activity at times as close as possible to the ST crash time was enhanced using a new analysis of fast magnetic fluctuation measurements based on the full toroidal array of magnetic probes.

The key feature of this analysis is the use of instantaneous spatial decomposition into toroidal mode components and integrated magnetic probe signals, in order to separate changes of the mode amplitude and phase velocity that occur on similar time scales.

A detailed analysis of the dynamics of the seeding of NTMs by ST crashes shows evidence that seed islands for both, 3/2 and 2/1 NTMs, are already present in the plasma within a few microseconds after the ST crash time. This is consistent with the time scale of about 100 Alfvén times obtained from numerical simulations [125, 126]. Since seed islands can be observed in the plasma at a finite size within a few tens of microseconds, strategies for NTM prevention in ITER cannot reply on a slow growth of the mode amplitude. Understanding the underlying physics of the seeding and preemption of NTMs, as presented in this thesis, may now be used in the development of new strategies to avoid ST triggering of NTMs in ITER. This thesis showed that preemptive ECH enlarges TCV's plasma operational domain by increasing the critical island width through an improved plasma stability to tearing modes and by reducing the coupling between driving and driven modes, resulting in smaller ST generated seed islands. This two-fold beneficial effect increases with the ECH pulse duration and is more efficient when the pulse is closer to, but before, the ST crash.

This thesis showed that accurate knowledge of the timing of the upcoming ST crash can be a key factor in efficient EC usage and thus, improving plasma performance. Since ST period control also requires significant EC power, preemptive EC power coupled with real-time calculations of the time of the next ST crash may become the best strategy to minimize the amount of EC power necessary for NTM control in ITER.

5.2 Properties of the Snowflake Divertor

In DEMO and in future fusion power plants, the severity of the power handling in the divertor will substantially increase since the fusion power and corresponding auxiliary heating power are predicted to be around 3-10 times larger than those in ITER while its linear dimensions will increase by only about 50%. Successful power handling in DEMO and reactor-size machines requires over 80% of the total heating power to be radiated from the plasma core [31], assuming a conventional divertor with the same constraints of ITER. It remains unclear whether these conditions can be sustained and will be compatible with an acceptable energy confinement, motivating the research and development of new divertor concepts that increase the radiated fraction.

The snowflake [32] is one of several divertor configurations that have emerged as alternative options to the conventional divertor configuration. This work provides a detailed analysis of some of the exhaust properties of the SF divertor configurations generated on TCV. To provide a better insight into the physical processes involved in the plasma transport in the SOL of the SF divertor, the experimental characterization of its exhaust properties

were examined by modeling the particle, momentum and energy transport in the SOL using the EMC3-Eirene code. The well established SF configurations available on TCV makes it one of the few machines where details of the plasma transport in the complex topologies of the SF+ and SF- divertor can be studied. The unique capabilities of the TCV poloidal shaping coil system is used in this thesis to examine a wide range of SF configurations.

A comparison between the geometrical properties of the SOL of a SF configuration with those of a conventional divertor shows that SF features are only present on TCV in the vicinity of the separatrix. The fact that only a small part of the SOL exhibits SF features is a characteristic of a tokamak of the size of TCV. However, the properties of the SF are predicted to be significantly enhanced in a reactor-size device like DEMO [138]. While the TCV SOL is, therefore, not suited to demonstrate the sought of improved exhaust performance of a reactor, it remains an excellent device to investigate the underlying physics that will determine the exhaust performance of a reactor with a SF divertor.

The experiments presented herein demonstrated many basic properties of the SF+ and SF- configurations. Measurements of the power distribution between the four SPs show that the SF- configuration forks one side of the SOL towards two divertor legs with the power largely following the magnetic field lines. In configurations with a significant asymmetry between the power distribution to the primary SPs on the low- and high-field side, the SF- allows for a better distribution of the exhaust power on three of the four available SPs. With increased plasma density, the SN configuration radiates around 10% more power than the SF. Although this observation is in contradiction to the expected behavior, it is consistent with the slightly larger SOL volume in a SN configuration.

The complex magnetic geometry of the SF configuration was also used to challenge the existing models of edge plasma transport. A comparison between measurements and simulations shows that the observed fraction of the power distributed to secondary SPs in a SF+ configuration cannot be described by changes in the field line geometry with constant transport coefficients. This comparison suggests an additional cross-field transport channel in the null-point region. Diffusive cross-field transport alone is found to be insufficient to explain the observed double-peaked heat flux profiles. Qualitative extrapolations of the predicted effects of the $\vec{E} \times \vec{B}$ drift on the target particle and heat flux profiles show that the $\vec{E} \times \vec{B}$ drift can explain some discrepancies between measurements and simulations. Experiments in reversed toroidal magnetic field confirmed a significant influence of the $\vec{E} \times \vec{B}$ drift on the edge plasma transport in the SF. The qualitative agreement between the experiments and the predicted effects of the $\vec{E} \times \vec{B}$ drift on the simulated target profiles demonstrated that these $\vec{E} \times \vec{B}$ drifts are responsible for a significant fraction of the plasma transport in the SOL.

To reliably extrapolate these experimental results from TCV to reactor-size machines using modeling, an improved physical understanding of the SF divertor is required. This

thesis showed that the modified magnetic geometry of the SF divertor leads to an enhanced cross-field transport in the null-point region caused by the $\vec{E} \times \vec{B}$ drift. Therefore, these effects must be included in the present transport models to study the SF divertor, before these models can provide reliable and predictive tools for use in improving the design of the divertor for future fusion devices.

A Infrared Data Analysis

In this appendix, more details about the infrared thermography systems of TCV and the data analysis procedures will be provided.

A.1 Main features of an optical system

In the following, the main features of an optical system will be reviewed and used to describe the vertical and horizontal IR optical systems of TCV.

In an image-forming optical system composed of the object of interest, the optical system and a detector, only the fraction of the total number of photons that are emitted by a material surface into the solid angle of the optical system, $d\Omega = A_{EP}/d^2$, are transferred to the detector. Here, A_{EP} is the area of the entrance pupil of the optical system and d the distance between the emitting surface and the entrance pupil.

The size of the emitting surface seen by a detector with a pixel area A_{pixel} is determined by the magnification of the optical system, $\beta = \pm\sqrt{A_{pixel}/A_{target}}$. For real images, the magnification is negative whilst for virtual images it is positive. The number of photons arriving on the entrance pupil per second, with wavelength between λ and $\lambda + d\lambda$, being received by the detector then becomes

$$\frac{d\Phi_{Det}}{d\lambda} = \int\int \frac{d^3\Phi_{ph}}{dAd\Omega d\lambda} dAd\Omega = \frac{d^3\Phi_{ph}}{dAd\Omega d\lambda} A_{target} \frac{A_{EP}}{d^2} = \frac{A_{pixel}}{\beta^2} \frac{A_{EP}}{d^2} \frac{d^3\Phi_{ph}}{dAd\Omega d\lambda}. \quad \text{(A.1)}$$

Using the relation $f/d = \beta/(\beta - 1)$ and the definition of the F-number,

$$F/\# = \frac{f}{D_{EP}} = \sqrt{\frac{\pi}{4A_{EP}}} f, \tag{A.2}$$

equation A.1 can be written, for a real image, as

$$\frac{d\Phi_{Det}}{d\lambda} = \frac{\pi}{4} \frac{A_{pixel}}{(F/\#)^2} \frac{1}{(1+|\beta|)^2} \frac{d^3\Phi_{ph}}{dAd\Omega d\lambda}. \tag{A.3}$$

In the above equations, f is the focal length and D_{EP} is the diameter of the entrance pupil. In non ideal systems, the number of photons available for electron-hole pair production in the detector is further reduced by (i) the emissivity of the target ($\epsilon < 1$), (ii) the limited transmission of the optical system ($\tau < 1$), and (iii) the quantum efficiency of the detector, q_{Det}. Considering the above mentioned loss mechanisms into equation A.3, and assuming that the IR detector is sensitive to wavelengths between λ_1 and λ_2, the number of generated electron-hole pairs per second in the detector can be estimated by

$$\Phi_{Det}(T) = \frac{\pi}{2} \frac{A_{pixel}}{(F/\#)^2} \frac{1}{(1+|\beta|)^2} \int_{\lambda_1}^{\lambda_2} \frac{c}{\lambda^4} \frac{\epsilon(\lambda)\ \tau(\lambda)\ q_{Det}(\lambda)}{exp\left(\frac{hc}{\lambda k_B T}\right) - 1} d\lambda \tag{A.4}$$

In order to produce an image frame, the number of electron-hole pairs generated in each detector within a certain time, Δt (the exposure time), has to be counted thus providing the image signal. The output signal from each detector, $N_{Det}(T, \Delta t)$, is accompanied by a background value, N_{BG}, caused by different effects. Some of them are incomplete absorption of the radiation coming from other IR emitters, the IR emission of the optical components with transmission $\tau < 1$, which heats up during the measurement, and small electric "dark currents" flowing through the detector even when no photons are arriving on it [194]. While these effects vary with time, they are slow compared with the temperature changes of the tokamak wall during a discharge. For this reason, they are assumed to be constant during the discharges, and the total number of counts measured by one detector is given by

$$N_{Det}(T, \Delta t) = N_{BG}(\Delta t) + \frac{\pi c}{2} \frac{A_{pixel}}{(F/\#)^2} \frac{\Delta t}{(1+|\beta|)^2} \int_{\lambda_1}^{\lambda_2} \frac{1}{\lambda^4} \frac{\epsilon(\lambda)\ \tau(\lambda)\ q_{Det}(\lambda)}{exp\left(\frac{hc}{\lambda k_B T}\right) - 1} d\lambda. \tag{A.5}$$

Assuming that the parameters ϵ, τ and q_{Det} have a weak dependence on λ within the range of sensitivity of the detectors ($\lambda_1 = 1.5\,\mu$m and $\lambda_2 = 5.1\,\mu$m for the TCV IR camera) and that the measured temperatures stay below approximately 1000 K, equation A.5 can be approximated by

$$N_{Det}\left(T, \Delta t\right) = N_{BG}\left(\Delta t\right) + \frac{\pi}{2}\frac{A_{pixel}}{(F/\#)^2}\frac{\epsilon\,\tau\,q_{Det}\,\Delta t}{(1+|\beta|)^2}\frac{k_B T}{h\lambda_2^2} exp\left(-\frac{hc}{\lambda_2 k_B T}\right) \tag{A.6}$$

This expression is found to be in good agreement with the experimental calibration curves of the IR diagnostic systems of TCV, as it will be shown later.

A.2 The infrared data analysis workflow

Although equation A.6 can be used to interpret the number of detected photons, N_{Det}, in each detector of the FPA, there are other effects that have to be considered in order to obtain estimates of the tile surface temperature. These effects are: (*i*) the individually different gain and offset of each detector, (*ii*) non-uniformities in the image, (*iii*) "bad" pixels, and (*iv*) vibration of the IR diagnostic system with respect to the image scene. Each of these effects are considered in the data analysis of the IR thermography diagnostic system on TCV and a workflow diagram can be seen in figure A.1.

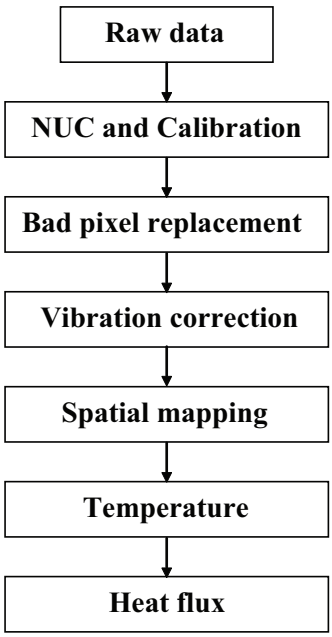

Figure A.1: Workflow diagram of the data analysis of the IR thermography diagnostic systems on TCV.

In this diagram, the first step corresponds to the files containing the raw data acquired during a TCV discharge and stored for a post processing. The details of the hardware related to this step are described in [66]. The other steps of the data analysis will be further discussed in the following apart from the heat flux simulations, which were describe in section 2.2.8.

A.3 Non-uniformity correction and calibration methods

Most of the temperature measurements using IR cameras are based on the relation between the photon flux emitted by a body and its temperature (equation 2.15). If an extended black body is viewed by an IR detector, the acquired image will be simply a measure of the fixed pattern noise caused by the difference in the detector gain and its offset. In order to compensate for these irregularities of the response among pixels, a non-uniformity correction (NUC) must be applied on the acquired image. Several methods exist to correct for non-uniformities [195, 196, 197].

In this work, the calibration-based method was chosen since it is the simplest, most accurate and most common NUC used to correct for non-uniformities. Calibration-based methods include the single point correction (SPC), two point correction (TPC) and the multiple point correction (MPC). In these different methods, the gain and offset of each pixel are estimated by exposing the FPA to uniform black body sources at different temperatures.

The SPC method is used for correcting only the offset of each pixel in the FPA. This is performed by acquiring the image of a non-reflecting body of homogeneous temperature and subtracting it from the acquired images of the objects of interest. This method removes the fixed pattern noise and, therefore, only provides a non-calibrated image.

The TPC method is the most common and widely used method for correcting the non-uniformity of a FPAs. In this method, a constant factor is used for correcting the non-uniformities in the image caused either by the so-called "$\cos^4$" shading, vignetting, or a combination. The $\cos^4$ shading occurs due to the variation of the optical irradiance incident on the FPA relative to an "on axis" circular optical aperture [198] whilst vignetting causes a darkening of the image towards the image corners [199]. This method assumes that the corrected image, I_{NUC}, depends linearly with the photon flux on the detector (equation A.4), which can be written as

$$I_{NUC}\left(T, \Delta t\right) = A\left(\Delta t\right) + B\left(\Delta t\right)\ \Phi_{Det}\left(T\right). \tag{A.7}$$

In this equation, the elements of the integration time-dependent matrix A correspond to the individual pixel offsets while the gain matrix $B = \Delta t\, F$. The elements of the matrix F correspond to the NUC factors of each pixel of the FPA. The offset and gain matrices of an IR optical system are determined by using two images of a black body ($I_{NUC,1}$ and $I_{NUC,2}$) taken at the two different temperatures sufficiently apart (T_1 and T_2). Using equation A.7, the matrices A and B are then given by

$$A\,(\Delta t) = \frac{I_{NUC,1}\ \ \Phi_{Det}\,(T_2) - I_{NUC,2}\Phi_{Det}\,(T_1)}{\Phi_{Det}\,(T_2) - \Phi_{Det}\,(T_1)} \tag{A.8}$$

and

$$B\,(\Delta t) = \frac{I_{NUC,2} - I_{NUC,1}}{\Phi_{Det}\,(T_2) - \Phi_{Det}\,(T_1)}. \tag{A.9}$$

The MPC method is an extension of the TPC method, in which more measurements at different temperatures provide a more precise calibration taking into account possible non-linearities of the detector response.

In TCV, the TPC method is used for the calibration of the VIR system [66] whereas the MPC method is used for calibrating the HIR system, as it will be discussed in the following sections.

A.4 The calibration of the VIR system

The VIR optical system is characterized by a spectral range of 3.4 - 5.1 μm and has specifically been designed for the present BWIR TCV camera (1.5 - 5.1 μm). For this system, the TPC method was used for the NUC and temperature calibration of the VIR system [66]. For this, two black body sources were used to estimate the matrices A and B: a large area black body source of dimensions 304 mm$\times$304 mm and emissivity $\epsilon = (0.96 \pm 0.02)$, which can reach temperatures up to 350°C, figure A.2(a), and a small area black body source (cavity) with a circular aperture of diameter 25.4 mm and emissivity $\epsilon > 0.99$, which can reach temperatures up to 1050°C, figure A.2(b). Since the calibration is performed using a black body source with $\epsilon \approx 1$, the measured temperature of the carbon tiles using IR thermography is expected to be lower than the real value. In the previous work, this was corrected by assuming an emissivity for the graphite tiles of $\epsilon = 0.85$.

In order to improve the temperature calibration of the VIR system, the emissivity of the carbon tiles was estimated. For this, a heated tile in the field-of-view of the VIR camera was used in combination with the small area black body source, which was placed inside the TCV vessel. The carbon tile emissivity was estimated by using equation 2.12, in which the radiation emitted by the heated tile, $I(T, \lambda)$, is compared with the radiation emitted by the black body source, $I_{BB}(T, \lambda)$, at the same temperature. This procedure was performed for different temperatures and exposure times, which allowed to determine the value of the emissivity of the graphite tiles $\epsilon = (0.73 \pm 0.08)$. This result allows to determine the average transmission coefficient of the VIR system in the range of sensitivity of the camera, through equation A.6, which is found to be $\tau = (0.76 \pm 0.08)$. This correction in the calibration is found to reduce the uncertainty of the temperature measurements to approximately 5%.

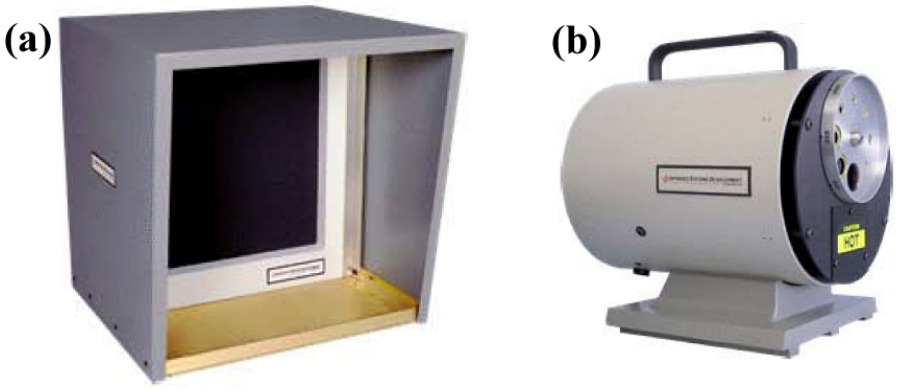

Figure A.2: (a) Large area and (b) circular small area black body sources used for the NUC and temperature calibration of the VIR system.

A.5 The calibration of the HIR system

The HIR optical system was originally designed to be used with a no longer operating IR camera sensitive to longer wavelengths (8.0 - 12.0 μm) compared to those of the present BWIR TCV camera (1.5 - 5.1 μm). Owing to the different wavelength ranges of the HIR optical system and the present TCV IR camera, a reduced transmission of the optical components is expected in the camera wavelength range. This implies in a strong decrease of the number of photons emitted by the tiles surface and arriving on the camera FPA. In addition, the dynamic range of the temperature measurements is also expected to decrease since the low transmission of the optical components in front of the FPA behave as IR emitters and increase the background radiation level. In spite of the reduced number of photons from the tiles surface and the narrower range of observable surface temperatures, the HIR system was found to be able of providing reliable measurements of the surface temperature of the central column tiles.

Since the increased background radiation level could imply that the measurements have to be taken in the non-linear region of the detector response, the MPC method was used for the NUC and temperature calibration. For this purpose, a heated tile was designed and installed in the field-of-view of the HIR camera system. The calibration was performed by acquiring images of the heated tile at different values of temperature, which was monitored by six embedded thermocouples in order to insure that the temperature distribution at the tile surface is approximately homogeneous. Figure A.3(a) and (b) shows the mechanical drawings of the heated tile as well as the cabling of the six thermocouples and of the heating element. Figure A.3(c) shows the heated tile installed on the right side of the tiles housing the Langmuir probes.

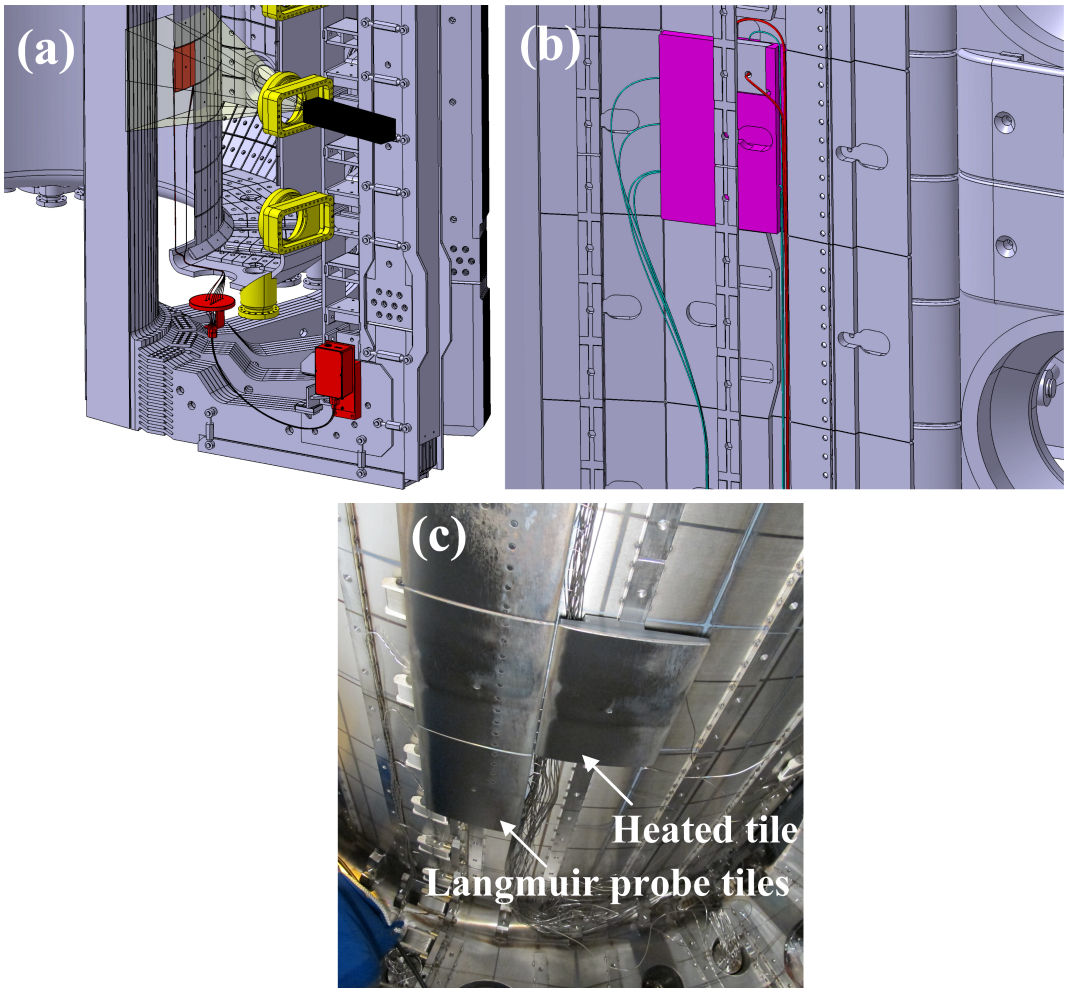

Figure A.3: (a) Mechanical drawing of the heated tile and cabling of the six thermocouples and of the heating element. (b) Close view of the mechanical drawing of the back side of the heated tile. (c) A photo of the heated tile on the right side of the tiles housing the Langmuir probes.

As an example, a calibration curve of the HIR camera system is shown in figure A.4. Due to the reduced transmission of the system, the maximum exposure time ($\Delta t = 1.52\,\mathrm{ms}$)

had to be used during the experiments. Using the parameters of the HIR optical system (F/# = 3.6 and $|\beta| = 49$), the parameters of the IR camera ($A_{pixel} = 40\,\mu\text{m} \times 40\,\mu\text{m}$ and $q_{Det} = 0.8$) and assuming that the tile emissivity of the central column heated tile is approximately equal to that of the floor heated tile ($\epsilon = 0.73$), the fitting of the calibration curve using equation A.6 provides an estimate of the optical transmission of the HIR system $\tau \approx 0.1$, figure A.4.

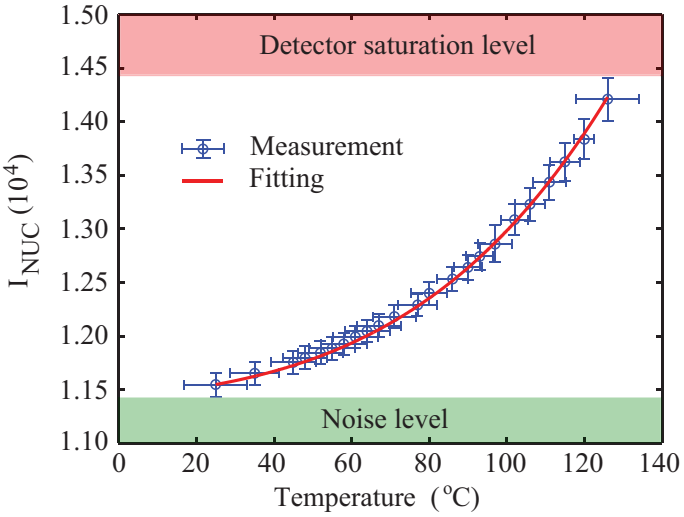

Figure A.4: Calibration curve of the HIR system for an exposure time $\Delta t = 1.52\,\text{ms}$ and fitting of the data using equation A.6.

A.6 Bad pixel detection and replacement

An important issue related to the quality of the IR images is the presence of "bad" pixels. Bad pixels have to be detected and corrected, since they have a large impact on both the image quality and the accuracy of the measurement besides reducing the spatial resolution of the measurements.

When an extended black body is viewed by an IR camera, the temperature measured by the individually calibrated pixels should be close to an average value. However, if the value measured by a pixel diverge excessively from the average value, due to a high noise level during the NUC procedure, or if a high noise level is present during the measurement, the pixel is labelled as a bad pixel. Pixels that cannot be satisfactorily corrected by a NUC procedure are also labelled as bad pixels.

The bad pixel replacement process is highly dependent on the NUC process. There exist various algorithms used to characterize and replace bad pixels, and the one used in this work is the nearest neighbourhood algorithm [200], where the signal of the bad pixel is replaced by the average of its neighbouring pixels. The only condition for this algorithm to be effective is that the neighbouring pixels should not be bad.

A.7 Vibration correction

During a discharge, the mechanical structure of the HIR and VIR systems is found to oscillate with respect to the tokamak. These vibrations have larger amplitudes during the plasma current ramp up and ramp down and are thought to be caused by induced currents in the mechanical structures of the optical systems. In order to reduce the vibrations, the mechanical supports of the systems have been modified. However, a residual image shaking is still observed in the acquired images. Since these vibrations can still lead to erroneous heat flux measurements, the image shaking has to be compensated. In this work, the vibrations in the images have been corrected by estimating the total displacement of a frame, with respect to a reference frame, and displacing the measured frame accordingly. The total displacement of a frame is estimated by calculating the 2D cross-correlation between each frame and the reference frame. The precision of this method is in the sub-pixel range and it has been found to be good enough for correcting the acquired data.

A.8 Spatial mapping

Once the issues related to the quality of the IR images have been solved (NUC, temperature calibration, bad pixel replacement and vibration correction), the individual pixels of the image can be mapped to points in real space. Since the image plane is approximately parallel to the surface of the analysed tiles and the distance between the TCV window and the image plane is significantly larger than the typical distances across a tile, the images can be treated as a planar mesh with equidistant grid points in real space (Z and ϕ for the HIR system, and R and ϕ for the VIR system).

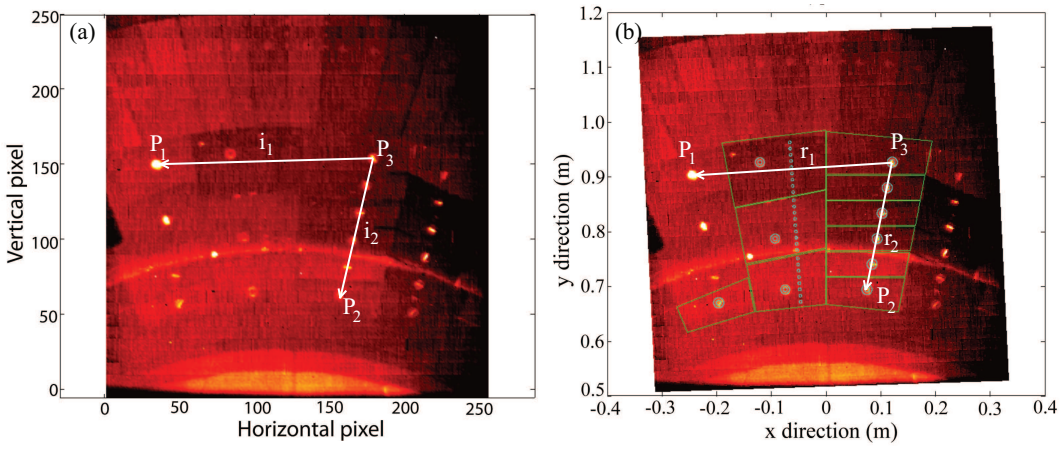

Figure A.5: IR images from the VIR system (a) before and (b) after the spatial mapping.

The spatial mapping is performed by selecting three points in the image that can be recognized in the technical drawings, e.g. tile corners, tile-fixing screws or Langmuir

probes. From these three points (P_1, P_2 and P_3), a 2D vector basis in the image frame can be created

$$\begin{aligned}\vec{i}_1 &= (P_{1h} - P_{3h})\ \hat{e}_h + (P_{1v} - P_{3v})\ \hat{e}_v = i_{1h}\ \hat{e}_h + i_{1v}\ \hat{e}_v \\ \vec{i}_2 &= (P_{2h} - P_{3h})\ \hat{e}_h + (P_{2v} - P_{3v})\ \hat{e}_v = i_{2h}\ \hat{e}_h + i_{2v}\ \hat{e}_v.\end{aligned} \tag{A.10}$$

The same three points also define a basis vector in a Cartesian coordinate system

$$\begin{aligned}\vec{r}_1 &= (P_{1x} - P_{3x})\ \hat{e}_x + (P_{1y} - P_{3y})\ \hat{e}_y = r_{1x}\ \hat{e}_x + r_{1y}\ \hat{e}_y \\ \vec{r}_2 &= (P_{2x} - P_{3x})\ \hat{e}_x + (P_{2y} - P_{3y})\ \hat{e}_y = r_{2x}\ \hat{e}_x + r_{2y}\ \hat{e}_y.\end{aligned} \tag{A.11}$$

Imposing that the vector basis in the IR image be equal to the vector basis in the real space,

$$\begin{bmatrix} i_{1h} & i_{1v} \\ i_{2h} & i_{2v} \end{bmatrix} \begin{bmatrix} e_h \\ e_v \end{bmatrix} = \begin{bmatrix} r_{1x} & r_{1y} \\ r_{2x} & r_{2y} \end{bmatrix} \begin{bmatrix} e_x \\ e_y \end{bmatrix}, \tag{A.12}$$

one finds the coefficients of the transformation matrix M,

$$\begin{bmatrix} e_h \\ e_v \end{bmatrix} = \underbrace{\begin{bmatrix} i_{1h} & i_{1v} \\ i_{2h} & i_{2v} \end{bmatrix}^{-1} \begin{bmatrix} r_{1x} & r_{1y} \\ r_{2x} & r_{2y} \end{bmatrix}}_{M} \begin{bmatrix} e_x \\ e_y \end{bmatrix}, \tag{A.13}$$

that translates, rotates and magnify the IR image. After this procedure, a $Z \times \phi$ (HIR) or $R \times \phi$ (VIR) coordinate is associated to each pixel index. An example of the mapping of an IR image obtained with the VIR system can be seen in figure A.5.

A.9 The heat transmission coefficient

As is the custom with the THEODOR code, the heat transmission coefficient α is adjusted by a fitting procedure, in which the value of α is chosen such that the estimated heat flux to the tile surface be zero for all the times after the end of the discharge. As an example, figure A.6(a) shows the total deposited energy on tile 334 estimated from five THEODOR

simulations with different values of α. As it is shown in the panel (b), the simulation with $\alpha = 9\,\mathrm{kW/m^2/K}$ provides zero deposited power on the tile for all the times after the end of the discharge. In addition, panel (a) shows that this simulation is found to agree with calorimetric estimates based on the thermocouples.

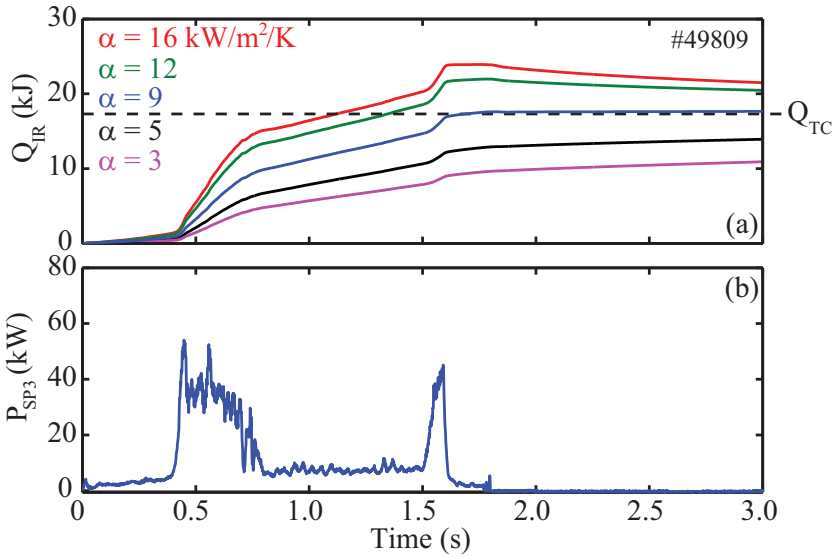

Figure A.6: (a) Comparison between the estimates of the energy stored in tile 334 from the thermocouples and IR thermography. The different curves correspond to different values used in the THEODOR code. (b) Total power deposited in tile 334 estimated assuming $\alpha = 9\,\mathrm{kW/m^2/K}$.

On TCV, the values of α depend on the graphite tile used for the analysis. In 2007, the surface of almost all the TCV graphite tiles were treated using blast with fine B_4C particles. However, in order to study the effects of the tile surface properties on the surface temperature measurements using IR thermography, the three tiles housing the Langmuir probes on the TCV floor were left untreated. For these tiles, the properties of the layer result from approximately one decade of TCV operation and reasonable values of α are found to be approximately $10\,\mathrm{kW/m^2/K}$. For the cleaned/treated tiles, α can be as large as $50\,\mathrm{kW/m^2/K}$. Nevertheless, the estimates of the heat flux from these two surfaces with different properties yields similar values of heat fluxes.

A.10 Errors in the temperature and heat flux measurements

The uncertainty of the temperature measurement is estimated using equation A.5. For simplicity, one assumes that the sensitivity of each detector has a narrow wavelength bandwidth centred at λ_0 such that it can be modelled by a Dirac delta function, $q_{Det}(\lambda) =$

$q_{Det}(\lambda_0)\ \lambda\,\delta(\lambda-\lambda_0)$. Substituting this expression into equation A.5 leads to

$$T=\frac{hc}{\lambda_0 k_B}\frac{1}{\ln\left[1+\frac{K\ \epsilon\ \tau\ q_{Det}}{N_{Det}-N_{BG}}\right]}, \tag{A.14}$$

with $K=\frac{\pi c}{2}\frac{A_{pixel}}{(F/\#)^2}\frac{\Delta t}{(1+|\beta|)^2}\frac{1}{\lambda_0^3}$. The error in the measured temperature is estimated by

$$\Delta T=\left[\left(\frac{\partial T}{\partial K}\right)^2\Delta K^2+\left(\frac{\partial T}{\partial \epsilon}\right)^2\Delta\epsilon^2+\left(\frac{\partial T}{\partial \tau}\right)^2\Delta\tau^2+ \right. \\ \left. +\left(\frac{\partial T}{\partial q_{Det}}\right)^2\Delta q_{Det}^2+\left(\frac{\partial T}{\partial N_{BG}}\right)^2\Delta N_{BG}^2\right]^{1/2}, \tag{A.15}$$

where ΔK is the uncertainty of the constant K, $\Delta\epsilon$ the uncertainty of the tile emissivity, $\Delta\tau$ the uncertainty of the transmission of the optical system, Δq_{Det} the uncertainty of the detector sensitivity and ΔN_{BG} the uncertainty of the background level of the output signal of the detector. Finally, the expression for the relative error of the temperature measurements is given by

$$\frac{\Delta T}{T}=\frac{\lambda_0 k_B T}{hc}\left[1-e^{-\frac{hc}{\lambda_0 k_B T}}\right]\left[\left(\frac{\Delta K}{K}\right)^2+\left(\frac{\Delta\epsilon}{\epsilon}\right)^2+ \right. \\ \left. +\left(\frac{\Delta\tau}{\tau}\right)^2+\left(\frac{\Delta q_{Det}}{q_{Det}}\right)^2+\left(\frac{\Delta N_{BG}}{N_{Det}(T)-N_{BG}}\right)^2\right]^{1/2}. \tag{A.16}$$

It is interesting to note that the uncertainty from the different components of the optical system is modulated by a factor that depends on the temperature. For the range of temperatures encountered during this thesis, this factor is found to be about 0.1 and, even if an uncertainty of 25% is assumed for the value of each of the different contributions in equation A.16, the total uncertainty of the temperature measurements is found to be approximately 5%.

For estimating the error in the target heat flux measurements, equations 2.17 and A.16 are used. Applying the error propagation procedure described above and neglecting the uncertainty of the variable T_{bulk} due to the lack of an estimate, a lower boundary for the

relative error of the target heat flux estimates is

$$\frac{\Delta q_t}{q_t} = \left[\left(\frac{\Delta \alpha}{\alpha} \right)^2 + \left(\frac{\alpha\, T}{q_t} \frac{\Delta T}{T} \right)^2 \right]^{1/2} . \tag{A.17}$$

Here, $\Delta\alpha$ is the uncertainty of the heat transmission coefficient, which is equal to the interval between the values of α in the different THEODOR simulations. The typical value of $\Delta\alpha$ during this work is $0.5\,\mathrm{kW/m^2/K}$ implying that the uncertainty of the heat flux estimates is completely dominated by the uncertainty of the temperature measurements. For the measurements presented in the chapter 4, the uncertainty of the heat flux measurements around the strike points is usually found to be smaller than approximately 25%.

A.11 Infrared thermography vs calorimetric measurements

Since the estimates of the target heat flux based on the IR thermography depend on the value of the α assumed in the THEODOR simulation, the total amount of energy deposited in the tile estimated from the IR thermography is compared against calorimetric measurements (see section 2.2.7). As it can be seen in figure A.7, the values of the energy deposited in a tile estimated using IR thermography are found to be consistent with those obtained from calorimetric measurements.

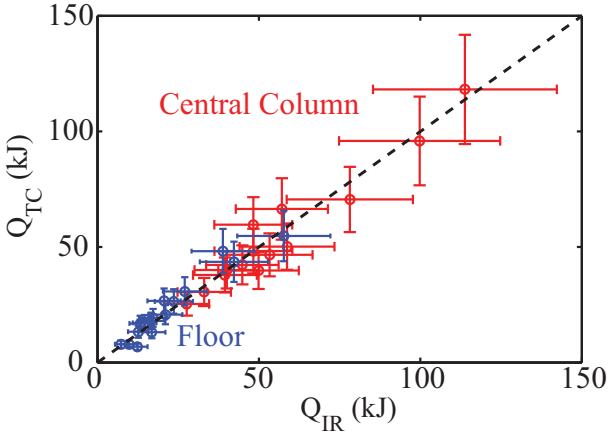

Figure A.7: Comparison between the stored energy in the TCV wall from IR thermography and calorimetric measurements.

Bibliography

[1] J.P. Graves. Kinetic stabilisation of the internal kink mode for fusion plasmas. *PhD thesis no.323191, University of Nottingham, Nottingham NG7 2NR, United Kingdom*, 1999. http://hdl.handle.net/10068/678755.

[2] W.A.J. Vijvers *et al.* Power exhaust in the snowflake divertor for L- and H-mode TCV tokamak plasmas. *Nuclear Fusion*, 54(2):023009, 2014. http://stacks.iop.org/0029-5515/54/i=2/a=023009.

[3] International Energy Agency. World Energy Outlook (November 2013). 2013. http://www.worldenergyoutlook.org/publications/weo-2013/.

[4] U.S. Department of Energy. International Energy Outlook (July 2013). 2013. http://www.eia.gov/forecasts/ieo/index.cfm.

[5] D.J.C. MacKay. Sustainable Energy - without the hot air. *UIT Cambridge Ltd*, 2009. http://www.inference.phy.cam.ac.uk/sustainable/book/tex/cft.pdf.

[6] J.P. Freidberg. *Plasma Physics and Fusion Energy.* Cambridge University Press, London, 2007.

[7] J.A. Wesson. *Tokamaks.* Clarendon Press, Oxford, 2^{th} edition, 1997.

[8] L.A. Artsimovich. Tokamak devices. *Nuclear Fusion*, 12(2):215, 1972. http://stacks.iop.org/0029-5515/12/i=2/a=012.

[9] L.A. Artsimovich *et al.* Experiments in tokamak devices. *3^{rd} International Conference on Plasma Physics and Controlled Fusion Research*, 1:157, 1968.

[10] R.J. Bickerton *et al.* Diffusion driven plasma currents and bootstrap tokamak. *Nature Physical Science*, 229:110–112, 1971. http://www.nature.com/nature-physci/journal/v229/n4/abs/physci229110a0.html.

[11] C.E. Kessel. Bootstrap current in a tokamak. *Nuclear Fusion*, 34(9):1221–1238, 1994. http://stacks.iop.org/0029-5515/34/i=9/a=I04.

[12] A.G. Peeters. The bootstrap current and its consequences. *Plasma Physics and Controlled Fusion*, 42(12B):B231, 2000. http://stacks.iop.org/0741-3335/42/i=12B/a=318.

[13] O. Sauter *et al.* Steady-state fully noninductive current driven by electron cyclotron waves in a magnetically confined plasma. *Physical Review Letters*, 84:3322–3325, 2000. http://link.aps.org/doi/10.1103/PhysRevLett.84.3322.

[14] O. Sauter *et al.* Steady-state fully noninductive operation with electron cyclotron current drive and current profile control in the tokamak à configuration variable (TCV). *Physics of Plasmas*, 8(5):2199–2207, 2001. http://scitation.aip.org/content/aip/journal/pop/8/5/10.1063/1.1355317.

[15] P.C. Stangeby. *The Plasma Boundary of Magnetic Fusion Devices.* Institute of Physics Publishing, London, 2000.

[16] L. Spitzer. US atomic energy commission report. *Technical Report*, NYO-993 (PM-S-1), 1951.

[17] L. Spitzer. The stellarator concept. *The Physics of Fluids*, 1(4):253–264, 1958. http://scitation.aip.org/content/aip/journal/pof1/1/4/10.1063/1.1705883.

[18] C.S. Pitcher and P.C. Stangeby. Experimental divertor physics. *Plasma Physics and Controlled Fusion*, 39(6):779–930, 1997. http://stacks.iop.org/0741-3335/39/i=6/a=001.

[19] J. Friedberg. *Ideal Magnetohydrodynamics.* Plenum Press, New York, 1987.

[20] J.D Lawson. Some criteria for a power producing thermonuclear reactor. *Proceedings of the Physical Society. Section B*, 70(1):6, 1957. http://stacks.iop.org/0370-1301/70/i=1/a=303.

[21] T.C. Hender *et al.* Chapter 3: MHD stability, operational limits and disruptions. *Nuclear Fusion*, 47(6):S128–S202, 2007. http://stacks.iop.org/0029-5515/47/i=6/a=S03.

[22] Z. Chang *et al.* Observation of nonlinear neoclassical pressure-gradient-driven tearing modes in TFTR. *Physical Review Letters*, 74(23):4663–4666, 1995. http://link.aps.org/doi/10.1103/PhysRevLett.74.4663.

[23] O. Sauter *et al.* Beta limits in long-pulse tokamak discharges. *Physics of Plasmas*, 4(5):1654–1664, 1997. http://scitation.aip.org/content/aip/journal/pop/4/5/10.1063/1.872270.

[24] http://www.iter.org/.

[25] H.R. Koslowski *et al.* Operational limits and limiting instabilities in tokamak machines. *Transactions of Fusion Science and Technology*, 61(2T):96–103, 2012. http://epubs.ans.org/download/?a=13496.

[26] I.T. Chapman *et al.* Empirical scaling of sawtooth period for onset of neoclassical tearing modes. *Nuclear Fusion*, 50(10):102001, 2010. http://stacks.iop.org/0029-5515/50/i=10/a=102001.

[27] I.T. Chapman *et al.* The physics of sawtooth stabilization. *Plasma Physics and Controlled Fusion*, 49(12B):B385–B394, 2007. http://stacks.iop.org/0741-3335/49/i=12B/a=S35.

[28] O. Sauter *et al.* On the requirements to control neoclassical tearing modes in burning plasmas. *Plasma Physics and Controlled Fusion*, 52(2):025002, 2010. http://stacks.iop.org/0741-3335/52/i=2/a=025002.

[29] R.A. Pitts *et al.* Status and physics basis of the iter divertor. *Physica Scripta*, 2009(T138):014001, 2009. http://stacks.iop.org/1402-4896/2009/i=T138/a=014001.

[30] M. Kotschenreuther *et al.* On heat loading, novel divertors, and fusion reactors. *Physics of Plasmas*, 14(7):072502, 2007. http://scitation.aip.org/content/aip/journal/pop/14/7/10.1063/1.2739422.

[31] H. Zohm *et al.* On the physics guidelines for a tokamak DEMO. *Nuclear Fusion*, 53(7):073019, 2013. http://stacks.iop.org/0029-5515/53/i=7/a=073019.

[32] D.D. Ryutov. Geometrical properties of a snowflake divertor. *Physics of Plasmas*, 14(6):064502, 2007. http://scitation.aip.org/content/aip/journal/pop/14/6/10.1063/1.2738399.

[33] F. Hofmann *et al.* Creation and control of variably shaped plasmas in TCV. *Plasma Physics and Controlled Fusion*, 36(12B):B277, 1994. http://stacks.iop.org/0741-3335/36/i=12B/a=023.

[34] F. Hofmann. FBT - a free-boundary tokamak equilibrium code for highly elongated and shaped plasmas. *Computer Physics Communications*, 48(2):207–221, 1988. http://www.sciencedirect.com/science/article/pii/0010465588900410.

[35] M.R. Perrone *et al.* Stability of axisymmetric modes in JET. *Nuclear Fusion*, 21(7):871–879, 1981. http://stacks.iop.org/0029-5515/21/i=7/a=009.

[36] F. Hofmann *et al.* Stability and energy confinement of highly elongated plasmas in TCV. *Plasma Physics and Controlled Fusion*, 43(12A):A161–A173, 2001. http://stacks.iop.org/0741-3335/43/i=12A/a=312.

[37] F. Piras *et al.* Snowflake divertor plasmas on TCV. *Plasma Physics and Controlled Fusion*, 51(5):055009, 2009. http://stacks.iop.org/0741-3335/51/i=5/a=055009.

[38] W.A.J. Vijvers *et al.* Power exhaust in all geometric variations of the snowflake divertor on TCV. *Conference on Plasma Physics: 55th APS, Denver*, 58(16):PP8.47, 2013. http://meetings.aps.org/Meeting/DPP13/Session/PP8.47.

[39] W.A.J. Vijvers *et al.* First experimental demonstration of heat load mitigation with an X-divertor in a tokamak. *To be submitted to Nuclear Fusion*, 2014.

[40] T.P. Goodman *et al.* Design and installation of the electron cyclotron wave system for the TCV tokamak. *Fusion Technology 1996*, pages 565 – 568, 1997. url-http://www.sciencedirect.com/science/article/pii/B9780444827623501117.

[41] T.P. Goodman. Experience in integrated control of the multi-megawatt electron cyclotron heating system on the TCV tokamak: the first decade. *Nuclear Fusion*, 48(5):054011, 2008. http://stacks.iop.org/0029-5515/48/i=5/a=054011.

[42] F. Felici *et al.* Integrated real-time control of MHD instabilities using multi-beam ECRH/ECCD systems on TCV. *Nuclear Fusion*, 52(7):074001, 2012. http://stacks.iop.org/0029-5515/52/i=7/a=074001.

[43] R.A. Pitts *et al.* The design of central column protection tiles for the TCV tokamak. *Nuclear Fusion*, 39(10):1433–1449, 1999. http://stacks.iop.org/0029-5515/39/i=10/a=306.

[44] I.H. Hutchinson. *Principles of plasma diagnostics*. Cambridge University Press, New York, 2005.

[45] S. Barry *et al.* Far-infrared polarimetry on the TCV tokamak. *Proceedings of the 8$^{\text{th}}$ International Symposium on Laser-aided Plasma Diagnostics (LAPD-8), Doorwerth*, 1997.

[46] S. Barry. The extension of the FIR interferometer of TCV to a polarimeter and measurements of the Faraday rotation caused by the poloidal magnetic field. *PhD thesis, National University of Ireland, Cork, Ireland - also available as Lausanne Report LRP 638/99*, 1999. http://infoscience.epfl.ch/record/121172/files/lrp_638_99_hq.pdf.

[47] S. Franke. Application of Thomson scattering at 1.06 mm as a diagnostic for spatial profile measurements of electron temperature and density on the TCV tokamak. *PhD thesis no.1654, École Polytechnique Fédérale de Lausanne (EPFL), CH-1015 Lausanne, Switzerland*, 1997. http://dx.doi.org/10.5075/epfl-thesis-1654.

[48] A. Pitzschke. Pedestal characteristics and MHD stability of H-mode plasmas in TCV. *PhD thesis no.4917, École Polytechnique Fédérale de Lausanne (EPFL), CH-1015 Lausanne, Switzerland*, 2011. http://dx.doi.org/10.5075/epfl-thesis-4917.

[49] K.F. Mast *et al.* Bolometric diagnostics in JET. *Review of Scientific Instruments*, 56(5):969–971, 1985. http://scitation.aip.org/content/aip/journal/rsi/56/5/10.1063/1.1138007.

[50] K.F. Mast *et al.* A low noise highly integrated bolometer array for absolute measurement of VUV and soft x radiation. *Review of Scientific Instruments*, 62(3):744–750, 1991. http://scitation.aip.org/content/aip/journal/rsi/62/3/10.1063/1.1142078.

[51] J.C. Fuchs *et al.* Radiation distribution and energy balance during type-I ELMs in ASDEX Upgrade. *Journal of Nuclear Materials*, 337–339(0):756–760, 2005. http://www.sciencedirect.com/science/article/pii/S0022311504009444.

[52] A. Sushkov *et al.* High-resolution multiwire proportional soft x-ray diagnostic measurements on tcv. *Review of Scientific Instruments*, 79(2), 2008. http://scitation.aip.org/content/aip/journal/rsi/79/2/10.1063/1.2833822.

[53] Y. Camenen. Étude du transport d'énergie thermique dans les plasmas du tokamak à configuration variable au moyen de chauffage électronique cyclotronique. *PhD thesis no.3618, École Polytechnique Fédérale de Lausanne (EPFL), CH-1015 Lausanne, Switzerland*, 2006. http://dx.doi.org/10.5075/epfl-thesis-3618.

[54] F. Hofmann *et al.* Tokamak equilibrium reconstruction using faraday rotation measurements. *Nuclear Fusion*, 28(10):1871–1878, 1988. http://stacks.iop.org/0029-5515/28/i=10/a=014.

[55] J.-M. Moret *et al.* Magnetic measurements on the TCV tokamak. *Review of Scientific Instruments*, 69(6):2333–2348, 1998. http://scitation.aip.org/content/aip/journal/rsi/69/6/10.1063/1.1148940.

[56] H. Reimerdes. MHD stability limits in the TCV tokamak. *PhD thesis no.2399, École Polytechnique Fédérale de Lausanne (EPFL), CH-1015 Lausanne, Switzerland*, 2001. http://dx.doi.org/10.5075/epfl-thesis-2399.

[57] H.M. Mott-Smith and I. Langmuir. The theory of collectors in gaseous discharges. *Physical Review*, 28(4):727–763, 1926. http://link.aps.org/doi/10.1103/PhysRev.28.727.

[58] I.M. Podgornyi. *Topics in Plasma Diagnostics.* Institute of Cosmic Studies, Moscow, 1971.

[59] L. Talbot P.M. Chung and K.J. Touryan. *Electric Probes in Stationary and Flowing Plasmas.* Springer-Verlag, New York, 1975.

[60] R.H. Huddlestone and S.L. Leonard. *Plasma Diagnostic Techniques.* Academic Press, New York, 2001.

[61] D. Bohm. *The Characteristics of Electrical Discharges in Magnetic Field.* McGraw-Hill, New York, 1949.

[62] K.-U. Riemann. The Bohm criterion and sheath formation. *Journal of Physics D: Applied Physics*, 24(4):493, 1991. http://stacks.iop.org/0022-3727/24/i=4/a=001.

[63] M. Bagatin *et al.* Automatic fast fitting of single langmuir probe characteristics on rfx. *Review of Scientific Instruments*, 68(1):365–368, 1997. http://scitation.aip.org/content/aip/journal/rsi/68/1/10.1063/1.1147831, doi = http://dx.doi.org/10.1063/1.1147831.

[64] J. Marki *et al.* Sheath heat transmission factors on TCV. *Journal of Nuclear Materials*, 363–365(0):382–388, 2007. http://www.sciencedirect.com/science/article/pii/S0022311507000761.

[65] G.F. Matthews *et al.* Divertor energy distribution in JET H-modes. *Journal of Nuclear Materials*, 290–293:668 – 672, 2001. http://www.sciencedirect.com/science/article/pii/S0022311500004827.

[66] J. Márki. Infrared thermography of divertor ELM heat loads on TCV. *PhD thesis no.5021, École Polytechnique Fédérale de Lausanne (EPFL), CH-1015 Lausanne, Switzerland*, 2012. http://dx.doi.org/10.5075/epfl-thesis-5021.

[67] W. Herschel *et al.* Experiments on the refrangibility of the visible rays of the sun. *Philosophical Transactions of the Royal Society of London*, 90:284–292, 1800. http://dx.doi.org/10.1098/rstl.1800.0015.

[68] A.F. Milton *et al.* Influence of non-uniformity on infrared focal plane array performance. *Optical Engineering*, 24(5):855–862, 1985. http://dx.doi.org/10.1117/12.7973588.

[69] A. Herrmann *et al.* Limitations for divertor heat flux calculations of fast events in tokamaks. *Controlled Fusion and Plasma Physics: Proc. 28th EPS, Funchal*, ECA Vol. 25A, 2001. http://epsppd.epfl.ch/Madeira/html/pdf/P5.104.pdf.

[70] G.P. Canal *et al.* Fast seeding of NTMs by sawtooth crashes in TCV and their preemption using ECRH. *Nuclear Fusion*, 53(11):113026, 2013. http://stacks.iop.org/0029-5515/53/i=11/a=113026.

[71] S. von Goeler *et al.* Studies of internal disruptions and m=1 oscillations in tokamak discharges with soft x-ray techniques. *Physics Review Letter*, 33(20):1201–1203, 1974. http://link.aps.org/doi/10.1103/PhysRevLett.33.1201.

[72] O. Sauter *et al.* Marginal beta-limit for neoclassical tearing modes in JET H-mode discharges. *Plasma Physics and Controlled Fusion*, 44(9):1999–2019, 2002. http://stacks.iop.org/0741-3335/44/i=9/a=315.

[73] I.T. Chapman. Controlling sawtooth oscillations in tokamak plasmas. *Plasma Physics and Controlled Fusion*, 53(1):013001, 2011. http://stacks.iop.org/0741-3335/53/i=1/a=013001.

[74] F.A.A. Felici. Real-time control of tokamak plasmas: from control of physics to physics-based control. *PhD thesis no.5203, École Polytechnique Fédérale de*

Lausanne (EPFL), CH-1015 Lausanne, Switzerland, 2011. http://dx.doi.org/10.5075/epfl-thesis-5203.

[75] F. Porcelli *et al.* Model for the sawtooth period and amplitude. *Plasma Physics and Controlled Fusion*, 38(12):2163–2186, 1996. http://stacks.iop.org/0741-3335/38/i=12/a=010.

[76] C. Angioni *et al.* Neutral beam stabilization of sawtooth oscillations in JET. *Plasma Physics and Controlled Fusion*, 44(2):205–222, 2002. http://stacks.iop.org/0741-3335/44/i=2/a=305.

[77] J.P. Graves *et al.* Sawtooth-control mechanism using toroidally propagating ion-cyclotron-resonance waves in tokamaks. *Physical Review Letter*, 102(6):065005, 2009. http://link.aps.org/doi/10.1103/PhysRevLett.102.065005.

[78] J.P. Graves *et al.* Recent advances in sawtooth control. *Fusion Science and Technology*, 59(3):539–548, 2011. http://epubs.ans.org/download/?a=11695.

[79] J.P. Graves *et al.* Control of magnetohydrodynamic stability by phase space engineering of energetic ions in tokamak plasmas. *Nature Communications*, 3(624), 2012. http://dx.doi.org/10.1038/ncomms1622.

[80] C. Angioni *et al.* Effects of localized electron heating and current drive on the sawtooth period. *Nuclear Fusion*, 43(6):455, 2003. http://stacks.iop.org/0029-5515/43/i=6/a=308.

[81] Y.R. Lin-Liu *et al.* Modeling of 110 ghz electron cyclotron wave propagation and absorption on DIII-D. *Radio Frequency Power in Plasmas: 12th Topical Conference*, CP403:195, 1997. http://scitation.aip.org/content/aip/proceeding/aipcp/10.1063/1.53363.

[82] T.P. Goodman *et al.* Sawtooth pacing by real-time auxiliary power control in a tokamak plasma. *Physics Review Letter*, 106(24):245002, 2011. http://link.aps.org/doi/10.1103/PhysRevLett.106.245002.

[83] F. Troyon *et al.* MHD-limits to plasma confinement. *Plasma Physics and Controlled Fusion*, 26(1A):209–215, 1984. http://stacks.iop.org/0741-3335/26/i=1A/a=319.

[84] R.J. La Haye *et al.* Neoclassical tearing modes and their control. *Physics of Plasmas*, 13(5):055501, 2006. http://scitation.aip.org/content/aip/journal/pop/13/5/10.1063/1.2180747.

[85] Z. Chang *et al.* Global energy confinement degradation due to macroscopic phenomena in tokamaks. *Nuclear Fusion*, 30(2):219–233, 1990. http://stacks.iop.org/0029-5515/30/i=2/a=003.

[86] S Günter *et al.* Influence of neoclassical tearing modes on energy confinement. *Plasma Physics and Controlled Fusion*, 41(6):767–774, 1999. http://stacks.iop.org/0741-3335/41/i=6/a=306.

[87] H. Zohm *et al.* Neoclassical MHD in ASDEX Upgrade and COMPASS-D. *Plasma Physics and Controlled Fusion*, 39(12B):B237, 1997. http://stacks.iop.org/0741-3335/39/i=12B/a=018.

[88] R.J. Buttery *et al.* Neoclassical tearing modes. *Plasma Physics and Controlled Fusion*, 42:B61–B73, 2000. http://stacks.iop.org/0741-3335/42/i=12B/a=306.

[89] R.J. La Haye *et al.* High beta tokamak operation in DIII-D limited at low density/collisionality by resistive tearing modes. *Nuclear Fusion*, 37(3):397–401, 1997. http://stacks.iop.org/0029-5515/37/i=3/a=I08.

[90] M.F.F. Nave *et al.* Mode locking in tokamaks. *Nuclear Fusion*, 30(12):2575–2583, 1990. http://stacks.iop.org/0029-5515/30/i=12/a=011.

[91] T.C. Luce *et al.* High performance stationary discharges in the DIII-D tokamak. *Physics of Plasmas*, 11(5):2627–2636, 2004. http://scitation.aip.org/content/aip/journal/pop/11/5/10.1063/1.1704644.

[92] E. Westerhof *et al.* Tearing mode stabilization by electron cyclotron resonance heating demonstrated in the TEXTOR tokamak and the implication for ITER. *Nuclear Fusion*, 47(2):85–90, 2007. http://stacks.iop.org/0029-5515/47/i=2/a=003.

[93] O. Sauter *et al.* Neoclassical conductivity and bootstrap current formulas for general axisymmetric equilibria and arbitrary collisionality regime. *Physics of Plasmas*, 6(7):2834–2839, 1999. http://scitation.aip.org/content/aip/journal/pop/6/7/10.1063/1.873240.

[94] O. Sauter *et al.* Erratum: "Neoclassical conductivity and bootstrap current formulas for general axisymmetric equilibria and arbitrary collisionality regime [phys. plasmas 6, 2834 (1999)]". *Physics of Plasmas*, 9(12):5140–5140, 2002. http://scitation.aip.org/content/aip/journal/pop/9/12/10.1063/1.1517052.

[95] H.P. Furth *et al.* Finite-resistivity instabilities of a sheet pinch. *The Physics of Fluids*, 6(4):459–484, 1963. http://scitation.aip.org/content/aip/journal/pof1/6/4/10.1063/1.1706761.

[96] H.P. Furth *et al.* Tearing mode in the cylindrical tokamak. *The Physics of Fluids*, 16(7):1054–1063, 1973. http://scitation.aip.org/content/aip/journal/pof1/16/7/10.1063/1.1694467.

[97] P.H. Rutherford *et al.* Nonlinear growth of the tearing mode. *The Physics of Fluids*, 16(11):1903–1908, 1973. http://scitation.aip.org/content/aip/journal/pof1/16/11/10.1063/1.1694232.

[98] R. Fitzpatrick *et al.* Helical temperature perturbations associated with tearing modes in tokamak plasmas. *Physics of Plasmas*, 2(3):825–838, 1995. http://scitation.aip.org/content/aip/journal/pop/2/3/10.1063/1.871434.

[99] A.H. Glasser *et al.* Resistive instabilities in general toroidal plasma configurations. *The Physics of Fluids*, 18(7):875–888, 1975. http://scitation.aip.org/content/aip/journal/pof1/18/7/10.1063/1.861224.

[100] A.H. Glasser *et al.* Resistive instabilities in a tokamak. *The Physics of Fluids*, 19(4):567–574, 1976. http://scitation.aip.org/content/aip/journal/pof1/19/4/10.1063/1.861490.

[101] H.R. Wilson *et al.* Threshold for neoclassical magnetic islands in a low collision frequency tokamak. *Physics of Plasmas*, 3(1):248–265, 1996. http://scitation.aip.org/content/aip/journal/pop/3/1/10.1063/1.871830.

[102] A.B. Mikhailovskii. Theory of magnetic islands in tokamaks with accenting neoclassical tearing modes. *Contributions to Plasma Physics*, 43(3-4):125–177, 2003. http://dx.doi.org/10.1002/ctpp.200310013.

[103] J.W. Connor *et al.* The role of polarization current in magnetic island evolution. *Physics of Plasmas*, 8(6):2835–2848, 2001.

[104] E. Poli *et al.* Reduction of the ion drive and ρ_θ^* scaling of the neoclassical tearing mode. *Physical Review Letters*, 88:075001, 2002. http://link.aps.org/doi/10.1103/PhysRevLett.88.075001.

[105] C.C. Hegna *et al.* On the stabilization of neoclassical magnetohydrodynamic tearing modes using localized current drive or heating. *Physics of Plasmas*, 4(8):2940–2946, 1997. http://scitation.aip.org/content/aip/journal/pop/4/8/10.1063/1.872426.

[106] A.M. Popov *et al.* Simulation of neoclassical tearing modes in the DIII-D tokamak. II. Suppression by radially localized electron cyclotron current drive. *Physics of Plasmas*, 9(10):4229–4240, 2002. http://scitation.aip.org/content/aip/journal/pop/9/10/10.1063/1.1505843.

[107] G. Gantenbein *et al.* Complete suppression of neoclassical tearing modes with current drive at the electron-cyclotron-resonance frequency in ASDEX Upgrade tokamak. *Physical Review Letters*, 85:1242–1245, 2000. http://link.aps.org/doi/10.1103/PhysRevLett.85.1242.

[108] R. Prater. Heating and current drive by electron cyclotron waves. *Physics of Plasmas*, 11(5):2349–2376, 2004. http://scitation.aip.org/content/aip/journal/pop/11/5/10.1063/1.1690762.

[109] E. Westerhof. Tearing mode stabilization by local current drive density perturbations. *Nuclear Fusion*, 30(6):1143–1147, 1990. http://stacks.iop.org/0029-5515/30/i=6/a=017.

[110] D. De Lazzari *et al.* On the merits of heating and current drive for tearing mode stabilization. *Nuclear Fusion*, 49(7):075002, 2009. http://stacks.iop.org/0029-5515/49/i=7/a=075002.

[111] D. De Lazzari *et al.* Erratum: "On the merits of heating and current drive for tearing mode stabilization [nuclear fusion 49, 075002 (2009)]". *Nuclear Fusion*, 50(7):079801, 2010. http://stacks.iop.org/0029-5515/50/i=7/a=079801.

[112] M.F.F. Nave *et al.* Triggering of neoclassical tearing modes by mode coupling. *Nuclear Fusion*, 43(3):179–187, 2003. http://stacks.iop.org/0029-5515/43/i=3/a=303.

[113] R.J. La Haye *et al.* Increasing the beta limit due to neoclassical tearing modes by raising the axial safety factor q(0) $>$ 1. *Nuclear Fusion*, 40(1):53–58, 2000. http://stacks.iop.org/0029-5515/40/i=1/a=304.

[114] O. Sauter *et al.* Control of neoclassical tearing modes by sawtooth control. *Physics Review Letter*, 88(10):105001, 2002. http://link.aps.org/doi/10.1103/PhysRevLett.88.105001.

[115] A. Gude *et al.* Seed island of neoclassical tearing modes at ASDEX upgrade. *Nuclear Fusion*, 39(1):127–131, 1999. http://stacks.iop.org/0029-5515/39/i=1/a=308.

[116] B.W. Rice *et al.* Progress towards sustainment of advanced tokamak modes in DIII-D. *Nuclear Fusion*, 39(11Y):1855–1864, 1999. http://stacks.iop.org/0029-5515/39/i=11Y/a=326.

[117] H. Reimerdes *et al.* From current-driven to neoclassically driven tearing modes. *Physics Review Letter*, 88(10):105005, 2002. http://link.aps.org/doi/10.1103/PhysRevLett.88.105005.

[118] D.P. Brennan *et al.* Tearing mode stability studies near ideal stability boundaries in DIII-D. *Physics of Plasmas*, 9(7):2998–3006, 2002. http://scitation.aip.org/content/aip/journal/pop/9/7/10.1063/1.1481504.

[119] R.J. Buttery *et al.* The influence of rotation on the normalized beta threshold for the 2/1 neoclassical tearing mode in DIII-D. *Physics of Plasmas*, 15(5):056115, 2008. http://scitation.aip.org/content/aip/journal/pop/15/5/10.1063/1.2894215.

[120] J.W. Connor *et al.* Tearing modes in toroidal geometry. *The Physics of Fluids*, 31(3):577–590, 1988. http://scitation.aip.org/content/aip/journal/pof1/31/3/10.1063/1.866840.

[121] C.C. Hegna *et al.* Dynamics of seed magnetic island formation due to geometrically coupled perturbations. *Physics of Plasmas*, 6(1):130–136, 1999. http://scitation.aip.org/content/aip/journal/pop/6/1/10.1063/1.873265.

[122] R. Fitzpatrick *et al.* Stability of coupled tearing modes in tokamaks. *Nuclear Fusion*, 33(10):1533–1576, 1993. http://stacks.iop.org/0029-5515/33/i=10/a=I11.

[123] P. Maget *et al.* MHD activity triggered by monster sawtooth crashes on Tore Supra. *Plasma Physics and Controlled Fusion*, 47(2):357–377, 2005. http://stacks.iop.org/0741-3335/47/i=2/a=010.

[124] R.J. Buttery *et al.* Onset of neoclassical tearing modes on JET. *Nuclear Fusion*, 43(2):69–83, 2003. http://stacks.iop.org/0029-5515/43/i=2/a=301.

[125] A.M. Popov *et al.* Simulation of neoclassical tearing modes (NTMs) in the DIII-D tokamak. I. NTM excitation. *Physics of Plasmas*, 9(10):4205–4228, 2002. http://scitation.aip.org/content/aip/journal/pop/9/10/10.1063/1.1505842.

[126] D.P. Brennan *et al.* A categorization of tearing mode onset in tokamaks via nonlinear simulation. *Nuclear Fusion*, 45(9):1178–1190, 2005. http://stacks.iop.org/0029-5515/45/i=9/a=018.

[127] A.M. Popov *et al.* Nonlinear three-dimensional self-consistent simulations of negative central shear discharges in the DIII-D tokamak. *Physics of Plasmas*, 8(8):3605–3619, 2001. http://scitation.aip.org/content/aip/journal/pop/8/8/10.1063/1.1380235.

[128] C.R. Sovinec *et al.* Nonlinear magnetohydrodynamics simulation using high-order finite elements. *Journal of Computacional Physics*, 195(1):355–386, 2004. http://www.sciencedirect.com/science/article/pii/S0021999103005369.

[129] K. Ikeda *et al.* Progress in the ITER physics basis. *Nuclear Fusion*, 47(6):S128–S202, 2007. http://stacks.iop.org/0029-5515/47/i=6/a=E01.

[130] J.P. Graves *et al.* Experimental verification of sawtooth control by energetic particles in ion cyclotron resonance heated JET tokamak plasmas. *Nuclear Fusion*, 50(5):052002, 2010. http://stacks.iop.org/0029-5515/50/i=5/a=052002.

[131] D.J. Campbell *et al.* Stabilization of sawteeth with additional heating in the JET tokamak. *Physics Review Letter*, 60(21):2148–2151, 1988. http://link.aps.org/doi/10.1103/PhysRevLett.60.2148.

[132] P.A. Duperrex *et al.* Global sawtooth instability measured by magnetic coils in the JET tokamak. *Nuclear Fusion*, 32(7):1161–1180, 1992. http://stacks.iop.org/0029-5515/32/i=7/a=I07.

[133] R.J. Buttery *et al.* Cross-machine NTM physics studies and implications for ITER. *Fusion Energy - 20th IAEA Proceedings of an International Conference*, pages EX/7–1, 2004. http://www-naweb.iaea.org/napc/physics/fec/fec2004/papers/ex_7-1.pdf.

[134] M. Schittenhelm *et al.* Analysis of coupled MHD modes with mirnov probes in ASDEX Upgrade. *Nuclear Fusion*, 37(9):1255–1270, 1997. http://stacks.iop.org/0029-5515/37/i=9/a=I06.

[135] K. Nagasaki *et al.* Stabilization of neoclassical tearing mode by ECCD and its evolution simulation on JT-60U tokamak. *Nuclear Fusion*, 45(12):1608–1617, 2005. http://stacks.iop.org/0029-5515/45/i=12/a=016.

[136] R. Prater *et al.* Stabilization and prevention of the 2/1 neoclassical tearing mode for improved performance in DIII-D. *Nuclear Fusion*, 47(5):371–377, 2007. http://stacks.iop.org/0029-5515/47/i=5/a=001.

[137] M. Lauret *et al.* Demonstration of sawtooth period locking with power modulation in TCV plasmas. *Nuclear Fusion*, 52(6):062002, 2012. http://stacks.iop.org/0029-5515/52/i=6/a=062002.

[138] H. Reimerdes *et al.* Power distribution in the snowflake divertor in TCV. *Plasma Physics and Controlled Fusion*, 55(12):124027, 2013. http://stacks.iop.org/0741-3335/55/i=12/a=124027.

[139] T. Lunt *et al.* First EMC3-Eirene simulations of the TCV snowflake divertor. *Plasma Physics and Controlled Fusion*, 56(3):035009, 2014. http://stacks.iop.org/0741-3335/56/i=3/a=035009.

[140] H. Reimerdes *et al.* Experimental investigation of neon seeding in the snowflake configuration. *Submitted to Journal of Nuclear Materials*, 2014.

[141] G.P. Canal *et al.* The influence of the $\vec{E} \times \vec{B}$ drift on the target profiles of the TCV snowflake divertor. *To be submitted to Nuclear Fusion*, 2014.

[142] D.D. Ryutov *et al.* A snowflake divertor: a possible way of improving the power handling in future fusion facilities. *Fusion Energy - 22th IAEA Proceedings of an International Conference*, pages IC/P4–8, 2008. http://www-naweb.iaea.org/napc/physics/FEC/FEC2008/papers/ic_p4-8.pdf.

[143] M.V. Umansky *et al.* Analysis of geometric variations in high-power tokamak divertors. *Nuclear Fusion*, 49(7):075005, 2009. http://stacks.iop.org/0029-5515/49/i=7/a=075005.

[144] R.J. Goldston and P.H. Rutherford. *Introduction to plasma physics.* Institute of Physics Publishing, London, 1997.

[145] J.A. Bittencourt. *Fundamentals of Plasma Physics.* Springer, New York, 2004.

[146] F.L. Hinton and R.D. Hazeltine. Theory of plasma transport in toroidal confinement devices. *Reviews of Modern Physics*, 48(2):239–308, 1976. http://link.aps.org/doi/10.1103/RevModPhys.48.239.

[147] W.M. Tang *et al.* Microinstability theory in tokamaks. *Nuclear Fusion*, 18(8):1089–1160, 1978. http://stacks.iop.org/0029-5515/18/i=8/a=006.

[148] F.M. Levinton *et al.* Improved confinement with reversed magnetic shear in TFTR. *Physical Review Letters*, 75:4417–4420, 1995. http://link.aps.org/doi/10.1103/PhysRevLett.75.4417.

[149] E.A. Lazarus *et al.* Higher fusion power gain with current and pressure profile control in strongly shaped DIII-D tokamak plasmas. *Physical Review Letters*, 77:2714–2717, 1996. http://link.aps.org/doi/10.1103/PhysRevLett.77.2714.

[150] P.C. Efthimion *et al.* Observation of neoclassical transport in reverse shear plasmas on TFTR. *Nuclear Fusion*, 39(11Y):1905–1909, 1996. http://stacks.iop.org/0029-5515/39/i=11Y/a=333.

[151] J.W. Connor and H.R. Wilson. Survey of theories of anomalous transport. *Plasma Physics and Controlled Fusion*, 36(5):719–795, 1994. http://stacks.iop.org/0741-3335/36/i=5/a=002.

[152] A.V. Chankin *et al.* The effect of BT reversal on the asymmetries between the strike zones in single null divertor discharges: experiment and theories. *Plasma Physics and Controlled Fusion*, 36(11):1853–1864, 1994. http://stacks.iop.org/0741-3335/36/i=11/a=011.

[153] I.H. Hutchinson *et al.* The effects of field reversal on the Alcator C-mod divertor. *Plasma Physics and Controlled Fusion*, 37(12):1389–1406, 1995. http://stacks.iop.org/0741-3335/37/i=12/a=004.

[154] A.V. Chankin *et al.* Classical drifts in the tokamak SOL and divertor: models and experiment. *Journal of Nuclear Materials*, 241-243(0):199–213, 1997. http://www.sciencedirect.com/science/article/pii/S0022311597800402.

[155] R.D. Monk *et al.* Interpretation of ion flux and electron temperature profiles at the JET divertor target during high recycling and detached discharges. *Journal of Nuclear Materials*, 241-243(0):396 – 401, 1997. http://www.sciencedirect.com/science/article/pii/S0022311597800712.

[156] A. Loarte *et al.* Plasma detachment in JET Mark I divertor experiments. *Nuclear Fusion*, 38(3):331–371, 1998. http://stacks.iop.org/0029-5515/38/i=3/a=303.

[157] J.A. Boedo *et al.* Electric field-induced plasma convection in tokamak divertors. *Physics of Plasmas*, 7(4):1075–1078, 2000. http://scitation.aip.org/content/aip/journal/pop/7/4/10.1063/1.873915.

[158] A.V. Chankin *et al.* Possible explanation for doubly peaked profiles at the divertor target in JET. *Plasma Physics and Controlled Fusion*, 43(3):299–304, 2001. http://stacks.iop.org/0741-3335/43/i=3/a=305.

[159] F.L. Hinton and G.M. Staebler. Collisional transport near the separatrix of a tokamak and the H-mode. *Nuclear Fusion*, 29(3):405–414, 1989. http://stacks.iop.org/0029-5515/29/i=3/a=004.

[160] A.V. Chankin *et al.* Global circulation of drift flows in the sol and divertor and its impact on divertor asymmetries. *Controlled Fusion and Plasma Physics: Proc. 30th EPS, St. Petersburg*, ECA Vol. 27A, 2003. http://epsppd.epfl.ch/StPetersburg/PDF/O4_001C.PDF.

[161] H. Takase. Guidance of divertor channel by cusp-like magnetic field for tokamak devices. *Journal of the Physical Society of Japan*, 70(3):609–612, 2001. http://journals.jps.jp/doi/abs/10.1143/JPSJ.70.609.

[162] M. Kotschenreuther *et al.* Scrape off layer physics for burning plasmas and innovative divertor solutions. *Fusion Energy - 20th IAEA Proceedings of an International Conference*, pages IC/P6–43, 2004. http://www-naweb.iaea.org/napc/physics/fec/fec2004/papers/ic_p6-43.pdf.

[163] M. Kotschenreuther *et al.* Magnetic geometry and physics of advanced divertors: The x-divertor and the snowflake. *Cornell University Library*, 2013. http://arxiv.org/abs/1309.5289.

[164] P.M. Valanju *et al.* Super-X divertors and high power density fusion devices. *Physics of Plasmas*, 16(5):056110, 2009. http://scitation.aip.org/content/aip/journal/pop/16/5/10.1063/1.3110984.

[165] G. Fishpool *et al.* Mast-upgrade divertor facility and assessing performance of long-legged divertors. *Journal of Nuclear Materials*, 438, Supplement(0):S356 – S359, 2013. http://www.sciencedirect.com/science/article/pii/S0022311513000755.

[166] F. Piras *et al.* "Snowflake" H-mode in a tokamak plasma. *Physical Review Letters*, 105:155003, 2010. http://link.aps.org/doi/10.1103/PhysRevLett.105.155003.

[167] V.A. Soukhanovskii *et al.* Snowflake divertor configuration in NSTX. *Journal of Nuclear Materials. Proceedings of the 19th International Conference on Plasma-Surface Interactions in Controlled Fusion*, 415(1, Supplement):S365 – S368, 2011. http://www.sciencedirect.com/science/article/pii/S0022311510003570.

[168] V.A. Soukhanovskii *et al.* Snowflake divertor configuration studies in National Spherical Torus Experiment. *Physics of Plasmas*, 19(8):082504, 2012. http://scitation.aip.org/content/aip/journal/pop/19/8/10.1063/1.4737117.

[169] V.A. Soukhanovskii *et al.* Advanced divertor configurations with large flux expansion. *Journal of Nuclear Materials*, 438, Supplement(0):S96–S101, 2013. http://www.sciencedirect.com/science/article/pii/S0022311513000238.

[170] S.L. Allen *et al.* Initial snowflake divertor physics studies on DIII-D. *Fusion Energy - 24th IAEA Proceedings of an International Conference*, pages PD/1–2, 2012. http://www-naweb.iaea.org/napc/physics/FEC/FEC2012/presentations/801_PD12.pdf.

[171] S.Yu. Medvedev *et al.* Edge stability and pedestal profile sensitivity of snowflake diverted equilibria in the TCV tokamak. *Contributions to Plasma Physics*, 50(3-5):324–330, 2010. http://dx.doi.org/10.1002/ctpp.201010053.

[172] D.D. Ryutov *et al.* The magnetic field structure of a snowflake divertor. *Physics of Plasmas*, 15(9):092501, 2008. http://scitation.aip.org/content/aip/journal/pop/15/9/10.1063/1.2967900.

[173] D.D. Ryutov *et al.* A snowflake divertor: a possible solution to the power exhaust problem for tokamaks. *Plasma Physics and Controlled Fusion*, 54(12):124050, 2012. http://stacks.iop.org/0741-3335/54/i=12/a=124050.

[174] D.D. Ryutov *et al.* Local properties of the magnetic field in a snowflake divertor. *Plasma Physics and Controlled Fusion*, 52(10):105001, 2010. http://stacks.iop.org/0741-3335/52/i=10/a=105001.

[175] D.D. Ryutov *et al.* Plasma convection near the magnetic null of a snowflake divertor during an ELM event. *Contributions to Plasma Physics*, 52(5-6):539–543, 2012. http://dx.doi.org/10.1002/ctpp.201210046.

[176] A.A. Ivanov *et al.* The SPIDER code. Solution of direct and inverse problems for free boundary tokamak plasma equilibrium. *Keldysh Institute preprint*, 39, 2009. http://www.keldysh.ru/papers/2009/prep39/prep2009_39.pdf.

[177] A.A. Ivanov *et al.* The SPIDER code. Solution of tokamak plasma equilibrium problem with anisotropic pressure and rotation. *Keldysh Institute preprint*, 81, 2012. http://www.keldysh.ru/papers/2012/prep2012_81.pdf.

[178] B. Labit *et al.* Properties of snowflake diverted H-mode plasmas in TCV. *Conference on Plasma Physics: 39th EPS, Stockholm*, ECA Vol. 36F:P5.091, 2012. http://ocs.ciemat.es/epsicpp2012pap/pdf/P5.091.pdf.

[179] A. Loarte *et al.* Multi-machine scaling of the divertor peak heat flux and width for L-mode and H-mode discharges. *Journal of Nuclear Materials*, 266–269(0):587 – 592, 1999. http://www.sciencedirect.com/science/article/pii/S002231159800590X.

[180] A.M. Runov *et al.* 3D Monte Carlo modelling of edge plasmas in fusion experiments. *Journal of Plasma Physics*, 72(6):1109–1112, 2006. http://dx.doi.org/10.1017/S0022377806005745.

[181] Y. Feng *et al.* 3D edge modeling and island divertor physics. *Contributions to Plasma Physics*, 44(1-3):57–69, 2004. http://dx.doi.org/10.1002/ctpp.200410009.

[182] Y. Feng *et al.* Formulation of a Monte Carlo model for edge plasma transport. *Controlled Fusion and Plasma Physics: Proc. 27th EPS, Budapest*, ECA Vol. 24B, 2000. http://epsppd.epfl.ch/Buda/pdf/p3_098.pdf.

[183] H.G Frerichs. Three-dimensional plasma transport in open chaotic magnetic fields: A computational assessment for tokamak edge layers. *PhD thesis no.82, Rheinisch-Westfaelische Technische Hochschule (RWTH), 52062 Aachen, Germany*, 2010. http://darwin.bth.rwth-aachen.de/opus3/volltexte/2010/3272/.

[184] S.I. Braginskii. Transport processes in plasma. *Reviews of Plasma Physics*, 1:205–311, 1965. http://people.hao.ucar.edu/judge/homepage/PHSX515/fall2012/Braginskii1965.pdf.

[185] D. Reiter. http://www.eirene.de.

[186] D. Reiter *et al.* The EIRENE and B2-EIRENE codes. *Fusion Science and Technology*, 47(2):172–186, 2005. http://epubs.ans.org/download/?a=698.

[187] R.K. Janev *et al.* http://www.eirene.de/report_4105.pdf.

[188] T.D. Rognlien *et al.* Two-dimensional electric fields and drifts near the magnetic separatrix in divertor tokamaks. *Physics of Plasmas*, 6(5), 1999. http://scitation.aip.org/content/aip/journal/pop/6/5/10.1063/1.873488.

[189] T.D. Rognlien *et al.* Influence of ExB and ∇B drift terms in 2-D edge/SOL transport simulations. *Journal of Nuclear Materials*, 266–269(0), 1999. http://www.sciencedirect.com/science/article/pii/S0022311598008356.

[190] M.J. Schaffer *et al.* Large E x B convection near the divertor X-point. *Journal of Nuclear Materials*, 290-293(0):530–536, 2001. http://www.sciencedirect.com/science/article/pii/S0022311500004980.

[191] G.P. Canal *et al.* Comparison between experiments and EMC3-Eirene simulations of the snowflake divertor in TCV. *Conference on Plasma Physics: 55th APS, Denver*, 58(16):PP8.46, 2013. http://meetings.aps.org/Meeting/DPP13/Session/PP8.46.

[192] P.C. Stangeby *et al.* Radial and poloidal ExB drifts in the scrape-off layers of a divertor tokamak: Effects on in/out asymmetries, plasma detachment at the targets, and divertor biasing. *JET Preprints and Reports*, JET-P(95)07, 1995. http://www.iop.org/Jet/article?JETP95001&JETP95007.

[193] P.C. Stangeby and A.V. Chankin. Simple models for the radial and poloidal E x B drifts in the scrape-off layer of a divertor tokamak: Effects on in/out asymmetries. *Nuclear Fusion*, 36(7):839, 1996. http://stacks.iop.org/0029-5515/36/i=7/a=I02.

[194] L. Enke *et al.* Nonuniformity correction algorithms of IRFPA based on radiation source scaling. *5th International Conference on Information Assurance and Security*, 1:317–321, 2009. http://dx.doi.org/10.1109/IAS.2009.110.

[195] A.E. Mudau. Non-uniformity correction and bad pixel replacement on LWIR and MWIR images. *Electronics, Communications and Photonics Conference (SIECPC),*

Saudi International, pages 1–5, 2011. http://dx.doi.org/10.1109/SIECPC.2011.5876937.

[196] D.A. Scribner *et al.* Nonuniformity correction for staring IR focal plane arrays using scene based techniques. *Procedings of the SPIE: Infrared Detectors and Focal Plane Arrays*, 1308:224–233, 1990. http://dx.doi.org/10.1117/12.21730.

[197] W.S. Ewing. Silicide mosaic array compensation. *Proceedings of the SPIE: Technical Issues in Infrared Detectors and Arrays*, 0409:102, 1983. http://dx.doi.org/10.1117/12.935743.

[198] E.L. Dereniak. *Optical radiation detectors.* Wiley, New York, 1984.

[199] http://toothwalker.org/optics/vignetting.html#ref1.

[200] W. Isoz *et al.* Nonuniformity correction of infrared focal plane arrays. *Proceedings of the SPIE: Infrared Technology and Applications XXXI*, 5783:949–960, 2005. http://dx.doi.org/10.1117/12.606691.

Gustavo Paganini Canal
Curriculum Vitae

July/2014

Gustavo Paganini Canal

Personal Information

Full Name	Gustavo Paganini Canal (Brazilian nationality)
Date of Birth	August 2nd, 1983 (30 years old)
Professional Address	École Polytechnique Fédérale de Lausanne EPFL SB CRPP, Station 13 CH-1015 Lausanne, Switzerland Office: PPH 277 Tel: (+41) 21 693 3485 Cell: (+41) 79 379 9835 Web: crpp.epfl.ch
Electronic Address	gustavo.canal@epfl.ch or gustavocanal@hotmail.com

Education

2010 - 2014 **PhD. in Physics**
École Polytechnique Fédérale de Lausanne - EPFL
Lausanne, Switzerland
Title: **Sawtooth generated magnetic islands and the properties of the snowflake divertor**
Supervisor: Dr. Basil P. Duval and Dr. Holger Reimerdes
Keywords: Nuclear fusion, MHD, NTMs, tokamak edge physics, snowflake divertor, simulations of plasma edge, infrared thermography, Langmuir probes, simulations of heat transport deposited by plasma-wall interaction, diagnostics data interpretation.

2007 - 2009 **Msc. in Physics**
Brazilian Center for Physics Research - CBPF
Rio de Janeiro, Brazil
Title: **Development and characterization of a plasma cleaner for nanotechnology processes**.
Supervisor: Prof. Dr. Ricardo M. O. Galvão
Keywords: Inductively coupled plasmas, RF systems, nanotechnology and plasmas produced by pulsed lasers.

2003 - 2006 **Bachelor in Physics**
Federal University of Espírito Santo - UFES
Espírito Santo, Brazil
Keywords: Basic plasma physics, plasma processing of natural gas and petroleum at low and atmospheric pressure, DBD discharges.

2001 - 2002 **Technical Education in Electrotechnics**
Federal Center of Technological Education - CEFET
Espírito Santo, Brazil
Keywords: Design and construction of electrical and electronic devices; electrical projects and facilities.

Research & Professional Experience

2010 - 2014 **École Polytechnique Fédérale de Lausanne - EPFL, Switzerland**

1. Responsible for an infrared camera for diagnosing plasma-wall interactions in TCV:
   - Development of a heated tile for image calibration
   - Hardware maintenance
   - Data interpretation via simulations based on 2D (THEODOR) and 3D (ANSYS) heat flux analysis codes

2. Competence in running the code-package EMC3, a code used for plasma edge simulations in 3D configurations, coupled to Eirene, a neutral gas transport code.

3. Knowledge on the use of electron cyclotron resonance heating and current drive for sawtooth control and NTM stabilization, and on experimental data analysis/interpretation, e.g. for providing a better insight into the triggering mechanism of NTMs by sawteeth.

4. Teaching activities (Exercises):
   Plasma Physics I and II (Bachelor); Quantum Effects (Bachelor); Nuclear Fusion and Plasma Physics (Master)

2007 - 2009 **Brazilian Center for Physics Research - CBPF, Brazil**

1. Development of an RF power supply, based on vacuum tubes, for an inductively coupled plasma system used for surface cleaning and treatment.

2. Development of a system for deposition of thin films via plasmas produced by laser ablation

2004 - 2006 **Federal University of Espírito Santo - UFES, Brazil**

1. Development of a system for surface treatment of stainless steel via plasma nitriding using low pressure glow discharges.

2. Hydrogen production from natural gas via hydrogen reforming using plasma torch and development of an alternative way using low pressure glow discharges.

3. Development of two systems for plasma processing of heavy and extra heavy petroleum:
   - High voltage atmospheric pressure hydrogenic plasmas using discharges with dielectric barrier (DBD).
   - Low pressure hydrogenic glow discharges.

Honors & Awards

1. **Invited Talk at the 18th MHD Control Workshop - MHD Control for Steady State Burning Plasmas, New Mexico - USA**
   "*Fast seeding of NTMs by sawtooth crashes and implications on their preemption*"
   November 18-20, 2013

2. **Best Poster Prize at the 10th Brazilian Meeting on Plasma Physics, São Paulo - Brazil**
   "*Corrections to the electron energy distribution function in Langmuir probe measurements*"
   November 22-25, 2009

Languages Skills

Portuguese	First language
English	Proficiency level (C2)
Spanish	Independent user level (B1)
French	Independent user level (B1)

Computational & Professional Skills

Well versed in MATLAB programming
Basic knowledge in IDL programming
Expertise in electrical and electronic circuitry
Specialization in infrared imaging systems
Ability to work in a team

Reference Contact

Prof. Ambrogio Fasoli
EPFL SB CRPP, Station 13
CH-1015 Lausanne, Switzerland
Phone: (+41) 21 693 3492
E-mail: ambrogio.fasoli@epfl.ch

Dr. Holger Reimerdes
EPFL SB CRPP, Station 13
CH-1015 Lausanne, Switzerland
Phone: (+41) 21 693 6003
E-mail: holger.reimerdes@epfl.ch

Dr. Basil Duval
EPFL SB CRPP, Station 13
CH-1015 Lausanne, Switzerland
Phone: (+41) 21 693 3428
E-mail: basil.duval@epfl.ch

Dr. Olivier Sauter
EPFL SB CRPP, Station 13
CH-1015 Lausanne, Switzerland
Phone: (+41) 21 693 5478
E-mail: olivier.sauter@epfl.ch

Dr. Tilmann Lunt
Max-Planck-Institut für Plasmaphysik, E2M
Boltzmannstr. 2, 85748 Garching bei München, Germany
Phone: (+49) 89 3299 1213
E-mail: tilmann.lunt@ipp.mpg.de

Prof. Ricardo M. O. Galvão
Instituto de Física/USP
Rua do Matão, Travessa R, 187, Cidade Universitária
05508090 São Paulo, Brasil
Phone: (+55) 11 3091 7069
E-mail: rgalvao@if.usp.br

Publications

First Author Peer-Reviewed Journal Articles

1. **G.P. Canal** *et al.*, "*The influence of particle drifts on the target profiles of the TCV snowflake divertor*", to be submitted to Nuclear Fusion.

2. **G.P. Canal** *et al.*, "*Fast seeding of NTMs by sawtooth crashes in TCV and their preemption using ECRH*", Nuclear Fusion 53 (2013) 113026.

3. **G.P. Canal** *et al.*, "*Characterization of the transition from collisional to stochastic heating in RF discharges*", Journal of Physics D: Applied Physics 43 (2010) 025209.

4. **G.P. Canal** *et al.*, "*Design and characterization of an RF plasma cleaner*", Brazilian Journal of Physics 40 (2010) 108.

5. **G.P. Canal** *et al.*, "*An approach to a non-LTE Saha equation based on the Druyvesteyn energy distribution function: a comparison between the electron temperature obtained from OES and the Langmuir probe analysis*", Journal of Physics D: Applied Physics 42 (2009) 135202.

Co-Author Peer-Reviewed Journal Articles

1. W.A.J. Vijvers *et al.*, "*First experimental demonstration of heat load mitigation with an X-divertor in a tokamak*", to be submitted to Nuclear Fusion.

2. N.A. Kirneva *et al.*, "*Experimental characterization of Ohmic and ECRH L-mode plasmas at high density plasmas*", submitted to Plasma Physics and Controlled Fusion.

3. H. Reimerdes *et al*., "*Experimental investigation of neon seeding in the snowflake configuration*", submitted to Journal of Nuclear Materials

4. F. Nespoli *et al*., "*Heat loads in inboard limited L-mode plasmas in TCV*", submitted to Journal of Nuclear Materials

5. H. Reimerdes *et al.*, "*Power distribution in the snowflake divertor in TCV*", Plasma Physics and Controlled Fusion 55 (2013) 124027.

6. T. Lunt *et al.*, "*First EMC3-Eirene simulations of the TCV snowflake divertor*", Plasma Physics and Controlled Fusion 56 (2014) 035009.

7. W.A.J. Vijvers *et al.*, "*Power exhaust in the snowflake divertor for L- and H-mode TCV tokamak plasmas*", Nuclear Fusion 45 (2014) 023009.

8. V.A. Soukhanovskii *et al., "Advanced divertor configurations with large flux expansion",* Journal of Nuclear Materials, 438 (2013) 96.

9. Yu.K. Kuznetsov *et al.*, ''*Long-distances correlations in TCABR biasing experiments*'', Nuclear Fusion, 52 (2012) 063004.

10. A. Pochelon *et al.*, ''*Recent TCV results – innovative plasma shaping to improve plasma properties and insight*'', Journal of Plasma and Fusion Research 7 (2012) 2502148.

11. F. Felici *et al.,* ''*Integrated real-time control of MHD instabilities using multi-beam ECRH/ECCD systems on TCV*'', Nuclear Fusion 52 (2012) 074001.

12. S. Nowak *et al.*, "*Evidence of neoclassical toroidal viscosity on the neoclassical tearing modes in TCV*", Journal of Physics 401 (2012) 012017.

13. H. Luna *et al.*, "*Nanostructured europium oxide thin films deposited by pulsed laser ablation of a metallic target in a He buffer atmosphere*", Journal of Vacuum Science & Technology A 28 (2010) 1092.

14. D.A. Souza *et al.*, "*Plasma nitriding of AISI304L and AISI 316L stainless steel: effect of time on the formation of S-phase and chromium nitrite*", Brazilian Journal of Vacuum Applications 28 (2009) 39.

First Author Contribution to Conferences

1. **G.P. Canal** *et al.*, "*Comparison between experiments and EMC3-Eirene simulations of the snowflake divertor in TCV*", 54th Annual Meeting of the APS Division of Plasma Physics, November 11-15, 2013.

2. **G.P. Canal** *et al.,* ''*Fast seeding of neoclassical tearing modes by sawtooth crashes in TCV*'', 39th EPS Conference on Plasma Physics, July 2-6, 2012.

3. **G.P. Canal** *et al.*, ''*Coupling between sawteeth and tearing modes in TCV*'', 38th EPS Conference on Plasma Physics, June 27 - July 1, 2011.

4. **G.P. Canal** *et al.*, ‘‘*Coupling between sawteeth and tearing modes in the TCV Tokamak*’’, Joint Annual Meeting of the Swiss Physical Society and Austrian Physical Society with Swiss and Austrian Society for Astronomy and Astrophysics, June 15 - 17, 2011.

5. **G.P. Canal** *et al.*, “*Corrections to the electron energy distribution function in Langmuir probe measurements*”, 10th Brazilian Meeting on Plasma Physics, November 22-25, 2009.

6. **G.P. Canal** *et al.*, “*Design and development of a plasma cleaner for microscopy*”, 9th Brazilian Meeting on Plasma Physics, November 25-28, 2007.

Co-Author Contribution to Conferences

1. S. Nowak *et al.,* “*(N)TM onset by central EC power deposition in FTU and TCV tokamak*”, 25th IAEA Fusion Energy Conference, October 13-18, 2014 (to be presented).

2. N. Kirneva *et al.,* “*High density regime in Ohmic TCV discharges with positive and negative triangularity*”, 25th IAEA Fusion Energy Conference, October 13-18, 2014 (to be presented).

3. B. Labit *et al.*, “*Overview of recent snowflake divertor studies in TCV*”, 41st EPS Conference on Plasma Physics, June 23-27, 2014.

4. F. Nespoli *et al.*, ‘‘*Heat loads in inboard limited plasmas in TCV*’’, Joint Annual Meeting of the Swiss Physical Society and Austrian Physical Society with Swiss and Austrian Society for Astronomy and Astrophysics, June 30 – July 02, 2011.

5. F. Nespoli *et al*., “*Heat loads in inboard limited L-mode plasmas in TCV*”, 21st PSI - International Conference on Plasma Surface Interactions in Controlled Fusion Devices, May 26-30, 2014.

6. H. Reimerdes et al., “*Experimental investigation of neon seeding in the snowflake configuration in TCV*”, 21st PSI - International Conference on Plasma Surface Interactions in Controlled Fusion Devices, May 26-30, 2014.

7. W.A.J. Vijvers *et al.*, “*Power exhaust in all geometric variations of the snowflake divertor on TCV*”, 54th Annual Meeting of the APS Division of Plasma Physics, November 11-15, 2013.

8. H. Reimerdes *et al.*, “*Power distribution in the Snowflake Divertor in TCV*”, 40th EPS Conference on Plasma Physics, July 01-05, 2013.

9. T.P. Goodman *et al.*, “*Real-Time multi-EC-actuator MHD control in TCV*”, Joint Meeting of the 20th Topical Conference on Radio Frequency Power in Plasmas and the US Japan RF Physics, June 25-28, 2013.

10. S. Nowak *et al.*, "*Plasma rotation and NTM onset driven by central EC deposition in TCV Tokamak*", Joint Meeting of the 20th Topical Conference on Radio Frequency Power in Plasmas and the US Japan RF Physics, June 25-28, 2013.

11. B. Labit *et al.*, "*Edge physics in TCV plasmas with snowflake divertor*", U.S – E.U. Joint Transport Task Force Workshop, April 9-12, 2013.

12. H. Reimerdes *et al.,* "*Divertor configurations, Results and Plans on TCV*", 20th European Fusion Physics Workshop, December 3-5, 2012.

13. B.P. Duval *et al.,* "*Status of experimental snowflake configurations worldwide*", 20th European Fusion Physics Workshop, December 3-5, 2012.

14. D. Testa *et al.,* "*Sawtooth and triggering mechanism for tearing modes on the tokamak à configuration variable*", 54th Annual Meeting of the APS Division of Plasma Physics, October 29 – November 2, 2012.

15. E. Lazzaro *et al.,* "*Triggerless onset and effect of natural rotation on neoclassical tearing modes in the TCV tokamak*", 24th IAEA Fusion Energy Conference, October 8-13, 2012.

16. W.A.J. Vijvers *et al.,* ''*Reduction of peak wall power loads in L- and H-mode tokamak plasmas in TCV with the snowflake divertor*'', 24th IAEA Fusion Energy Conference, October 8-13, 2012.

17. B.P. Duval *et al., ''Real time ELM, NTM and sawtooth control on TCV''*, 24th IAEA Fusion Energy Conference, October 8-13, 2012.

18. N.A. Kirneva *et al.,* ''*Experimental investigation of plasma confinement in reactor relevant conditions in TCV plasmas with dominant electron heating*'', 24th IAEA Fusion Energy Conference, October 8-13, 2012.

19. S. Nowak *et al.,* ''*Evidence of neoclassical toroidal viscosity on the neoclassical tearing modes in TCV tokamak*'', Theory of Fusion Plasmas, Joint Varenna-Lausanne International Workshop, August 27-31, 2012.

20. T.P. Goodman *et al.,* ''*Real-time control of MHD instabilities with multi-source EC actuators*'', 39th EPS Conference on Plasma Physics, July 02-06, 2012.

21. B. Labit *et al.,* ''*Properties of snowflake diverted H-Mode plasmas in TCV*'', 39th EPS Conference on Plasma Physics, July 02-06, 2012.

22. F. Felici *et al.,* ''*Real-time control of multiple MHD instabilities on TCV by ECRH/ECCD*'', 17th Joint Workshop on Electron Cyclotron Emission and Electron Cyclotron Resonance Heating, May 7-10, 2012.

23. A. Pochelon *et al.*, ''*Recent TCV results – Innovative plasma shaping to improve plasma properties and insight*'', 21st International Toki Conference, November 28 – December 1, 2011.

24. H. Reimerdes *et al.*, ‘‘*Transport studies in the snowflake divertor in TCV*’’, 53rd Annual Meeting of the APS Division of Plasma Physics, November 14-18, 2011.

25. D. Testa *et al.*, ‘‘*Recent sawtooth studies on the TCV tokamak à configuration variable*’’, 53rd Annual Meeting of the APS Division of Plasma Physics, November 14-18, 2011.

26. T.P. Goodman *et al.*, ‘‘*Individual sawtooth pacing by synchronized ECCD in TCV*’’, Joint Meeting of the 19th Topical Conference on Radio Frequency Power in Plasmas and the US Japan RF Physics, June 1-3, 2011.

27. R. Heringer *et al.*, “*Decomposition of natural gas using electrical discharge with non-confined arc*”, XXIX Brazilian Meeting on Condensed Matter Physics, 2006.